# Commonalities in the emplacement of cooling-limited lavas: insights from the 2011-2012 Cordón Caulle rhyolitic eruption

Presented for the degree of Doctor of Philosophy by

**Nathan Alec Magnall MESci (Lpool)**

Initial submission January 2018

Final submission July 2018

Lancaster Environment Centre,

Lancaster University

**Declaration**

I, Nathan Alec Magnall, hereby declare that the contents of this thesis result from my own work, and that no part of the work has been submitted in substantially the same form for the award of a higher degree elsewhere.

“The entire universe has been neatly divided into things to (a) mate with, (b) eat, (c) run away from, and (d) rocks”

*– Terry Pratchett, Equal Rites –*

The following is a rather lengthy discussion of something that, under normal conditions, classifies as d, exceptional circumstances classifies as c, and should under no circumstances be considered as either a or b.

**Abstract**

Lava flows pose a risk to infrastructure and communities near many volcanoes. Although the emplacement processes of low-viscosity basaltic lava flows are relatively well studied, the infrequency of silicic eruptions has limited our understanding of the emplacement of high-viscosity rhyolitic lavas. The 2011-2012 eruption of Puyehue-Cordón Caulle in southern Chile provided a unique opportunity to make scientific observations of an active rhyolitic lava flow. The thesis utilises a multiscale approach to draw comparisons between the emplacement of mafic and silicic lavas by building on the established understanding of basaltic flows. The thesis demonstrates the similarities and differences in the emplacement of cooling-limited lavas at contrasting ends of the compositional spectrum.

Observations and quantitative models of lava flow lengthening demonstrate that advance of the Cordón Caulle lava flow was controlled in its latter phases by a cooled surface crust, which suggests similarities to the rheological control of cooling-limited basaltic lava flows. Cessation in flow advance was followed by breakout formation, the first such observations in a rhyolitic lava flow. Breakout formation was triggered by a pressure build-up at the flow margins, due to continued supply of lava along preferential thermal pathways, as well as late stage vesiculation of the flow core. The breakouts developed a morphological range classified into domed, petaloid, rubbly and cleft-split, which reflect the results of advance and inflation processes. Many silicic lavas show pumice diapirs and crease structures at their surface, but such features were rarely observed at Cordón Caulle. The inferred strong surface crust of the Cordón Caulle lava flow, as well as higher viscosity than other rhyolite lava flows, may have locally impeded upwelling to the lava surface, so favouring breakout formation. Insights gained from Cordón Caulle will aid the interpretation of ancient silicic lava flows, and help anticipate the hazards posed by future eruptions of rhyolitic lava.

## Acknowledgements

Contrary to the declaration on the first page, the substantial contribution of my supervisors to this thesis cannot be ignored. I wish to thank Mike James and Hugh Tuffen for their continuous help and support over the last three years, as well as Charlotte Vye-Brown (BGS) for her assistance throughout the project. I am further indebted to Mike and Hugh for opening opportunities for me to have adventures in Chile, Sicily, Germany and the USA. Highlights have included flying in a helicopter (courtesy of BBC Earth), bivvying under the southern hemisphere stars, and watching the glow from an erupting Mt Etna. None of which would have been possible without the financial support of my funders: NERC Envision, BGS BUFI, Lancaster University FST, and Lancaster University Graduate College.

I am also grateful to my co-authors Ian Schipper, Jon Castro, Ashley Davies, Jon Fink, Steve Anderson, and Einat Lev for their assistance on various aspects of the project. I am thankful to Jon Fink, Steve Anderson, and Curtis Manley for my introduction to the complexities of rhyolite lava flows in the USA, and for their continuous encouragement throughout the project (including some very late night skype meetings). In Lancaster, the support of the rest of the research group, as well as those that I shared an office with over the years is greatly appreciated. A special thanks also goes to all those who helped distract me from the PhD through climbing, hiking, fencing or trips to the pub. Furthermore, a big thanks to my parents for their support and the regular meet ups in the fells. Finally, I am not sure I would have got this done without Dani, thanks for sticking it out alongside me.

**Contents**

## List of figures

### Section Two



### Section Three

## List of tables

**Digital supplementary material**

**Flow_length_models.xlsx** EXCEL spreadsheet of flow length modelling

**3D_model_breakout.pdf** 3-D PDF of a Cordón Caulle breakout

**3D_model_diapir.pdf** 3-D PDF of a pumice diapir

**Buoyant_rise_models.xlsx** EXCEL spreadsheet of buoyant rise

# 1 Introduction

Volcanic eruptions produce a number of hazards that can pose a risk to local and distal communities. These include the products of explosive eruptions, such as ash, pyroclastic density currents and bombs, as well as the production of lava flows and domes in effusive eruptions. Unlike the hazards presented by explosive eruptions (Nakada, 2000; Prata and Rose, 2000), effusive eruptions rarely present a risk to human life (Peterson and Tilling, 2000) due to their slow advance rate (from metres up to ~2 kilometres per hour). However, lava flows present a direct hazard to infrastructure and, as a consequence, communities can require evacuation, particularly if attempts to halt or divert the lava flows fail (Pinkerton, 1987). In contrast, where lava flows and domes emplace on steep slopes, collapse of their front can represent a direct threat to life by generating highly hazardous pyroclastic density currents (e.g. Nakada et al., 1995; Sparks et al., 2000; Watts et al., 2002).

Extensive studies of frequently erupted basaltic lava flows have facilitated attempts to reduce the potential risk of lava flow inundation through mitigation strategies (Williams and Moore, 1983; Barberi et al., 1993; Williams, 1997). Such strategies have included spraying seawater onto lava flows during the eruption of Eldfell on Heimaey (Iceland) in 1973, with the aim of cooling the lava, thus increasing the viscosity and promoting the development of a restraining surface crust (Williams and Moore, 1983; Williams, 1997). Attempts have also been made to block lava tubes in the upper reaches of the 1991-1992 Mt Etna lava flow in order to trigger proximal breakout formation, reducing the volume of lava that reached the flow front (Barberi et al., 1993). Artificial barriers have also been used to some success to reduce the advance rate of a lava flow (Barberi et al., 1993). The success of such mitigation strategies is predicated on a thorough understanding of the processes that control lava flow emplacement.

In addition to direct mitigation strategies, numerous attempts have been made to model likely areas of lava inundation, in order to assess the most at risk areas (Crisci et al., 1986; Hidaka et al., 2005; Vicari et al., 2007; Hérault et al., 2011). Such flow modelling studies have primarily focussed on the emplacement of frequently erupted higher temperature, low-viscosity, and low-silica (basaltic) lava flows. Fewer studies have modelled the emplacement of high-viscosity, high-silica content (e.g. dacitic and rhyolitic) lava flows (e.g. Manley, 1992; Castruccio et al., 2013), partially due to the lack of observable, contemporaneous eruptions with which to compare modelled results.

The 2011-2012 eruption of Puyehue-Cordón Caulle provides a unique opportunity to build upon established models of the emplacement of rhyolitic lava flows. This eruption began on 4 June 2011 with an explosive Plinian phase (Silva Parejas et al., 2012; Castro et al., 2013). The Plinian activity subsided into an explosive-effusive eruption with the production of an extensive rhyolite lava flow (Schipper et al., 2013). Advance of this lava flow was observed to stall whilst effusion continued, and numerous (>80) breakouts formed (Tuffen et al., 2013; Farquharson et al., 2015). Effusion from the vent ended in March 2012, as indicated by the ceasing of seismicity at the vent, but the lava flow was observed to still be advancing in January 2013 (Tuffen et al., 2013). Breakouts have been previously documented from basaltic flows, and thus their presence at Cordón Caulle points towards commonalities in cooling-limited flow development that transcend orders of magnitude differences in magma rheology (Tuffen et al., 2013).

This work aims to understand potential process similarities in the emplacement of mafic and silicic cooling-limited lava flows. To this end, the focus on Cordón Caulle provides novel information on the emplacement of a cooling-limited silicic lava flow. The three papers presented in this thesis aim to improve our understanding of the rheological controls on the emplacement of the Cordón Caulle lava flow, the processes that contributed to breakout formation, and the processes that occurred during the

emplacement of comparable Holocene rhyolite lava flows in the western USA. Finally, commonalities in the emplacement processes, and subsequent flow features, between mafic and silicic lava flows are suggested.

The results presented within this thesis can aid our forecasting of the outcomes from future eruptions of silicic lava flows. The relative infrequency of such eruptions means that a more immediate opportunity would be in the re-interpretation of ancient volcanic facies, for which considerable effort has already been expended (Section 2; Fink, 1980a; Fink, 1980b; Bonnichsen, 1982; Fink, 1983; Bonnichsen and Kauffman, 1987; Manley and Fink, 1987; Stevenson et al., 1994a; Stevenson et al., 1994b; Smith and Houston, 1995; Smith, 1996; Castro and Cashman, 1999; Castro et al., 2002a). Finally, the analysis of the processes that contribute to breakout formation in silicic lava flows may prove useful for the forecasting of breakout locations during flow emplacement, as such features pose a challenge when predicting lava advance patterns.

## 1.1 Glossary of terms

For clarity, a glossary of terms as used in the thesis is as follows:

- *Breakout* – A new lobe that forms from a stalled or slowed portion of a lava flow. Breakouts are associated with cooling-limited lava flows, and usually form when flow advance slows or stops whilst magma supply continues. Under these conditions, the internal flow pressure increases until it exceeds the strength of the restraining surface crust and a breakout is formed.
- *Cooling-limited lava flow* – A lava flow that has ceased to advance due to the formation of a strong cooled surface crust, despite continued effusion at the vent.
- *High-silica/silicic lava* – Lavas with a $SiO_2$ content greater than ~60%, i.e. dacitic and rhyolitic lavas.
- *High-silica rhyolite* – Rhyolite lavas with a bulk $SiO_2$ content greater than 70%.

- *High-viscosity* – Lavas with a viscosity/apparent viscosity greater than ~$10^7$ Pa s; note that this is linked to composition.
- *Lava coulée* – A thick (up to 250 m) body of lava formed when a lava dome has started to spread and advance downslope.
- *Lava dome* – A domed build-up of lava over the vent. The lava typically has a substantial yield strength.
- *Lava flow* – Lava that, when effused, flows away from the vent, forming a long and thin morphological shape, i.e. not a dome that has spread and advanced downslope.
- *Lava tube* – Where a lava channel has developed a self-supporting roof that retains its shape when lava drains from within. These are mostly associated with pāhoehoe lava flows, but have been observed in 'a'ā flows.
- *Low-silica/mafic* – Lavas with a $SiO_2$ content less than ~60%, i.e. basaltic and andesitic lavas.
- *Low-silica rhyolite* – Rhyolite lavas with a bulk $SiO_2$ content between 68 – 70%.
- *Low-viscosity* – Lavas with a viscosity/apparent viscosity less than ~$10^7$ Pa s; note that this is linked to composition.
- *Preferential thermal pathway* – A connected region of mobile lava beneath a static surface crust along which most lava is supplied to a flow front. Unlike a lava tube, when lava drains from the thermal pathway there will not be a self-supporting roof.
- *Surface crust* – The confining outer portion of a lava flow. This includes the brittle surface clinker or rubble, which has little strength, and the more influential underlying cooled visco-elastic layer, which merges with the core of the lava.
- *Volume-limited lava flow* – A lava flow that stalls due to the cessation of effusion at the vent.

# 2 Lava flows and their emplacement

Our understanding of the emplacement processes of basaltic lava flows is relatively strong due to almost continuous, easily accessible, eruptions at volcanoes in locations such as Hawaii (e.g. Macdonald, 1953; Shaw et al., 1968; Swanson, 1973; Peterson and Tilling, 1980), and Italy (e.g. Pinkerton and Sparks, 1976; Guest et al., 1980; Kilburn and Lopes, 1988; Polacci and Papale, 1997). These lavas, typically divided into pāhoehoe and 'a'ā morphological types (Macdonald, 1953), can advance as lobes or channel-fed flow fronts (of order decimetre to metres in width for pāhoehoe, and metres to tens of metres for 'a'ā) that stall due to the presence of a cooled surface crust. The lobes can then inflate, due to the continued supply of lava, and the surface crust ruptures, leading to the development of a secondary flow, or breakout (Pinkerton and Sparks, 1976; Blake and Bruno, 2000; Lyman et al., 2005a). In contrast to basaltic lava flows, our understanding of the emplacement of high-viscosity and high-silica lavas has been hampered by a lack of observable eruptions. However, our understanding of the controls on the emplacement of andesitic and dacitic lava flows has been improved partly due to observations of recent eruptions (Kerr and Lyman, 2007; Castruccio et al., 2013; Castruccio and Contreras, 2016). These include the 1988-1990 Lonquimay eruption in Chile (Naranjo et al., 1992; Kerr and Lyman, 2007), eruptions at Arenal

Table 2.1: Contemporary eruptions of rhyolite lava flows and domes

| Volcano | Country | Year | Volume | Reference |
|---|---|---|---|---|
| Novarupta | USA (Alaska) | 1912 | ~0.005 $km^3$ | Fierstein and Hildreth (1992), Hildreth and Fierstein (2012) |
| Puyehue-Cordón Caulle | Chile | 1921-1922 | ~0.4 $km^3$ | Singer et al. (2008) |
| Tuluman | Papua New Guinea (St Andrew Strait) | 1953-1957 | N/A | Johnson and Smith (1974), Reynolds et al. (1980) |
| Puyehue-Cordón Caulle | Chile | 1960 | ~0.25 $km^3$ | Katsui and Katz (1967), Lara et al. (2004) |
| Chaitén | Chile | 2008-2009 | 0.8 $km^3$ | Bernstein et al. (2013), Pallister et al. (2013) |

volcano in Costa Rica (e.g. Linneman and Borgia, 1993), and the ongoing effusion from Santiaguito volcano in Guatemala (Harris and Flynn, 2002; Harris et al., 2003).

Rhyolite lava flows and domes are relatively rare eruptive products, with four such eruptions in the 20$^{th}$ century (Table 2.1), for which only limited observations were made during their emplacement. The recent eruption of Chaitén, Chile, in 2008-2009, allowed for detailed observations of the emplacement of a rhyolite lava dome, including both endogenous and exogenous growth, and a phase of spine extrusion (Bernstein et al., 2013; Major and Lara, 2013; Pallister et al., 2013). The rarity of effusive rhyolitic eruptions means that our understanding of the emplacement of rhyolite lava flows is reliant on interpreting observations of ancient flows from the USA (Fink, 1980a; Fink and Manley, 1987; Manley, 1992; Befus et al., 2015), New Zealand (Dadd, 1992; Stevenson et al., 1994a), Australia (Smith and Houston, 1995; Smith, 1996), and Japan (Furukawa et al., 2010; Furukawa and Uno, 2015). The following sections first outline the concepts of lava flow emplacement at their broadest, before providing details on the emplacement processes and features generated by mafic lava flows. The present understanding of the emplacement processes and features generated in silicic lava flows are then outlined. Finally, the factors influencing lava rheology are discussed, as rheology can have substantial impacts on lava emplacement processes and flow development.

## 2.1 Lava emplacement

Lava flows have been documented in a multitude of volcanic settings and show a variety of morphologies and types. The following sections outline current understanding of lava flow emplacement in both low and high-viscosity systems, focussing on late stage emplacement processes (e.g. breakout formation) and the development to cooling-limited lava flows.

### *2.1.1 Lava flow types*

Lava flows are classified by morphology into three main types (Macdonald, 1953; Harris et al., 2016): pāhoehoe, 'a'ā, and blocky (Fig. 2.1). Pāhoehoe flows are characterised by a smooth coherent surface crust, and develop as thin toes that are later inflated, often due to supply by a lava tube (Macdonald, 1953; Hon et al., 1994; Anderson et al., 1999). Many pāhoehoe flows have a ropy texture on their surface caused by compression of a ductile surface crust (Fink and Fletcher, 1978; Hon et al., 1994), while others have a slabby surface crust (Guest and Stofan, 2005). These surface crusts insulate the hotter flow interior (Swanson, 1973). 'A'ā flows lack a smooth coherent surface crust and are instead covered in rubble and clinker (Fig. 2.1B) relating to constant breakup of the surface crust (Macdonald, 1953; Kilburn, 1981; Hon, 2003). This clinker insulates a hotter flow core (Hon, 2003) and has no tensile strength, but the clinker can act to slow the advance of the flow front where it forms a barrier (Applegarth et al., 2010a). Pāhoehoe and 'a'ā are terms typically limited to mafic lava flows and are classifications derived from observations of the surfaces of Hawaiian lava flows. Numerous terms exist to further sub-divide these lava types, such as slabby pāhoehoe and spiny pāhoehoe (Harris et al., 2016; Pedersen et al., 2017) as well as toothpaste lava (Fig. 2.1; Rowland and Walker, 1987; Sheth et al., 2011).

In some cases, pāhoehoe surface morphologies transition into 'a'ā morphologies as they move away from the vent (Peterson and Tilling, 1980; Kilburn, 1981; Lipman and Banks, 1987; Kilburn, 1993; Hon, 2003). This partly occurs due to the changing rheology of the surface of the lava, with the lava cooling, crystallising and developing a yield strength at its surface, favouring brittle failure of the surface lava (Cashman et al., 1999; Sehlke et al., 2014). The transition to 'a'ā morphologies can also be triggered by an increase in the strain rate (Soule and Cashman, 2005), caused either by a localised increased effusion rate, flow rate (Pinkerton and Sparks, 1976), or the lava

advancing over steeper topography, which all lead to brittle failure of the lava surface (Hon, 2003). Under certain conditions, a break in slope from steep to less steep reverses the transition, i.e. from 'a'ā to pāhoehoe surface morphologies, due to the associated reduction in strain rate (Hon, 2003).

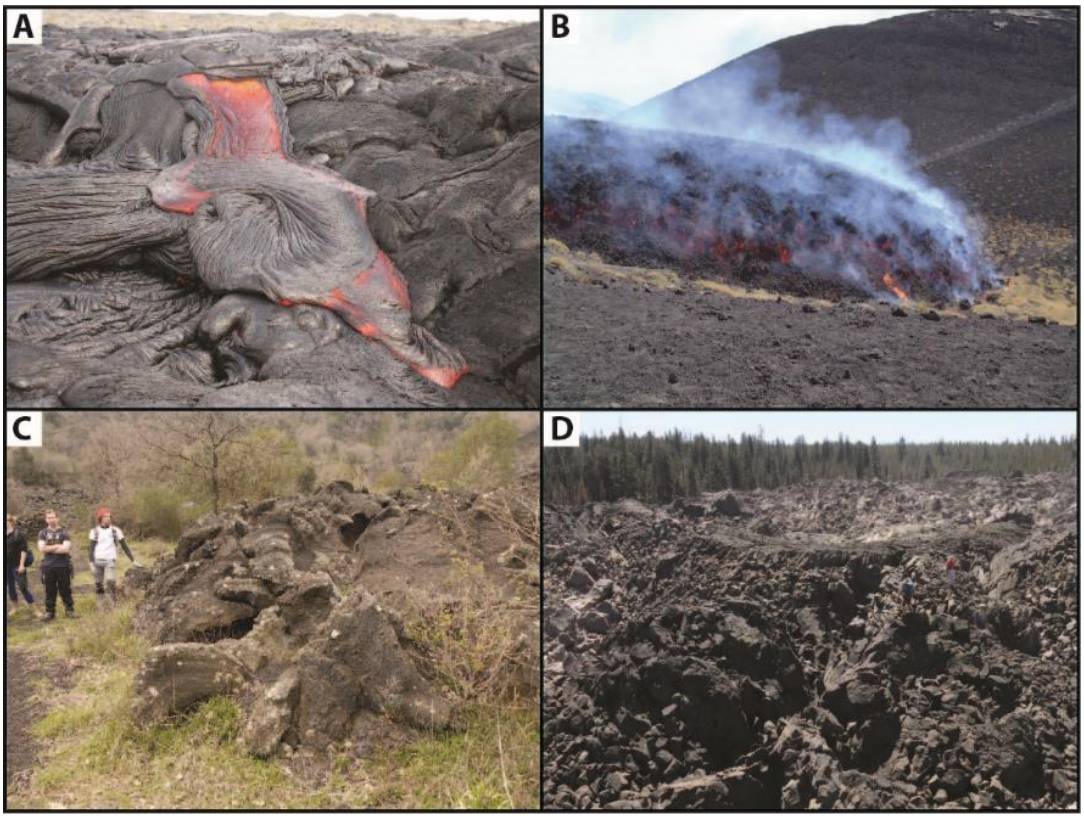


Figure 2.1: (**A**) Pāhoehoe lava from Hawaii, image from the USGS. (**B**) 'A'ā lava flow erupted during the 2001 Mt Etna eruption. (**C**) Toothpaste lava from the flow front of the 1991-1992 Mt Etna lava flow. C. Blocky rhyolite lava flow, Little Glass Mountain, Medicine Lake Volcano, California.

Many high-viscosity and intermediate to high-silica lava flows are termed blocky flows (Fig. 2.1D). Such flows are covered in fractured blocks tens of centimetres to metres in size, formed from disruption of the surface crust, and these blocks insulate the flow core (Macdonald, 1953; Kilburn and Lopes, 1991; Linneman and Borgia, 1993; Harris and Flynn, 2002). Pāhoehoe, 'a'ā, and blocky lavas are usually treated as separate flow types but there are many similarities in their formation processes and

characteristic features. All of the flow types develop surface folds on differing scales, from wavelengths of centimetres to tens of metres (pāhoehoe – ropes, 'a'ā and blocky – ogives), due to slowing of the flow front and folding/buckling of the cooled surface crust, whether intact or broken into blocks (Fink and Fletcher, 1978; Fink, 1980a; Gregg et al., 1998). The variation in scale of the surface folds reflects the mechanical properties of the lava (under similar conditions of a slowing flow front), and surface fold size has been used to infer lava viscosity (Fink and Fletcher, 1978; Fink, 1980a; Castro and Cashman, 1999). The difference between 'a'ā and blocky flows can be characterised purely by block size and morphology, with 'a'ā clinker typically smaller (centimetres to tens of centimetres) with a rough spinose surface compared to blocky lava, which is usually larger (tens of centimetres to metres), more angular and less spinose (Macdonald, 1953). However, the flow mechanism in both cases relates to advance of a sheet or channel with a steep flow front that continuously collapses, with the cooled surface lava fragmented to form clinker and blocks during flow emplacement (Macdonald, 1953; Kilburn and Lopes, 1991).

Lava flows can be further divided into channelized and non-channelized flows. Many 'a'ā and blocky flows are channelized (e.g. Applegarth et al., 2010c) by levées that stop lateral spreading (Sparks et al., 1976) and, at their front, have an area of dispersed flow as well as the flow toe (Lipman and Banks, 1987; Kilburn and Lopes, 1991). Channelized flows are more prevalent on steeper slopes (Favalli et al., 2010). Non-channelized mafic flows are not constrained by levées and are commonly associated with pāhoehoe lava (e.g. Swanson, 1973; Mattox et al., 1993; Hon et al., 1994; Hon, 2003). Pāhoehoe lava flows can develop lava tubes that supply lava to the flow front and continue the flow field advance or inflation (e.g. Guest et al., 1980; Guest et al., 1984; Sakimoto and Zuber, 1998). Non-channelized silicic lava flows develop on low gradients and have a domed pancake-like morphology, where the lava has spread out

from the vent without developing levées (Fink, 1983; Fink et al., 1993; de Silva et al., 1994; Stofan et al., 2000).

### *2.1.2 Volume and cooling-limited lava flows*

Lava flow advance is initially controlled by the rate at which lava is effused from the vent (Pinkerton and Wilson, 1994). A volume-limited lava flow will advance until the supply of fresh lava to the flow front ceases, often due to cessation of the eruption. When lava continues to be supplied, a cooled surface crust will form, this crust will retard flow advance and eventually halt the flow, at which point the flow is considered cooling-limited (Walker, 1971; Pinkerton and Sparks, 1976; Calvari and Pinkerton, 1998; Cashman et al., 1998; Blake and Bruno, 2000). Lava still being effused at the vent is added to the stalled flow front, which causes a pressure build-up and flow front inflation until the surface crust ruptures and a secondary flow, or breakout, forms from the stalled flow front and margins (Calvari and Pinkerton, 1998; Blake and Bruno, 2000; Hon, 2003). Some cooling-limited lava flows can develop into compound flows that have multiple channels, which can lead to flow superposition whereby flows override one another. Superposition can lead to the reactivation of the underlying channel due to the added pressure from the overlying lava flow (Applegarth et al., 2010b). Although Tuffen et al. (2013) referred to the Cordón Caulle lava flow as a compound lava flow, the lava appears to lack the characteristic multiple divergent channels typical of compound mafic lava flows (e.g. Walker, 1971; Pinkerton and Sparks, 1976; Blake and Bruno, 2000; Applegarth et al., 2010b), thus I prefer the use of the term cooling-limited lava flow.

Channelized volume-limited flows are characterised by well-developed levées often with sections of drained channel that formed when the supply of fresh lava ceased. These flows commonly have well developed transitions from snout frontal zone to rear

frontal zone to channel zone (Kilburn and Lopes, 1991). Cooling-limited flows are characterised by the presence of breakouts from the flow front or margins (Pinkerton and Sparks, 1976). However, it is worth noting that some cooling-limited flows share similar features of volume-limited flows, such as sections of drained channel, partly due to the complex variability in lava effusion (Applegarth et al., 2010c).

Lava advance can stall when a lower slope angle is encountered or when a sufficiently strong crust or core yield strength is developed. Lavas are further impeded by topographic barriers, which can cause lava flows to diverge (Dietterich and Cashman, 2014). This is particularly pronounced on steeper gradients, where flows thin due to increased flow velocity. As such, smaller barriers can cause lava flows to split, influencing the final flow field pattern (Hamilton et al., 2013; Dietterich and Cashman, 2014). It is not known how influential topographic barriers were in the development of the Cordón Caulle lava flow (discussed in Sections 3 and 4). Contact of lava flows with ice, particularly on stratovolcanoes, can further influence the morphology of a lava flow, with lavas infilling the available space in the ice, leading to the formation of a lobate margin (Lescinsky and Fink, 2000).

Numerous observations have been made of cooling-limited mafic lava flows (e.g. Calvari and Pinkerton, 1998; Blake and Bruno, 2000; Hon, 2003), but cooling-limited behaviour is rarely discussed in the literature for silicic lava flows, potentially due to their inability to form a dominant surface crust, and the paucity of observational studies. The 2011-2012 Cordón Caulle lava flow allowed for some of the first detailed observations of the onset of cooling-limited behaviour in a silicic lava flow (Tuffen et al., 2013; Farquharson et al., 2015). In mafic lavas, such transitions are suggestive of a dominant surface crust, with a yield strength, capable of stalling flow advance; whether this was also the case for the 2011-2012 Cordón Caulle lava flow is discussed in Section 3.

### *2.1.3 Modelling lava flows*

Analogue materials, such as paraffin wax, have been used to inform lava emplacement processes (Fink and Griffiths, 1990; Blake and Bruno, 2000; Gregg and Fink, 2000). Analogue models have successfully represented the formation and influence of lava cooling, leading to the development of a surface crust (e.g. Fink and Griffiths, 1990; Griffiths and Fink, 1993; Stasiuk et al., 1993; Griffiths and Fink, 1997; Lyman et al., 2005b), as well as crystallisation and the development of a yield strength (Hulme, 1974; Lyman et al., 2005b; Soule and Cashman, 2005). Analogue models have also been used to study the potential influence of slope angle (Gregg and Fink, 2000) and topographic barriers on flow advance (Dietterich et al., 2015), as well as the influence of channel morphology (Cashman et al., 2006). Ultimately these analogue models aim to improve the suitability of applied numerical models, and provide insight into lava advance processes.

Few quantitative models of lava emplacement have been applied to high-silica lava flows (e.g. Manley, 1992). However, numerous models of lava emplacement have been applied to mafic lava flows, ranging in complexity from simple models that indicate flow length (e.g. Pinkerton and Wilson, 1994; Harris and Rowland, 2001; Kerr and Lyman, 2007; Castruccio et al., 2013; Castruccio and Contreras, 2016; Chevrel et al., 2018), to more complex 2D and 3D models that can indicate likely regions of lava inundation for a given eruption (e.g. Crisci et al., 1986; Hidaka et al., 2005; Vicari et al., 2007; Connor et al., 2012; Richardson et al., 2017). Testing the validity of these models is of critical importance for indicating possible at risk areas during an eruption (Dietterich et al., 2017). Numerical models of lava inundation require understanding of properties such as the lava rheology (and how this may change through time and space), the effusion rate, and the topography underlying the flow (Dietterich et al., 2017), as well as their inherent uncertainties in each of these. Some of these models are

dimensionless, or use dimensionless values, and can thus be applied across the compositional spectrum (e.g. Griffiths and Fink, 1997). Many quantitative models of flow advance are focussed towards the emplacement of mafic lavas, with relatively few extending their application to silicic lava flows. In Section 3, I extend the use of simple quantitative models of lava length to attempt to model the lengthening of the Cordón Caulle lava flow.

### *2.1.4 Emplacement processes in mafic lava flows*

#### 2.1.4.1 Pāhoehoe

Pāhoehoe lavas advance as small toes, which stall and inflate prior to breakout formation; a new toe then undergoes the same process (Macdonald, 1953; Swanson, 1973; Anderson et al., 1999). Large pāhoehoe flow fields are emplaced when preferential pathways develop, forming lava tubes, which continue to feed lava to the flow front, insulated from the atmosphere (Guest et al., 1980; Polacci and Papale, 1997; Calvari and Pinkerton, 1998). Such insulation leads to cooling rates of ~1 °C/km (Swanson, 1973; Cashman et al., 1994; Sakimoto and Zuber, 1998), and potentially as low as 0.02-0.04 °C/km (Ho and Cashman, 1997), compared to ~7 °C/km in an open channel (Cashman et al., 1999). Continued supply through lava tubes can lead to inflation of the lava to form large flow units, contributing to the formation of large igneous provinces (Mattox et al., 1993; Anderson et al., 1999; Duraiswami et al., 2003; Vye-Brown et al., 2013).

The importance of preferential thermal pathways and lava tubes is well documented in mafic lava flows, but our understanding of their influence on the emplacement of silicic lava flows is limited. The presence of breakouts at Cordón Caulle and prolonged endogenous flow to the lava front (Tuffen et al., 2013), could indicate that preferential thermal pathways had developed. It is further possible that enhanced supply to one

breakout could lead to a change in supply to another region of the lava flow (discussed in Section 4).

#### 2.1.4.2 'A'ā

'A'ā lava flows are characterised by a surface comprised of rounded or angular clinker. They typically advance with a caterpillar track motion, whereby clinker cascades down the flow front before being overridden by the main channel (Walker, 1971). These lava flows form channels bounded by levées formed from a mixture of clinker and coherent lava from channel overflows (Sparks et al., 1976). Unlike pāhoehoe lava flows, 'a'ā lavas are not typically associated with extensive lava tubes, although they have been observed (Calvari and Pinkerton, 1998). Instead, preferential thermal pathways supply fresh lava to the flow front beneath the surface crust. 'A'ā lava advance stalls either due to a ceasing of supply or when a sufficiently cooled surface crust develops (Guest and Stofan, 2005; Lyman et al., 2005a; Castruccio et al., 2013). Once a flow front stalls, the continued supply of lava leads to the development of a number of features including breakouts, tumuli, squeeze-ups and toothpaste lavas (Rowland and Walker, 1987; Applegarth et al., 2010c; Sheth et al., 2011). Squeeze-ups and toothpaste lava are associated with the extrusion of lava with a yield strength and are common on Mt Etna (Applegarth et al., 2010c; Sheth et al., 2011).

#### 2.1.4.3 Surface and flow front features

The following section outlines the processes that lead to the formation of features of mafic lava flows, including breakouts, squeeze-ups, spines, and tumuli. Of interest within this thesis are the potential similarities of these features, and the processes that drive their formation, to those observed on silicic lava flows.

Breakouts are observed in many basaltic lava flows and breakout formation is a common process in the development of pāhoehoe and 'a'ā lava flow fields (e.g. Walker, 1971; Pinkerton and Sparks, 1976; Mattox et al., 1993; Blake and Bruno, 2000). Breakouts originate from pervasive weaknesses in the ductile and brittle portions of the surface crust, or where a portion of the flow front talus collapses and exposes the hotter core lava (Pinkerton and Sparks, 1976). Many breakouts develop with a similar morphology to that of their main channel, but some develop a substantially different morphology (Fig. 2.2). Breakouts from the 2001 Mt Etna lava flow are of variable sizes and morphologies (Applegarth et al., 2010c; Favalli et al., 2010), with the largest being ~1.8 km long, branched, 'a'ā lavas. The smallest breakouts are only 50-100 m long and have a substantially different surface morphology (Fig. 2.2), comprising blade-like fragments (top one metre) that become fragmented away from the bocca (Applegarth et al., 2010c). These are similar to the toothpaste extrusions documented for other basaltic lava flows, thought to reflect extrusion of lava with a higher yield strength

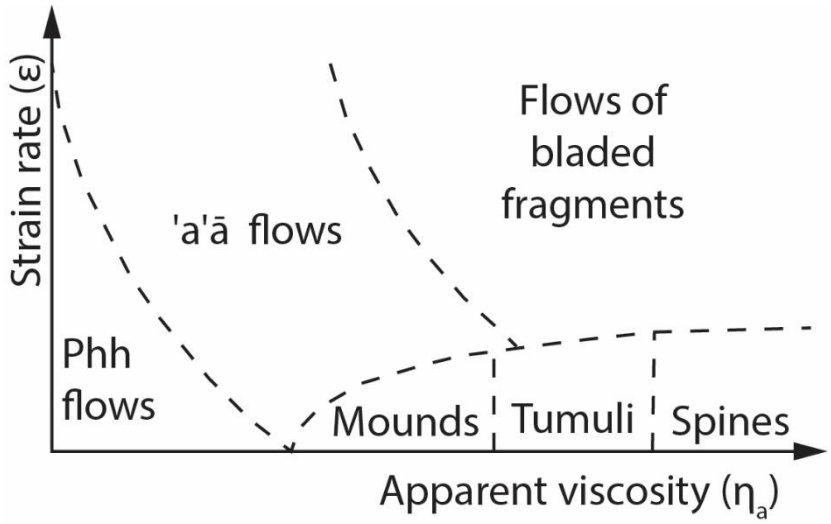


Figure 2.2: Schematic representation of breakout/squeeze-up morphology in basaltic lava flows. If the lava is assumed to behave as a Bingham fluid then apparent viscosity can take into account both the Bingham viscosity and the yield strength (Kilburn, 1981). The lines here likely represent diffuse transitional regions, rather than absolute transitions. From Applegarth et al. (2010c).

compared to the rest of the lava (Rowland and Walker, 1987; Sheth et al., 2011). The morphology of breakouts from the Cordón Caulle lava flow could similarly be influenced by the rheological properties of the lava, or the strain rate that it experiences (discussed in Section 4).

Spines and squeeze-ups are found at the surface of some basaltic lava flows, and reflect locations where core lava has risen up through the surface crust of the lava (Applegarth et al., 2010c; Sheth et al., 2011). Spines on basaltic 'a'ā lava flows are somewhat rare but, where observed, they can be up to ~2 m high and form in association with a hillock on the surface of the lava (Applegarth et al., 2010c). Spines are thought to form due to the ramping of core lava to the surface along inclined shear planes behind a stalling flow front (Christiansen and Lipman, 1966). In silicic lava flows spines are more common and are of a similar scale to those in basaltic lavas (Fink,

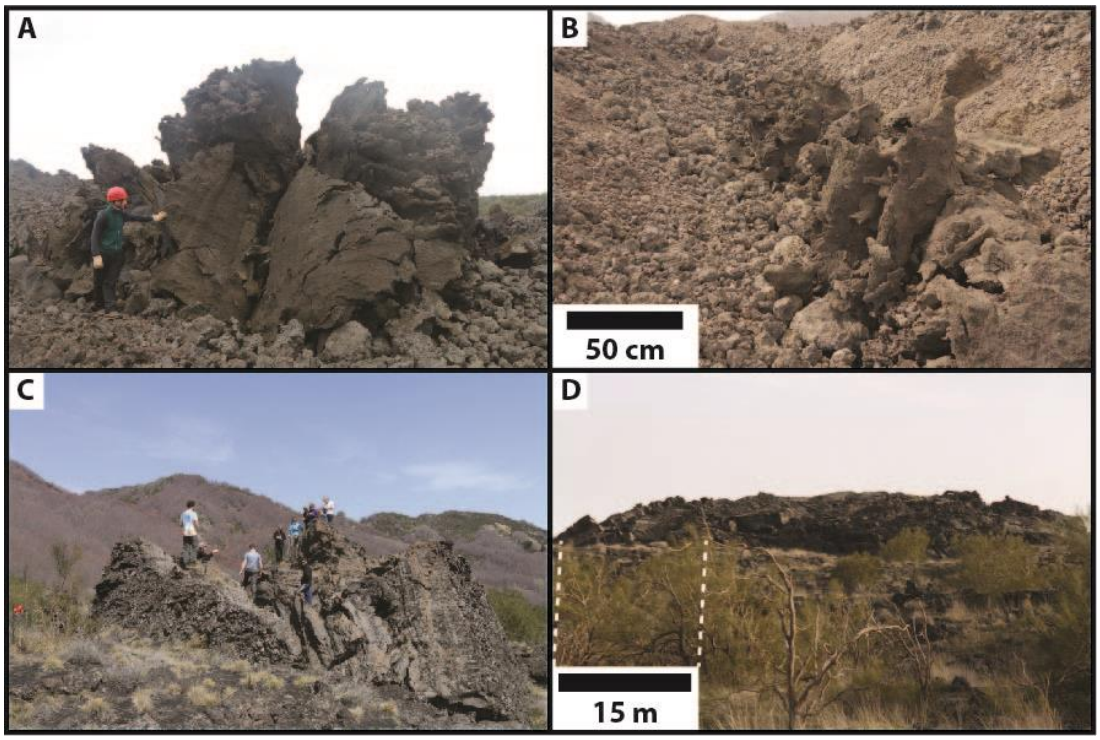


Figure 2.3: (**A**) Squeeze-up on the surface of the 2001 Mt Etna lava flow. (**B**) Linear squeeze-up on the 2001 Mt Etna lava flow. (**C, D**) Tumuli on the 1792-1793 Mt Etna lava flow, the tumuli have variably morphologies and can vary substantially in size.

1983; Griffiths, 2000; DeGroat-Nelson et al., 2001; Latutrie et al., 2016). Squeeze-ups have variable morphologies (Fig. 2.3A, B) and form in both pāhoehoe and 'a'ā lava flows. They typically protrude from the surface of the lava flow in discreet patches or as more linear features (Hon et al., 1994; Harris et al., 2009; Applegarth et al., 2010c; Sheth et al., 2011). Squeeze-ups of the 2001 Mt Etna lava flow often have a spiny appearance and can form complex shapes; the squeeze-ups are thought to represent the late extrusion of pressurised core lava though the surface of the flow (Applegarth et al., 2010c; Sheth et al., 2011). Thus, squeeze-ups could be considered a type of vertically orientated breakout.

Tumuli are found at the surface of some basaltic pāhoehoe and 'a'ā lava flows and comprise elevated areas of inflated and upturned surface crust (Guest et al., 1984; Walker, 1991; Calvari and Pinkerton, 1998). Tumuli can vary in size from a few metres to one kilometre in width, over a network of tubes (Fig. 2.3C ,D), and can be tens of metres high (Guest et al., 1984). Tumuli form above lava tubes, typically where there is a reduction in slope, due to a pressure build-up in the tube that leads to inflation of the surface, lava can then push through the fractures between surface slabs (Guest et al., 1984; Walker, 1991; Calvari and Pinkerton, 1998). Tumuli often have an axial split (a.k.a. cleft) parallel to the orientation of the underlying lava tube (Walker, 1991). As a tumulus is associated with an underlying tube it can be hollow where lava has drained from the tube system (Guest et al., 1984). These inflationary features are common in mafic lava flows; of interest is whether similar features form in silicic lava flows because the formation of tumuli can act to accommodate pressure within the lava flow core, reducing the pressure available to form breakouts. However, as silicic lava flows are not thought to form lava tubes, due to their very large viscosities, tumuli may not form in these lavas, but inflation of silicic lava flows could conceivably lead to simpler features such as the “lava-inflation clefts” observed by Walker (1991).

### *2.1.5 Emplacement processes in silicic lava flows*

The effusion of viscous magma can lead to the formation of lava domes, coulées, and flows. Lava domes, comprising lava with a high yield strength or effused at a very low rate, can build-up over the vent to form prominent features that range in size from tens of metres to over a kilometre in width (Fink and Anderson, 2000). Dome morphology ranges from slabbed to relatively rubbly, and domes can also form features such as spines, whalebacks, and lobes during their emplacement (Swanson et al., 1987; Anderson and Fink, 1990; Nakada et al., 1995; Ryan et al., 2010; Pallister et al., 2013). When a lava dome begins to spread and advance downslope it is termed a lava coulée (de Silva et al., 1994; Fink and Anderson, 2000). The point at which a lava dome becomes a coulée lacks formal definition, but the term coulée is usually applied when a dome has undergone significant (order kilometres) lateral advance. The point at which a coulée could be considered as a lava flow is also unclear. Numerous observations have been made of the emplacement of lava domes at Mt St Helens (Swanson et al., 1987; Anderson and Fink, 1990) and Mt Unzen (Nakada et al., 1995; Hale and Wadge, 2008; Cichy et al., 2011). However, these domes developed over the vent, and underwent little lateral advance, so provide limited insight into the emplacement of the Cordón Caulle lava flow. Here, the primary interests are the

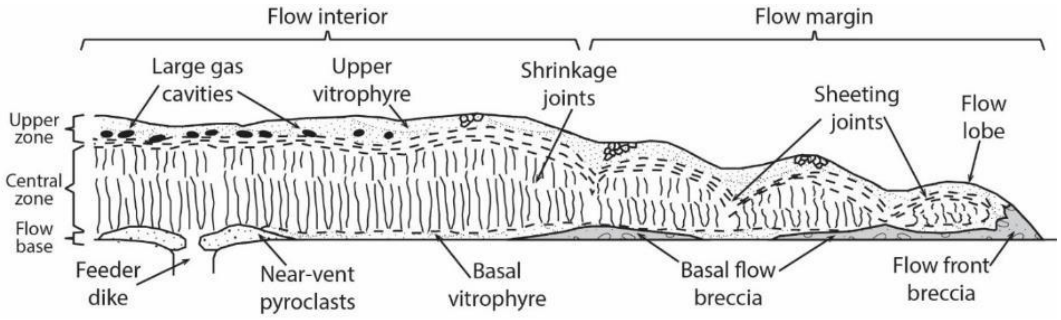


Figure 2.4: Schematic cross section through a rhyolite lava flow in southwestern Idaho. Large gas cavities can be seen beneath the flow surface. Lobes are also observed at the flow margin. Adapted from Bonnichsen (1982).

processes that contributed to the advance and emplacement of silicic lavas, whether or not they are best termed coulées or flows.

Detailed structural analysis of ancient rhyolite flow facies in the Western USA (Fink, 1980b; Fink and Manley, 1987; Castro et al., 2002a), New Zealand (Stevenson et al., 1994a), and Australia (Smith and Houston, 1995) have led to models whereby these flows advance with a caterpillar track motion (Manley and Fink, 1987), similar to observed dacite lava flows at Santiaguito (Harris and Flynn, 2002). During their emplacement, slowing of the flow front formed large-scale (hundreds of metres long, tens of metres in wavelength, and metres in amplitude) surface folds, or ogives (Fink, 1980a; Fink, 1983). These lavas can also form a lobate margin, with lobes observed in some ancient dissected rhyolite lava flows (Fig. 2.4; Bonnichsen, 1982). Whether these lobes were as a result of breakout formation is unknown, and may be difficult to determine post-emplacement.

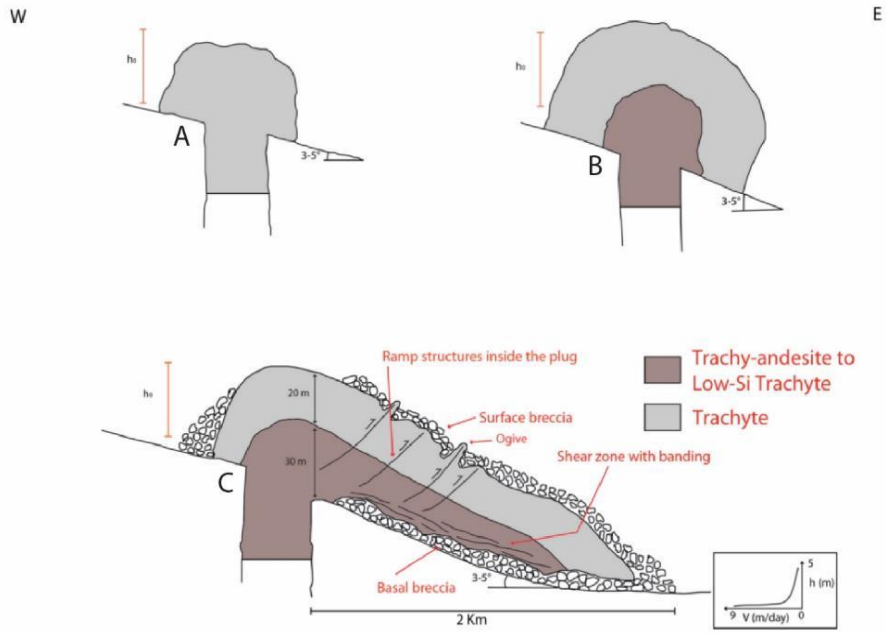


Figure 2.5: (**A-C**) Emplacement model of the Puy de Cliergue silicic lava flow (France). Note the shear zones and the ramping of core lava to the surface. From Latutrie et al. (2016).

Not all high-viscosity lava flows emplace with a caterpillar track motion. The advance of crystal-rich andesite and dacite lava flows can, in some cases, be approximated as a flowing plug, whereby there is little shear distributed over the bulk of the flow depth. Instead, the shear is accommodated at the base of the lava flow (Fig. 2.5) and the main flow body undergoes little strain. A basal breccia is observed in these lavas, which likely relates to limited collapse at the front of the lava flow (Latutrie et al., 2016). This different advance style likely relates to the crystallinity of the lava, with the onset of a yield strength limiting flow in the bulk of the lava (Latutrie et al., 2016). This emplacement model has similarities with the emplacement of glaciers, whereby they advance over a basal shear zone (Ives et al., 1976; Benn and Evans, 2014), as well as with plug flow in conduits, where much of the shear is accommodated in a thin region near the conduit margins (e.g. Kendrick et al., 2012).

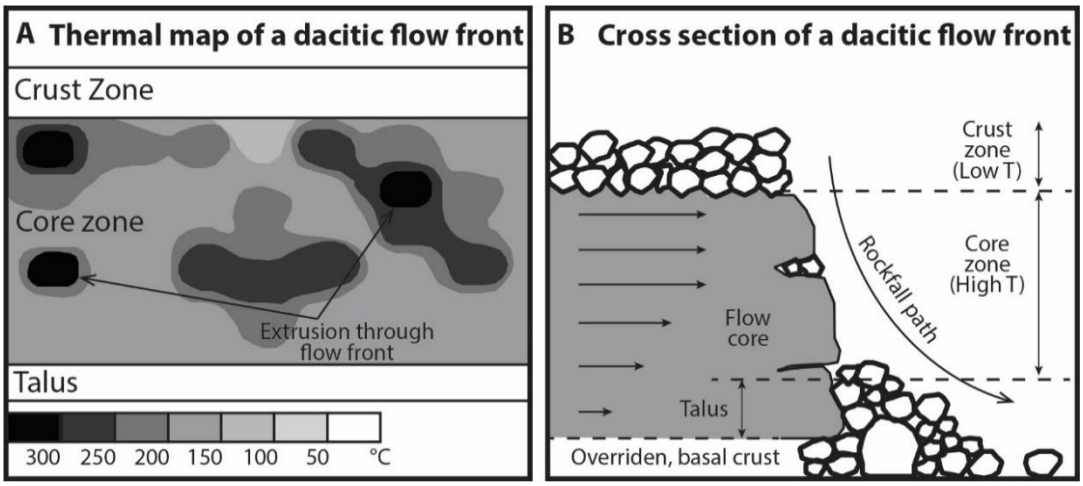


Figure 2.6: (**A**) Thermal map of the Santiaguito dacitic lava flow front in January 2000. Hot spots show portions of collapsed flow front talus or where the flow core has extruded through the flow front. (**B**) Cross section through the flow front of the dacitic lava flow, the lava is inferred to advance in a caterpillar-track style, whereby the collapsed flow front talus is overridden by the bulk of the lava flow. Adapted from Harris and Flynn (2002).

#### 2.1.5.1 Observations of emplacement

Observations made during the emplacement of a crystal-rich dacitic lava flow on Santiaguito Volcano in Guatemala (Anderson et al., 1995; Harris and Flynn, 2002; Harris et al., 2003) have yielded insights into the emplacement of laterally extensive silicic lava flows. These observations identified that the lava flow advanced in a caterpillar track motion, whereby flow surface blocks would cascade down the flow front to form a talus apron (Fig. 2.6). The core of the flow then advanced over this talus apron (Harris and Flynn, 2002; Harris et al., 2004), similar to the advance of basaltic 'a'ā lava flows (e.g. Walker, 1971). During collapse of the flow front, the hotter flow interior was exposed (Fig. 2.6) and thermal imagery showed that the flow core underwent little cooling from vent to flow front, giving blocky lava flows the potential to travel large distances (Harris and Flynn, 2002). Furthermore, during emplacement,

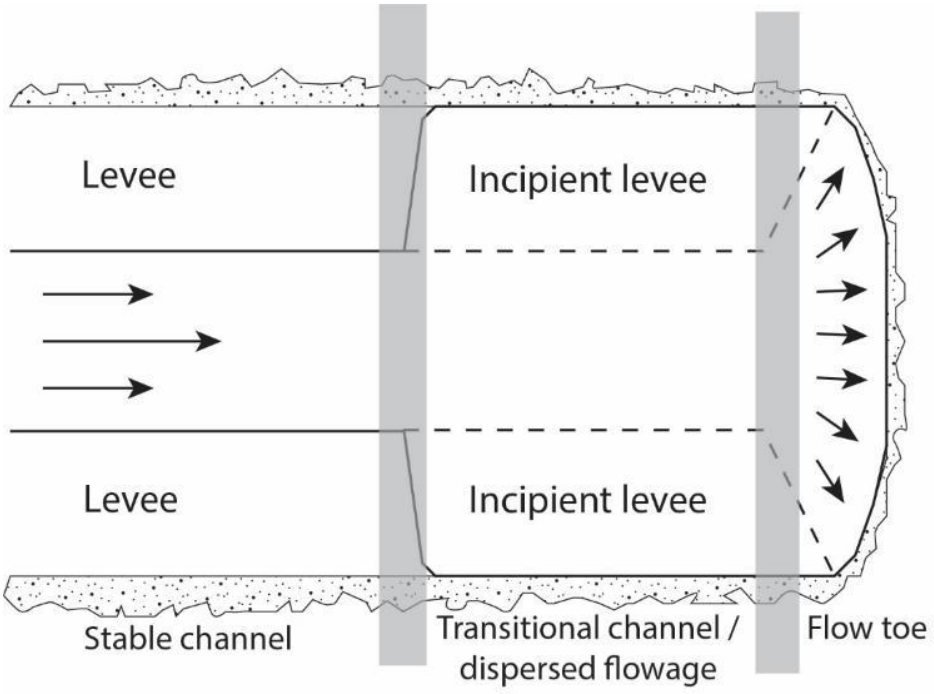


Figure 2.7: The three distal zones of an emplacing channelized 'a'ā or blocky lava flow. These are the flow toe, transitional channel (which usually has incipient levées), and stable channel (with developed levées). Adapted from Kilburn and Lopes (1991).

toothpaste-like extrusions of core lava formed from the base of the flow front (Harris and Flynn, 2002), potentially promoting flow front collapse. These small extrusions are unlikely to be breakouts, as they formed synchronous with the main flow advance. This dacitic lava produced a channelized flow comprising a flow toe (Fig. 2.7), transitional channel/dispersed flow zone (with incipient levées), and stable channel (Harris et al., 2004), analogous to the flow zones observed in channelized basaltic 'a'ā lava flows (Lipman and Banks, 1987; Kilburn and Lopes, 1991). Initial observations of the Cordón Caulle lava flow suggest this flow may be similarly channelized, with observed shear zones between stalled margins and a more mobile central channel (Tuffen et al., 2013).

#### *2.1.5.1.1 Observations of the 2011-2012 Cordón Caulle rhyolitic lava flow*

The 2011-2012 eruption of Puyehue-Cordón Caulle allowed for the first detailed scientific observations of an emplacing rhyolitic lava flow. The lava was erupted between June 2011 and March 2012. Field and satellite observations indicated that the 0.4 $km^3$ lava flow developed a blocky morphology and advanced in a caterpillar track motion (Tuffen et al., 2013). When advance ceased, numerous breakouts formed from the flow front and margins, these breakouts had a slabbier and blockier morphology compared to the main channel (Tuffen et al., 2013; Farquharson et al., 2015). The breakouts were observed to inflate, resulting in the fracturing of the breakout surface slabs (Tuffen et al., 2013; Farquharson et al., 2015). Field observations indicated that some breakouts were still advancing in January 2013 (Tuffen et al., 2013), suggesting substantial thermal insulation and slow cooling (Fig. 2.8) of the core of the lava flow by the overlying surface crust (Manley, 1992; Farquharson et al., 2015). Camera-derived digital elevation models of breakouts during their emplacement indicated a breakout viscosity for Cordón Caulle of ~$1\times10^{10}$ – $4\times10^{10}$ Pa s (Farquharson et al., 2015). The observation of breakout formation from a rhyolite lava flow suggests that its advance was cooling-limited. Such cooling-limited behaviour is indicative of the flow becoming

dominated by a retarding surface crust and Section 3 explores whether the Cordón Caulle lava flow was controlled in its latter phases by a cooled surface crust. Furthermore, it is currently unclear whether the processes that drove the formation of breakouts at Cordón Caulle were similar to the process that contribute to breakout formation in mafic lava flows. The potential similarities, and differences, between the formation of breakouts in mafic and silicic lava flows are discussed in Sections 4 and 6.

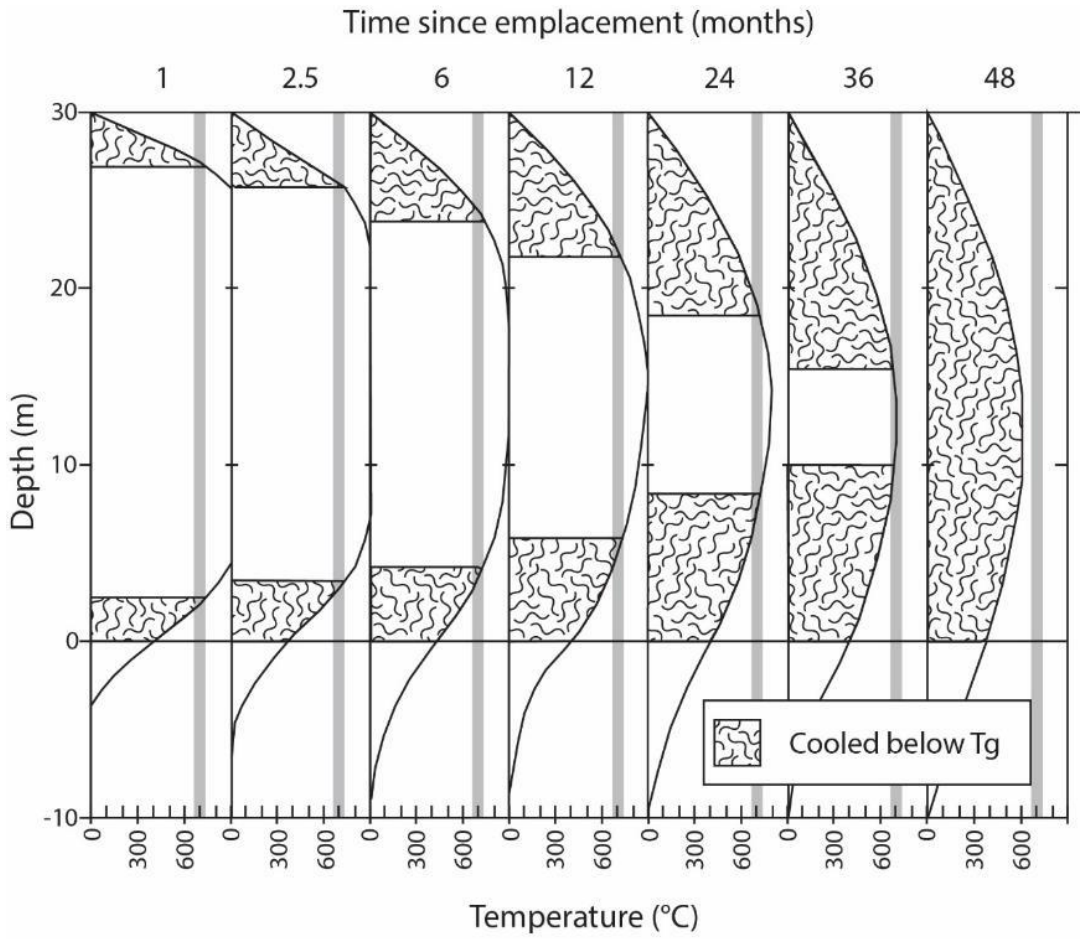


Figure 2.8: Quantitative modelling of a cooling rhyolitic lava body from an initial temperature of 900 °C. Panels show time since emplacement of 1, 2.5, 6, 12, 24, 36 and 48 months. Shaded areas show cooling of the crust below the inferred glass transition temperature, Tg (grey band). Adapted from Farquharson et al. (2015).

### 2.1.5.2 Structure of a rhyolite lava flow

Much of our understanding of the structure of rhyolite lava flows is based on the analysis of ancient lava flows. Studies of dissected ancient rhyolite lava flows (e.g. Bonnichsen, 1982; Bonnichsen and Kauffman, 1987), as well as drill coring (e.g. Eichelberger et al., 1984; Fink and Manley, 1987; Manley and Fink, 1987; Furukawa and Uno, 2015), have revealed the complex interior structure of some rhyolite lava flows. These studies have identified variable lithologies (Fig. 2.9, 2.10), with an upward stratigraphy of: basal breccia (overridden during caterpillar-track advance), lower obsidian (OBS; a.k.a. vitrophyre) that cooled quickly after effusion, crystalline rhyolite (RHY), interbanded obsidian and coarsely vesicular pumice (CVP), and a surface breccia of finely vesicular pumice (FVP), although not all of these layers may be present (Fig. 2.9). These lithologies most likely formed during and after emplacement.

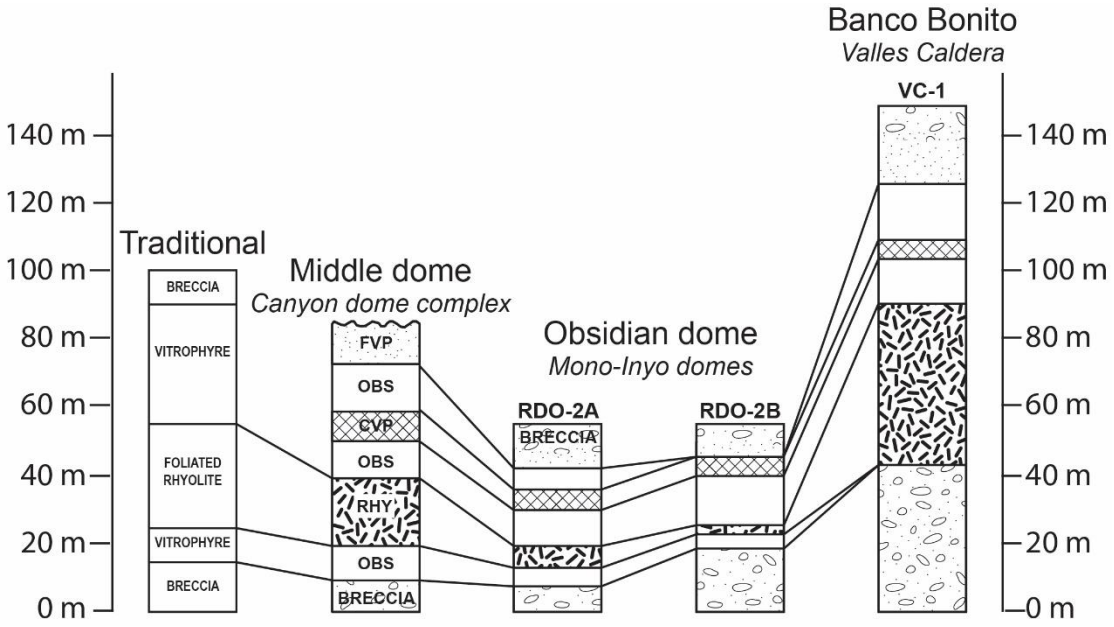


Figure 2.9: Textural stratigraphy of obsidian rhyolite lava flows as determined by drill cores. The upper breccia in cores from Obsidian dome and Banco Bonito composes FVP. From Manley and Fink (1987).

The different lithologies are distinct from one another. OBS is typically crystal-poor (<5 volume%) and vesicle poor, with only the occasional lithophysae observed (Manley and Fink, 1987). The low crystal content of the OBS suggests that it cooled faster than crystals could grow. RHY is crystal-rich, comprising a large volume of microlites (>70 volume%, Schipper et al., 2015), and is thought to form due to slow cooling of the flow interior at depths that are unlikely to vesiculate (Fink, 1983; Swanson et al., 1989). The CVP is vesicular with vesicles ranging in shape from angular and contorted to spherical, and 0.1 – 1 cm in diameter. CVP is typically interlayered with centimetre-thick bands of OBS (Manley and Fink, 1987). The CVP is thought to form due to the accumulation of volatiles by anhydrous crystallisation of the flow, with the gases then migrating to a layer beneath the surface crust (Fink and Manley, 1987; Manley and Fink, 1987; Furukawa and Uno, 2015). Indeed, measurements of CVP volatile contents have found elevated $H_2O$ volumes, e.g. 0.3 – 0.5 wt% in the CVP compared to 0.1 – 0.2 wt% in the bulk of the lava (Manley and Fink, 1987).

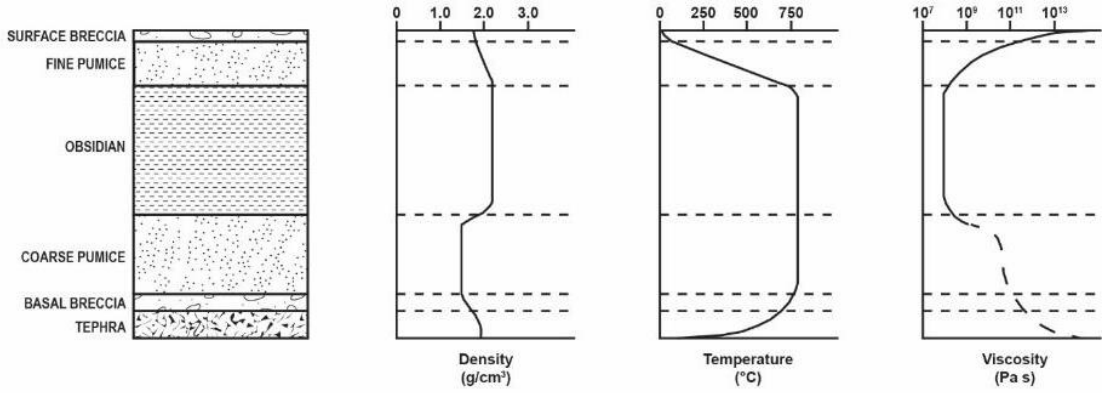


Figure 2.10: Stratigraphy of a “typical” 35 m thick rhyolite obsidian lava flow with the corresponding density measurements and temperature estimates from Fink (1983) and viscosity measurements based on Friedman et al. (1963). Note the decreased density beneath the obsidian layer. From Fink (1983).

The FVP formed at the lowest pressure at the surface of the lava flow and is crystal-poor and vesicular, with vesicles typically small compared to within the CVP, irregular and ~0.5 mm in diameter (Manley and Fink, 1987). Some of the FVP is microcrystalline and can form a dome over the eruptive vent, suggestive that this may comprise some of the last effused lava (Fink, 1983). Two primary hypotheses exist for the origin of the FVP; the first suggests that the FVP formed due to collapse of an inflated permeable foam upon extrusion at the surface (Eichelberger et al., 1986). The second suggests that the rhyolite effuses as a dense lava, the surface of which vesiculates due to the associated drop in pressure at the surface (Manley and Fink, 1987; Fink et al., 1992). The potential origin of the FVP is discussed in Section 6.

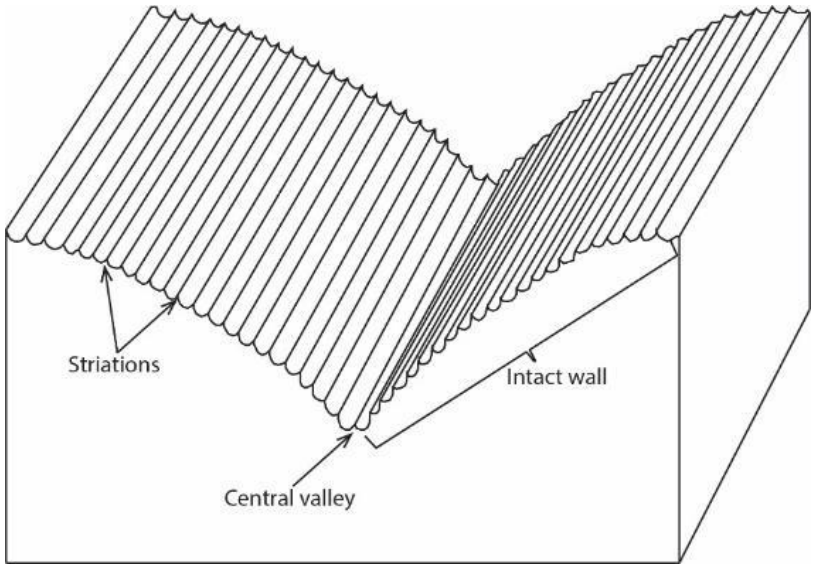


Figure 2.11: Schematic cross section through a crease structure showing striations around a central fracture. From Anderson and Fink (1992).

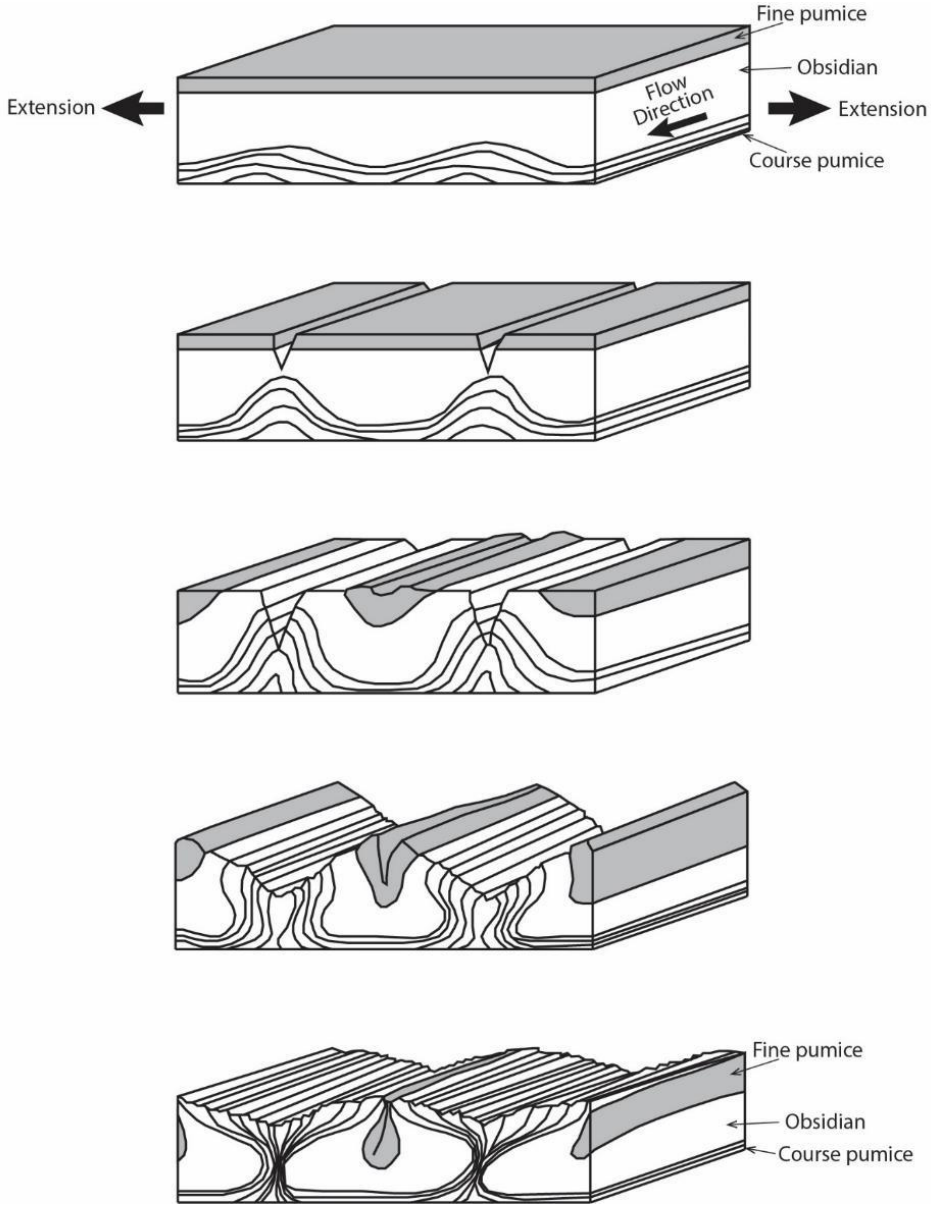


Figure 2.12: The formation of a pumice diapir in a rhyolitic obsidian lava flow. Spreading of the flow surface due to flow widening perpendicular to the advance direction, as well as possible buoyant upwelling of coarsely vesicular pumice (CVP), leads to the fracturing of the surface crust. As this fracture grows the CVP is able to upwell into the opening fracture, to form a CVP diapir. From Fink (1980b).

### 2.1.5.3 Surface features

Many silicic lava flows have unique surface features that help to identify the processes that occurred during the emplacement of these flows. Some features, such as surface spines, are similar to those in mafic lava flows, but others, such as large gas cavities and pumice diapirs, are unique to silicic lavas. Thus, it is useful to understand the processes that lead to the formation of these unique features, in order to determine possible comparable emplacement processes within mafic lava flows. The surfaces of silicic lava flows and domes are characterised by the formation of crease structures, pumice diapirs, and spines that develop during lava emplacement. Extensional crease structures are common (Anderson and Fink, 1990, 1992; Lescinsky and Merle, 2005) and have smooth convex fracture walls that merge with the lava surface (Fig. 2.11).

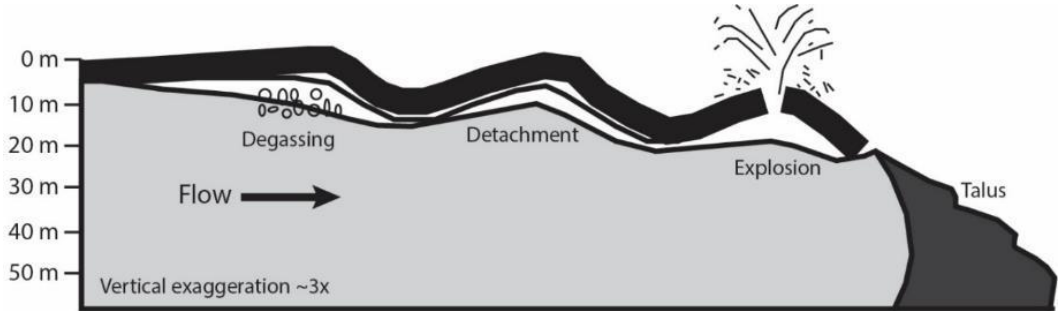


Figure 2.13: Schematic model of the formation of gas cavities. Folding of the surface crust leads to layer detachment and void formation, magmatic and meteoric volatiles become concentrated in these voids and can explosively vent from the surface. From Castro et al. (2002a).

The sides of these fractures are lined with parallel striations (i.e. chisel marks), indicative of incremental fracture advance into a ductile interior (Anderson and Fink, 1992; Degraff and Aydin, 1993; Forbes et al., 2014). Crease structure formation has been related to extensional fracturing of the surface crust and synchronous upwelling of lava to merge with the surface of the main channel (Anderson and Fink, 1992).

Crease structures in some rhyolite lava flows in the Western USA are associated with the formation of diapirs of CVP (Fig. 2.12) at the lava surface (Fink, 1983; Fink and

Manley, 1987). These diapirs are thought to form during emplacement of the flow due to the accumulation of volatiles in a layer beneath the surface crust, which leads to vesiculation (Fink and Manley, 1987; Manley and Fink, 1987). The resulting lower density layer then rises to the surface (Fig. 2.12), either driven solely by the density contrast or aided by upwelling into an opening and spreading crease structure (Fink, 1980b, 1983). It is currently unclear what conditions promote pumice diapir formation in some silicic lava flows and not others; it may be partly reflective of compositional variations between flows, and associated variations in crystallinity and rheology, with pumice diapirs only observed in the most silica-rich and crystal-poor rhyolite lavas. The factors that may favour or restrict the formation of pumice diapirs in silicic lava flows are discussed in Section 5.

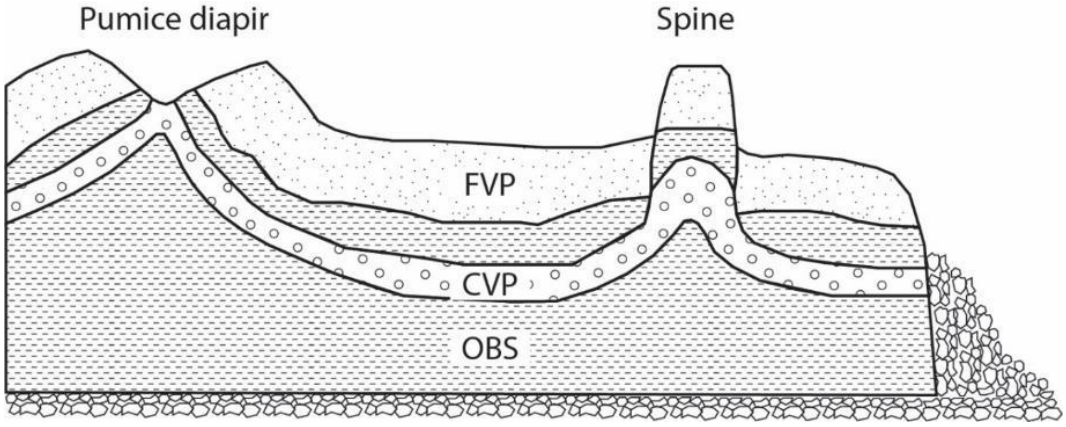


Figure 2.14: Schematic cross section of a rhyolite lava flow showing pumice diapirs and spines on a glassy rhyolite lava flow. Spines are interpreted as the product of partial upwelling of a CVP diapir, pushing up the overlying lava to form a spine. From DeGroat-Nelson et al. (2001).

In some cases, rather than forming a pumice diapir, the exsolved volatiles accumulate to form a large gas cavity as the surface crust buckles (Fig. 2.4, 2.13). This gas cavity can vent explosively from the surface, provided that the gas pressure exceeds the strength of the crust (Jensen, 1993; Castro et al., 2002a). Spines, typically a few metres tall, also form at the surface of many viscous lava flows (Fink, 1983; Griffiths, 2000; DeGroat-Nelson et al., 2001; Latutrie et al., 2016). Spine formation is most likely due

to the ramping of core lava to the surface of the lava flow (Fig. 2.5, 2.14) along inclined shear planes (Christiansen and Lipman, 1966; Cas and Wright, 1987; Latutrie et al., 2016). Alternatively, spines may be pushed up by underlying buoyant CVP (Fig. 2.14).

## 2.2 Rheology of lavas

The difference in the morphology of mafic and silicic lava flows is predominantly due to rheological differences between the lavas. Lavas are multicomponent fluids comprising a liquid, solid and gas phase. The relative proportions of each of these components can change throughout the course of an eruption and during lava emplacement, and this affects the development of a lava flow by changing its mechanical properties. Rheology describes the way in which a material responds to an applied stress and is one of the fundamental controlling factors on the behaviour of a lava flow during emplacement. Lava rheology is a function of the proportion of crystals and vesicles, as well as the composition and temperature of the melt (e.g. Spera, 2000; Mader et al., 2013) and can be described as either Newtonian or non-Newtonian.

### *2.2.1 Models of Newtonian and non-Newtonian rheology*

Newtonian fluids deform continuously under any applied stress (Fig. 2.15, line (i)). The internal resistance to flow is the viscosity of a fluid and can be described by the equation:

$$\tau = \eta\dot{\varepsilon}, \qquad [Eq.\,2.1]$$

where $\tau$ is the applied shear stress, $\eta$ is the dynamic viscosity, and $\dot{\varepsilon}$ is the strain rate. For some fluids with a non-Newtonian rheology, a yield strength must first be exceeded before the fluid will deform (Fig. 2.15, line (ii)), this behaviour is also known as a Bingham rheology as described by the equation:

$$\tau = \sigma_y + \eta_B \dot{\varepsilon}, \qquad [Eq. 2.2]$$

where $\sigma_y$ is the yield strength and $\eta_B$ is the Bingham viscosity. Fluids may also exhibit shear thinning and shear thickening behaviours. In shear thinning fluids apparent viscosity decreases as the applied stress increases (Fig. 2.15, line (iii)). Conversely, in shear thickening fluids viscosity increases as the applied stress increases (Fig. 2.15 (iv)). These rheologies can be described using the Herschel-Bulkley relationship:

$$\tau = \sigma_y + K(\dot{\varepsilon})^n\,, \qquad [Eq. 2.3]$$

where $K$ is the flow consistency index, and the exponent $n$ is the flow behaviour index. In shear thinning behaviour the exponent $n < 1$ and in shear thickening behaviour $n > 1$; $n = 1$ represents a linear stress-strain relationship, i.e. a Newtonian rheology when $\sigma_y = 0$ (Fig. 2.15).

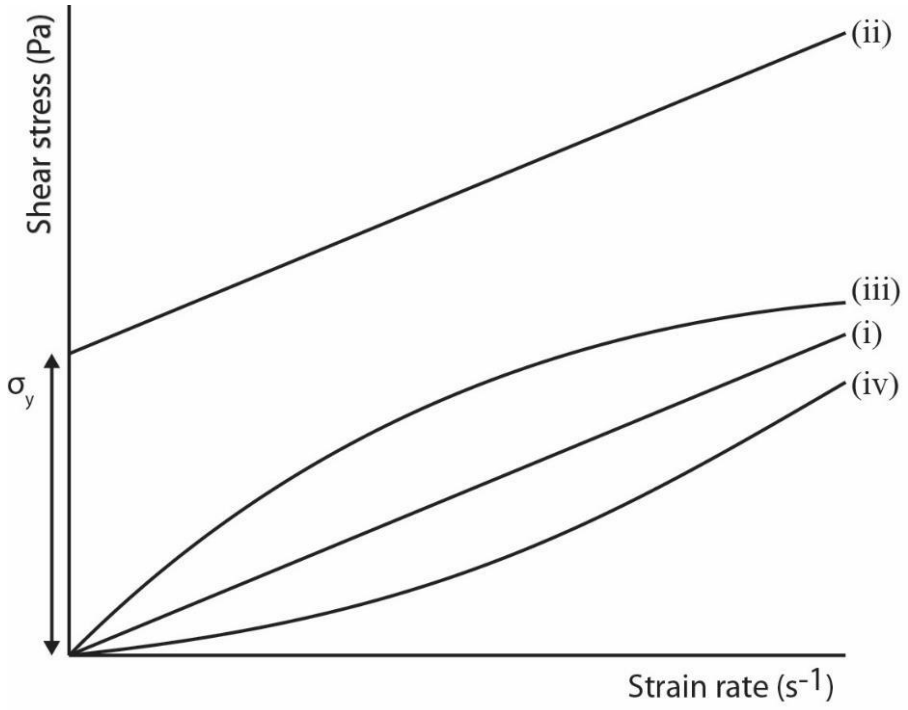


Figure 2.15: Fluid rheologies (i) Newtonian, (ii) Bingham, (iii) shear thinning, (iv) shear thickening.

Lavas rarely have a Newtonian rheology, except where erupted at close to their liquidus, such as some Hawaiian basaltic lavas (Hon et al., 1994). Instead, most lavas are erupted sufficiently cooler than their liquidus temperature, due to gas loss during decompression in the conduit, for a yield strength to have developed due to crystallisation and vesiculation (Cashman et al., 1999; Saar et al., 2001), outlined in Section 2.2.3. Low-silica (e.g. basaltic) melts can have a Newtonian viscosity above the liquidus (Pinkerton and Stevenson, 1992), but high-silica (e.g. rhyolitic) melts are thought to exhibit a non-Newtonian power-law behaviour above the liquidus (Spera et al., 1988). As such, the Cordón Caulle lava flow is unlikely to have had a purely Newtonian rheology, particularly once the influence of crystals and bubbles are accounted for (Sections 3 and 5).

### *2.2.2 Effect of melt chemistry and temperature on rheology*

Increasing the silica content of the melt phase leads to higher melt viscosities (Fig. 2.16; Bottinga and Weill, 1972; Shaw, 1972). In a silicate melt, flow depends on the relative movement of silicon-oxygen chains (Bottinga and Weill, 1972). In more mafic melts, the larger proportion of metallic oxides (primarily aluminium and iron) act to replace the silica-oxygen bond with a weaker metal-oxygen bond, reducing silica chain lengths (Bottinga and Weill, 1972). Such reduced silica chain lengths (i.e. molecular weight) facilitates flow at lower applied stresses (Bottinga and Weill, 1972). As such, basalts can have viscosities over six orders of magnitudes less than rhyolitic lava flows (Fig. 2.16).

The addition of water to a silicate melt acts to reduce the melt viscosity (Shaw, 1963; Bottinga and Weill, 1972; Shaw, 1972; Schulze et al., 1996; Giordano et al., 2008) in much the same way as the addition of metals, and is termed melt depolymerisation (Schulze et al., 1996). Hydroxyl ions replace the silica-oxygen bond, resulting in

reduced silica chain lengths and a lower viscosity (Giordano et al., 2008). Conversely, as water is lost during degassing, melt viscosity increases due to increasing polymerisation, and increased molecular weight. The addition of other volatile species, in particular fluorine, and to a lesser extent chlorine, can have a similar affect, acting to depolymerise the melt and reduce viscosity (Dingwell et al., 1985; Giordano et al., 2004; Zimova and Webb, 2007). As a melt cools, the viscosity increases (Spera, 2000) as the space between silica chains is reduced. The cooling of a lava also leads to the growth of crystals, which in turn act to increase the bulk lava viscosity (Kerr and Lister, 1991; Costa, 2005; Castruccio et al., 2010).

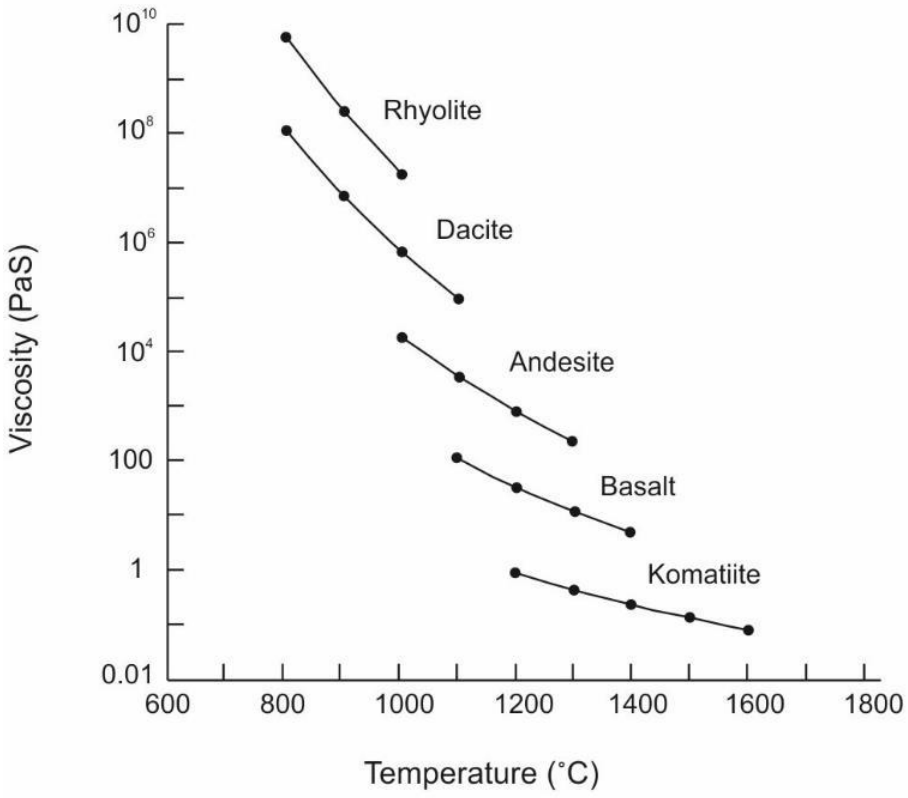


Figure 2.16: Viscosity ranges for different melt compositions across their eruptive temperature range. Adapted from Shaw (1972).

### *2.2.3 Crystals*

#### 2.2.3.1 Crystallisation

Microstructural observations of the Cordón Caulle lava have identified phenocrysts, microlites, and devitrification crystals (Schipper et al., 2015). Understanding the conditions that drive the formation of these crystals is important for our broader understanding of flow processes as crystallisation profoundly affects lava rheology and reflects its cooling and degassing history. In general, crystals will begin to form once the temperature of the melt falls beneath the liquidus temperature, with many mafic minerals forming at higher temperatures than more felsic minerals. The undercooling of a melt can be driven by a temperature drop or by degassing, which increases the liquidus temperature (Cashman and Blundy, 2000; Sparks et al., 2000), and degassing is a slightly endothermic process (Richet et al., 2006; Applegarth et al., 2013a). The rate at which crystals grow is controlled by the diffusivity of elements within a melt and the supersaturation (undercooling), which is further influenced by the melt temperature and composition. Thus, the slowest crystal growth occurs in melts with lower temperatures and higher silica contents due to the low element diffusivities (Donaldson, 1979; Cashman, 1992; Simakin et al., 2000; Castro et al., 2008). As such, the most silica-rich lava flows or domes are often the most crystal-poor, despite emplacement timescales of order months (Swanson et al., 1989).

Phenocrysts, the largest crystals of a lava body, form in the magma chamber prior to eruption. The phenocryst content of erupted lava varies substantially, with some of the most phenocryst-rich basaltic to dacitic lava flows having phenocryst contents of 40 – 60 volume% (Pinkerton and Sparks, 1976; Klemetti and Grunder, 2008; Wadge et al., 2014). In contrast, many rhyolite flows are phenocryst-poor, making up only 1 – 5 volume% of the lava (Smith, 2002; Schipper et al., 2015).

Microlites are small (micron-sized), rod or plate-like crystals typically composed of feldspar, pyroxene, or metal oxides. They form as a consequence of a significant undercooling of a melt (50 –200 ℃), which drives rapid nucleation and crystallisation of small crystals due to low diffusivities and supersaturation of the melt (Westrich et al., 1988; Swanson et al., 1989; Sharp et al., 1996). Microlites also form at smaller undercoolings at the onset of crystallisation. The necessary undercooling can result from decompression-driven volatile loss during ascent within the conduit; such decompression is rapid compared to the timescales of crystal growth (Swanson et al., 1989; Cashman, 1992; Cashman and Blundy, 2000; Applegarth et al., 2013a). The microlite population of many rhyolite flows are thought to form in the conduit (Swanson et al., 1989; Befus et al., 2015). However, some rhyolite flows undergo significant microlite growth during lava emplacement, particularly in the insulated flow core where diffusivities are highest, due to the extended timescales over which crystallisation can occur (Stevenson et al., 1994a; Furukawa and Uno, 2015; Schipper et al., 2015).

Devitrification crystals, such as spherulites, are near-spherical crystalline masses that can form in response to high degrees of undercooling (>150 ℃) in high-silica lava bodies (Swanson et al., 1989; Castro et al., 2008). Spherulites are composed of radiating, fibrous, alkali feldspar crystals that typically nucleate on a crystal or vesicle (Lofgren, 1971b; Swanson et al., 1989). When these devitrification structures lack a clear radiating structure they are termed globulites (Lofgren, 1971a; Schipper et al., 2015). Spherulites and devitrification crystalline masses have been experimentally produced at pressures from 0.05 – 0.4 MPa (comparable to the pressure within a lava flow) and temperatures from 240 – 700 °C (Lofgren, 1971a). Spherulites preferentially form in volatile-rich portions of the lava and can develop extensive crystalline bands (Seaman et al., 2009). The growth of spherulites also concentrates volatiles in the surrounding melt (Castro et al., 2008; von Aulock et al., 2013), and their growth can

lead to the formation of lithophysae, which are cavities with a spherulite halo, when the growth of the anhydrous spherulite concentrates water in a central vesicle (Breitkreuz, 2013).

Understanding how the relative proportions of these crystal populations changes throughout the emplacement of a lava flow is vital for constraining its evolving rheological properties. The changes in crystallinity during emplacement of basalts are relatively well understood (e.g. Cashman et al., 1999), but knowledge of the crystallisation history of rhyolitic lava flows is limited to inferences from ancient rhyolitic lavas (e.g. Smith, 2002). Work conducted at Cordón Caulle suggests that the crystallinity of the lava increases from ~20 volume% at the vent, to ~50 volume% in breakouts, to 80 volume% in the flow core (Schipper et al., 2015). Such increases in crystallinity could have substantial impacts on lava rheology, as well as potentially driving bubble growth (Section 4). Section 4 utilises microstructural observations to determine the crystallisation history of the Cordón Caulle lava flow (Appendix 8C.3) and the potential implications that crystallisation may have on flow processes, such as breakout and pumice diapir formation (Sections 4 and 5).

#### 2.2.3.2 Effect of crystals on rheology

As indicated in the previous section, the Cordón Caulle lava flow has a substantial crystal population. As such, it is important to determine the potential impact of these crystals on lava rheology. Crystals increase the viscosity of a lava (Fig. 2.17, 2.18) by dissipating energy through fluid-crystal and crystal-crystal interactions (Caricchi et al., 2007; Mueller et al., 2011). Crystal-crystal interactions have the greater viscosity effect and are usually responsible for the transition to non-Newtonian, shear-thickening behaviour (Smith, 2000; Caricchi et al., 2007; Lavallée et al., 2007; Costa et al., 2009; Mueller et al., 2011). At a crystal content of 30 – 50 volume%, crystals form a

framework where one particle cannot move relative to the other, and at this point the magma develops a yield strength (Kerr and Lister, 1991; Saar et al., 2001; Costa, 2005; Mader et al., 2013). The effect of equant crystals on viscosity ($\eta$) can be determined using the Einstein Roscoe Equation:

$$\eta = \eta_0(1 - R\phi)^{-Q}\,, \qquad [Eq.\,2.4]$$

where $\eta_0$ is the melt viscosity, $R$ is the inverse of the maximum concentration which can be attained by the solids ($1/\phi_{max}$), set at 1.67 or a maximum solid fraction of 60 volume% (Marsh, 1981), $Q$ is a constant equal to 2.5, and $\phi$ is the crystal packing fraction.

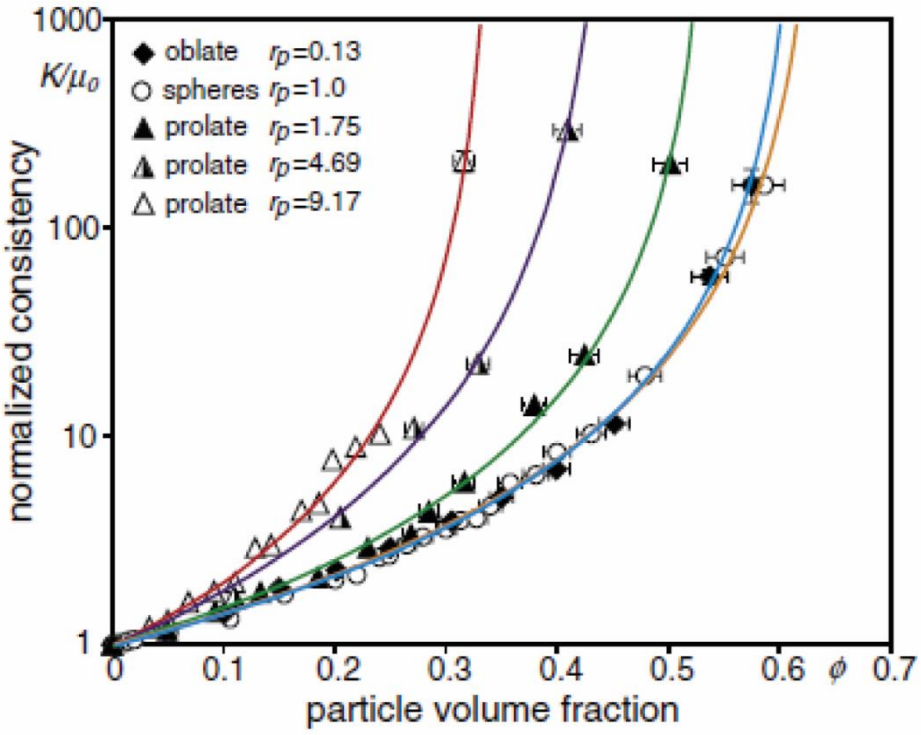


Figure 2.17: Normalised consistency as a function of particle volume fraction and particle aspect ratio, where $K$ is the consistency index, $\mu_0$ is the melt viscosity, $\phi$ is the particle volume fraction, and $r_p$ is the particle aspect ratio. From Mader et al. (2013) using data from Mueller et al. (2011).

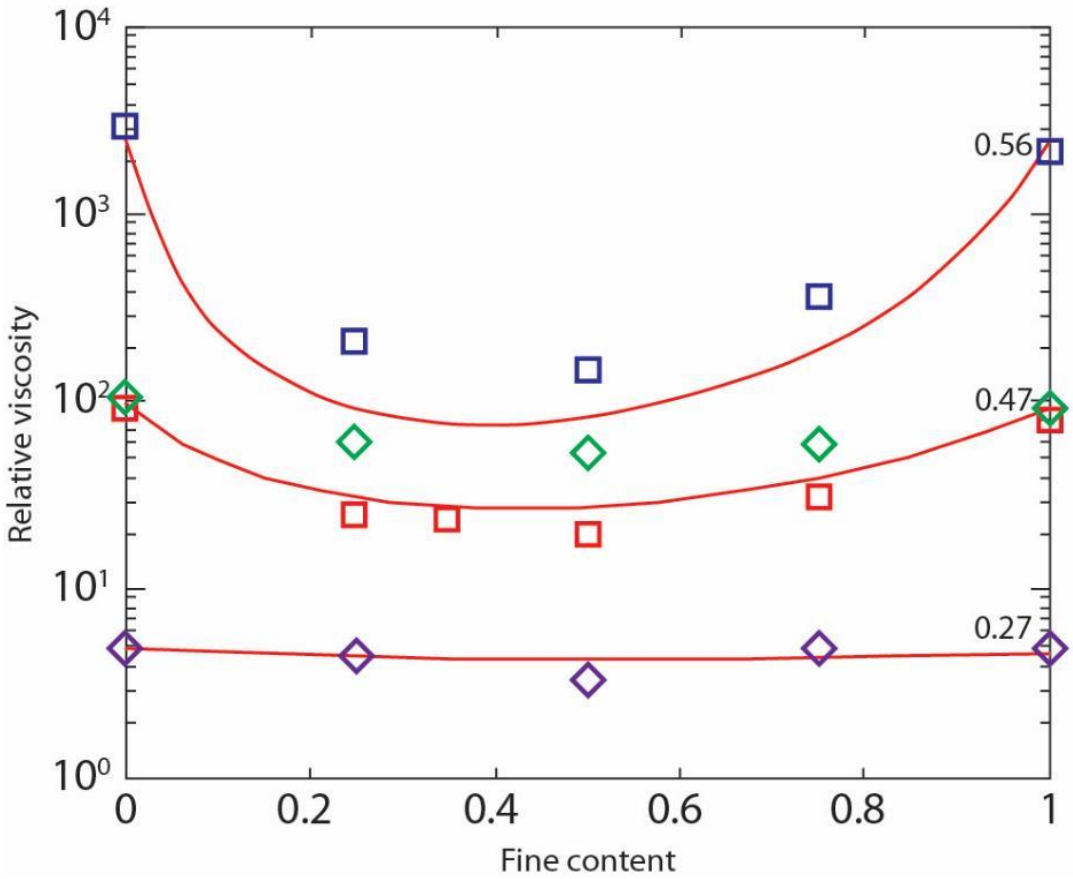


Figure 2.18: The effect on viscosity of varying the fine particulate proportion (0-1) as well as the crystal content (0.27, 0.47, 0.56) in a fluid (in this case syrup). Red lines show the theoretical Einstein-Roscoe determination, with the crystal volume given on the right hand side of the line. Squares are experiments with a particle size ratio of 10:1 between large and small particles. Diamonds show experiments with a particle size ratio of 5:1. Adapted from Castruccio et al. (2010).

Crystal shape and size distribution also affect the viscosity of the bulk fluid (Kerr and Lister, 1991; Castruccio et al., 2010; Mueller et al., 2011). Elongate particles act to increase viscosity of the bulk fluid more than spherical particles, because the drag of a particle is proportional to the length of its longest axis (Kerr and Lister, 1991; Mader et al., 2013). The rotation of an elongate particle also encompasses a greater volume for crystal-crystal interactions than the rotation of a spherical particle of similar volume (Fig. 2.19), so that increasing particle aspect ratio can have a similar effect to increasing the volume of crystals (Fig. 2.17; Mueller et al., 2011). The effect of crystals on viscosity is also governed by the distribution of crystal sizes (Fig. 2.18). A bimodal

distribution of large and small crystals will have less of an impact on viscosity, compared to a unimodal crystal population, as small crystals are able to pass through the gaps between larger crystals (Castruccio et al., 2010). This factor is particularly pronounced at higher crystal volumes (Fig. 2.18). Furthermore, the alignment of elongate crystals during shear can lead to shear thinning lava behaviour as elongate crystals are able to move past one another (Smith, 2002). Thus, understanding the proportion, shape, size distribution, and orientation of crystals, and how these change with time, is vital when attempting to understand lava rheology.

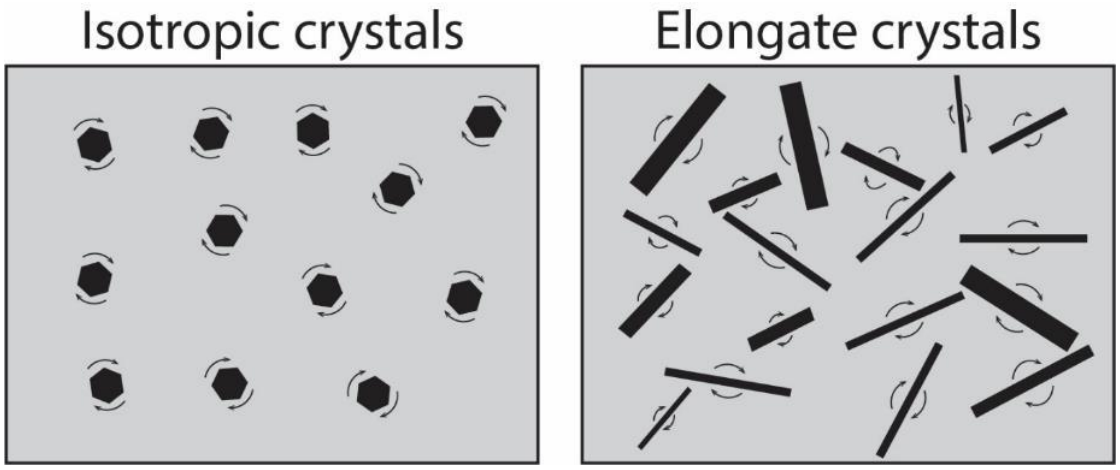


Figure 2.19: (**A**) The rotation of isotropic crystals due to shear in a melt. (**B**) The rotation if elongate crystals due to shear in a melt. The rotation of elongate crystals incorporates more crystal-crystal interactions, leading to a greater viscosity.

Given the crystal population of the Cordón Caulle lava flow, any determination of lava viscosity must incorporate the influence of crystals. The Einstein-Roscoe equation is used in Section 3 to make a broad estimate of the viscosity of the Cordón Caulle lava flow. In Section 5 a more sophisticated approach is taken to incorporate crystal aspect ratio (determined from microstructural observations) into an estimate of bulk viscosity using the rheological model of Mueller et al. (2011). The resulting values are used for modelling lava flow advance rates (Section 3), as well as understanding the processes that may occur in these lavas, such as bubble growth and migration (Section 6).

### *2.2.4 Bubbles*

#### 2.2.4.1 Bubble growth

Previous studies of rhyolite lava flows (Section 2.1.5) have identified the importance of bubble growth (i.e. vesiculation) on the development of late stage lava flow features, such as pumice diapirs (Fink, 1980b; Fink and Manley, 1987; Manley and Fink, 1987; Baum et al., 1989). Bubbles form in a melt through three main processes: 1) decompression, 2) concentration of volatiles in a melt, through anhydrous crystal

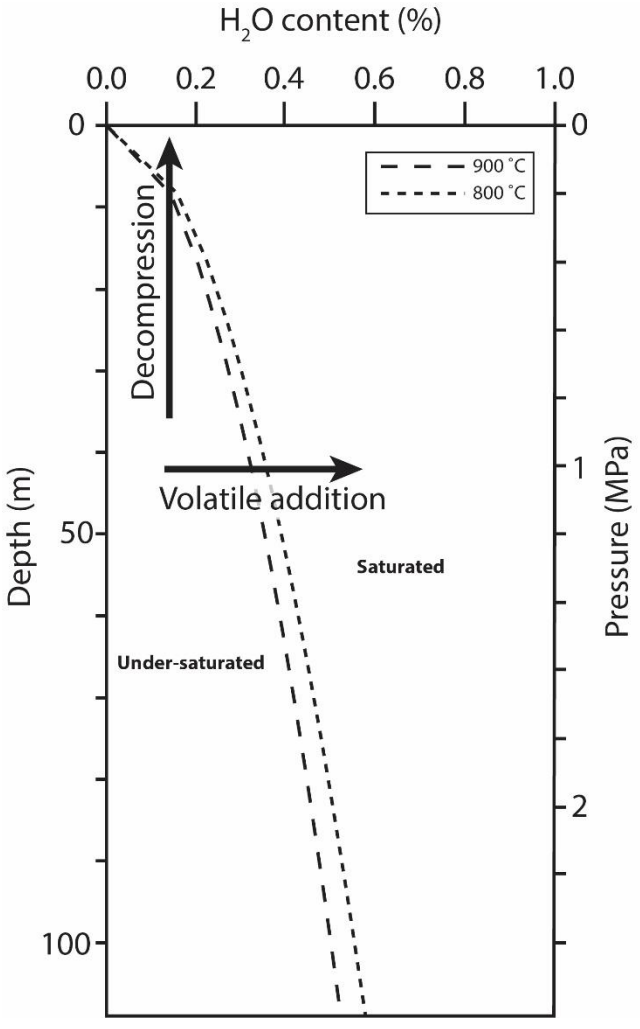


Figure 2.20: Volatile saturation curves for a rhyolite lava flow generated with VOLATILECALC (Newman and Lowenstern, 2002). The three ways to move a melt from under-saturated to saturated are shown. These are: 1) reducing confining pressure, 2) increasing the volatile content of the melt, 3) increasing the temperature of the melt.

growth (second boiling), and 3) heating of the lava body, due to the associated lower volatile solubilities. Bubbles form at various stages throughout an eruption, and here I focus on the processes that are pertinent to high-silica and high-viscosity lava flow emplacement.

Bubbles will grow provided there is a sufficient volatile content in the melt to exceed the supersaturation pressure (Fig. 2.20). Decompression can move a melt from undersaturated to saturated (Fiege and Cichy, 2015), with high decompression rates in the volcanic conduit (Spieler et al., 2004) contributing to magma vesiculation and potentially triggering explosive activity, provided the fragmentation threshold is reached (~75% vesicularity; Eichelberger, 1995). As a lava dome is extruded, it can undergo decompression as it is exposed to the atmosphere; this slow decompression can result in a vesicular and scoracious carapace shortly after exposure (Swanson et al., 1987; Anderson and Fink, 1990; Anderson et al., 1995). As breakouts emerged from the core of the Cordón Caulle lava flow (Tuffen et al., 2013), a similar process may have occurred, as the fresh lava was exposed to the atmosphere (Section 4), potentially contributing to their observed inflation (Tuffen et al., 2013; Farquharson et al., 2015).

The growth of anhydrous crystals concentrates volatiles in the remaining melt body, which can drive volatile saturation and bubble growth (Fig. 2.20), in a process termed second boiling (Sparks et al., 1994; Eichelberger, 1995). Second boiling can redistribute volatiles within a lava, leading to the formation of highly vesicular layers within rhyolite lava flows (Fink and Manley, 1987; Furukawa and Uno, 2015). As the crystallinity of the Cordón Caulle lava flow is known to increase between the vent and flow front (~20 volume% at the vent increasing to ~80 volume% in the flow core, Schipper et al., 2015), crystallisation could drive bubble growth in the flow core, potentially leading to a pressure increase within the flow (Fink and Kieffer, 1993). The associated latent heat of crystallisation could also increase diffusivities, promoting

vesicle growth. Such vesiculation could contribute some of the pressure required to initiate a breakout (discussed in Section 4). The trapping of bubbles within a lava will also be more prominent in silicic lavas compared to basaltic lavas due to their higher viscosity impeding bubble migration and escape (e.g. Vergniolle and Jaupart, 1986; Pistone et al., 2017).

Water can also be added to a lava from external sources, although they may not dissolve into the lava. Meteoric sources, such as rain, can add water to a lava. Lava flows can also advance over wet ground, incorporating water from below, which, in basaltic lava flows, can be associated with explosive activity and rootless cone formation (e.g. Thorarinsson, 1953; Fagents and Thordarson, 2007). The Cordón Caulle lava flow advanced over a stream bed and numerous fumeroles (Sepulveda et al., 2004), which could have added water to the lava flow from below.

Hotter magmas are able to vesiculate at lower volatile contents (Fig. 2.20), due to lower volatile solubilities at higher temperatures. As such, heating a magma body through the latent heat of crystallisation (e.g. up to 100 °C, Blundy et al., 2006), viscous heating, or frictional heating, can cause volatile exsolution and bubble growth (Lavallée et al., 2015). This process could be pervasive within a volcanic conduit, where high shear rates could generate large temperature increases (e.g. 250 °C for viscous heating, and up to 1000 °C for frictional heating, Lavallée et al., 2015), leading to volatile oversaturation of 0.26 – 0.35 wt% (Lavallée et al., 2015). It is unclear whether viscous or frictional heating could drive vesiculation of a slow moving thick lava flow, where shear rates will be lower compared to in a volcanic conduit.

### 2.2.4.2 Effect of bubbles on rheology

Many rhyolite lava flows have bubble rich layers within them (Fink, 1980b; Eichelberger et al., 1984; Fink and Manley, 1987; Manley and Fink, 1987), which may affect the overall bulk flow rheology, but this effect is minor compared to the influence of crystals. The effect of bubbles on magma rheology is dependent on the capillary number (*Ca*), which reflects the relative importance of viscous forces (deforming) versus surface tension (reforming) on the bubble shape. *Ca* can be given as:

$$Ca = \frac{\mu_0 a \dot{\gamma}}{\Gamma}, \qquad [Eq. 2.5]$$

where $\mu_0$ is the liquid viscosity, *a* is the radius of the undeformed (spherical) bubble, $\dot{\gamma}$ is the shear strain-rate, and Γ is the surface tension at the bubble-liquid interface.

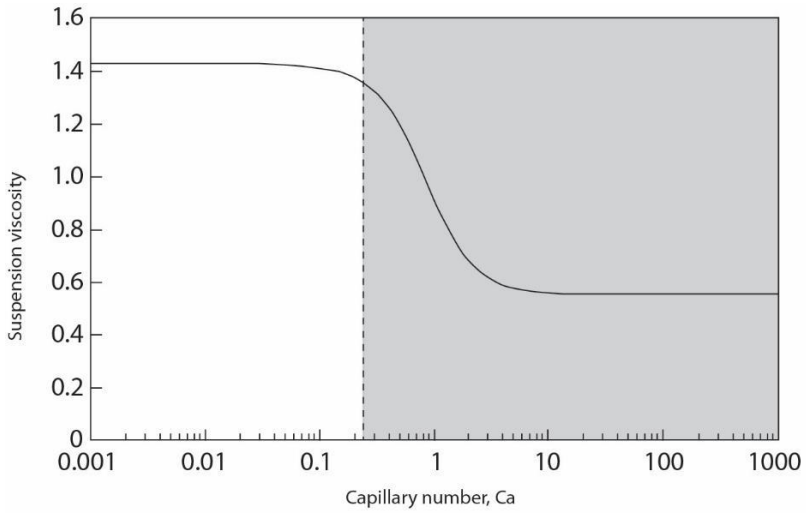


Figure 2.20: Effect of vesicles of different capillary number on viscosity for a vesicle packing fraction of 0.3. The grey box marks the transition to what is considered a large capillary number. Adapted from Truby et al. (2015).

When *Ca* is large, the bubble easily deforms as the reforming force is small compared to the deforming force, when *Ca* is small, surface tension dominates and the bubble retains its equilibrium shape (i.e. a sphere) after changes in strain rate, and acts as a

low-density solid particle (Llewellin et al., 2002; Truby et al., 2015). At low *Ca,* bubbles will increase viscosity (Fig. 2.21) as they retain their shape and act as a barrier to flow (Mader et al., 2013). In melts that contain a large number of low Ca bubbles, the melt can develop a yield strength, provided the bubbles form a framework (i.e. a foam) where one bubble cannot move relative to the others due to their surface tension (Kerr and Lister, 1991).

Bubbles with a high *Ca* act to decrease the viscosity of a melt (Fig. 2.21; Mader et al., 2013). As a bubble with a high *Ca* is subjected to shear it will become elongated, with the direct effect of providing less of an obstacle to flow (Mader et al., 2013). Bubbles also present areas of low-viscosity, as there is less viscous dissipation in the annulus around a bubble, due to the negligible viscosity of the gas in the bubble, than if the bubble was not there (Kerr and Lister, 1991; Rust and Manga, 2002; Mader et al., 2013). Therefore, the presence of bubbles can act to decrease the bulk viscosity (Llewellin et al., 2002; Mader et al., 2013). The potential influence of bubbles on flow rheology are important when discussing the formation of pumice diapirs, with bubbles either acting to increase or decrease the bulk viscosity of a vesicular layer depending on whether the bubbles deform (discussed in Section 5).

The rheology of two phase magmas containing either bubbles in melt or crystals in melt is well studied (Mader et al., 2013). Recent work has started to address the rheology of three phase magmas, with the dominant influence on rheology dependent on whether the proportion of crystals is greater than bubbles, or vice versa (Pistone et al., 2012; Truby et al., 2015). The interaction of crystals and bubbles is an important consideration in silicic lavas, with experimental studies suggesting that high crystal concentrations in lavas (>60 volume%) can inhibit bubble escape (Pistone et al., 2017). As a consequence the bubbles can become pressurised, potentially increasing the

likelihood of explosive activity (Pistone et al., 2017). The potential impact of crystals on bubble growth, and migration, in rhyolitic lava flows are discussed in Section 5.

### *2.2.5 Determining lava viscosity*

Although direct measurements of viscosity are not made in this thesis, it is useful to briefly outline how such measurements are made, as these are often used to inform viscosity calculators, utilised in Sections 3 and 5. Numerous attempts have been made to either infer, or directly measure, lava flow viscosity. Laboratory experiments have been conducted to directly measure the viscosity of silicate melts at magmatic conditions. The methods include using a falling sphere/indentation, where the time for either a sphere of known density, or an indenter, to descend into a melt is measured (e.g. Shaw, 1963; Hess et al., 1995; Schulze et al., 1996; Dingwell and Hess, 1998). Rotational spindles are also used (otherwise known as the concentric cylinder method), whereby a rod is inserted into a melt and rotated, with the resistance to shear informing the viscosity (e.g. Dingwell, 1989; Dingwell and Hess, 1998). An alternative method involves deforming a sample between two parallel aluminium plates at a range of stresses and strain rates (e.g. Stevenson et al., 1998). The large number of experiments conducted have allowed the development of numerical viscosity calculators that can be applied across a broad compositional spectrum, for appropriate magmatic temperatures (Giordano et al., 2008). Some of these numerical approaches to determining viscosity are however, specific to a narrow compositional range, such as crystal-poor rhyolites (e.g. Romine and Whittington, 2015). Such narrow calculators may be more accurate for a specific composition.

Jeffreys (1925) equation has been used to derive apparent lava viscosity ($\eta_A$):

$$\eta_A = \left(\frac{\rho g d^2 sin\beta}{nU}\right), \qquad [Eq. 2.6]$$

where $\rho$ is the density, $d$ is the flow depth, $\beta$ is the slope angle, $n$ is an empirical constant for channelized flow, and $U$ is the mean flow surface velocity. This has been applied to a broad compositional spectrum of lavas from mafic (e.g. Nichols, 1939; Naranjo et al., 1992) to silicic (Farquharson et al., 2015). Here, the approach of Jeffreys (1925) is used to determine the bulk viscosity of the Cordón Caulle lava flow in Section 3. Castruccio et al. (2013) used an alternative approach, using the flow front advance rate to estimate bulk lava viscosity. Attempts have also been made to take laboratory techniques into the field, in order to determine the rheological properties of active lavas, by using a field viscometer comprising a shear vein attached to a torque gauge that could be inserted into an active lava flow (Pinkerton and Sparks, 1978) or lava lake (Shaw et al., 1968).

### 2.3 Thesis aims and structure

The observation of breakout formation during the 2011-2012 Puyehue-Cordón Caulle lava emplacement is unique, and breakouts are not generally considered to occur within rhyolite lavas. Instead, breakout formation is typically associated with the emplacement of mafic lava flows (e.g. Pinkerton, 1987; Cashman et al., 1994; Blake and Bruno, 2000). Thus, despite the large differences in composition and viscosity, observations of rhyolitic breakout formation suggests underlying fundamental processes in the emplacement of lava flows (Tuffen et al., 2013). The thesis aims to draw comparisons between the emplacement of silicic lava flows and mafic lava flows. To this end, I focus on the 2011-2012 Cordón Caulle eruption as an exceptional example of a cooling-limited rhyolite lava flow, a type of lava flow for which there has previously been little observational data. Specifically, the project addresses four main questions:

1. What was the rheological control on the development of the Cordón Caulle lava flow, and how does it compare to other cooling-limited lava flows?
2. What processes contributed to the formation and evolution of breakouts from the Cordón Caulle lava flow?
3. What conditions favour core upwelling to the surface of a silicic lava flow, instead of breakout formation?
4. What commonalities exist in the emplacement of mafic and silicic lava flows?

To address these aims, the work uses a multiscale approach, utilising a mixture of remote sensing, field observations, microstructural characterisation, and analytical models. The three papers within this thesis provide an overview of the methods used and a detailed methodology, and associated data, can be found in the appendices (Appendix 8A – 8D).

The results of this project are given in three papers:

1. Paper 1 aims to provide a better understanding of the rheological controls on the emplacement of two cooling-limited lava flows by incorporating observations of lava emplacement to constrain straightforward quantitative models of lava lengthening. The controls on a basaltic lava flow from Mt Etna were examined first and then the same models were applied to understand the rheological control on the emplacement of the Cordón Caulle rhyolitic lava flow.
2. Paper 2 addresses the processes that led to the formation of breakouts at Cordón Caulle. The paper uses detailed observations of breakout formation and morphology from satellite imagery and a field campaign to characterise breakout morphology. I then incorporate microstructural observations to determine the processes that contributed to breakout formation.

3. Paper 3 determines the conditions that favour the development of coarsely vesicular pumice diapirs instead of breakouts in some rhyolite lava flows. This paper uses a combination of field studies of rhyolite lava flows in the USA, satellite imagery and microstructural characterisation.

Finally, Section 6 draws the findings from the three papers together, and lava flow emplacement is discussed more broadly, incorporating evidence from observations of basaltic and silicic compositions to suggest common processes inherent in lava flow emplacement.

# 3 Emplacing a cooling-limited rhyolite lava flow: similarities with basaltic lava flows

N. Magnall[1], M.R. James[1], H. Tuffen[1], C. Vye-Brown[2]

*[1]Lancaster Environment Centre, Lancaster University, Lancaster, UK*

*[2]British Geological Survey, The Lyell Centre, Edinburgh, UK*

The following paper originally appeared in Frontiers in Earth Science, subsection Volcanology, published 8 June 2017 (DOI: 10.3389/feart.2017.00044). It was first submitted to the journal 27 February 2017 and was accepted for publication 22 May 2017 after revisions suggested by Luis Lara (editor), Jon Major, and Colin Wilson (reviewers). The modelling within the paper, the remote sensing work, fieldwork at Cordón Caulle and Mt Etna, as well as the bulk of the writing, was conducted by myself. The main role of the co-authors was with the initial conception of the project, field assistance, and the writing of the manuscript. The detailed methodology for this paper can be found in the appendices: Appendix 8A details the remote sensing techniques used, Appendix 8B expands on the data gathered in the field and Appendix 8D outlines details of the quantitative modelling.

The paper focusses on the rheological controls on the emplacement of the 2001 Mt Etna basaltic lava flow and the 2011-2012 Cordón Caulle rhyolitic lava flow. To do this we used simple quantitative models (Kerr and Lyman, 2007; Castruccio et al., 2013), which assumed that the lengthening of the lava flow was controlled by either its Newtonian viscosity, non-Newtonian yield strength, or by the strength of a surface crust. The predicted lengthening was then compared to the observed flow lengthening. In order to improve the applicability of such models (Kerr and Lyman, 2007; Castruccio et al., 2013) we first identify the changes in rheological control through observations from satellite, field, and published observations. For both lava flows the formation of

breakouts indicated a strong crustal control during emplacement, suggesting a crustal control model is the most applicable for the latter stages of emplacement. This is typical of basaltic lava flows but had not been inferred for the emplacement of high-silica content lava flows, which Castruccio et al. (2013) suggested were primarily controlled by a non-Newtonian yield strength.

The combination of techniques used within this study allowed for an improved understanding of the rheological controls on rhyolite lava flow emplacement:

- Observations of the development of breakouts and large surface fractures during lava flow emplacement at both Cordón Caulle and Mt Etna, suggested the influence of a surface crust on the latter phases of lava flow emplacement.
- Quantitative modelling suggested that for both the 2001 Mt Etna basaltic lava flow and the Cordón Caulle rhyolite lava flow, the flows were initially controlled by a Newtonian viscosity, and later by the yield strength of the surface crust. Suggesting similarities in their emplacement.
- The initial Newtonian viscosity control on the Cordón Caulle rhyolite lava flow suggests a fundamental difference between the emplacement of crystal-poor (e.g. rhyolite) and crystal-rich (e.g. dacite) siliceous lava flows, which are likely controlled by their yield strength.

## 3.1 Abstract

Accurate forecasts of lava flow length rely on estimates of eruption and magma properties and, potentially more challengingly, on an understanding of the relative influence of characteristics such as the apparent viscosity, the yield strength of the flow core, or the strength of the surface crust of the flow. For basaltic lavas, the relatively high frequency of eruptions has resulted in numerous opportunities to test emplacement models on such low-silica lava flows. However, the flow of high-silica lava is much less well understood due to the paucity of contemporary events and, if observations of flow length change are used to constrain straightforward models of lava advance, remaining uncertainties can limit the insight gained.

Here, for the first time, we incorporate morphological observations from during and after flow field evolution to improve model constraints and reduce uncertainties. After demonstrating the approach on a basaltic lava flow (Mt. Etna, 2001), we apply it to the 2011-12 Cordón Caulle rhyolite lava flow, where unprecedented observations and syn-emplacement satellite imagery of an advancing silica-rich lava flow have indicated an important influence from the crust of the lava flow on flow emplacement. Our results show that an initial phase of viscosity-controlled advance at Cordón Caulle was followed by later crustal control, accompanied by formation of flow surface folds and large-scale crustal fractures. Where the lava was unconstrained by topography, the cooled crust ultimately halted advance of the main flow and led to the formation of breakouts from the flow front and margins, influencing the footprint of the lava, its advance rate, and the duration of flow advance. Highly similar behaviour occurred in the 2001 Etna basaltic lava flow. In our comparison, we find close similarities between the processes controlling the advance of a crystal-poor rhyolite and a basaltic lava flow, suggesting a common crustal control on latter flow emplacement that transcends the profound viscosity and compositional differences of the lavas.

## 3.2 Introduction

Lava flows present a significant hazard in the immediate vicinity of volcanic complexes and can, in some cases, also present a hazard to more distal communities. However, despite the sophisticated numerical models that have been developed for basaltic lava flows (Crisci et al., 1986; Hidaka et al., 2005; Vicari et al., 2007; Hérault et al., 2011), a full understanding of the factors controlling the rate and extent of lava flow advance, which is essential for adequate hazard forecasting over a broad range of lava geochemistries, remains elusive due to the complexity of lava flow rheology, internal architecture, and interactions with topography. The frequency of basaltic eruptions has provided many examples for modelling low-silica lavas (Crisci et al., 1986; Hidaka et al., 2005; Vicari et al., 2007; Hérault et al., 2011), but equivalent studies of high-silica flows are relatively rare and poorly constrained, and thus reflect weaknesses in our universal understanding of lava emplacement processes. Here, we use observations of the 2011-2012 Cordón Caulle rhyolite lava flow as an unparalleled opportunity to study a high-silica flow, and we present the first modelling study to our knowledge that examines the advance of a high-viscosity and crystal-poor lava. Our results significantly improve constraints on the rheological controls of high-viscosity flows.

Lava flow advance is thought to be initially controlled by the effusion rate at the vent and topographic slope (Pinkerton and Wilson, 1994). Volume-limited flows are those lavas that cease to advance when fresh material is no longer supplied to the flow front, due to cessation of effusion at the vent or a redirecting of fresh lava away from the flow front (Walker, 1971). If, instead, a flow continues to advance, it will eventually reach its cooling-limited length, at which point cooling has formed a crust, comprising a rheologically stiff layer and a brittle surface, sufficiently strong to inhibit flow advance (Cashman et al., 1998; Blake and Bruno, 2000; Hon, 2003). A clinker dam can also inhibit the flow advance (Applegarth et al., 2010a). Pressure builds within the flow as

new material is supplied to the flow front, causing inflation and eventually breaking the crust to form a secondary flow or breakout (Calvari and Pinkerton, 1998; Blake and Bruno, 2000). This is a common process in basaltic eruptions (Walker, 1971; Kilburn and Guest, 1993; Hon et al., 1994; Calvari and Pinkerton, 1998; Applegarth et al., 2010c) but has been observed rarely in high-silica lava flows (Harris et al., 2004), partly due to the infrequency with which such eruptions occur.

The 2011-2012 eruption of Cordón Caulle in southern Chile (low-silica rhyolite, 69.7 wt% $SiO_2$) permitted the first detailed scientific observations of the emplacement of a crystal-poor, silica-rich lava flow (Silva Parejas et al., 2012; Castro et al., 2013; Schipper et al., 2013; Tuffen et al., 2013; Bertin et al., 2015). Prior to this eruption the only detailed observations of rhyolitic lava emplacement came from the 2008-2009 Chaitén eruption in Chile, in which a composite rhyolite dome was emplaced without the development of a laterally extensive flow field (Bernstein et al., 2013; Pallister et al., 2013). Initial observations of the flow at Cordón Caulle indicated that over the duration of the ~10 month eruption the flow front stalled, in some places against topographic barriers, and breakouts formed at the flow front and margins, creating a complex flow field (Tuffen et al., 2013). With flow fronts typically 30 m thick, models of conductive cooling suggest that the flow interior may have retained sufficient heat to permit advance for 36 – 48 months after emplacement (Farquharson et al., 2015), and breakouts were observed to advance for up to 10 months after the eruption ceased (Tuffen et al., 2013; Farquharson et al., 2015). The formation of breakouts in both basalts and rhyolites suggests that both compositional endmembers can generate cooling-limited lava flows and, hence, flow front advance may be controlled in the latter phases of emplacement by a cooled crust.

Previous studies of rhyolitic lava flows have focussed mostly on higher-silica (72 – 74 wt% $SiO_2$) Holocene flows in the US such as Big and Little Glass Mountain at Medicine

Lake (Fink, 1980b, 1983; Grove and Donnelly-Nolan, 1986; Manley and Fink, 1987) and Big Obsidian Flow in Newberry Caldera (Castro et al., 2002a). Detailed studies of lava flow morphology led to conceptual models in which slowly-spreading crystal-poor lava moved over talus derived from the flow front (Fink, 1980a; Fink, 1983) before stopping when supply ceased (i.e. volume-limited). This style of advance has been observed in active dacitic flows at Santiaguito, Guatemala (Harris and Flynn, 2002). However, the characteristics of the surface facies of Holocene lava flows additionally inspired models that included a cooled surface crust to account for features such as ogives, formed by crustal folding as the flow front slowed (Fink, 1980a; Castro and Cashman, 1999), crease structures (Anderson and Fink, 1992; Lescinsky and Merle, 2005), and large gas cavities (Castro et al., 2002a). Such crusts have been inferred to significantly influence lava flow growth (Griffiths and Fink, 1993; Fink and Griffiths, 1998), and would also act to thermally insulate the flow, facilitating prolonged mobility and advance (Manley, 1992), as later observed at Cordón Caulle (Tuffen et al., 2013).

Straightforward analytical models to forecast lava flow length have been based on a number of different lava rheologies (Huppert, 1982; Lister, 1992; Kerr and Lyman, 2007; Castruccio et al., 2013). In these models, lava flow advance is assumed to be controlled by either an apparent Newtonian viscosity, a non-Newtonian flow core, or a surface crust of defined strength (Fig. 3.1). Control may switch between rheology types as the flow advances, as suggested by a transition between best-fit models during emplacement (Castruccio et al., 2013). However, for most studied examples of silicic lava emplacement, relatively few parameter values or constraints are available (e.g. syn-eruptive flow lengths and widths only) and models are thus vulnerable to correlated parameter uncertainties, which weaken confidence in the resulting interpretations of rheological control. Nevertheless, previous modelling studies have proposed that

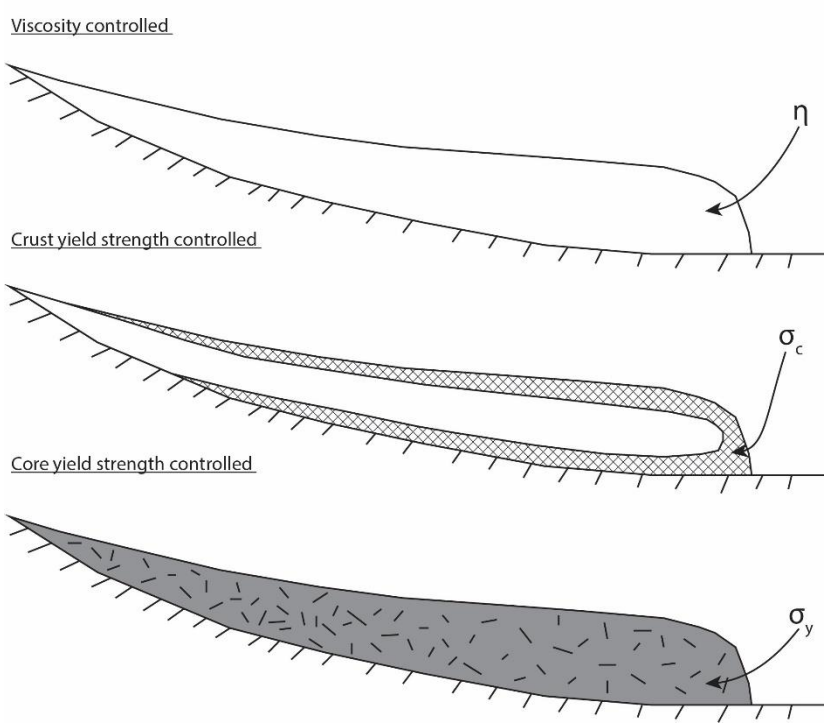


Figure 3.1: The three flow regimes that can control lava flow behaviour: viscosity dominated, crust yield strength dominated, and core yield strength dominated (after Castruccio et al; 2013). The control on flow advance may change throughout the duration of the lava flow emplacement.

advancing crystal-rich high-viscosity lava flows are yield strength controlled (Castruccio et al., 2013).

Here we examine model robustness by using field data in addition to morphological observations from sequential satellite images of evolving flow fields, to help constrain the time of transition between rheological models. We test the application of these additional observations on a basaltic lava from the 2001 Mt Etna eruption and then extend their application to the 2011-2012 Cordón Caulle rhyolitic flow field. Our overall aims are to 1) assess the consilience of such quantitative models with morphological evidence for rheological change and 2) apply lava flow models to the Puyehue-Cordón Caulle lava flow field to explore the role of a physically thickening crust on the advance of a crystal-poor, high-viscosity rhyolite flow. We show that whereas both the Etna and

Cordón Caulle lava flows were initially under Newtonian viscous control, their subsequent development was predominantly controlled by the evolving surface crust.

### 3.3 Flow length models

The models used in this study are given in Kerr and Lyman (2007) and Castruccio et al. (2013), where their derivations are presented in detail. The methodology for the flow length models is given in Appendix 8D. If a lava flow is treated as a Newtonian viscous fluid emplaced into an environment of negligible density, its length *L* can be given by

$$L = C_{vs}\left[\frac{g\rho sin\beta q^2 t}{\eta}\right]^{1/3}, \qquad [Eq.\,3.1]$$

(Huppert, 1982; Lister, 1992; Kerr and Lyman, 2007), where $C_{vs}$ is a constant defined as $(3/2)^{2/3} = 1.31$, $g$ is gravitational acceleration, $\rho$ is lava density, $\beta$ is the ground slope, $q$ is the volume erupted per unit width of the flow front, $t$ is the elapsed time, and $\eta$ is the effective lava viscosity (Table 3.1).

As a lava flow advances, its surface cools to form a crust of thickness $\delta$, which can be assumed to thicken diffusively as $\delta \sim (kt)^{1/2}$ (Griffiths and Fink, 1993), where $k$ is the thermal diffusivity. If the strength of the crust controls the flow motion, the lava flow length is given by

$$L = C_c\left[\frac{g\rho}{\sigma_c}\right]^{1/2} q(kt)^{-1/4}, \qquad [Eq.\,3.2]$$

(Griffiths and Fink, 1993; Lyman et al., 2005b; Kerr and Lyman, 2007), where $C_c$ is an unknown constant of the order 1, and $\sigma_c$ is the crustal yield strength. Eq. 3.2 does not include ground slope because, as a $cos\beta$ multiplier term (Griffiths and Fink, 1993), for the low slope angles examined here, it can be assumed $cos\beta \approx 1$ (Lyman and Kerr, 2006).

Although useful for first order estimates, Eq. 3.1 and 3.2, termed here the fixed parameter approach, do not enable down-flow variations in parameters (e.g. slope) to be accounted for. Thus, Castruccio et al. (2013) derived equivalent models, but using a summative approach to enable parameter variation during emplacement. In this case, the length of an advancing flow dominated by a Newtonian viscosity is given by

$$L = C_1 \sum_{i=1}^{n} \left[ \frac{V_i^2 \rho g sin\beta_i t_i}{\eta_i W_i^2} \right]^{1/3}, \qquad [Eq. 3.3]$$

where $C_1$ is a constant in the viscous regime defined as $(3/2)^{2/3} = 1.31$ (in line with equation 1), $V_i$ is the volume added at each time step, $\beta_i$ is the terrain slope, $t_i$ is the time interval between each step, and $\eta_i$ and $W_i$ represent the lava viscosity and flow width at a given time step (Castruccio et al., 2013).

In the case of flow advance limited by a crustal yield strength, the evolving flow length can be given by

$$L = C_3 \sum_{i=1}^{n} \left[ \frac{V_i^2 \rho g sin\beta_i}{W_i^2 \sigma_{ci} \sqrt{kt}} \right]^{1/2}, \qquad [Eq. 3.4]$$

where $t$ is the total time elapsed, $C_3$ is a constant of order 1 (Castruccio et al., 2013), and $\sigma_{ci}$ is the crustal yield strength at a given time interval (Castruccio et al., 2013), which here is assumed not to change with time.

A third case represents flow behaviour as a bulk non-Newtonian fluid rather than Newtonian. In this case a yield strength must be exceeded before the flow can advance (Castruccio et al., 2013), and flow length can be given by

$$L = C_2 \sum_{i=1}^{n} \left[ \frac{V_i \rho g sin\beta_i}{\sigma_{yi} W_i} \right], \qquad [Eq. 3.5]$$

where $C_2$ is a constant of order 1, and $\sigma_{yi}$ is the bulk yield strength at a given time interval (Castruccio et al., 2013). These three models are collectively termed the flexible parameter approach throughout this paper. Here we attempt to improve upon the application of these models by incorporating observations of lava flow advance and morphology to better constrain the timing of key rheological changes during lava flow emplacement.

Table 3.1: Summary of parameters used in the quantitative approach

| Symbol | Unit | Description |
|---|---|---|
| L | m | flow length |
| W | m | flow width |
| $C_{vs}$, $C_c$ | | constants in viscous flow and crust regime (Kerr and Lyman, 2007) |
| $C_1$, $C_2$, $C_3$ | | constant in the viscous, core and crust regime (Castruccio et al., 2013) |
| $U$ | m $s^{-1}$ | flow surface velocity |
| $g$ | m $s^{-2}$ | acceleration due to gravity – 9.81 m $s^{-2}$ |
| ρ | kg $m^{-3}$ | density of the lava |
| β | ° | slope angle |
| $q$ | $m^2$ | erupted volume per unit width |
| η | Pa s | lava viscosity |
| $\eta_A$ | Pa s | apparent viscosity |
| $\eta_0$ | Pa s | melt viscosity |
| $\sigma_c$ | Pa | yield strength of the crust |
| $\sigma_y$ | Pa | bulk yield strength |
| Φ | | crystal packing fraction |
| V | $m^3$ | volume erupted |
| $k$ | $m^2$ $s^{-1}$ | thermal diffusivity |
| $t$ | s | time |
| $R$ | | constant in Einstein-Roscoe equation |
| $Q$ | | constant in Einstein-Roscoe equation |
| $n$ | | constant in Jeffreys (1925) equation |

## 3.4 Basaltic lava from 2001 Mt Etna eruption

The 2001 eruption of Mt Etna produced several lava flows from numerous vents (INGV, 2001; Behncke and Neri, 2003; Coltelli et al., 2007; Applegarth, 2008). The eruption of the largest lava flow began from an altitude of ~2100 m near La Montagnola (Fig. 3.2) in the early hours of 18 July 2001 (Behncke and Neri, 2003; Applegarth, 2008). The flow that issued from this vent was the largest of the eruption, reaching over 6 km long and with a volume of 0.02 km$^3$. The lava flow was active for 23 days but reached its maximum length after 7 days, after which activity was dominated by breakout development farther up-flow (Behncke and Neri, 2003; Coltelli et al., 2007).

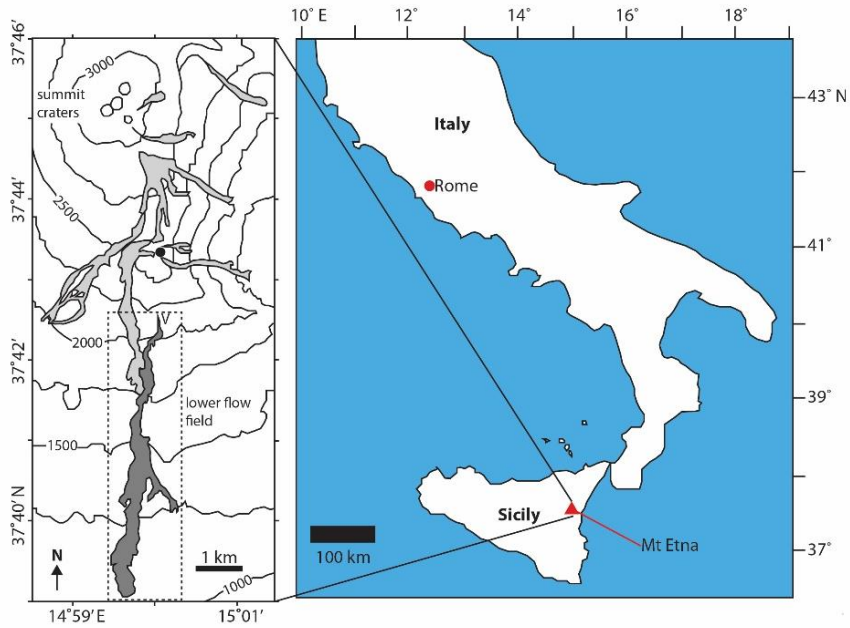


Figure 3.2: Location of Mt Etna and the 2001 lavas. The flow examined in this work (dark grey and highlighted by the dashed box) was erupted from a vent at 2100 m elevation. This flow can be seen to be joined by others erupted from higher elevations (light grey), but this occurred after it had attained its final length and so did not contribute to the main flow advance (Coltelli et al., 2007).

The 2001 Mt Etna lava flow was described by Applegarth (2008) as a thin (up to 2 m) sheet at ~150 m per hour before becoming concentrated in a channel at its eastern margin. By the evening of the 19 July, the flow had attained a length of 3.4 km and was

advancing at a rate of ~45 m per hour. On the morning of the 20th the flow front had reached an altitude of 1350 m, and was 100 m wide and ~5 m high with an incandescent interior visible beneath a cover of black scoria. The flow continued to move down the volcano flanks at a rate of ~50 m per hour, eventually reaching an area of slightly flatter topography at 1055 m on 23 July (Behncke and Neri, 2003; Applegarth, 2008). The flow reached its maximum length on 25 July, at which point the flow front was 200 – 300 m wide and 10 – 20 m high (Applegarth, 2008). The eruption continued and numerous small breakouts formed at the most distal flow margins and larger breakouts formed further up-flow until the eruption ceased on 9 August 2001 (Behncke and Neri, 2003; Coltelli et al., 2007; Applegarth, 2008). Between 26 – 27 July, a lava flow that had erupted from higher elevations merged with the lower 2001 lava flow (Lanzafame et al., 2003; Coltelli et al., 2007). However, because this was after the main flow had attained its final length (Coltelli et al., 2007), it did not contribute to the overall flow advance, but likely contributed to the later breakout emplacement.

### *3.4.1 Field evidence for a late crustal control*

Field observations of the lava flow were made in April 2015 and focussed on morphology and late stage flow features. The main portion of the lava is a channelized 'a'ā flow with well-developed levées and a significant portion of drained channel (>2 km long), whereas the distal region lacks levées and has numerous breakouts from its margin. The 2001 flow deposit is almost entirely covered by loose clinker (rubble), making it difficult to observe any surface crust. However, breakouts are common and typically found at flow margins (Fig. 3.3A) and fronts, together with some areas of drained channel (Applegarth et al., 2010c). Most breakouts are hundreds of metres long but some are substantially longer.

The surface crust is visible at the boccas (feeder points) of some breakouts, where it can be buckled upwards due to inflation (Fig. 3.3B). Where observed, the crust is generally ~tens of centimetres thick, with a layer of incipiently welded clinker adhering to what would have been the top surface. However, this crustal thickness, formed in the latter stages of the eruption, may not be representative of the crust earlier in the flow evolution.

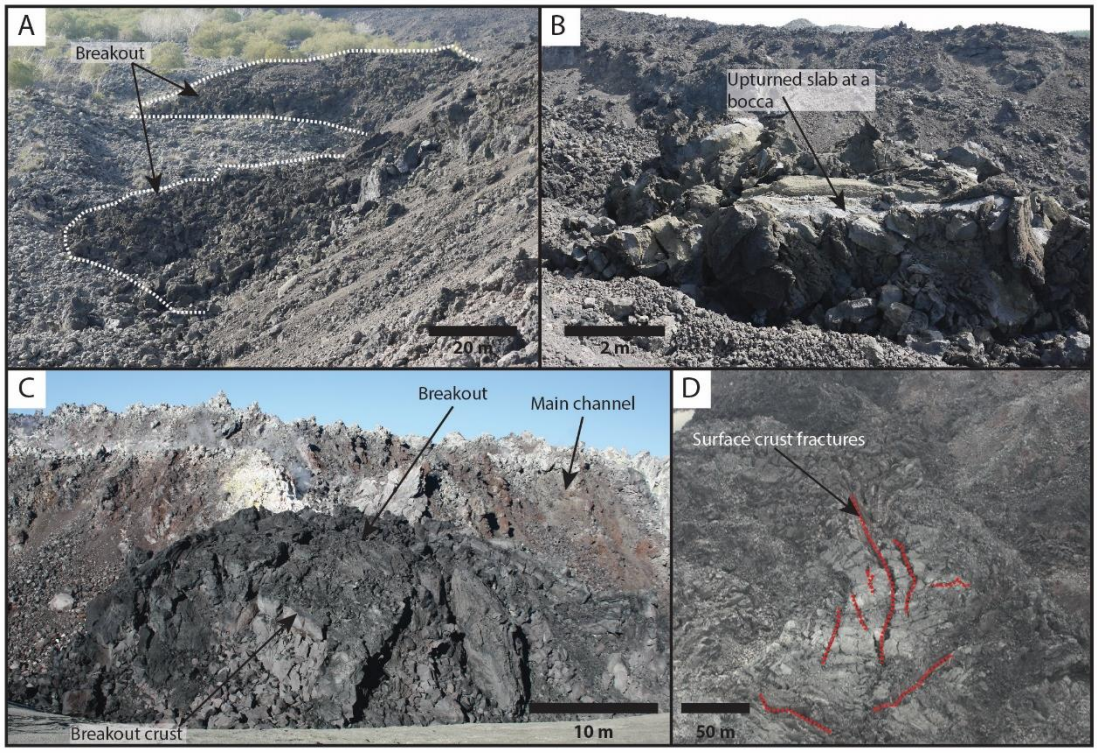


Figure 3.3: Field photographs from Mt Etna (**A** and **B**) and Cordón Caulle (**C** and **D**) that show evidence for the development of extensive surface crusts. (**A**) Breakouts from the margin of the 2001 Mt Etna lava flow, which formed in response to stalling of the flow front due to the development of an extensive surface crust. (**B**) An inflated bocca at the source of a breakout in a drained channel of the 2001 Mt Etna lava flow. Boccas are one of the few places that the surface crust is directly visible as it has been upturned when the breakout formed. (**C**) Breakout from the margin of the 2011-2012 Cordón Caulle rhyolite flow. The breakout has a domed morphology and an extensive surface crust. (**D**) Fractures in surface crust on the 2011-2012 Cordón Caulle rhyolite flow are tens to hundreds of metres long and likely several metres deep. These areas of crust provide direct evidence for the formation of a surface crust on the flow. Details of the field data gathered can be found in Appendix 8B.

### *3.4.2 Inferred changes in rheological control*

As there are relatively sparse published observations of the eruption and spatio-temporal development of the lava flow field, the timing of inferred changes in rheological control is uncertain. However, a reported reduction in flow front advance rate occurred after ~40 hours on a constant slope, and at a time when the vent effusion rate (Table 3.3) was increasing (Behncke and Neri, 2003; Coltelli et al., 2007). This suggests that surface cooling had generated a flow-retarding crust that had begun to exert significant influence.

The presence of breakouts, formed after the main flow front stalled, indicates the presence of a cooled crust that acted to halt, or substantially slow, the flow front and enabled breakout formation from the flow margins. Flow front halting was likely assisted by a reduced slope gradient (Appendix 8A.24). Direct observations of the crust at boccas show the development of a flow surface crust that could have influenced the flow development. The crust is visible only at areas of inflation or breakout formation, providing further evidence for the effectiveness of this crust, as it was able to accommodate an internal pressure increase within the flow due to material continuing to be supplied to the stalled front.. Here we assume flow behaviour was initially controlled by its Newtonian viscosity and there was insufficient cooling and crystallinity to acquire a yield strength in the first 40 hours.

### *3.4.3 Application of flow models to the 2001 Mt Etna flow*

Previous work based on surface velocity measurements from videos of channelized sections of the flow have estimated a Newtonian flow viscosity of $3.5\times10^4 – 5.6\times10^5$ Pa s (Applegarth, 2008) using Jeffreys (1925) equation

$$\eta_A = \left(\frac{\rho g d^2 sin\beta}{nU}\right), \qquad [Eq.3.6]$$

for flow in a wide channel, where $\rho$ is the density, $g$ is the acceleration due to gravity, $d$ is the flow depth, $\beta$ is the slope angle, $n$ is an empirical constant for channelized flow and $U$ is the flow surface velocity. It is assumed that the apparent viscosity $\eta_A$ is equivalent to the viscosity $\eta$ (Hulme, 1974; Stevenson et al., 2001; Harris et al., 2004; Farquharson et al., 2015). Here we use the central viscosity value of this range - $3.0\times10^5$ Pa s (Applegarth, 2008).

#### 3.4.3.1 Models of flow lengthening

To account for uncertainty in the timing of the transition from viscosity to crust-controlled flow, lava flow models are used with transition times of 12, 24 and 36 hours (Table 3.2 and 3.3), along with observed flow length changes from Applegarth (2008).

The modelled lengths using the fixed parameter approach (Eq. 3.1 and 3.2) suggest that the transition from viscosity to crustal control occurred after 12 – 24 hours, although in the case of a transition in control after 24 hours the final lava flow length was overestimated by ~1 km (Fig. 3.4A). The model may overestimate the advance rate during initial lava emplacement but this cannot be validated due to a lack of observed flow length data from this early stage. Such an overestimation could result from using too low a value of viscosity.

Modelled flow lengths using the flexible parameter approach (Eq. 3.3 and 3.4) show the best fit to observational data with a viscosity to crustal-control transition after 36 hours (Fig. 3.4B), but does not model the early phases well. The reduced advance rate in Figure 3.4B in the crust controlled regime, compared with the model in Figure 3.4A, is due to changes in the flow width and a reduction in the ground slope that is not accounted for in the fixed parameter approach. The modelled results using values of viscosity and crust yield strength from Castruccio et al. (2013) are shown in Figure 3.4C and discussed fully in Section 3.5.2.

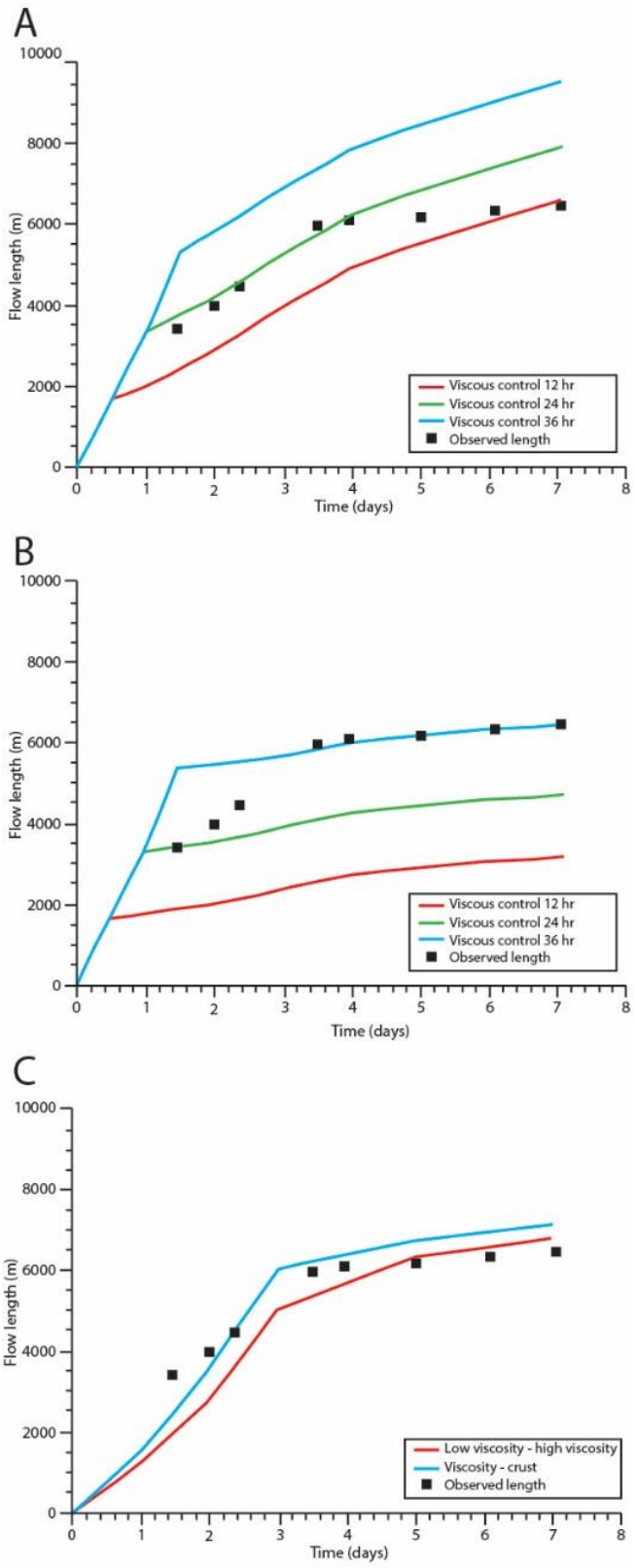
A
Flow length (m)
Time (days)
Viscous control 12 hr
Viscous control 24 hr
Viscous control 36 hr
Observed length
B
Flow length (m)
Time (days)
Viscous control 12 hr
Viscous control 24 hr
Viscous control 36 hr
Observed length
C
Flow length (m)
Time (days)
Low viscosity - high viscosity
Viscosity - crust
Observed length

← Figure 3.4: Modelled and actual flow length of the 2001 Mt Etna lava flow. (**A**) Results from the fixed parameter approach (Eq. 3.1 and 3.2) assuming the flow is controlled by its viscosity for 12, 24 or 36 hours. (**B**) Results from flexible parameter approach (Eq. 3.3 and 3.4) assuming that the flow is controlled by its viscosity for 12, 24 or 36 hours. (**C**) Results from flexible parameter approach (Eq. 3.3 and 3.4) using flow viscosities, crust yield strengths and transition times from Castruccio et al. (2013). Changes in flow control are inferred to occur after 3 days based on the modelling results.

#### 3.4.3.2 Model sensitivities

Most of the parameters used in the models are presented or calculated as a range. Here we briefly explore the effect of varying viscosity and crustal yield strength on the models. For viscosity, the plausible range of $3.5\times10^4$ to $5.6\times10^5$ Pa s (Applegarth, 2008) leads to final modelled flow lengths that vary by ~10 km (Fig. 3.5A, B). These substantial differences highlight the model sensitivity to viscosity and emphasise that strong constraints on the timing of rheological control transitions are vital, as well as for parameter values. However, within this range, some model results provide a good match to the observed flow lengthening e.g. those in Fig. 3.5D.

Table 3.2: Properties used in the quantitative approach

| Property | Cordón Caulle 2011 | Source | Mt Etna 2001 | Source |
|---|---|---|---|---|
| ρ - kg $m^{-3}$ | 2300 | Castro et al. (2013) | 2700 | Kilburn (2004) |
| β - ˚ | 7±2 | Determined from Aster DEM | 10 (main slope) – 3 (topographic break) | Determined from Aster DEM |
| η – Pa s | $3.6x10^{10}$ | Determined in text | $3.0x10^5$ | Applegarth (2008) |
| $\sigma_c$ - Pa | ~$1x10^8$ | Griffiths and Fink (1993), Bridges (1997), and Fink and Griffiths (1998) | ~$1x10^7$ | Griffiths and Fink (1993) and DeGroat-Nelson et al. (2001) |
| $\sigma_y$ - Pa | $2.5x10^5$ | Moore et al. (1978) | $1.3x10^4$ | Moore et al. (1978) |
| *k* – $m^2$ $s^{-1}$ | $5.5x10^{-7}$ | Romine et al. (2012) | $2.5x10^{-7}$ | Durham et al. (1987) |

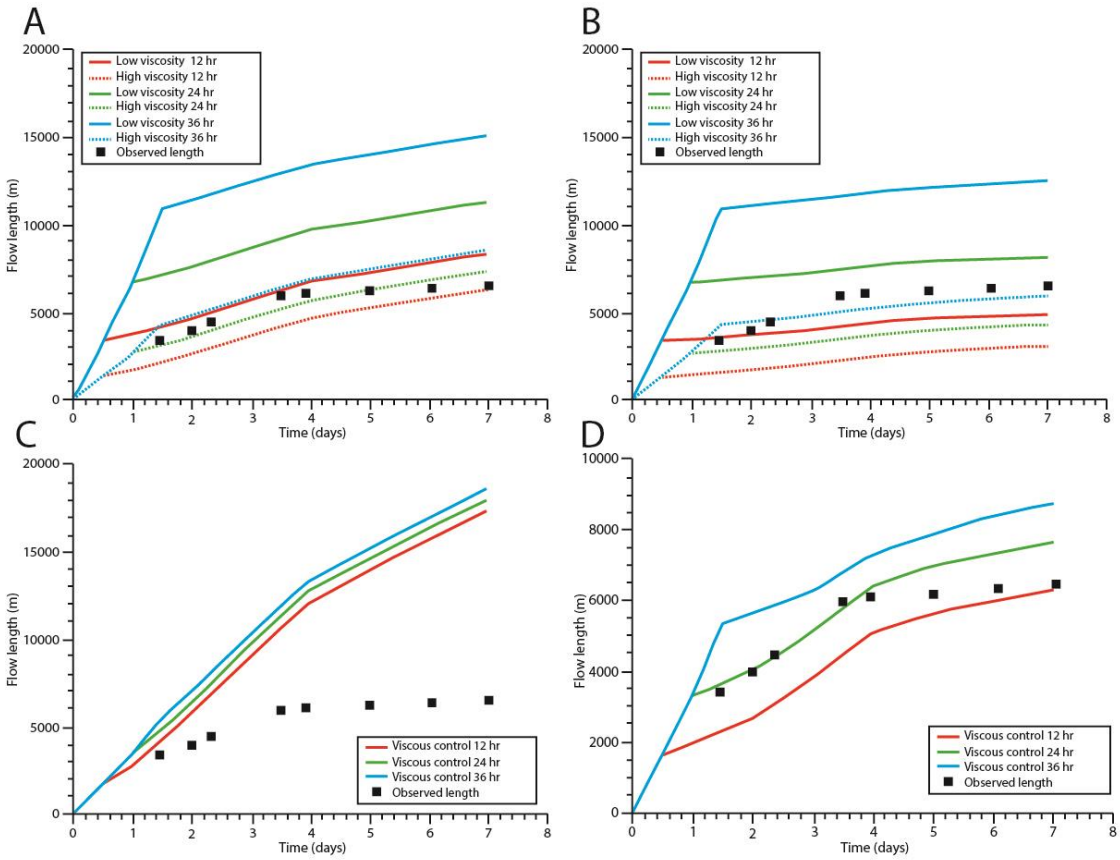


Figure 3.5: Modelled results for flow length of the 2001 Mt Etna lava flow showing variations in the material properties. (**A**) Range of possible flow lengths using viscosity range of $3.5x10^4$ to $5.6x10^5$ Pa s (Applegarth, 2008). Fixed parameter approach (Eq. 3.1 and 3.2). Dashed lines show the high-viscosity end member and solid lines the low-viscosity end member. (**B**) Similar to (**A**) but for the flexible parameter approach (Eq. 3.3 and 3.4). (**C**) Fixed parameter approach results (Eq. 3.1 and 3.2), showing changes from viscosity control to crustal yield strength control after 12, 24 and 36 hours, respectively, crustal yield strength of $10^6$ Pa, viscosity $3.0\times10^5$ Pa s. (**D**) Similar to (**B**) but for a flexible parameter approach (Eq. 3.3 and 3.4). The three model curves correspond to different transition times in the rheological control.

Models are similarly sensitive to the crustal yield strength value; for the fixed parameter approach (Eq. 3.1 and 3.2) decreasing yield strength from $10^7$ to $10^6$ Pa results in a final lava flow length overestimated by >10 km (Fig. 3.5C). For the flexible parameter approach (Eq. 3.3 and 3.4) the final flow length increased by ~2 km (Fig. 3.5D), with a transition in flow control after 36 hours. However, with transition in flow control after 12 or 24 hours, substantially earlier than inferred from Figure 3.4B and observations, the

model results give a closer fit to the observed flow front advance, reflecting a correlation between the parameters for crustal yield strength and the inferred timing of the onset of crustal control.

Table 3.3: Effusion rates and flow width variations

| Date | Effusion rate $m^3 s^{-1}$ - Bertin et al. (2015) | Date | South flow width m |
|---|---|---|---|
| Cordón Caulle 2011 | | | |
| 4/Jun/11 – 4/Jul/11 | 50 | 2/Jul/11 | 686 |
| 5/Jul/11 – 31/Dec/11 | 20 | 3/Jul/11 | 713 |
| 1/Jan/12 – 15/3/12 | 10 | 31/Jul/11 | 807 |
| | | 13/Aug/11 | 875 |
| | | 18/Aug/11 | 938 |
| | | 22/Oct/11 | 1148 |
| | | 4/Nov/11 | 1186 |
| | | 23/Dec/11 | 1325 |
| | | 26/Jan/12 | 1356 |
| | | 13/Jan/13 | 1579 |
| Etna 2001 | | | |
| Date | Effusion rate $m^3 s^{-1}$ - (Coltelli et al., 2007; Applegarth, 2008) | | Flow width m |
| 18/Jul/01 | 10 | | 90 - 300 |
| 19/Jul/01 | 14 | | |
| 20/Jul/01 | 24 | | |
| 21/Jul/01 | 30 | | |
| 22/Jul/01 | 30 | | |
| 23/Jul/01 | 18.5 | | |
| 24/Jul/01 | 18.5 | | |
| 25/Jul/01 | 18.5 | | |
| 26/Jul/01 | 18.5 | | |
| 27/Jul/01 | 10 | | |
| 28/Jul/01 | 10 | | |
| 29/Jul/01 | 9 | | |
| 30/Jul/01 | 9 | | |
| 31/Jul/01 | 6 | | |
| 01/Aug/01 | 6 | | |
| 02/Aug/01 | 6 | | |
| 03/Aug/01 | 5 | | |
| 04/Aug/01 | 5 | | |
| 05/Aug/01 | 3.3 | | |
| 06/Aug/01 | 3.3 | | |
| 07/Aug/01 | 1.5 | | |
| 08/Aug/01 | 0.5 | | |
| 09/Aug/01 | 0.5 | | |

## 3.5 Rhyolitic lava from the 2011-2012 Cordón Caulle eruption

Puyehue-Cordón Caulle is a basaltic-rhyolitic volcanic complex in the southern volcanic zone of the Chilean Andes (Fig. 3.6). One of the world's most frequently active rhyolitic/rhyodacitic volcanoes, it has most recently erupted in 1921-1922 (Katsui and Katz, 1967), 1960 (Lara et al., 2004; Lara et al., 2006) and 2011-2012. The VEI 5 2011-2012 eruption of crystal-poor (<25 volume%, Schipper et al., 2015) rhyolite (69-70 wt % $SiO_2$) began on 4 June 2011, initially producing a 15 km high Plinian column (Castro et al., 2013). At the onset of lava effusion, from prior to 19 June 2011, the lava flux exceeded 50 $m^3s^{-1}$ (Bertin et al., 2015). Lava effusion was first identified from radar satellite images on 19 June 2011 (Bignami et al., 2014), with lava flowing into a gently-sloping (5 – 9˚) topographic depression. Much of the eruption constituted hybrid explosive-effusive activity, with simultaneous lava emission and pyroclastic venting from a common vent (Castro et al., 2013; Schipper et al., 2013). The eruption ended

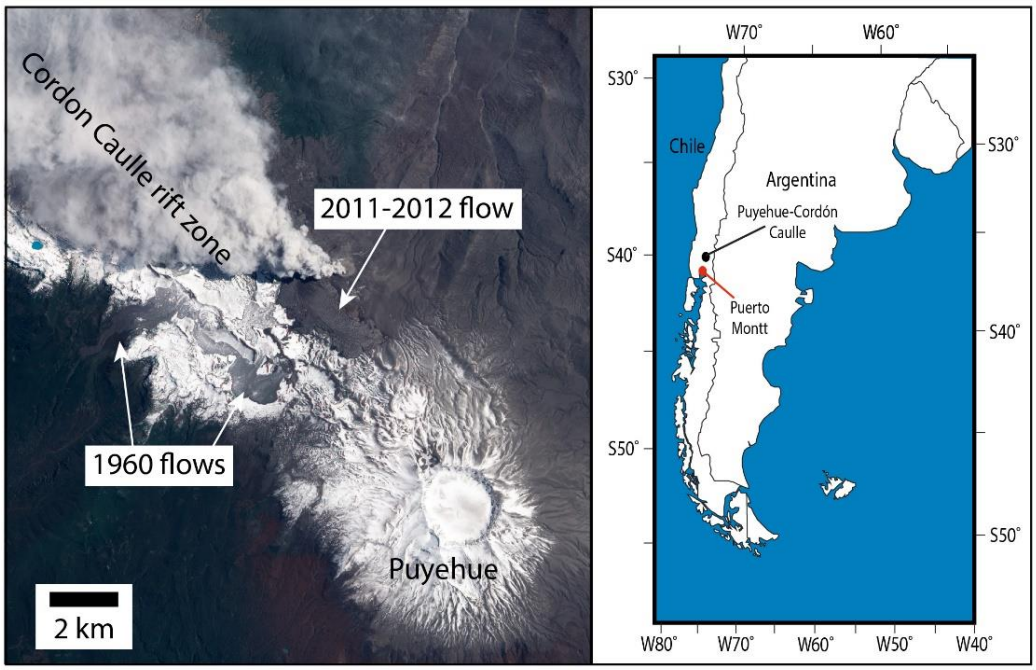


Figure 3.6: Satellite image (EO-1) showing the location of the Cordón Caulle lava flow and vent relative to the main Puyehue edifice. The Cordón Caulle rift zone is aligned NW-SE. Previous rhyolite flows from an eruption in 1960 are visible just south of the new lava flow. Inset shows the location Puyehue-Cordón Caulle within South America.

on 15 March 2012, but parts of the lava flow continued to advance into January 2013 (Tuffen et al., 2013). In total ~0.4 $km^3$ lava was emitted (Tuffen et al., 2013), alongside ~1 $km^3$ tephra (Pistolesi et al., 2015). We acknowledge that the 2011-2012 Cordón Caulle lava flow lies at the low-silica end of the rhyolitic spectrum, but its high-viscosity and crystal-poor nature does allow direct comparison with more typical higher-silica rhyolitic lava flows.

### *3.5.1 Lava flow advance and morphology*

Satellite images from GeoEye-1 and Earth Observing-1 ALI (EO-1 data available from the U.S. Geological Survey, https://eo1.usgs.gov/) show the evolution of the rhyolite flow during the eruption (Fig. 3.7). The images were used to derive the position of the flow front and supplemented by flow outlines derived from COSMO-SkyMed radar data from Bignami et al. (2014).

By 26 June 2011 (d = 22 where d is the number of days from the eruption onset) the flow had split into two channels, one heading north and one heading south, hereafter referred to as the northern and southern flows. These flows advanced synchronously but the northern flow stopped against a topographic high on around 22 October 2011 (d = 140) after advancing ~3 km. This portion of the lava flow was impeded by topography at both its margins and flow front, subsequent to stalling, breakouts formed from the western margin of the flow. The southern flow advanced throughout the ~285 day eruption, and continued to advance after eruption cessation, reaching ~4 km in total length. The lava advanced into a shallow topographic basin from a newly formed vent across a substrate of loose volcaniclastic material. The basin had numerous small gullies and ridges up to ~10 m in height/depth, which are minor compared to the 30 – 40 m thickness of the lava flow.

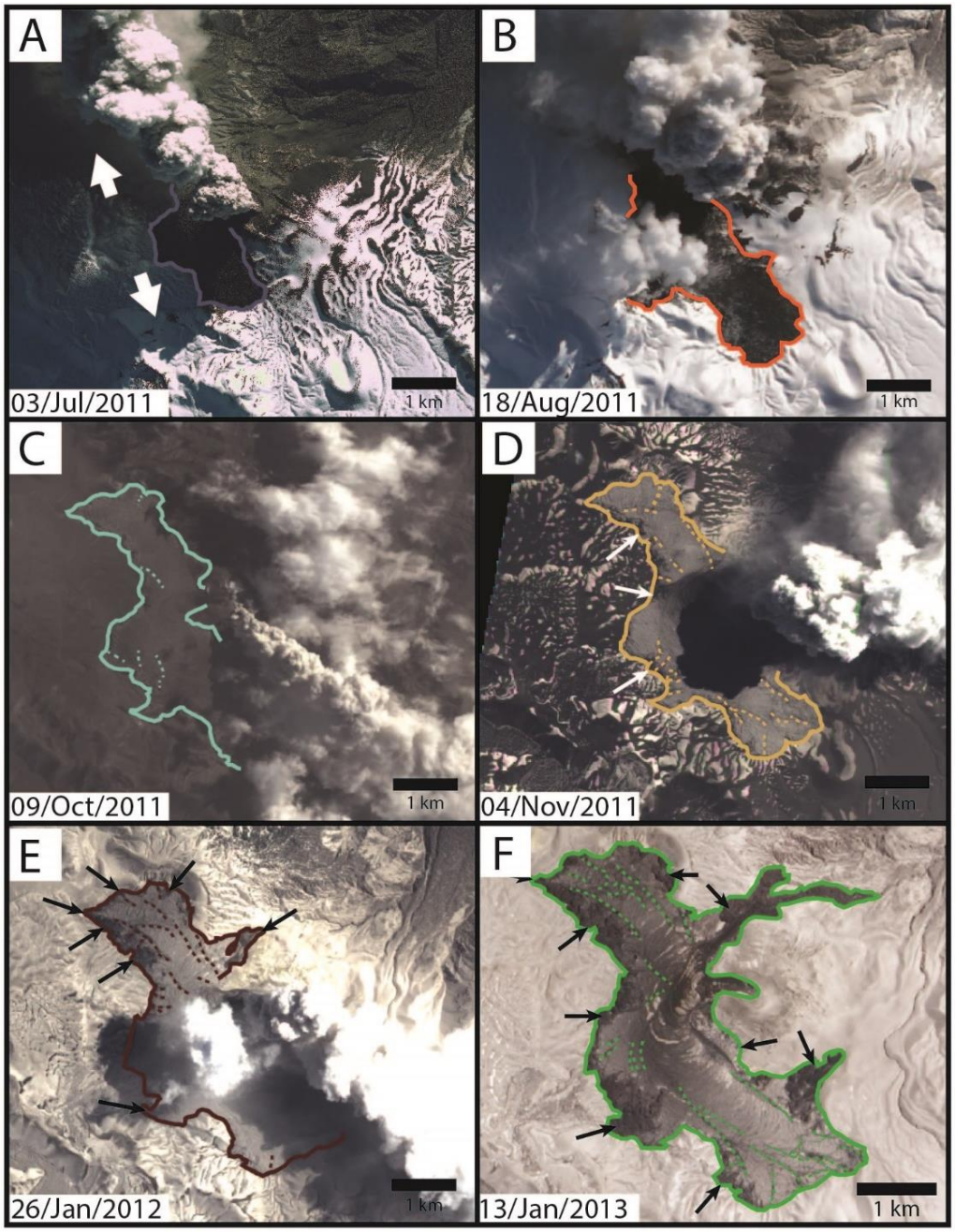


Figure 3.7: Satellite images taken during the 2011 eruption at Cordón Caulle, available in Appendix 8A.1-8A.15. (**A**) 3 July 2011 GeoEye-1 image, white arrows show the dominant flow directions, image provided by GeoEye Foundation (scene ID: 1050410001685D00). (**B-F**) Images from the Advanced Land Imager (ALI) on NASA's Earth Observing-1 (EO-1) satellite (NASA, 2011b, c, d, 2012a, 2013). Solid lines mark the flow front, dashed lines highlight surface fractures and the arrows show some of the areas of breakout formation. The two white arrows in part **A** show the dominant flow directions throughout the eruption. The flow initially spread over the topography. Over time, fractures (dashed lines) formed in the flow surface and shortly after this the first breakouts formed from the stalled flow front and margins.

The first two months of the eruption produced lava with a blocky appearance and no obvious large-scale structures (Fig. 3.7A), similar in appearance to other rhyolitic and high-silica flows, such as Big Glass Mountain in the US (Fink, 1980b; Fink et al., 1992; Castro et al., 2002a). By 18 August 2011 the flow had developed surface folds hundreds of metres in length, with a wavelength of ~30 – 40 m (Fig. 3.7B, d = 75).

By 9 October 2011 (d = 127, Fig. 3.7C) large-scale fractures (hundreds of metres or longer) had formed in the surface crust of the flow (Fig. 3.7C-3.7F). Two fracture types developed – tensional fractures (orientated perpendicular or parallel to the flow front) generated by coupling of the crust to the spreading flow core, and shear zones (orientated parallel to the advance direction) that separated the stalled flow margins from the mobile channel centre.

The first breakouts formed from stalled flow fronts and margins by 4 November 2011 (d= 153, Fig. 3.7D). Thereafter, almost all advance in the northern flow, from the front or margins, was via breakout formation (Fig. 3.7D). Such prevalent breakout formation from this portion of the flow was likely aided by the early stalling of the northern flow against large (up to 100 m high) topographic barriers. In contrast, the southern flow continued to advance during and beyond the remainder of the eruption (Tuffen et al., 2013). Breakouts in the southern flow mostly formed from the flow margins, whilst some small breakouts formed at the flow front (Fig. 3.7F, 3.8).

A secondary flow, 2 km in length, formed from one breakout on the northern flow after stalling of the main flow front. It began to form around 23 Dec 2011 (d = 202) on the eastern margin of the northern flow (Figs. 3.7E, 3.7F, 3.8). The secondary flow was narrow (100 – 400 m across), contained within a steep gully (~15˚ slope), and advanced onto the eastern flank of the volcano before halting. The southern flow began to advance into topographic barriers around 23 Dec 2011 (d = 202) and this may have impeded lava flow advance. A 50 – 150 m high ridge spanning the entire western side

of the northern and southern flows severely restricted westward spreading of the flow front. However, breakouts were able to form from the eastern margin, particularly where the lava overtopped pre-existing ridges.

Other flow surface features visible in the satellite imagery include light brown/yellow patches several tens of metres across, and mostly confined to the main flow channel,

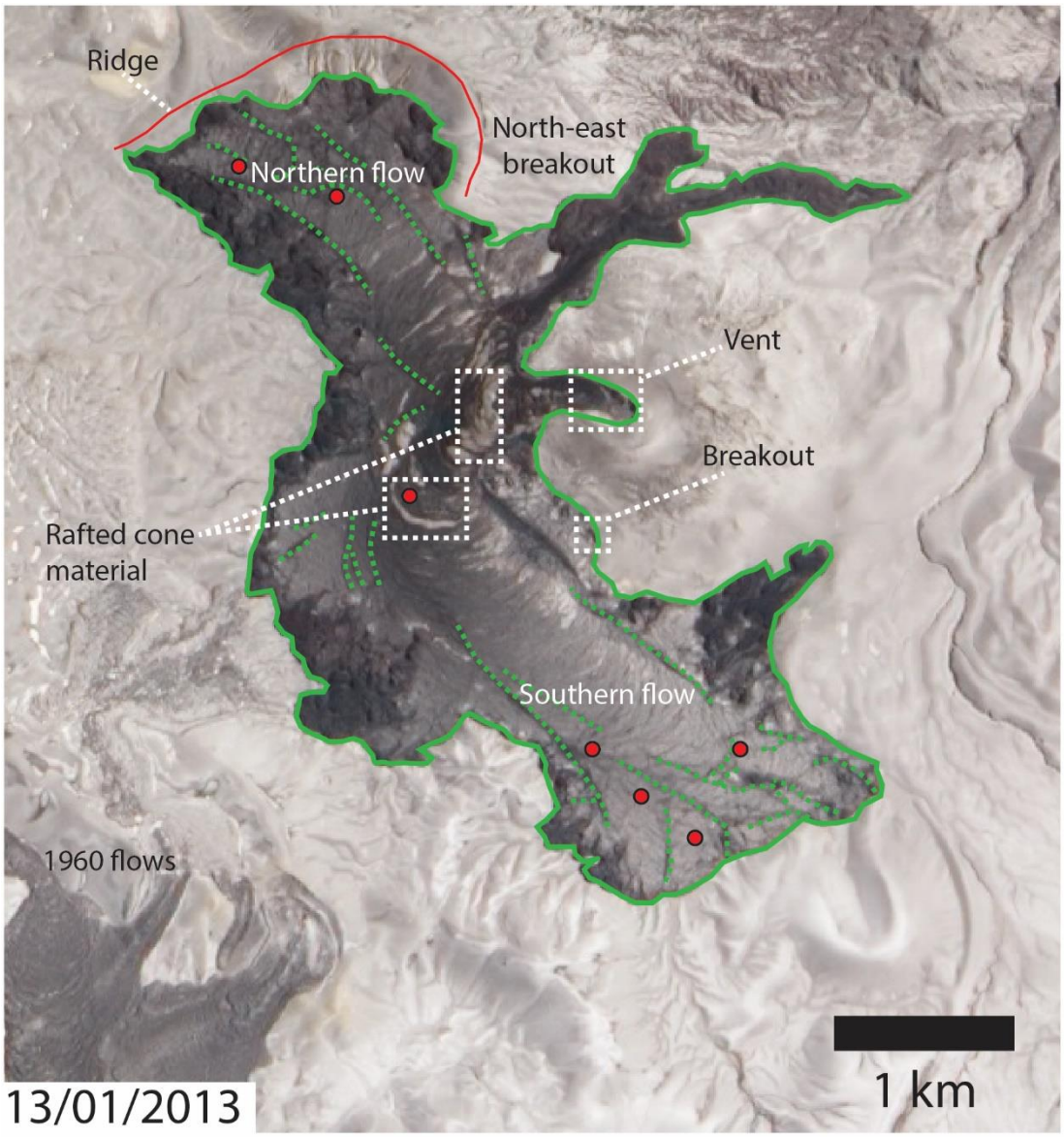


Figure 3.8: Cordón Caulle flow after the eruption ended and almost all flow movement had stopped. Features such as the rafted cone material are highlighted as well as the ridge to the north that acted to halt the northern flow. The location of the small breakout in Figure 4.3C is also shown. Red dots show approximate locations where flow surface velocities were calculated. Green dashed lines show locations of the large surface fractures.

which represent rafts of flow-top-pumice. Numerous rough, dark brown patches up to 500 m in length, visible in Figures 3.7F and 3.8, are elongate and ogive-parallel far from the vent, but occur as large, more equant patches closer to the vent. These consist of poorly-consolidated, coarse-grained pyroclastic deposits thought to derive from gravitational collapse of the tephra cone at the vent. Lava effusion ended around 15 March 2012 (d = 285) but local advance of breakouts in the southern flow continued for several months (Tuffen et al., 2013).

### *3.5.2 Field evidence for a late crustal control*

Field campaigns at Cordón Caulle were conducted in January 2013, 2014 and 2015. Fieldwork focussed on the morphological features of the flow as well as ground-truthing features observed in satellite images. The lava flow is blocky and ~30 – 40 m thick, with a surface consisting of loose fragments tens of centimetres to metres across that comprise fragments of surface crust and pumiceous material. The cover of loose debris may have contributed to the thermal insulation of the flow, but is unlikely to have had a substantial mechanical influence on the bulk flow advance. Direct evidence for a coherent surface crust beneath the surface debris is presented by extensional fractures metres to hundreds of metres in length (Fig. 3.3D). The depth of downward penetration of these fractures (several metres to >10 m) indicates a plausible crustal thickness. Determining crustal thickness ($\delta$) from $\delta \sim (kt)^{1/2}$ (Griffiths and Fink, 1993) gives crustal thicknesses of order metres by the time the eruption ceased (using values of $k$ from Table 3.1). Further evidence for vertical rheological variation is given by the presence of well-developed ogives (or surface ridges) that are 30 – 40 m in wavelength and several metres in amplitude.

Breakouts are widely distributed around the flow front and margins, where they display a range of morphologies. Many breakouts developed extensive surface crusts tens of

centimetres thick (Fig. 3.3C), which then fragmented as the breakout grew and inflated (Tuffen et al., 2013). Their presence indicates that although the main flow advance had halted, mobile lava remained available in regions close to the flow edges and was likely still being effused from the vent. Breakouts that initiated after vent effusion ceased were likely fed by lava drainage through the flow field, as observed at some basaltic lava flows (Dietterich et al., 2012), however there are currently no direct measurements of drainage at Cordón Caulle.

### *3.5.3 Inferred changes in rheological control*

In its initial stages, flow advance may have been controlled either by an apparent Newtonian viscosity or a non-Newtonian (yield strength) rheology. However, in its latter phases the field and satellite observations of folds and fractures suggest that a surface crust exerted a strong influence. Surface folds (ogives) form in response to a slowing flow front and subsequent buckling of a rheologically stiff surface crust behind it (Fink, 1980a). The extensional fractures that formed after ogive formation appear similar to those generated in analogue models of lava flows with a strong brittle crust (Lescinsky and Merle, 2005; Applegarth, 2008), and their orientation suggests that some fractures relate to the formation and spreading of flow front lobes. We infer that when surface fractures were produced the flow crust was significantly influencing flow advance. Furthermore, the presence of breakouts points towards sufficient crustal strength to slow or halt overall advance, despite the availability of mobile material in the flow core (Tuffen et al., 2013; Farquharson et al., 2015).

### *3.5.4 Application of flow models to the 2011-2012 Cordón Caulle lava flow*

#### 3.5.4.1 Calculation of bulk flow viscosity

In order to apply Newtonian flow lengthening models to the Cordón Caulle lava, the bulk flow viscosity must first be estimated using Table 3.6 (Jeffreys, 1925). We use a

lava density of 2300 kg $m^{-3}$ (Castro et al., 2013), a flow depth of ~30 m at the flow front (Farquharson et al., 2015), a slope of 7˚ (determined from a pre-eruption Aster DEM along the length of the southern flow, Appendix 8A.19), and $n$ = 2 for flow in a wide channel (Hulme, 1974; Stevenson et al., 2001; Harris et al., 2004; Farquharson et al., 2015).

In order to determine the lava flow surface velocity, surface features in the main channel of the flow (ogives, fractures in the flow crust, and pale pumice rafts) were tracked between two georeferenced satellite images taken in 9 October 2011 and 26 January 2012 (locations of the measurements are shown in Fig. 3.8). Surface velocities of 2.2-6.2×$10^{-5}$ m $s^{-1}$ were derived (mean 3.8×$10^{-5}$ m $s^{-1}$), giving a viscosity range of 2.0-5.6×$10^{10}$ Pa s (mean 3.6×$10^{10}$ Pa s). Here we assume that the surface velocity is comparable to the core velocity, which may not be the case if the crust is experiencing drag against the levées.

#### 3.5.4.2 Models of flow lengthening

Due to the northern flow being topographically constrained at its front, lava flow advance models are only relevant to the initial advance of the southern flow. We assume that the lava flow was initially controlled by either a Newtonian or non-Newtonian bulk rheology for the first 75 to 127 days (first identification of ogives and surface fractures respectively). Henceforth, the presence of ogives and surface fractures indicate that surface crust had attained sufficient thickness and strength to exert a controlling influence on flow behaviour. Model results should be disregarded for periods after the southern flow front began to interact with a topographic barrier (202 days). However, by this time the major changes in rheological control had already occurred, with the lava firmly in the crustal-control regime and breakouts forming at many points around the lava flow. The effusion rates (Table 3.3) are cited for the entire flow field (Bertin et al., 2015). As a best estimate, we assume that the north and south

flow branches were fed approximately equally – i.e. each at half the rate given in Table 3.3.

Models based on the fixed parameter approach (Eq. 3.1 and 3.2, utilising values in Table 3.2) underestimate final lava flow length by ~1500 – 1000 m for transitions from viscosity to crustal control after 75 and 127 days respectively (Fig. 3.9A). The biggest disparity is in the early stages of the eruption, when the observed lava flow advance rate far exceeded model predictions, suggesting that early-erupted lava was substantially less viscous than the later-erupted lava for which we have viscosity estimates (Farquharson et al. 2015). Such increases in the lava flow viscosity with time likely relate to cooling, degassing and crystallisation of the lava flow.

Models that employ the flexible parameter approach (Eq. 3.3 and 3.4, Eq. 3.4 and 3.5) and assume a core yield strength control underestimate the final flow length by ~2000 m (Fig. 3.9B). When an initial viscosity control and 75 day crustal control transition are used the final lava flow length is underestimated by ~900 m. However, when the crustal control transition occurs after 127 days, the modelled final lava flow length closely fits with observed values, showing the importance of constraining the timing of model transitions. Not surprisingly, the flexible parameter approach provides a better fit for the early stages of the lava evolution than the fixed parameter approach, because it accounts for variations in lava flow properties, such as the flow width.

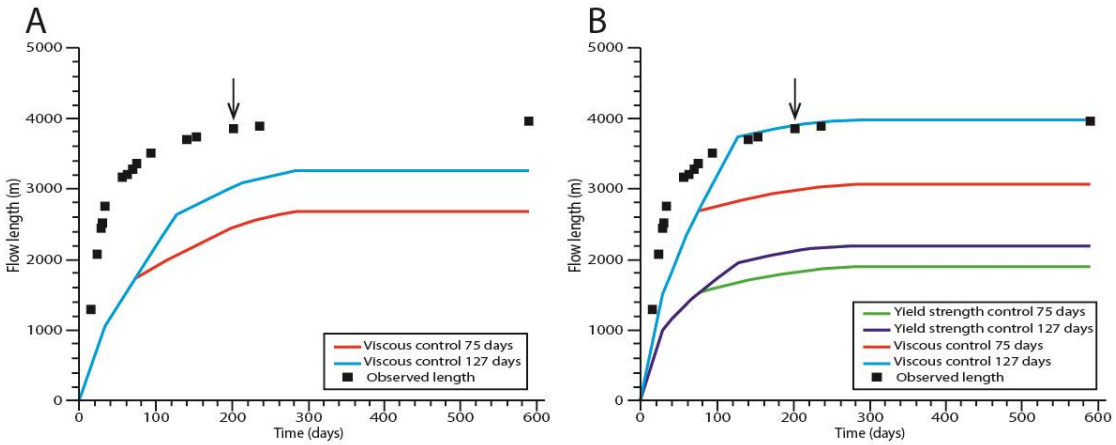


Figure 3.9: Modelled and actual flow length changes of the 2011 Cordón Caulle rhyolite lava flow. The black arrow shows the time at which the flow starts to interact with a topographic barrier. (**A**) Results from fixed parameter approach (Eq. 3.1 and 3.2) assuming the flow is initially controlled by its viscosity and then by the strength of a brittle crust. (**B**) Results from flexible parameter approach (Eq. 3.3 and 3.4, and Eq. 3.5 and 3.4) assuming the flow is initially controlled by either its viscosity or internal yield strength.

#### 3.5.4.3 Inferring Cordón Caulle flow properties

The Cordón Caulle lava flow gained most of its length in the first two to three months of the eruption, during inferred viscosity-controlled advance. However, reliable viscosity estimates could only be made from the latter stages of the eruption when recognisable surface features could be tracked and the flow was less obscured by the eruption plume. Thus, viscosity estimates are upper bounds because they are likely to be affected by the presence of a crust, and the later lava was likely cooler, more degassed and more crystalline than during the earlier stages (Schipper et al., 2015). Flow length models offer an alternative approach to constrain plausible values of flow viscosity, crust yield strength and internal yield strength.

The optimised fixed parameter model provides a best fit to observed flow lengthening for a viscosity of $3.3\times10^{9}$ Pa s, a crustal yield strength of $2.5\times10^{8}$ Pa and a transition from viscosity to crustal control after 60 days (Fig. 3.10A). This lower viscosity, an order

of magnitude less than estimates for later lava (Farquharson et al. 2015), could be representative of initially effused lava that was hotter, less crystalline and more volatile-rich. A viscosity value can also be estimated directly using the Einstein-Roscoe equation:

$$\eta = \eta_0(1 - R\Phi)^{-Q}\,, \qquad [Eq.\,3.7]$$

where $\eta_0$ is the melt viscosity which is determined here from Giordano et al. (2008), $R$ and $Q$ are constants equal to 1.67 and 2.5 respectively, and $\Phi$ is the crystal packing fraction. Using an eruptive temperature of 900 ˚C, a melt composition from Schipper et al. (2015) with a volatile content of 0.1%, and an initial crystal content of up to ~30 volume% at the vent (Schipper et al., 2015) gives a viscosity of ~$1.5\times10^9$ Pa s. This is in close agreement to the fixed parameter model suggested here (Eq. 3.1 and 3.2, Fig. 3.10A). We acknowledge that the Einstein-Roscoe equation is based on the assumption that the crystal population is isotropic. However, in the Cordón Caulle flow most crystals are rod-like microlites (Schipper et al., 2015), and such high aspect ratio crystals increase the magma viscosity more strongly than isotropic crystals (Mueller et al., 2011; Mader et al., 2013). Accordingly, this estimate could be taken as a minimum value, and viscosity likely increased with time due to degassing and crystallisation of the lava flow. Alternatively, the alignment of an initial randomly orientated microlite population could lead to shear thinning behaviour during lava flow emplacement and a reduction in apparent viscosity. Despite these limitations, the value independently derived from the Einstein-Roscoe equation does support the viscosity value derived through the optimised lava flow models, Eq. 3.1 and 3.2.

Optimising a flexible parameter model with Newtonian viscosity and subsequent crustal control (Eq. 3.3 and 3.4) gives the observed best fit to the actual flow lengthening for a rather higher viscosity of $1\times10^{10}$ Pa s, a lower crustal yield strength of $4\times10^{7}$ Pa and a similar flow control transition time of 50 days (Fig. 3.10B). A flexible parameter model that assumes initial core yield strength control provides best fit for a core yield strength of $9.8\times10^{4}$ Pa, a crustal yield strength of $4\times10^{7}$ Pa and a transition in flow control at 50 days. As these models are inherently non-unique and other combinations of flow properties and transition time in flow control can yield equally good fits to observations, it is valuable to compare the determined flow parameters to previously published results. The inferred values of crustal yield strength correspond with those proposed in other studies of silicic lava flows and domes, $10^{6}$ – $10^{7}$ Pa (Griffiths and Fink, 1993;

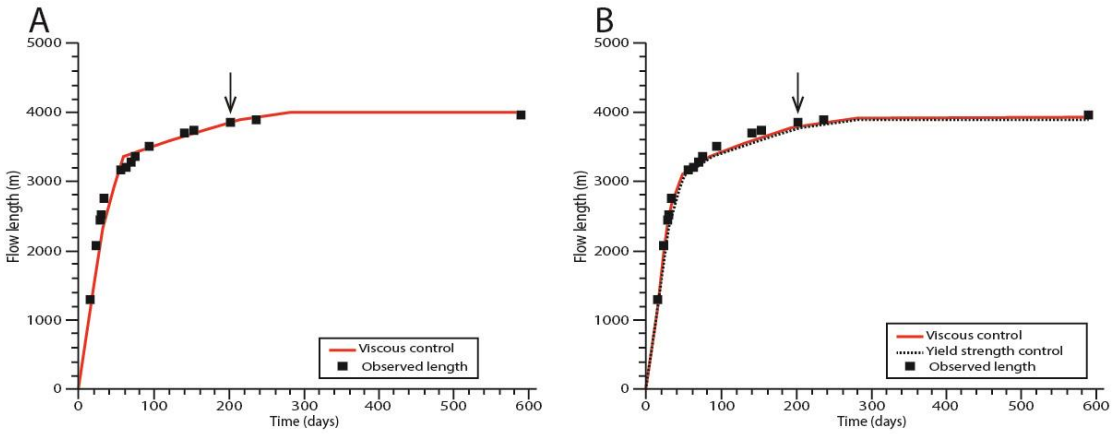


Figure 3.10: Model results for the Cordón Caulle lava flow. The black arrow shows the time at which the flow starts to interact with a topographic barrier. (**A**) Fixed parameter approach (Eq. 3.1 and 3.2) where flow properties have been inferred from the best fit of the applied models. (**B**) Flexible parameter approach (Eq. 3.3 and 3.4, and 3.5 and 3.4) where flow properties have been inferred from the best fit of the applied model.

DeGroat-Nelson et al., 2001) and the lower core yield strength determined here is in line with other estimations of high-silica content lava yield strength (Blake, 1990; Fink and Griffiths, 1998). The inferred viscosity from the idealised flexible parameter approach (Eq. 3.3 and 3.4, Fig. 3.10B) is in line with the lower viscosities calculated

using Jeffreys (1925) by Farquharson et al. (2015), based on velocities determined from structure-from-motion photogrammetry of breakouts ($1.21\times10^{10}$ to $4.01\times10^{10}$ Pa s) from the flow margin. This viscosity value is slightly lower than the inferred bulk lava viscosity determined from satellite observations.

#### 3.5.4.4 Model sensitivities

The uncertainties associated with model input result in uncertainties in model outputs; for example varying slope angle by 2˚ in all models leads to final flow length changes of ~2 – 10%, corresponding to flow length variations up to a few hundred metres. However, variations due to uncertainties in crustal yield strength and flow viscosity are much greater. Applying the range of viscosity values derived from initial range in flow channel velocities leads to a range in the final modelled flow lengths of ~1.5 km for the fixed parameter approach (Fig. 3.11A) and 2 km for the flexible parameter approach (Fig. 3.11B).

Previously published values for the crustal yield strength of silicic lavas range from $10^6$ to $10^8$ Pa (Griffiths and Fink, 1993; Bridges, 1997; Fink and Griffiths, 1998; DeGroat-Nelson et al., 2001; Kerr and Lyman, 2007; Castruccio et al., 2013). Reducing the crustal yield strength by an order of magnitude to $10^7$ Pa in the fixed parameter approach (Eq. 3.1 and 3.2) produces a significant increase in modelled lava flow advance rate in the crustal control regime (Fig. 3.11C) compared to the original model (Fig. 3.9A), and increases the final lava flow length by >1.5 km. An earlier transition in flow control (at day 75), results in a longer lava flow than when the transition occurs after 127 days. This is because at this time in the modelled scenario, the crust provided a lesser retarding force than the flow viscosity, leading to accelerated lava advance rates upon flow control transition. In reality though, the lava flow would have retained the viscous retardation and remained viscosity controlled until the crust became

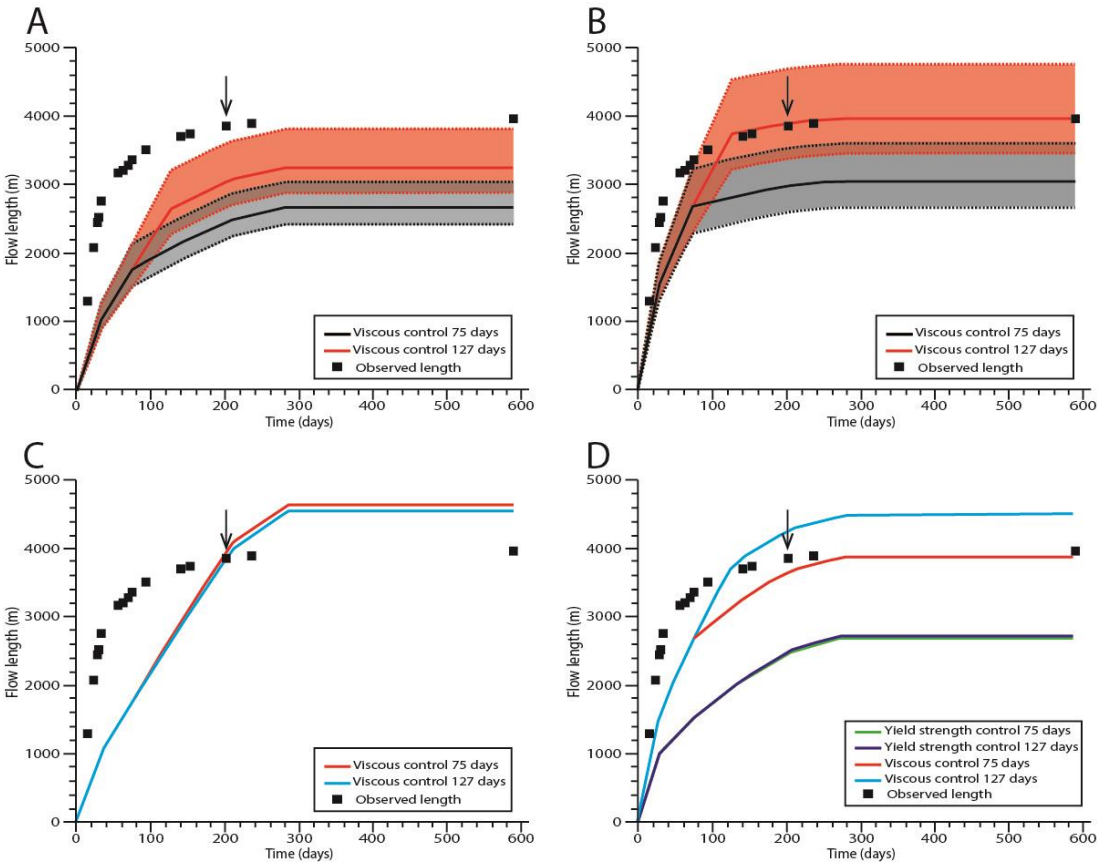


Figure 3.11: Model results for the Cordón Caulle lava flow. The black arrow shows the time at which the flow starts to interact with a topographic barrier. (**A**) Range of model results when viscosity is varied using the fixed parameter approach (Eq. 3.1 and 3.2). The red area represents a transition in rheological control after 127 days and the grey area represents a transition after 75 days. Dashed lines show the high and low-viscosity end members and the solid lines show the mean viscosity. (**B**) Similar to (**A**) but for a flexible parameter approach (Eq. 3.3 and 3.4). (**C**) Fixed parameter approach (Eq. 3.1 and 3.2) where the crust yield strength is reduced by an order of magnitude to $10^7$ Pa. (**D**) Similar to (**C**) but for a flexible parameter approach (Eq. 3.3 and 3.4 or Eq. 3.5 and 3.4). Flow is initially controlled by either its viscosity or core yield strength. Two core yield strength curves give similar results for a transition in control after 75 days and 127 days.

sufficiently strong to dominate over the viscous forces. Thus, this apparent increase in lava flow advance is an artefact of the modelling approach that considers rheological controls in isolation rather than combination. The effect on the flexible parameter models of lowering crust yield strength (Eq. 3.3 and 3.4) is not as pronounced (Fig.

3.11D), but leads to an increase in the final flow length compared to the original model (Fig. 3.9B), and provides a closer fit to the actual flow lengthening.

## 3.6 Discussion

Field and remote sensing observations, as well as straightforward flow advance models, suggest that both the 2001 Etna basaltic flow and the 2011-2012 Cordón Caulle rhyolitic lava flow were controlled in their latter stages by a cooled crust after an initial viscous control. The cooled crust acted to retard the lava flows, ultimately halting them before breakouts formed at the flow front and along flow margins (Behncke and Neri, 2003; Coltelli et al., 2007; Applegarth et al., 2010c; Tuffen et al., 2013).

### *3.6.1 Model limitations*

The models are limited by the uncertainties in parameter values and inherent in-model assumptions (aleatory and epistemic uncertainties). The models themselves are straightforward and their ability to simulate flow lengths across a broad compositional range demonstrates their generality (Kerr and Lyman, 2007; Castruccio et al., 2013). The flexible parameter approach (Eq. 3.3-3.5) will be most appropriate for lava flows that undergo substantial widening, such as the Cordón Caulle rhyolite flow, and likely explains the disparity among the model results. None of the models are valid for sections of uphill slope (i.e. negative $\beta$ values) and so breakdown when topographic barriers are encountered. For this reason, averaged slope angles and DEMs are typically used.

Values of crustal strength are poorly reported in the literature and often rely on scaling analysis from analogue experiments (Griffiths and Fink, 1993; Fink and Griffiths, 1998). The evolution of crustal strength through time is also unknown and very difficult to determine. The effusion rate is relatively well constrained for the 2001 Mt Etna eruption

(Behncke and Neri, 2003; Coltelli et al., 2007). However, the effusion rate for the 2011-2012 Cordón Caulle eruption is less well constrained, with only preliminary values currently available. Due to lack of data we assume that the north and south flows received an equal share of the vent effusion rate. Because both flows were continuously fed and active throughout the eruption (either through breakout formation or main flow advance) this assumption appears reasonable.

Error in imagery-derived lava flow velocity estimates mostly relate to potential georeferencing problems (Appendix 8A), although physical effects, such as compression of the flow surface during ogive formation giving an apparent shortening of the surface of the lava flow, will also contribute. Such errors are likely small compared with other uncertainties and the velocity values calculated encompass those estimated by Farquharson et al. (2015) for breakouts in the latter phases of flow emplacement ($3.57\times10^{-5}$ m $s^{-1}$). The topographic slope may also have changed during the eruption, as Castro et al. (2016) have shown that >200 m of uplift occurred around the Cordón Caulle vent in the first month of the eruption. This uplift, which is attributed to the emplacement of a shallow laccolith intrusion, may have increased the average gradient along the length of the southern flow by up to ~3°. However, such a magnitude of slope change has a minor effect on the model outputs when compared with other influences, as discussed in Section 3.4.4. However, this uplift may have accelerated the early phases of lava flow advance, helping to explain the early discrepancy between the modelled and observed lengths.

The frequency of available observational data remains a substantial factor within the uncertainties of model outputs. For Cordón Caulle, the precision in the timing of the transition between viscous and crustal control (identified through observations of crustal fracturing or the formation of features such as ogives and breakouts), is limited by the infrequent satellite image acquisitions (one to two partial images per month).

Despite these uncertainties, the models provide reasonable estimates of the evolution of compositionally diverse lava flows. Nevertheless, it is clear that good knowledge of the evolving flow architecture can help constrain models and identify when underpinning assumptions breakdown. Morphological considerations can thus aid model selection and improve the accuracy of estimated parameter values, as well as helping identify where the greatest remaining uncertainties lie.

### *3.6.2 Comparison to previously modelled results*

Due to the additional constraints that we impose, our model results for the 2001 Mt Etna flow have a poorer fit to the observed flow lengthening (Fig. 3.4) than those shown previously by Castruccio et al. (2013), in which more parameters were allowed to vary within the fitting process. Castruccio et al. (2013) suggests that the 2001 Etna flow advance was either controlled by an initial low-viscosity ($3.8\times10^6$ Pa s), which increased after 3 days ($2.4\times10^8$ Pa s), or by an initial low-viscosity ($4.5\times10^6$ Pa s) and then by the crustal yield strength ($1\times10^6$ Pa, Fig. 3.4C). We have initially constrained crustal yield strength to a greater value in our models, reflective of the large array of crustal yield strength values in the literature. However, when a value closer to that of Castruccio et al. (2013) is used, the modelled fit in the flexible parameter approach is much improved (Fig. 3.5D). This suggests that the crust of the 2001 Etna flow may have been weaker than indicated by Griffiths and Fink (1993), showing the difficulty in scaling crust yield strength. The models presented here, as well as flow observations, suggest that 1) the transition in the lava flow control at Mt Etna occurred much sooner, within 36 hours, than the three days suggested by Castruccio et al. (2013), and 2) the initial lava flow viscosity was considerably lower.

For high-viscosity (dacite) lava flows, Castruccio et al. (2013) suggested a core yield strength control. However, our findings suggest that the high-viscosity and relatively

crystal-poor Cordón Caulle lava flow was initially viscosity-controlled. This arguably reflects a fundamental difference between the emplacement of crystal-poor and crystal-rich high-silica flows. Rhyolitic lavas are typically extruded as degassed, crystal-poor melt, because their high melt viscosity makes diffusion sluggish (Eichelberger et al., 1986; Eichelberger, 1995). In contrast, water rich andesites and dacites typically have a significantly higher crystal content (Sparks et al., 2000), making a yield strength control far more likely. Indeed, the dacitic lava at Santiaguito is significantly more crystal-rich, 47 volume% by volume (Rose, 1987; Holland et al., 2011), than the initially effused Cordón Caulle rhyolite.

### *3.6.3 Development of a yield strength*

The advance rate of some high-silica lava flows is thought to be controlled by their core yield strength (Castruccio et al., 2013), which develops when the lava crystal content exceeds ~30 volume% (Saar et al., 2001; Castruccio et al., 2010). However, it is currently unclear whether the Cordón Caulle rhyolite could have developed substantial core yield strength during emplacement, as measured crystal contents in samples taken from the vent region are only ~10 – 30 volume%, compared to 50 – 60 volume% in breakouts (Schipper et al., 2015). Thus, initial crystallinities are generally beneath the threshold proposed by (Saar et al., 2001). Furthermore, such vent samples only represent the last-erupted material and may not typify earlier-effused material, which could have had even lower crystal contents.

In contrast, samples from breakouts exhibit significantly higher crystal content of 50 – 60 volume% (Schipper et al., 2015), clearly sufficient to generate a yield strength. Nevertheless, given the slow crystallisation kinetics of rhyolites (Swanson et al., 1989), it is unclear whether this crystal population could have formed before lava flow advance became dominated by a crust. However, crystallisation may have been enhanced by

degassing of the lava (Applegarth et al., 2013a; Applegarth et al., 2013b) and, as a result, the lava may have attained a yield strength. Swanson et al. (1989) suggest the bulk of crystallisation in rhyolites occurs only after lava has halted and had time to cool. Furthermore, much of the crystal population within a rhyolite lava flow may be products of devitrification, such as spherulites or globulites (Schipper et al., 2015), which largely form after lava has halted due to the lava diffusion timescales relative to emplacement timescales. Further work on detailed textural studies is needed in order to reconstruct the crystallisation history relative to the emplacement duration, and unravel to what effect, if any, crystal populations had on the evolution of an effective crust and broader flow processes (Sections 4 and 5, Appendix 8C).

### *3.6.4 Breakouts and crustal control*

Observations of Cordón Caulle demonstrate that not only was the lava flow controlled in its latter phases by a cooled crust, but the crust was able to halt the flow leading to breakout formation at the stalled front and flow margins. Such a strong crustal control had been inferred at other high-silica flows (Anderson and Fink, 1992; Castro et al., 2002a), but the absence of breakouts at these flows is intriguing. As the first Cordón Caulle breakouts formed only after ~150 days, the absence of breakouts at other rhyolite lava flows may reflect briefer emplacement timescales of lava flows that were volume-limited. Alternatively, a lack of breakouts may reflect the inability of other lava flows to develop a substantial surface crust, potentially indicative of higher flow advance rates than at Cordón Caulle caused either by higher effusion rates (Loewen et al., 2017) or steeper topography. In both cases, the greater lava flow velocity is likely to apply greater stress to the surface crust through developing greater velocity gradients, causing it to fail more regularly and potentially preventing development into a pervasive surface capable of halting the flow (Anderson et al., 1995; Kilburn, 2004). Similarly, pulses of higher effusion rate could result in periods of increased flow rate,

leading to increased disruption of the flow surface crust. Higher effusion rates would allow the flow to advance farther before cooling became a substantial controlling factor (Fink and Griffiths, 1998). Alternatively, surface crusts at other high-silica flows could be sufficiently strong to prevent breakout formation in the first place, with the internal pressure failing to exceed the crustal yield strength. Topographic barriers may also play an important role in promoting breakouts at Cordón Caulle, aiding the stalling of the lava flow front (Appendix 8A.19-8A.21).

A combination of these processes may have contributed to the lack of further breakouts from the late northeast breakout of the Cordón Caulle flow (Fig. 3.8). The northeast breakout displays pronounced levées and a possible area of drained channel, suggesting that its emplacement was volume-limited. This breakout advanced down a much steeper slope (~15˚) than the main flow field, potentially leading to increased deformation of any surface crust by the greater stresses involved. In contrast, the bulk of the flow field advanced over very gentle topography and, in some cases, abutted topographic barriers, which could have aided crust formation through putting the top surface under compression, reducing the degree to which the surface crust was ruptured by extensional fracturing.

Given the presence of very large fractures in the Cordón Caulle flow surface, the crust clearly behaved in a brittle manner for part of its lifetime. The models used here assume that the crust acts as a deforming viscoelastic layer that controls the lava flow advance. This layer is likely bounded by a cooled, strong, brittle layer that would fragment to form the blocky surface. The energy used in the fragmentation of a brittle surface layer can be accounted for (Kilburn, 2004) and future models could attempt to incorporate this additional factor in lava flow lengthening models, but the contribution of this factor is likely minor. It is also worth noting that, in many large basaltic lava flows, the crust not only halts flow advance but enables prolonged supply to the flow front through effective

insulation of the material in the lava flow core and tube formation (Anderson et al., 1999; Vye-Brown et al., 2013). This is also true of the Cordón Caulle rhyolite flow, where material continued to be supplied beneath the stalled crust to breakouts at the flow front and margins, enabling continued lava flow transport long after the eruption ended (Tuffen et al., 2013; Farquharson et al., 2015).

### *3.6.5 Crustal thicknesses*

Lava flow crustal thicknesses ($\delta$) can be estimated at the time of transition from viscosity to crustal control if we assume that the crust grows diffusively by $\delta \sim (kt)^{1/2}$ (Griffiths and Fink, 1993), and with values of $k$ given in Table 3.1. In the case of the 2001 Mt Etna flow, this suggests crustal thicknesses of 0.1 m, 0.15 m and 0.2 m after 12, 24 and 36 hours respectively, and 0.4 m by the time the lava flow reached its maximum length, broadly similar to thicknesses observed in the field. The Cordón Caulle flow would have attained a crustal thickness of ~1.9 and 2.5 m after 75 days and 127 days, and 4 m after 285 days at the eruption end. This is also a similar scale to the depths of fractures observed in the field and the estimated crust thickness at other rhyolite flows from fractures and ogive wavelengths (Fink, 1980a).

The point at which a lava flow becomes crustal controlled could be considered as a ratio between crustal thickness and the bulk flow thickness (Lescinsky and Merle, 2005). The timescale of crustal thickening is primarily controlled by the thermal diffusivity, with higher diffusivities, e.g. associated with low vesicularity, leading to a faster thickening and hence more rapid transition to crustal control. The effective crustal strength is a function of its thickness and yield strength. A crust with a higher yield strength ought to become a controlling factor more rapidly than a lower yield strength crust because it would not have to gain as great a thickness to have a commensurate effect on lava flow emplacement. The timing of the onset of crustal

control must therefore be sensitive to both the initial crystallinity of the lava and the rate of in-flow crystallisation, due to the effect that crystals would have on crust rheology.

The ratio of crustal thickness to flow thickness ($\Psi$) can be calculated for the moment of transition from viscosity to crustal control. In the case of the 2001 Etna flow, $\Psi$ is equal to 0.02 – 0.04, depending on the inferred transition time. Similarly, for Cordón Caulle $\Psi$ is equal to 0.06 – 0.08. We thus infer that the crust becomes a dominant influence when it accounts for 2 – 8% of the bulk flow thickness, but this proportion could be lower for crust with a higher yield strength. Such dimensionless numbers help to systematically define the timing of viscosity to crustal control transition. Crustal strength is clearly a key, but poorly understood, aspect of lava flow emplacement. Improved constraints are required to define and quantify the factors that influence it, which must include lava texture (i.e. crystallinity, vesicularity), composition, and cooling rate. Such an improved understanding could aid in defining the value of $\Psi$ required to control lava flow advance rate for a broad compositional range.

## 3.7 Conclusions

Observations of lava flow emplacement from published studies, field data and satellite imagery indicate that a strong crust may significantly influence the growth of both basalt and high-viscosity, crystal-poor, rhyolite lava flows. By using these observations to help constrain quantitative models of lava flow length change over time, we show that both the 2001 Mt Etna basaltic lava flow and the 2011-2012 Cordón Caulle rhyolite lava flow were initially controlled by their apparent Newtonian viscosities and then by their surface crusts. In the case of the rhyolite, this change in control occurred only after several months and our results underscore that relatively straightforward lava advance models, based on bulk rheological properties, can be effective across a large compositional range of lava flows. The emplacement of high-silica flows is not always

dominated by their internal yield strength, as previously inferred, but crystal-poor high-silica lavas, including rhyolites, may behave in a manner similar to initially viscosity controlled basalts, albeit over different temporal and spatial scales.

### 3.8 Acknowledgements

NM is supported by a NERC Envision studentship and a BUFI grant from the British Geological Survey. HT is supported by a Royal Society University Research Fellowship. CV-B publishes with the permission of the Executive Director of the British Geological Survey. We thank C. Bignami for the provision of additional flow outlines from COSMO SkyMed data, as well as the BBC Earth team for assistance with aerial photography of the Cordón Caulle lava flow. We are also grateful to J. Castro and C. I. Schipper for assistance during fieldwork in 2013 and 2014, plus discussion of lava emplacement at Cordón Caulle.

# 4 The origin and evolution of breakouts in a cooling-limited rhyolite lava flow

N. Magnall[1], M.R. James[1], H. Tuffen[1], C. Vye-Brown[2], C. I. Schipper[3], J. Castro[4], A. G. Davies[5]

*[1] Lancaster Environment Centre, Lancaster University, Lancaster, UK*

*[2] British Geological Survey, The Lyell Centre, Edinburgh, UK*

*[3]School of Geography, Environment and Earth Sciences, Victoria University of Wellington, New Zealand*

*[4]Institute of Geosciences, University of Mainz, Mainz, Germany*

*[5]Jet Propulsion Laboratory – California Institute of Technology, 4800 Oak Grove Drive, Pasadena, CA 91109, USA*

The following paper, at the time of writing, has been submitted for publication in Geological Society of America Bulletin. Processing and interpretation of remote sensing data, field data, and gathering of SEM imagery, as well as the bulk of the writing of the manuscript, was conducted by myself. All authors aided in the initial conception of the project as well as editing and writing the manuscript. Mike James and Hugh Tuffen aided with fieldwork and processing of remote sensing data as well as sample interpretation, Charlotte Vye-Brown aided with SEM imaging of thin sections, Ian Schipper contributed synchrotron-CT data of samples, Jon Castro contributed exported profiles of breakouts from a high resolution Pléiades DTM, and Ashley Davies assisted with the initial gathering of satellite data. The detailed methodology for this paper can be found in the appendices: Appendix 8A details the remote sensing techniques used, Appendix 8B expands on the data gathered in the field, and Appendix 8C outlines the microstructural techniques used.

The paper aims to determine the processes that contributed to breakout formation at the Cordón Caulle lava flow by utilising field and satellite observations to inform breakouts processes. We then incorporate microstructural observations from SEM microscopy and synchrotron-CT to determine the processes that contributed to

breakout formation. This combined approach ultimately allowed for the development of a conceptual model for breakout formation in high-silica lava flows.

The multiscale approach used in this paper allowed for a thorough understanding of the morphological variability of the breakouts. Furthermore, the study yielded insights into the processes that contributed to breakout formation:

- The breakouts have four primary morphologies that make up part of a continuum through breakout evolution, these morphologies are: domed, petaloid, rubbly, and cleft-split. With advance and inflation of a breakout contributing to their morphology and the amount of advance and inflation was partly dependent on the availability of material supply to the breakout.
- Breakout formation was triggered by the continued supply of lava to the stalled flow front along preferential thermal pathways. Furthermore, late stage volatile exsolution and vesiculation of the lava core, partly due to anhydrous crystallisation (from the vent to the flow front) and second boiling, may have contributed to the pressure increase that caused breakout formation.
- Spreading of flow front lobes generated fractures in the crust of the main channel of the lava flow. These were preferential sites of breakout formation.

## 4.1 Abstract

Understanding lava flow emplacement processes is important for interpreting existing lava deposits and for hazard assessments and substantial progress has been made for basaltic systems. However, in contrast, our understanding of silica-rich lava flows has seen limited recent advance. Here, we draw on the 2011-2012 rhyolite eruption of Puyehue-Cordón Caulle to examine the formation of lava flow breakouts, which represents a characteristic process in cooling-limited basaltic lavas, but has been neglected for silicic lava flows and is not described in established models of rhyolite emplacement. We develop the first conceptual framework to classify breakout types in silica-rich lavas, and to describe the processes involved in their progressive growth, inflation and morphological change. By integrating multi-scale satellite, field and textural data from Cordón Caulle, we interpret breakout formation to be driven by a combination of pressure increase (from local vesiculation in the lava flow core, as well as from continued supply via extended preferential thermal pathways) and a weakening of the surface crust through lateral spreading and fracturing. Small breakouts, potentially resulting more from local vesiculation than from continued magma supply, show a ‘domed’ morphology, developing into ‘petaloid’ as inflation increasingly fractures the surface crust. Continued growth and fracturing results in a ‘rubbly’ morphology, with the most inflated breakouts developing into a ‘cleft-split’ morphology, reminiscent of tumulus inflation structures seen in basalts. These distinct morphological classes result from the evolving relative contributions of continued breakout advance and inflation. The extended nature of some breakouts highlights the role of lava supply under a stationary crust, a process ubiquitous in inflating basalt lava flows that reflects the presence of preferential thermal pathways. Textural analyses of the Cordón Caulle breakouts also emphasise the importance of late-stage volatile exsolution and vesiculation within the lava flow. Although breakouts occur across the

compositional spectrum of lava flows, the greater magma viscosity of silicic lavas is likely to make late-stage vesiculation much more important for breakout development than in basalts, as gases are less able to escape from the lava. Furthermore, such late-stage vesiculation has direct implications for hazards previously recognized from silicic lava flows, enhancing the likelihood of flow front collapse, explosive decompression of the lava core and the generation of pyroclastic density currents.

## 4.2 Introduction

Studies of hazards from silicic volcanic eruptions usually focus on explosive activity (ash, bombs, and pyroclastic density currents), with effusive rhyolitic or rhyodacitic eruptions generally considered to be rare events. However, the emplacement of rhyolitic lava flows has been previously associated with hazards such as explosions from their surface (Jensen, 1993; Castro et al., 2002a), lava flow front collapse (Fink and Manley, 1987; Baum et al., 1989), and the potential generation of pyroclastic density currents (Fink and Kieffer, 1993). Of six such effusive eruptions in the 20$^{th}$ and 21$^{st}$ century (Katsui and Katz, 1967; Reynolds et al., 1980; Fierstein and Hildreth, 1992; Singer et al., 2008; Bernstein et al., 2013; Tuffen et al., 2013), three occurred at Puyehue-Cordón Caulle, southern Chile (in 1921-22, 1960, and 2011-2012; Katsui and Katz, 1967; Lara et al., 2004; Singer et al., 2008; Tuffen et al., 2013). Thus, for contemporary hazard assessment in some areas as well as for interpreting past deposits, improving our understanding of emplacement processes may be more pressing than previously considered.

Lava flows initially advance in the direction of steepest gradient and their preliminary paths are thus relatively easy to forecast. However, once flow front advance ceases, secondary lava flows, or breakouts, can form if effusion continues. Throughout this study we consider a breakout to be a new, morphologically distinct lava flow lobe, formed from the core of an otherwise stalled portion of the flow. Such breakouts extend or widen the inundated area and uncertainties in where they will occur pose a challenge for forecasting lava inundation hazard. In basaltic lava flows, continued supply of mobile lava to a stalled flow front leads to inflation, and breakouts occur through rupturing of the surface crust (e.g. Walker, 1971; Kilburn and Lopes, 1988; Blake and Bruno, 2000; Applegarth et al., 2010c). Flow lengthening can be substantial when such breakouts are long-lived and fed by preferential thermal pathways that mature into lava

tubes (e.g. Calvari and Pinkerton, 1998). However, breakouts in high-silica lava flows have only been identified from a collapsed portion of a dacite lava flow margin on Santiaguito volcano, Guatemala (Harris and Flynn, 2002; Harris et al., 2004). Consequently, little is known about breakouts in high-silica lavas and here, we present the first conceptual model for their formation and consider the processes involved.

Previous studies of high-silica lavas have interpreted their emplacement in terms of the slow spreading of crystal-poor domes, e.g. for Holocene rhyolite lava flows in the western USA (Fink, 1980a; Fink, 1980b; Fink, 1993; DeGroat-Nelson et al., 2001) and older rhyolites in Australia (Dadd, 1992; Smith and Houston, 1995) and New Zealand (Dadd, 1992; Stevenson et al., 1994a; Stevenson et al., 1994b). As a lava flow advances, cooled surface blocks cascade down the lava flow front and are overridden by the core in a caterpillar-track-style motion typical of blocky and 'a'ā lava flows (Fink, 1983; Harris et al., 2004). Rhyolite flows form a cooled surface crust that buckles into ogives as the lava flow front slows (Fink, 1980a; Castro and Cashman, 1999). The crust insulates the lava flow core, potentially maintaining core mobility long after effusion ceases (Manley, 1992; Farquharson et al., 2015). Just as for basalts, the crust can therefore exert a controlling influence on lava flow advance and emplacement (Magnall et al., 2017), making the formation of breakouts a possibility. However, although flow lobes have been previously observed in rhyolite lava flows (Bonnichsen and Kauffman, 1987; Manley, 1996), potential breakouts processes have not been discussed for rhyolitic lava flows, and work has focussed on other late-stage features such as pumice diapirs (Fink, 1980b; Fink and Manley, 1987). Nevertheless, aspects of these processes could be linked; pumice diapirs are inferred to be due to vesiculation of the flow core and buoyant rise to the surface of a lava, and vesiculation may also be important in breakout formation.

Although advances in our understanding of the emplacement of high-silica lava flows have been hampered by their infrequency, the 2011-2012 rhyolite eruption of Puyehue-Cordón Caulle in Chile (69.8 – 70.1 wt% $SiO_2$, Castro et al., 2013) enabled some of the first detailed scientific observations of emplacement processes. This lava flow produced numerous breakouts and, as such, provides a new resource to assess breakout processes in a cooling-limited rhyolite lava flow. Here, we use satellite and field observations to understand the processes occurring prior to, and during, breakout formation. Microtextural characteristics from thin sections and synchrotron CT help constrain crystallisation and vesiculation histories, allowing us to create a conceptual model for breakout formation in a silicic lava flow.

## 4.3 The 2011-2012 eruption of Puyehue-Cordón Caulle

Puyehue-Cordón Caulle is a basaltic to rhyolitic volcanic complex located in the southern volcanic zone of the Chilean Andes (Fig. 4.1). The 2011-2012 eruption began on 4 Jun 2011, producing a 15-km-high Plinian ash column (Castro et al., 2013), which subsided into coupled effusive-explosive activity with simultaneous emission of lava and pyroclasts from a common vent (Castro et al., 2013; Schipper et al., 2013; Tuffen et al., 2013; Bertin et al., 2015). Initial eruption discharge rates were up to 50 – 70 $m^3s^{-1}$ but reduced to ~10 – 20 $m^3s^{-1}$ after ~30 days (Bertin et al., 2015; Coppola et al., 2017). Lava effusion was identified first in synthetic aperture radar satellite images on 19 Jun 2011 (Bignami et al., 2014) and formed two channels that advanced to the north and south, before stalling and forming numerous (>80) breakouts from the lava flow front and margins (Tuffen et al., 2013; Magnall et al., 2017). Although the eruption ended on 15 March 2012, as indicated by the cessation of seismicity at the vent, some local areas of advance were still observable in January 2013 (Tuffen et al., 2013).

## 4.4 Methodology

Our multiscale data analysis of breakouts and the main lava flow brings together satellite imagery, digital elevation models (DEMs), 3-D photogrammetry models, as well as scanning electron microscopy (SEM) and synchrotron X-ray computed tomography (CT) imaging of samples collected in the field. Fieldwork at Cordón Caulle was carried out during and after the eruption, in 2012, 2013, and 2015 (always in January), and allowed for sample collection and a detailed examination of the structure of the lava, in particular breakout morphology. Approximately 50 in-situ samples were collected from the lava flow front and top surface, and from fallen blocks at the lava flow front. Fieldwork in 2015 was complemented by aerial photographs acquired out of the window of a helicopter. Full details of the methodology can be found in Appendix 8A, 8B, and 8C.

### *4.4.1 Satellite imagery*

The lava flow evolution was tracked using satellite images from the Earth Observing 1 (EO-1) Advanced Land Imager (ALI; e.g. Digenis et al., 1998), Landsat 5 and 7 ETM+, and the Terra Advanced Spaceborne Thermal Emission and Reflection Radiometer (ASTER; Yamaguchi et al., 1998). EO-1 and Landsat data are available from the U.S. Geological Survey, and ASTER data are distributed by the Land Processes Distributed Active Archive Center (LP DAAC), located at USGS/EROS, Sioux Falls, SD. http://lpdaac.usgs.gov. Google Earth imagery was also used. All images, except those from Google Earth, were processed in ENVI to create true colour images, or false colour images from the near infrared (VNIR) and short wave infrared (SWIR) bands, with spatial resolutions between 15 and 30 m. Where possible, the resolution was improved by combining the images with their corresponding panchromatic image (EO–1 10 m resolution, Landsat 7 ETM+ 15 m resolution) using the

NNDiffusePanSharpening function in ENVI, allowing the detection of lava flow features larger than a few tens of metres across. The resulting imagery was imported into ArcGIS and the coregistration refined using fixed points, such as roads, lakes and older lava flows that were assumed to be stationary throughout the duration of the eruption.

The qualitative thermal evolution of the lava flow surface was tracked using thermal infrared (TIR) images from Landsat 5, 7 (Band 6) and ASTER (L1T) sensors, visualised in ArcGIS. These TIR images have coarser resolution (Landsat 30 m, ASTER 90 m) than their VNIR and SWIR counterparts, and dense time-series analyses were restricted by the eruptive plume and cloud cover, which often obscured parts of the lava flow.

### *4.4.2 3-D models from field photos and DEM*

To determine the detailed structure of five example breakouts, 3-D surface models were generated from ground-based field photos using structure-from-motion photogrammetry (e.g. James and Robson, 2012). Approximately 100 photos were taken on foot at regular intervals in an arc around a feature of interest using a Canon 450D digital SLR camera, with fixed focus 28 mm lens. The photos were processed in Agisoft PhotoScan Professional (v1.3.2) to generate dense 3-D point clouds which were manually cleaned to remove outlying points. The models were scaled by recognising common features in georeferenced satellite images of the lava, giving an overall scale accuracy of 5–10%, suitable for qualitative assessments of lava morphology. Cross sections were obtained by first gridding the 3-D point clouds into 10-cm-resolution DEMs (Appendix 8A.28), then extracting the sections.

The morphology of the largest breakouts could not be observed fully from the ground so such areas were analysed using a post eruption Pléiades DEM (Elevation 1 dataset) with a 1 m horizontal resolution and 1.5 m horizontal and vertical accuracy. Due to the

DEM being generated from stereo satellite images, the bases of deep and narrow features, such as fractures, may not have been reconstructed due to being occluded in either one or both images. 2-D profiles were extracted by sampling the DEM at a 2 m resolution, to help reduce the noise from the highly uneven and blocky nature of the lava flow.

### *4.4.3 Samples and thin sections*

Microstructural characterisation of key representative lava facies was carried out by SEM analysis using a LEO 435VP variable pressure digital scanning electron microscope. Phase/mineral identification was aided by qualitative observation of energy-dispersive X-ray spectra recorded simultaneously during SEM observation, using an Oxford Instruments INCA energy-dispersive X-ray microanalysis (EDXA) system. Images were captured from thin sections in BSE mode for further image analysis, which included determining crystal contents using CSDCorrections software (Higgins, 2000). Up to ~400 microlites in SEM images of ~15 representative samples (including from four breakouts) were first isolated by tracing the crystal edges (Appendix 8C.2). The resulting image was analysed in ImageJ and CSDCorrections to determine total microlite volume fractions. The crystal volume fractions presented here (as percentages) are the stereologically corrected intersection data from CSDCorrections (Higgins, 2002) and have been compared with similar data from (Schipper et al., 2015). Vesicularity (Table 4.2) was estimated from the 2-D vesicle fraction in SEM images using ImageJ. This straightforward method only gives an approximate value of vesicularity, but enables comparisons between different flow facies.

Textures in breakout samples were examined in 3-D using synchrotron X-ray source computed tomography (CT), performed at the Australian Synchrotron (Clayton,

Victoria) in Hutch 3B of the Imaging and Medical Beamline. Images were captured with the in-house “Ruby” detector, with X-ray energy of 45 keV. Scans included the collection of 1,800 radiographs with 0.3 s exposure time over 180° rotation, with a pixel size of 13.7 µm. The length of the samples required three partially overlapping scans, which were reconstructed separately using the in-house MASSIVE supercomputing cluster, and then stitched together using ImageJ (Schneider et al., 2012). All renderings were performed with the Drishti visualization software package (Limaye, 2012).

## 4.5 Lava flow emplacement

Satellite observations from EO-1 ALI have been previously used to show that the ~40 m thick lava flow emplaced into a topographic depression (Appendix 8A.19 – 8A.21) and, within ~600 m of the vent, split into two channels 600 – 1000 m wide, of which one advanced north and the other south (Fig. 4.1; Magnall et al., 2017). The southern channel moved down a relatively constant slope of ~7° before interacting with a topographic barrier towards the end of its emplacement (Appendix 8A.19). The northern channel was similarly impeded by a ridge within the first 30 – 60 days of the eruption (from the eruption start on 4 June 2011; Magnall et al. (2017). This ridge halted the northern advance of the lava and led to a widening of the lava flow front (~200 m, see yellow and turquoise outlines in Fig. 4.1A).

The first breakouts were observed at the western margin of the northern channel, 153 days after the eruption started (Fig. 4.1C), and following the development of flow front lobes 50 – 250 m wide and 50 – 200 m long, separated by large fractures that extended 25 – 200 m backward from the flow front (Fig. 4.1C, Appendix 8A.18). In optical satellite images (Fig. 4.1C, D), the breakouts appear darker than the main lava flow but, in ASTER TIR data, breakouts appear as bright features at the lava flow front (Fig. 4.2C, D; Coppola et al., 2017). Some of the earliest breakouts were subsequently enveloped

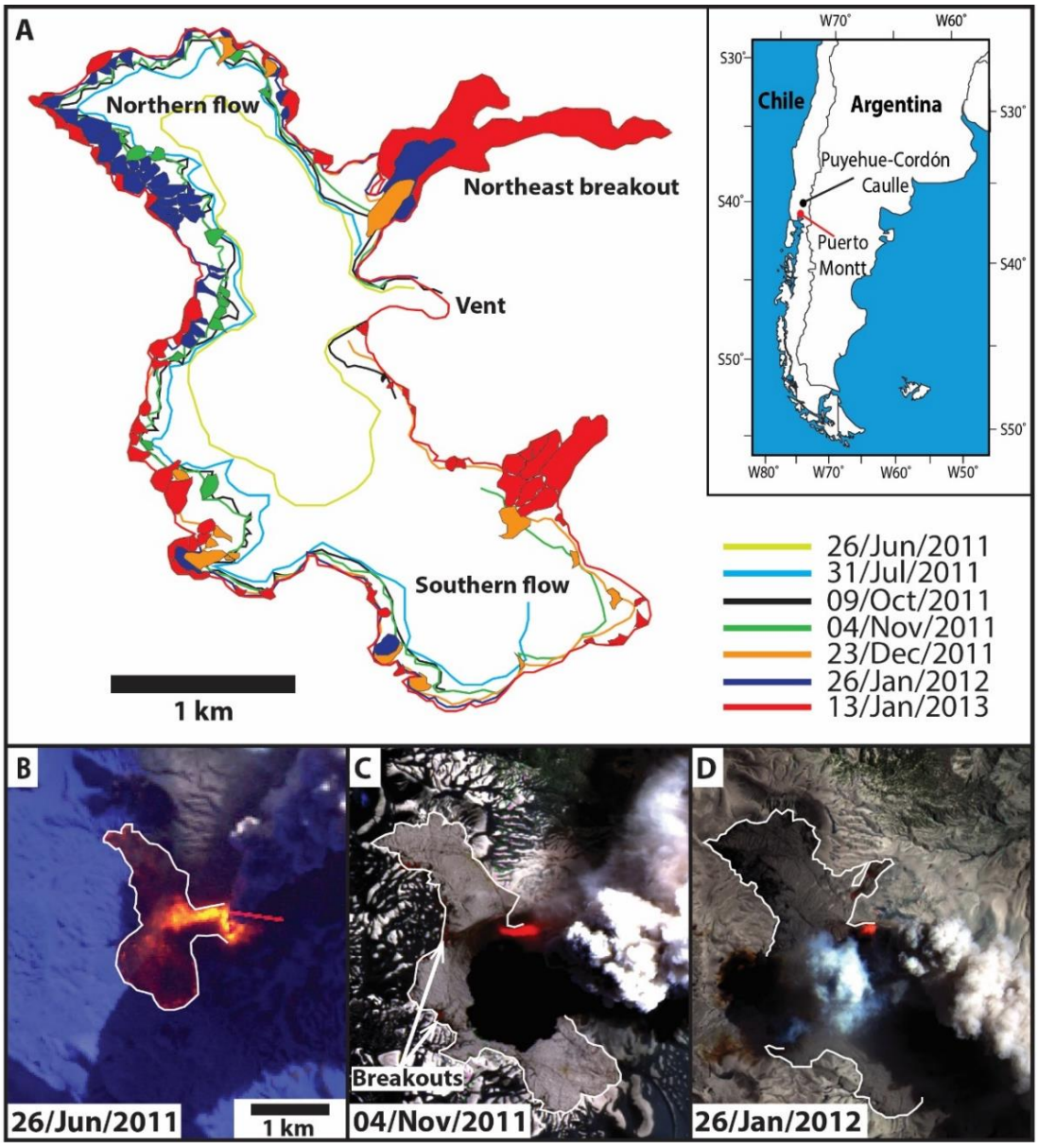


Figure 4.1: Flow outlines derived from Landsat 5 and Earth Observing 1 ALI satellite images (NASA, 2011c, d, a, f, e, 2012a, 2013), data available from the U.S. Geological Survey. (**A**) Position of the flow front through time and the timing of breakout formation. (**B**) Landsat 5 image of the initial lava effusion, with collapse related hot spots at the flow front. The red line trending E-W is likely a saturation effect/anomaly. (**C)** EO-1 ALI image of the initial breakout formation after a lobate flow front developed and the surface crust had extensively fractured. (**D**) EO-1 ALI image showing the continued breakout formation with the initial effusion of the NE lobe. A number of separated flow outlines can be found in Appendix 8A.18. Enlarged versions of **B, C, D** can be found in Appendix 8A.17.

by the forward advance of the main channel (Fig. 4.1), and became indistinguishable from the main lava flow. Most breakouts range in size from ~15 to 40 m tall, 30 to 150

m wide and 30 to 450 m long, with the longest occurring in areas with little topographic constraint. Breakouts from the southern channel developed predominantly from its margin, following lobe generation as seen in the northern channel, with some small breakouts (up to 60 m long and 50 m wide) forming from the front towards the end of the eruption (Fig. 4.1A).

After 200 days (first observed 23 December 2011) a breakout formed from the eastern margin of the northern channel, and developed a substantial length (~2 km; Magnall et al., 2017); hereafter this breakout is referred to as the northeast breakout (Fig. 4.1A). This new breakout entered a relatively steep (~15˚) and narrow (200 – 350 m wide) valley, and halted only when the eruption ended (Fig. 4.1). Here we observe that in TIR imagery the northeast breakout is brighter than the bulk of the main lava flow throughout its lifetime and for several months after the eruption ceased (Fig. 4.2B, C). The breakout developed distinct levées and appears to have sections of partially drained channel. After the establishment of this breakout, there was a noticeable reduction in the rate of initiation of new breakouts from the northern channel (Fig. 4.1); between December and January, tens of breakouts formed from the northern channel but, after 26 January 2012, when the northeast breakout had become established (Fig. 4.1), only five new breakouts were formed in the following two months before the eruption stopped on 15 March 2012.

Breakouts continued to form and evolve for some time after the eruption ended. In the NW, some of the breakouts continued to grow (Fig. 4.3B and 4.3C), but with some showing only limited post-eruption advance (<50 m). Instead, fractures (up to ~100 m long) developed within the breakouts and parallel to their advance direction (Fig. 4.3B and 4.3C). From the southern channel, ~5 new breakouts formed at its eastern margin (Fig. 4.1A, 4.3) and developed similar, large-scale fractures (up to 300 m long; Fig.

3E). One of these breakouts was observed advancing in January 2013, several months after the eruption ended (Tuffen et al., 2013; Farquharson et al., 2015).

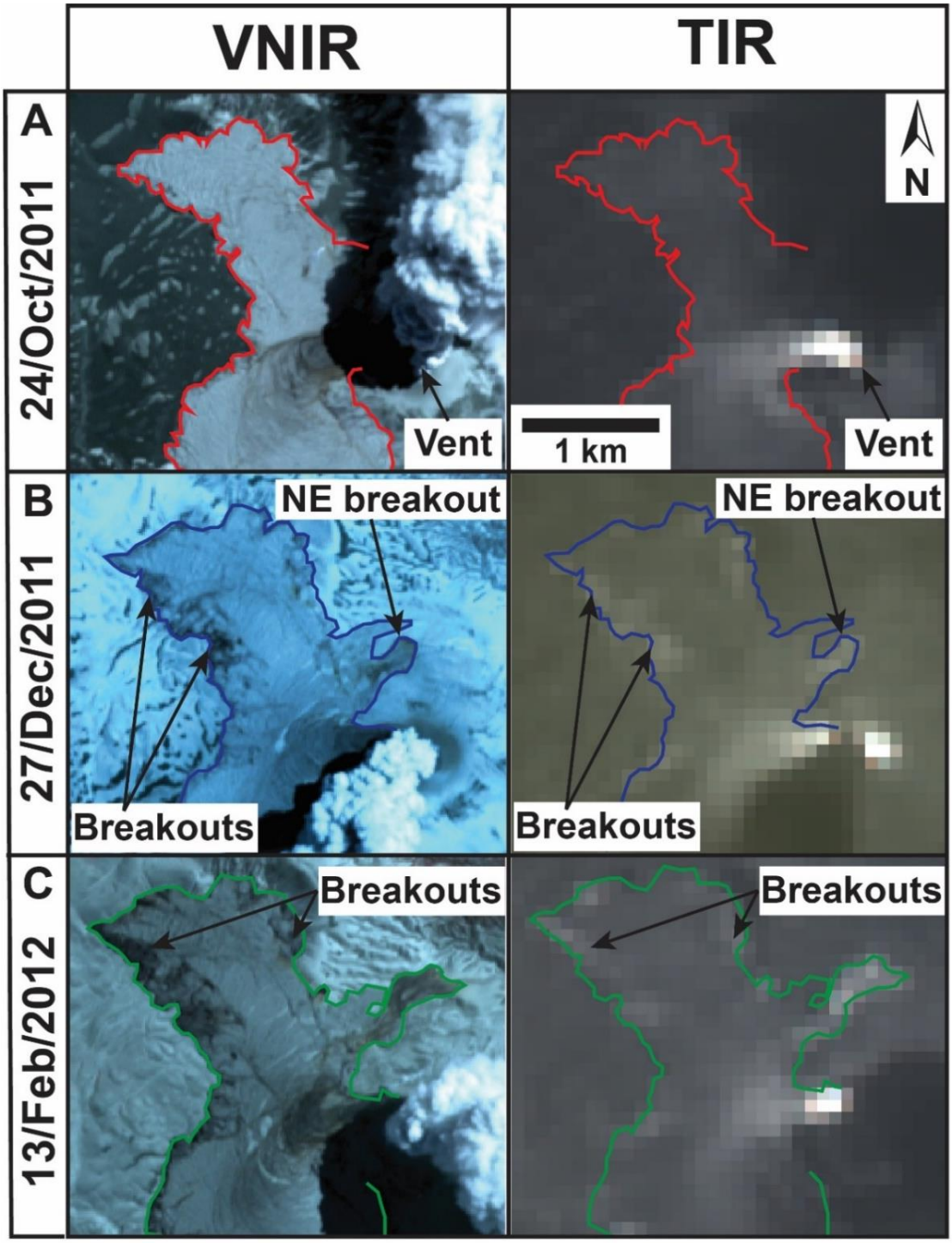

← Figure 4.2: ASTER VNIR and corresponding TIR images of the 2011-2012 Cordón Caulle lava flow (NASA/METI, 2011c, a, 2012c), these data are distributed by the Land Processes Distributed Active Archive Center (LP DAAC), located at USGS/EROS, Sioux Falls, SD. http://lpdaac.usgs.gov. **A**. Early phases of the lava emplacement prior to breakout formation. **B, C**. Later phases of lava emplacement when breakouts are observed. Breakouts correspond to bright spots at the lava flow front in the TIR images. The NE breakout is visible in images **B-C**. The pixelation of the TIR images relates to the 90 m pixel size of the ASTER TIR data. Enlarged versions can be found in Appendix 8A.10 – 8A.16.

In total, ~90 breakouts formed (Fig. 4.1), accounting for ~12% (±2%) of the total lava flow volume (as estimated from the areal coverage in satellite imagery and assuming an average breakout height of ~80% of the main channel height, i.e. ~32 m). The volume of the breakouts is thus equivalent to a 4 m increase in thickness of the main channels.

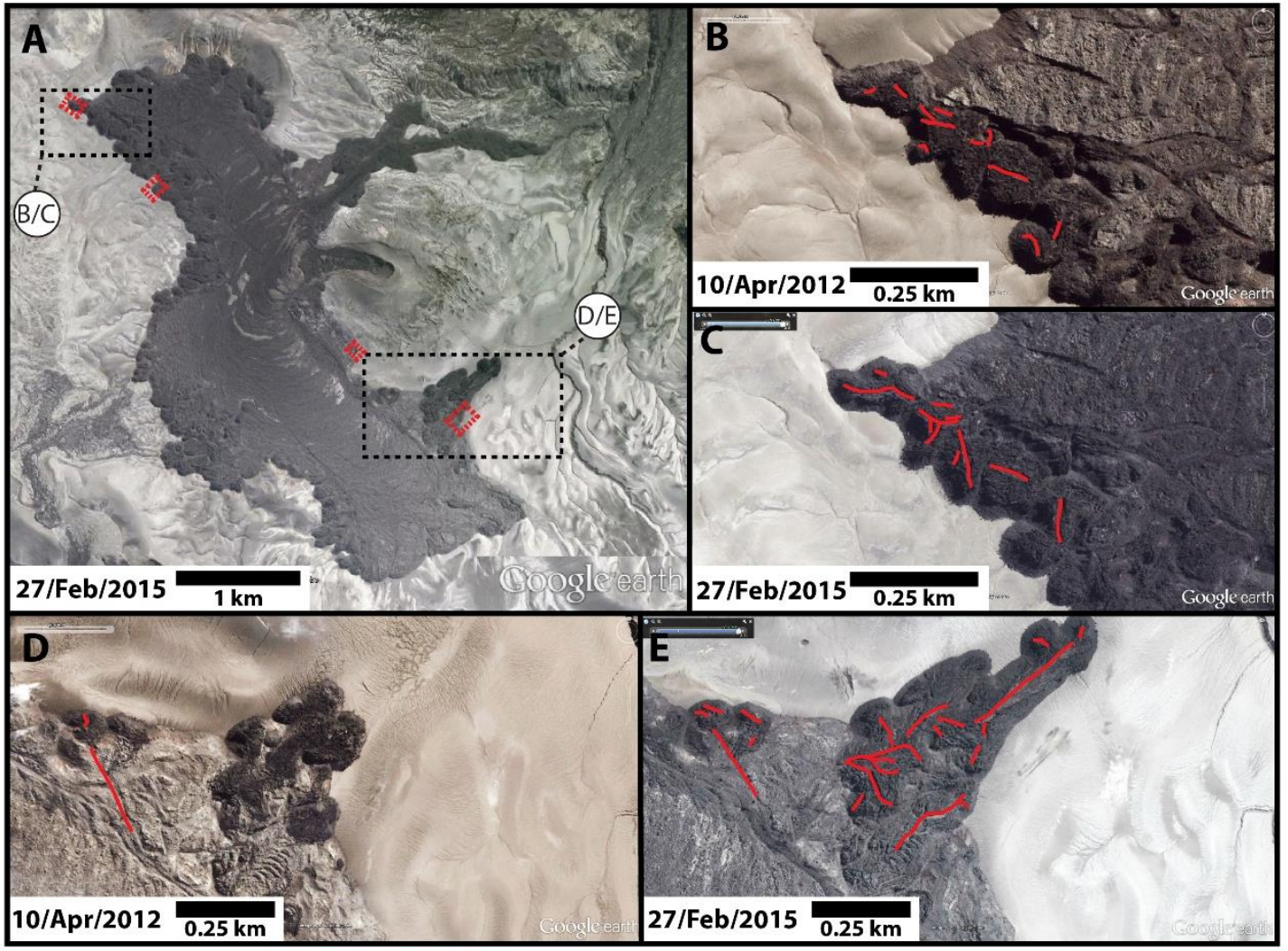
A
B/C
D/E
27/Feb/2015
1 km
Google earth
B
10/Apr/2012
0.25 km
Google earth
C
27/Feb/2015
0.25 km
Google earth
D
10/Apr/2012
0.25 km
Google earth
E
27/Feb/2015
0.25 km
Google earth

← Figure 4.3: Google Earth images of the rhyolite flow (DigitalGlobe, 2012, 2015). The two boxes in **A** show the location of images **B**, **C** and **D**, **E**. The red boxes show the locations of the breakouts in Figure 5.8. (**A**, **C**, **E**) Images from 2015, several years after the eruption ended. (**B**, **D**) Images from 2012, one month after the eruption ended when the flow was still developing and advancing locally. After the eruption ended breakouts continued to form from the flow front and margin. Red lines show the locations of fractures, some of which continued to form after the eruption ended as the breakouts evolved.

## 4.6 Main channels

The main northern and southern channels have coarse, red-brown rubble surfaces with blocks sizes of up to several metres, and are bounded by steep and blocky levées, comprising a mixture of loose rubble and coherent, dense, core lava (Fig. 4.4). Parts of the surface of the lava near the vent appear lighter in colour and less blocky, and represent areas where collapsed portions of the tephra cone have been rafted on the lava surface. The channel surfaces are systematically folded into ogives with a wavelength of ~40 m and an amplitude of order several metres (Magnall et al., 2017). They are also split by fractures, most of which are orientated perpendicular to the lava flow front (Appendix 8A.18), tens to hundreds of metres long and several metres deep, and many expose a surface crust of coherent and dense lava, beneath the loose brecciated debris.

### *4.6.1 Lithologies*

The blocks that comprise the top surface and lava flow front of the main channel are a mixture of dark vesicular and glassy rhyolite, golden coloured flow-top-pumice, and dense core lava (Fig. 4.4). The dark glassy rhyolite is the most abundant on the surface of the lava, whereas the flow-top-pumice occurs as isolated patches (~1 – 20 m wide; Fig. 4.4B, E, F). The core of the lava is exposed in areas where portions of the lava

flow front and margins have collapsed (Fig. 4.4A) and is grey to red-brown in colour, crystal-rich, with low porosity presented by sparse sub-millimetre vesicles (Table 4.1, Fig. 4.4C, D). Millimetre-spaced, parallel, platy fractures, associated with vapour phase cristobalite formation (Fig. 4.5A, B; Schipper et al., 2015), are laterally extensive over tens of centimetres (Fig. 4.4D).

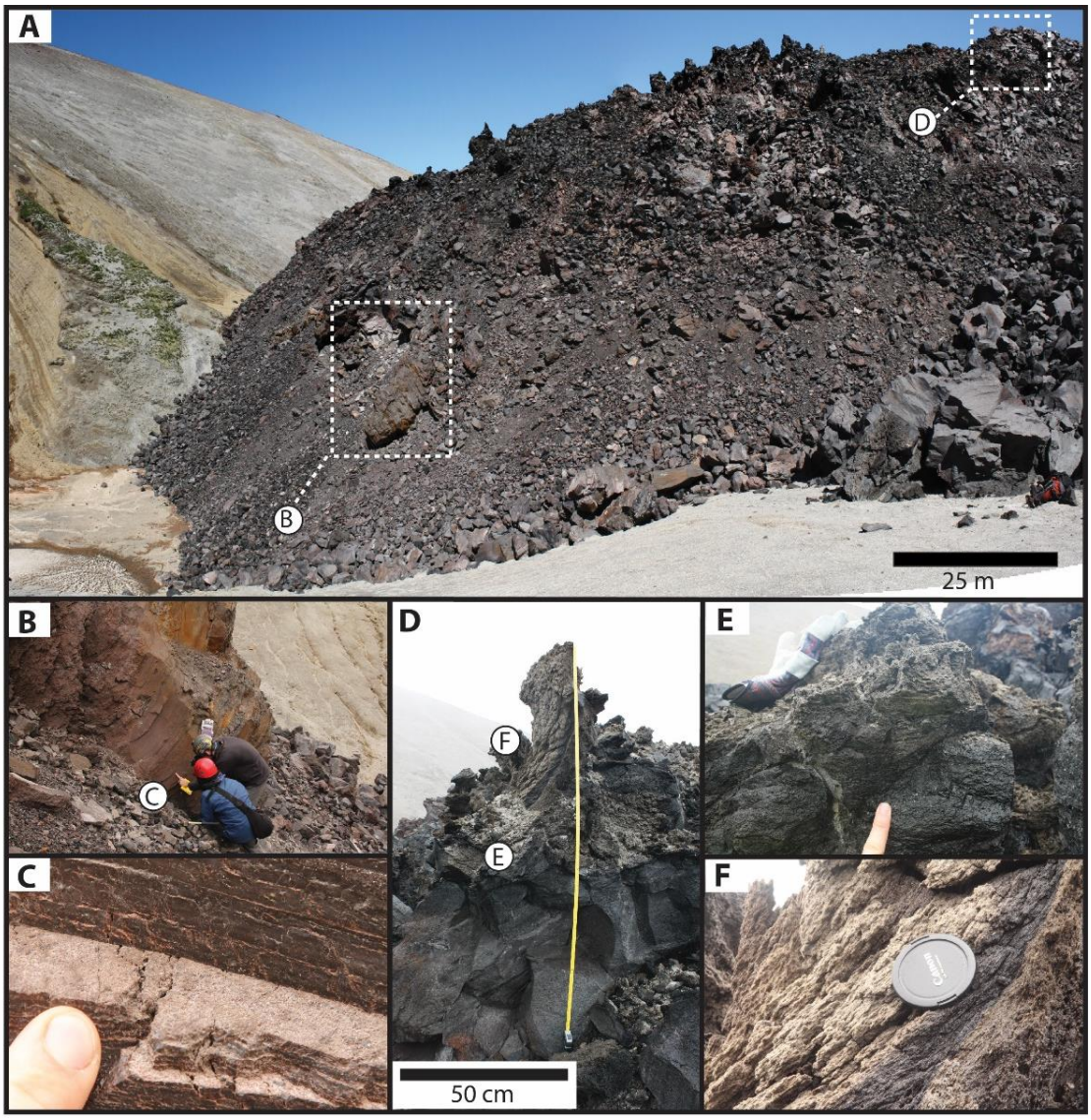


Figure 4.4: (**A**) Part of the flow front of the main channel. (**B**, **C**) The crystalline core of the flow is visible where large sections of flow front collapsed. The core is dense with very few vesicles and has closely spaced platy fractures that are filled with cristobalite. (**D**, **E**, **F**) In the surface crust of the main channel the denser crust lava grades into the much more vesicular flow-top-pumice.

### *4.6.2 Microstructure*

Samples from the main channel include from the lava flow core, surface and lava at the vent. The core samples are crystal-rich (~70 – 80 volume%) and display the extensive millimetre-spaced platy fractures observed in hand sample. In some cases, the fractures have a number of s-shaped shear arrays (0.5 – 1 mm long and 0.05 – 0.1 mm wide, Fig. 4.5A) and, in many places, the two sides of the fractures are connected by thin (1 – 8 µm wide) glassy filaments, indicating an element of ductile deformation.

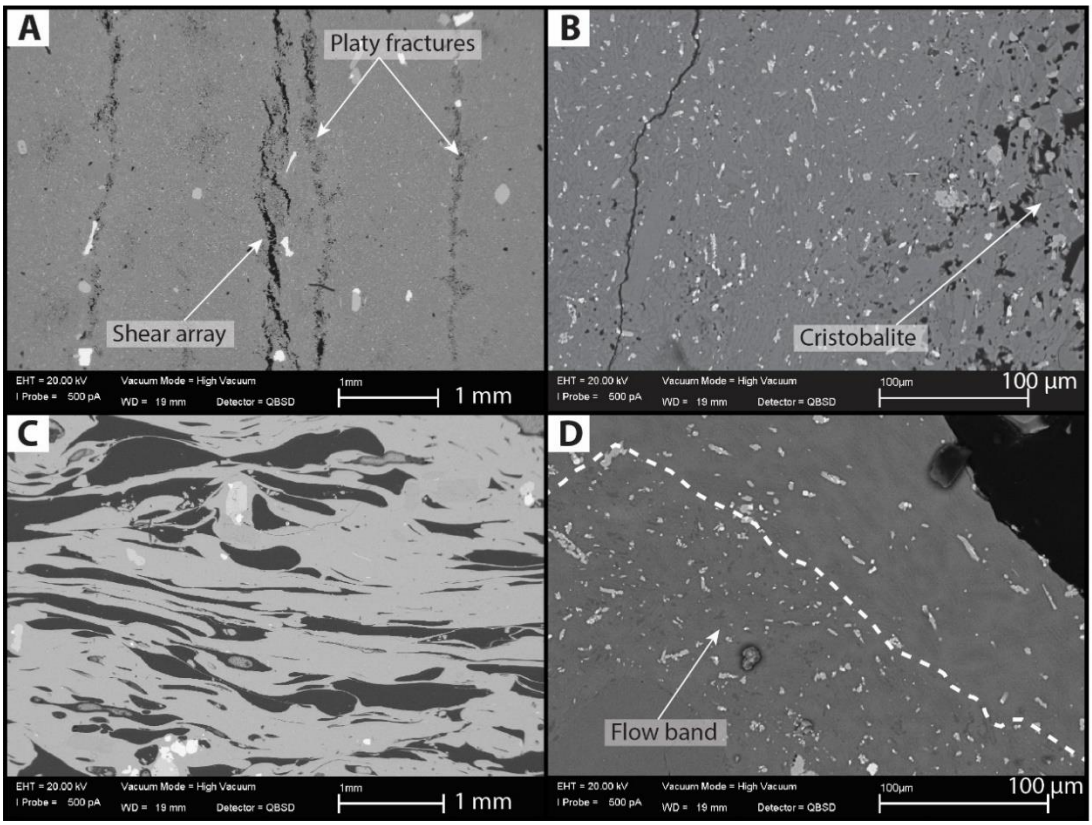


Figure 4.5: SEM images of main channel samples. (**A**) Crystalline core of the flow with platy fractures that are infilled with cristobalite and variably healed. Some shear zones are also found within these fractures. (**B**) Crystalline flow core with cristobalite infilling void spaces and platy fractures. (**C**) Glassy flow-top-pumice (from Fig. 4E) with a large number of elongate sheared and collapsed vesicles. (**D**) Flow band marked by a variation in microlite content in a portion of the vent lava.

The surface samples from the main channel are comprised of variably vesicular flow-top-pumice (Fig. 4.5C, 4.4B and 4.4F). The pumice is assumed to have quenched shortly after effusion and been rafted on the lava flow surface to the front and may represent some of the earlier erupted lava. Pumice samples have highly contorted, collapsed and elongate vesicles (Table 4.1, Fig. 4.5C) and a microlite crystal volume of ~5 volume%. Samples from the vent represent some of the last effused lava. The samples are vesicular (Table 4.1), with poorly-developed flow-bands marked by subtle variations in microlite content (~5 volume% variation, Fig. 4.5D), the microlite content of the vent samples is ~20 – 25 volume% (Table 4.1), which is high compared to some earlier effused lava.

Table 4.1: Lava flow facies properties (See Appendix 8C)

| Facies | Microlite content | Bulk crystallinity, X-ray diffraction (Schipper et al., 2015) | Vesicle sizes | Vesicularity |
|---|---|---|---|---|
| Pyroclastics | N/A | ~10-30% | N/A | N/A |
| Surface pumice | <5% | N/A | Up to 5 mm long, 0.2 mm wide. | ~30% (1-2 m depth) |
| Vent lava | 20-25% | ~20-25% | 0.1-5 mm diameter. | ~30-50% (surface) |
| Breakout lava | 30-40% | ~50% | Sheared: 0.2-10 mm long, 0.03-0.58 mm wide. Undeformed: 0.7-7 mm diameter. | ~15-30% (highest with undeformed vesicles) |
| Main channel core | 70-80% | ~70-100% | <0.05 mm diameter (sparse up to ~1 mm diameter) | ~5% |

## 4.7 Breakouts

The large number of breakouts give the overall flow an lobate outline in plan view, and their darker, more slabby and blocky morphology contrasts with the redder, more rubbly surface of the main channels (Tuffen et al., 2013). Analysis of breakouts utilized a mixture of satellite imagery (>50 breakouts analysed), aerial photography (10 breakouts), topographic cross sections from a high resolution DEM (20 breakouts), detailed field observations (20 breakouts), and 3-D photogrammetry models (5 breakouts). Although a comparison of bulk chemistry between breakouts and main

channel material has not been conducted, analysis of matrix glass compositions of breakout and main channel lava shows little chemical variation (Schipper et al., 2015).

### *4.7.1 Sources*

Field and satellite observations suggest that breakouts were sourced from either 1) the base or part way up the lava flow margin or 2) large fractures extending back into the main channel. For some breakouts (particularly those in the southern lava flow that tended to be obscured by the eruptive plume in satellite images), the source region is difficult to determine. Some source regions were also sites of preferential degassing, with a white precipitate covering many of the nearby blocks (Fig. 4.6A) and associated gas plumes observed in 2012. Similar degassing was observed at stalled portions of the main channel (Fig. 4.6C).

Based on field observations of smaller breakouts from the base of the lava flow front (Fig. 4.6A), some breakouts sourced from this region emerged as small (~10 – 15 m tall) lava bodies that then underwent inflation and advance. In some cases, the area of main channel behind these breakouts drained to form an amphitheatre-like structure up to 10 m deep (Fig. 4.6A and 4.7). Amphitheatres are typically associated with the smallest breakouts, suggesting that they can provide only a limited lava supply (Fig. 4.7).

Other breakouts are sourced from fractures (≤4 m deep, 5 – 10 m wide) that can extend ~50 – 150 m metres back into the main channel (Fig. 4.6B). The satellite data showed that breakouts from fracture zones were preceded by the formation of lobes at the flow margin and extensional fractures (Fig. 4.1, Appendix 8A.18). Breakouts sourced from these fractured regions formed the largest breakout complexes (multiple potentially branched breakouts, up to hundreds of metres long).

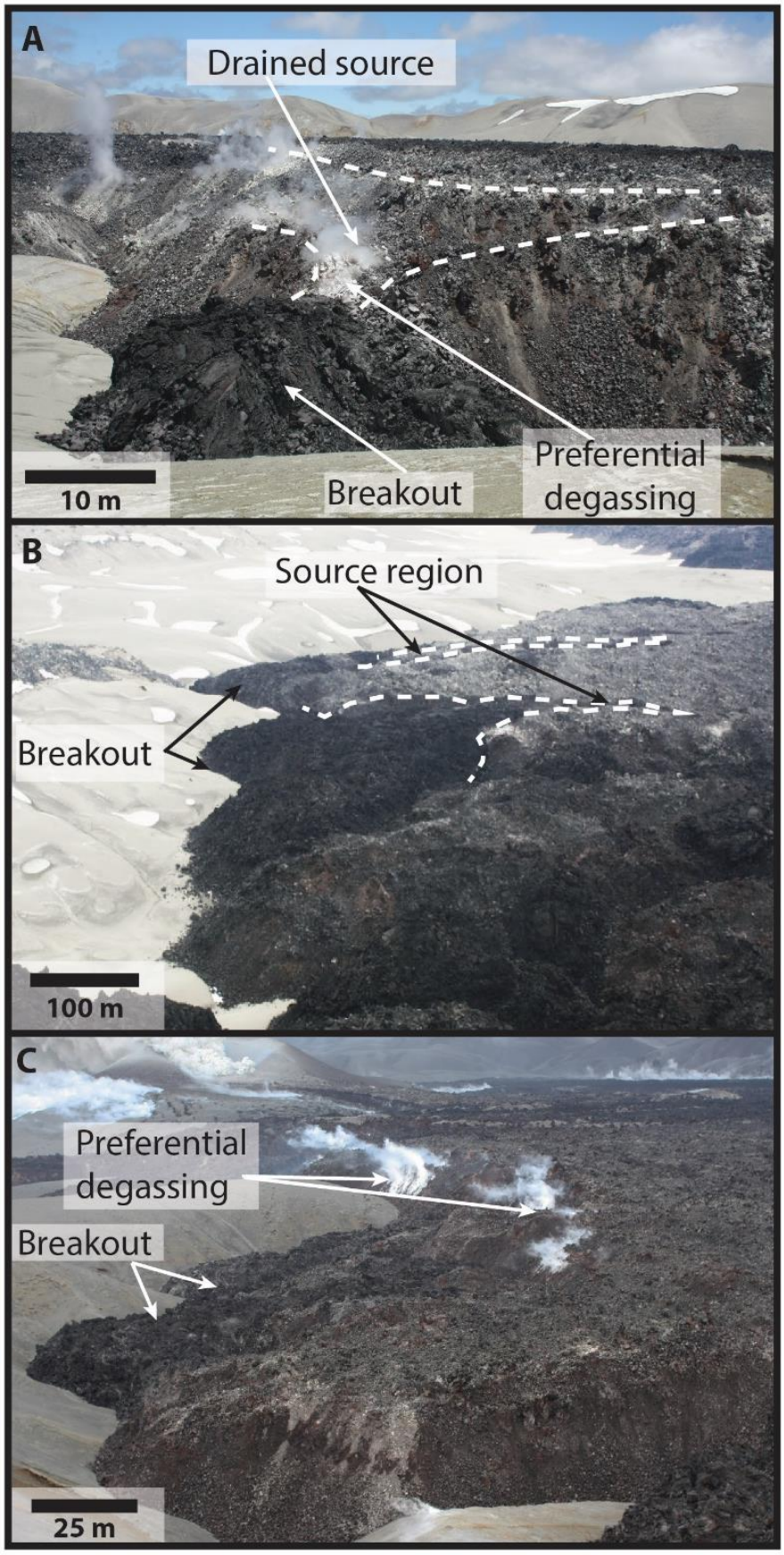
A
Drained source
Preferential degassing
Breakout
10 m
B
Source region
Breakout
100 m
C
Preferential degassing
Breakout
25 m

← Figure 4.6: (**A**) Base-fed breakout at the margin of Cordón Caulle's southern flow, in front of a drained amphitheatre. The drained region is a site of preferential degassing of the lava. (**B**) Aerial photo of a breakout that originated from a large fracture in the flow surface. This fracture can extend 50 -150 m back into the main channel and the breakout emerges from this fracture. (**C**) Basal fed breakouts from the flow margin. Note the preferential degassing at the flow front and behind the breakouts. Photo taken from a nearby ridge.

### *4.7.2 Morphologies*

The breakouts show a range of morphologies, which we describe in four general classes: domed, petaloid, rubbly, and cleft-split (Table 4.2, Fig. 4.8).

*Domed* breakouts are usually sourced from the base or part way up the lava flow margin (Fig. 4.7, 4.8). These breakouts have a domed shape and are wider than they are thick (Fig. 4.8). The surface comprises slabs (Table 4.1) of dark, glassy, surface crust (Fig. 4.7, 4.8), which retain a jig-saw fit pattern but are disrupted by fractures tens of metres long and several metres deep. Commonly, sections of the breakout have collapsed, to expose the lighter grey-coloured core lava.

*Petaloid* breakouts are steep sided and have an uneven surface due to a large number of upturned surface slabs (Fig. 4.8), which are up to ten of metres tall (Table 4.2) and can form prominent spines. Such spines have a dark, often polygonally jointed, glassy surface that grades into lighter coloured core lava. Regions between the slabs and spines are filled with rubble, and rubble forms a relatively narrow (<10 m) talus apron surrounding breakouts. The surface slabs of petaloid breakouts are more isolated than in domed breakouts, but locally retain jig-saw fit patterns.

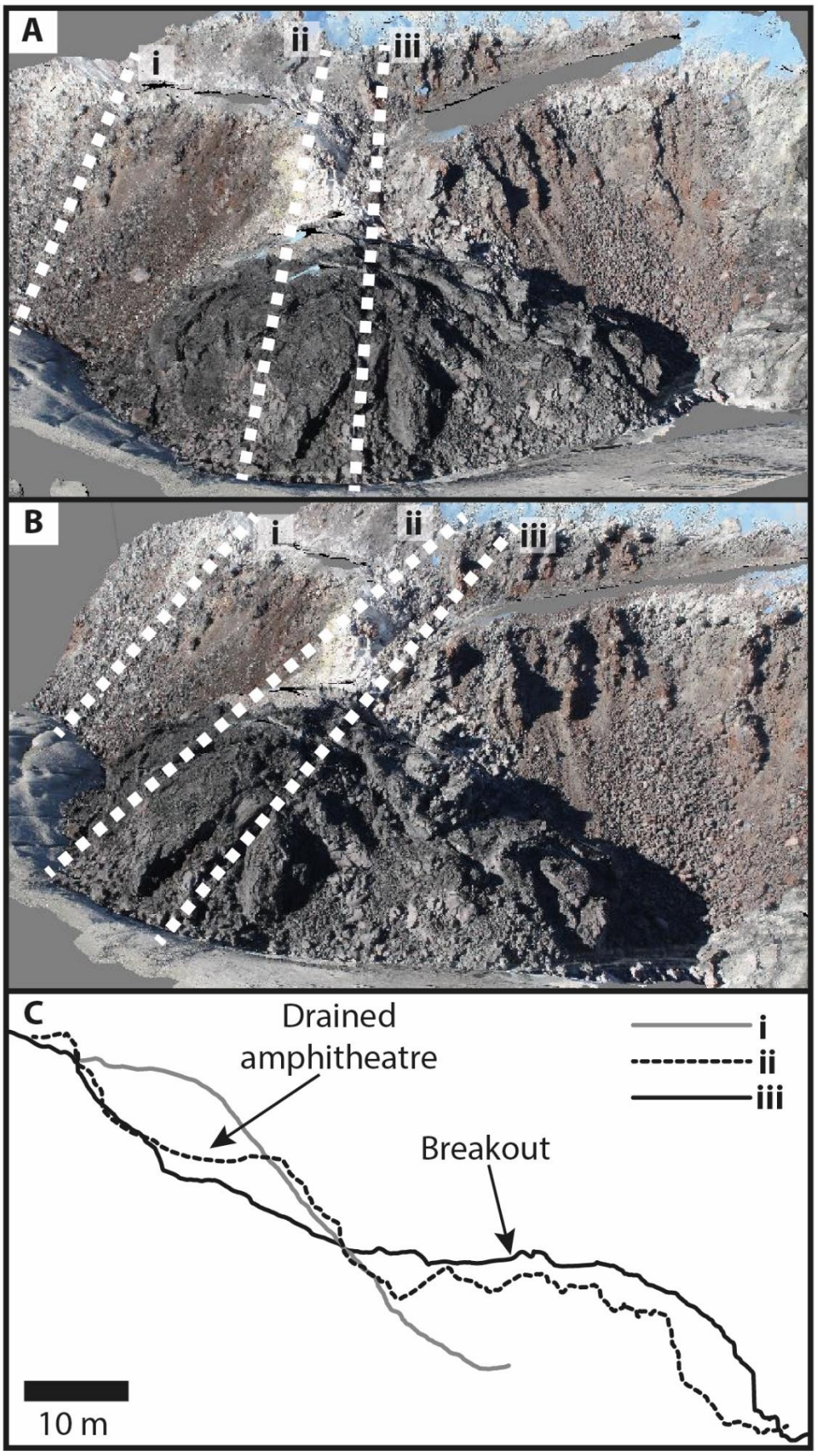
A
i
ii
iii
B
i
ii
iii
C
Drained
amphitheatre
Breakout
i
ii
iii
10 m

← Figure 4.7: 3D photogrammetry model of a domed breakout from the margin of the southern flow. Lines i, ii and iii show the approximate locations of the cross sections in **C**. The cross sections highlights a region of drained main channel behind the breakout. A section of main channel without a breakout is shown for comparison. A 3D PDF of this photogrammetry model can be found on the enclosed CD.

*Rubbly* breakouts have a surface that is almost entirely covered in rubble and disrupted surface sabs (Table 4.2, Fig. 4.8). The rubble comprises brecciated crust and core lava, with large rafted slabs that are similar to the surface slabs and spines observed in petaloid breakouts (Fig. 4.8), giving an uneven surface profile. However, slabs are sufficiently disjointed that any semblance of a jig-saw fit pattern is lost. Lateral collapses form larger talus aprons than around domed or petaloid breakouts (~20 – 40 m wide) and, in some cases, expose the lighter coloured core lava (Fig. 4.8).

*Cleft-split* breakouts have a large central cleft that is orientated parallel to the direction of advance, typically tens of metres long and several metres deep, and runs most, or the entire length, of the breakout (Fig. 4.8). Cleft surfaces are striated on a decimetre scale, marking repeated transitions from rough to smooth fracture surfaces. Outside of clefts, the breakout surface is comprised of either slabs or rubble (Table 4.2). Some of the most complex cleft-split breakouts are also branched and, in a few cases, formed subsidiary breakouts (Fig. 4.8).

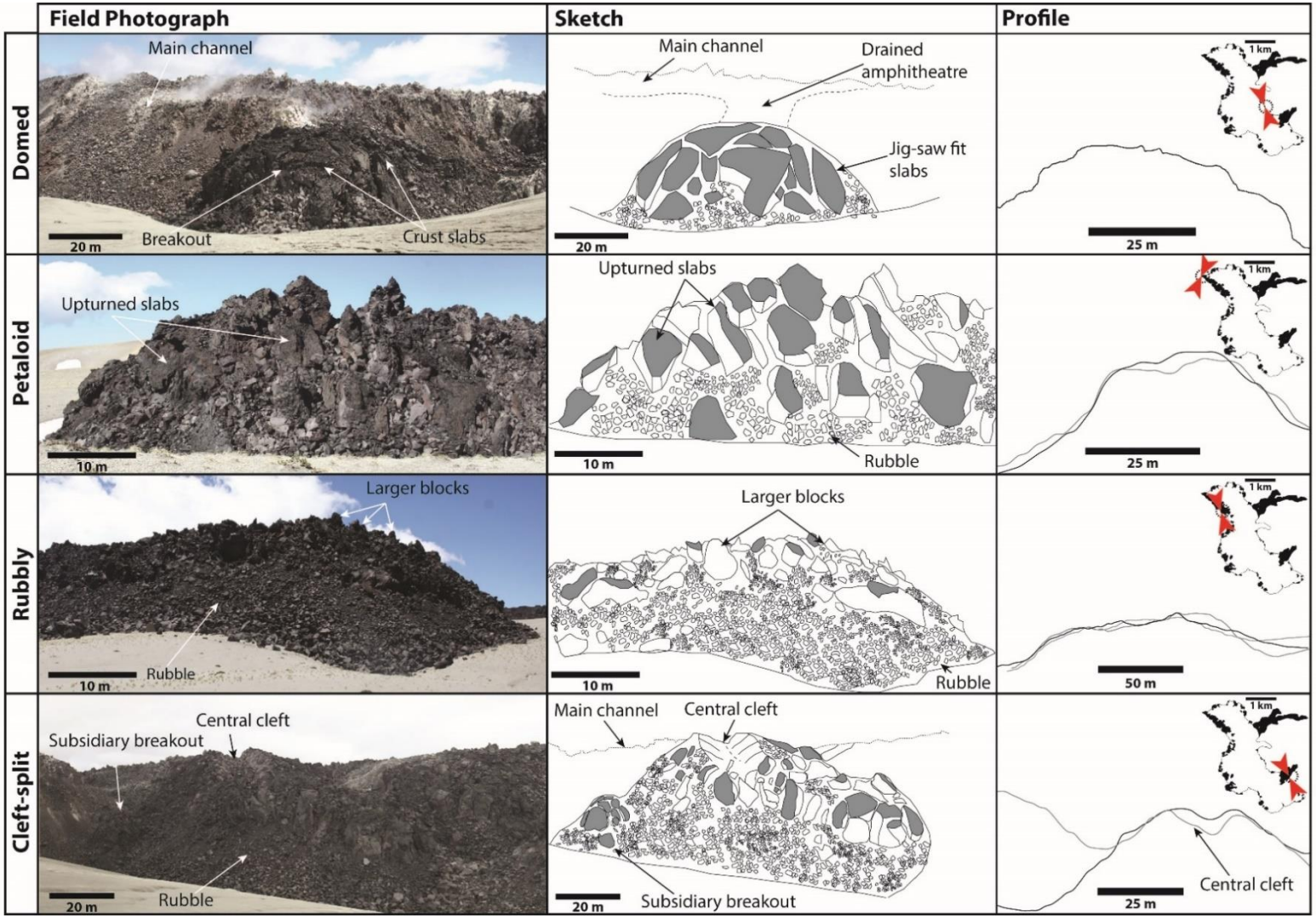
Field Photograph
Sketch
Profile
Domed
Main channel
Breakout
Crust slabs
20 m
Main channel
Drained amphitheatre
Jig-saw fit slabs
20 m
1 km
25 m
Petaloid
Upturned slabs
10 m
Upturned slabs
Rubble
10 m
1 km
25 m
Rubbly
Larger blocks
Rubble
10 m
Larger blocks
Rubble
10 m
1 km
50 m
Cleft-split
Central cleft
Subsidiary breakout
Rubble
20 m
Main channel
Central cleft
Subsidiary breakout
20 m
1 km
Central cleft
25 m

← Figure 4.8: Breakout morphologies with associated sketches, 2D profiles and location maps. The breakouts are categorised as domed, petaloid, rubbly and cleft-split. The profile for the domed breakout derives from a 3D photogrammetry model (Fig. 4.7), the others are derived from a Pleiades 1 m DTM, and the grey profiles are from similar breakout types. The red arrows in the sketch maps show the approximate locations of the breakouts and the orientation of the profiles. The clefts can be seen as a dip in the breakout profile, it is worth noting that the true depth of the cleft is unlikely to be resolved by the DTM (Appendix 8A). Details of the data gathered in the field can be found in Appendix 8B.

Table 4.2: Properties of the breakouts types (See Appendix 8B)

| Breakout type | Length (m) [a] | Width (m) [a] | Height (m) [b] | Volume ($m^3$) | Block size (m) |
|---|---|---|---|---|---|
| Domed | 15-80 | 15-100 | 15-30 | ~$4\times10^3$ - ~$2\times10^5$ | ~5-15 |
| Petaloid | 70-230 | 60-150 | 25-30 | ~$1\times10^5$ - ~$9\times10^5$ | ~5-10 |
| Rubbly | 110-2000 | 120-200 | 30 | ~$5\times10^5$ - ~$1\times10^7$ | ~1-5 |
| Cleft-split | 160-340 | 50-150 | 30-35 | ~$3\times10^5$ - ~$1\times10^6$ | ~1-15 |

[a] Measured from Google Earth imagery
[b] Measured from Pleiades DEM profiles

### *4.7.3 Lithologies*

Breakouts comprise dark, glassy lava with a black surface crust that grades into a lighter grey interior (Fig. 4.9A, 4.9B). In hand-specimen, the lava is vesicular, with a mixture of undeformed, near-spherical and more elongate flattened vesicles (Fig. 4.9C). Many of the vesicles display white walls, representing regions in which interstitial glass has been corroded from the groundmass during a vapour-phase cristobalite forming process (Schipper et al., 2015; Schipper et al., 2017), but these are not observed within the top few tens of centimetres of the surface crust. Flow-banding is also common, with lighter and darker bands typically a few millimetres thick but laterally extensive over tens of centimetres (Fig. 4.9B, 4.9D). Often, these bands are folded and wrap around vesicles (Fig. 4.10D).

A slightly different lithology was observed in one of the longest (400 m) rubbly breakouts at the western margin of northern channel. Here, the lava is glassy and has

a large population of white-walled, corroded vesicles, typical of breakout lava, but is also cut by the millimetre-spaced platy fractures (coated and partially filled with cristobalite) that are most commonly associated with the core of the main channel (Fig.

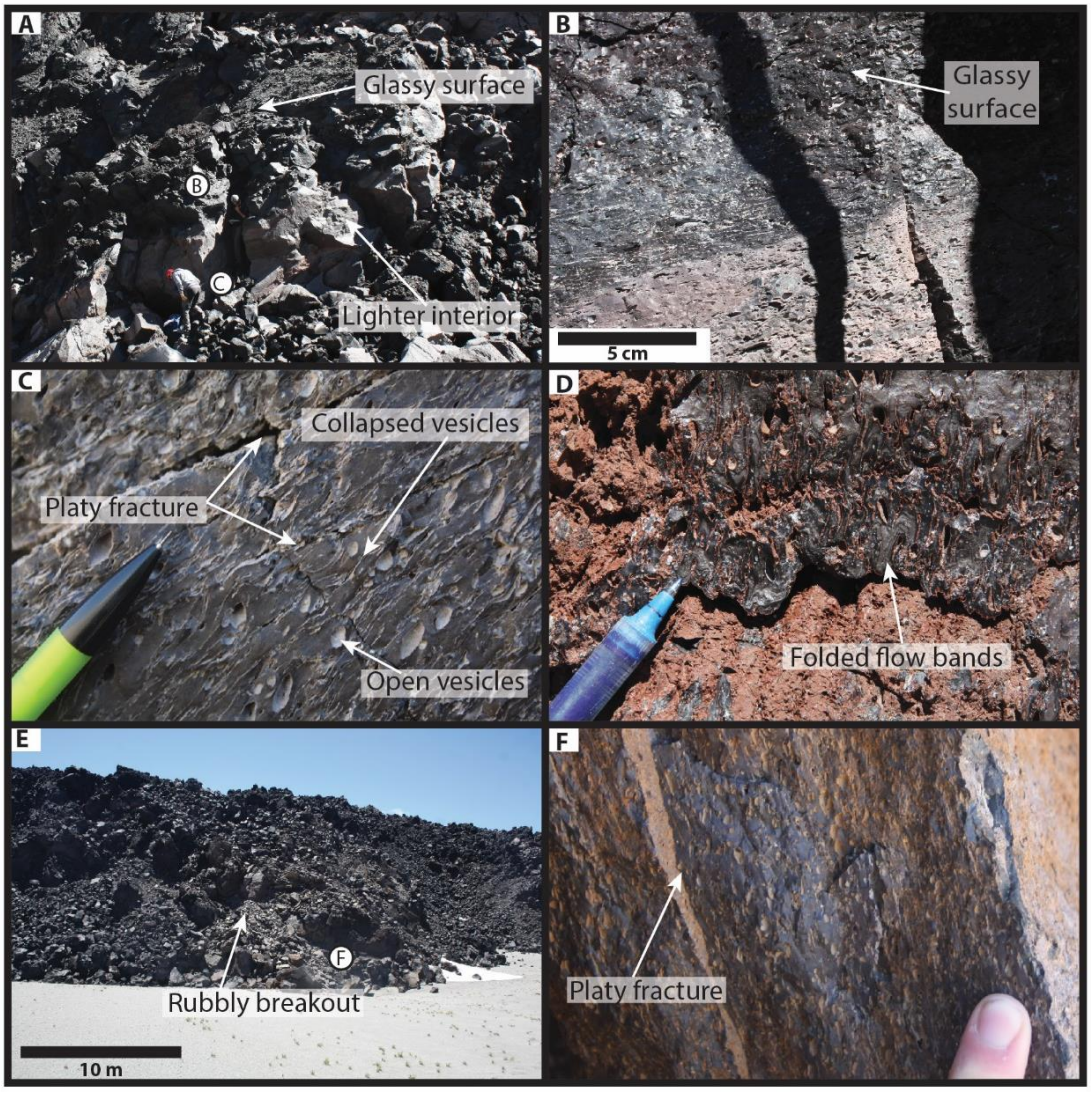


Figure 4.9: Breakout lava. (**A**) A surface slab at the front of a breakout, the darker surface is quenched glass while the interior is lighter in colour. (**B**) The contact between the glassy surface material and the lighter flow core. (**C**) The core of the breakout is lighter with a large number of cristobalite coated vesicles some of which are deformed or collapsed whilst others are undeformed and open. (**D**) Flow banded breakout lava in a fallen block at the flow front, the flow bands are extensively folded. (**E**) The base of a rubbly breakout, the vesicular rhyolite developed a small number of platy fractures similar to those observed in the crystalline flow core (**F**).

9F). The lithology represents an intermediate style between those of the fractured main channel core and the vesicular breakout lava.

### *4.7.4 Microstructure*

SEM images of breakout samples verify the presence of two vesicle populations and show three distinct crystal populations: phenocrysts, microlites and devitrification-related crystalline masses. For the purposes of this study, the phenocrysts (<5 volume% of the volume of the lava) will not be assessed further as they are unlikely to have had much, if any, influence on emplacement processes. The microlites are comprised primarily of plagioclase, some of which are subtly zoned (Fig. 4.10E), with some pyroxenes as well as accessory apatite and metal oxides (Fig. 4.10E). Microlites are 2 – 10 μm wide and 5 – 50 μm long, and typically aligned parallel to the flow-banding. They comprise 30 – 40 volume% (measured from four breakouts with petaloid, rubbly and cleft-split morphologies) in glassy flow-bands where devitrification crystallisation is absent. The microlite abundance varies slightly (~5 volume%) between individual millimetre to submillimetre bands.

Darker, spherical, crystalline masses (0.03 – 0.4 mm diameter, Fig. 4.10), some of which surround vesicles (Fig. 4.10C), are found in the core of breakouts. These crystalline masses are surrounded by small vesicles or fracture networks 1 – 2 μm wide but lack the radiating crystal structure commonly observed in spherulites and are best classified as globulites, which form as a result of devitrification (Lofgren, 1971a; Schipper et al., 2015). Globulites comprise ~70 volume% microlites (with overgrowths of 1 – 2 μm in width, Fig. 4.10F) and ~30 volume% cristobalite. Where globulites merge, they can form substantial flow-bands up to several centimetres thick. Globulites are observed in all breakout samples except those from the quenched surface carapace.

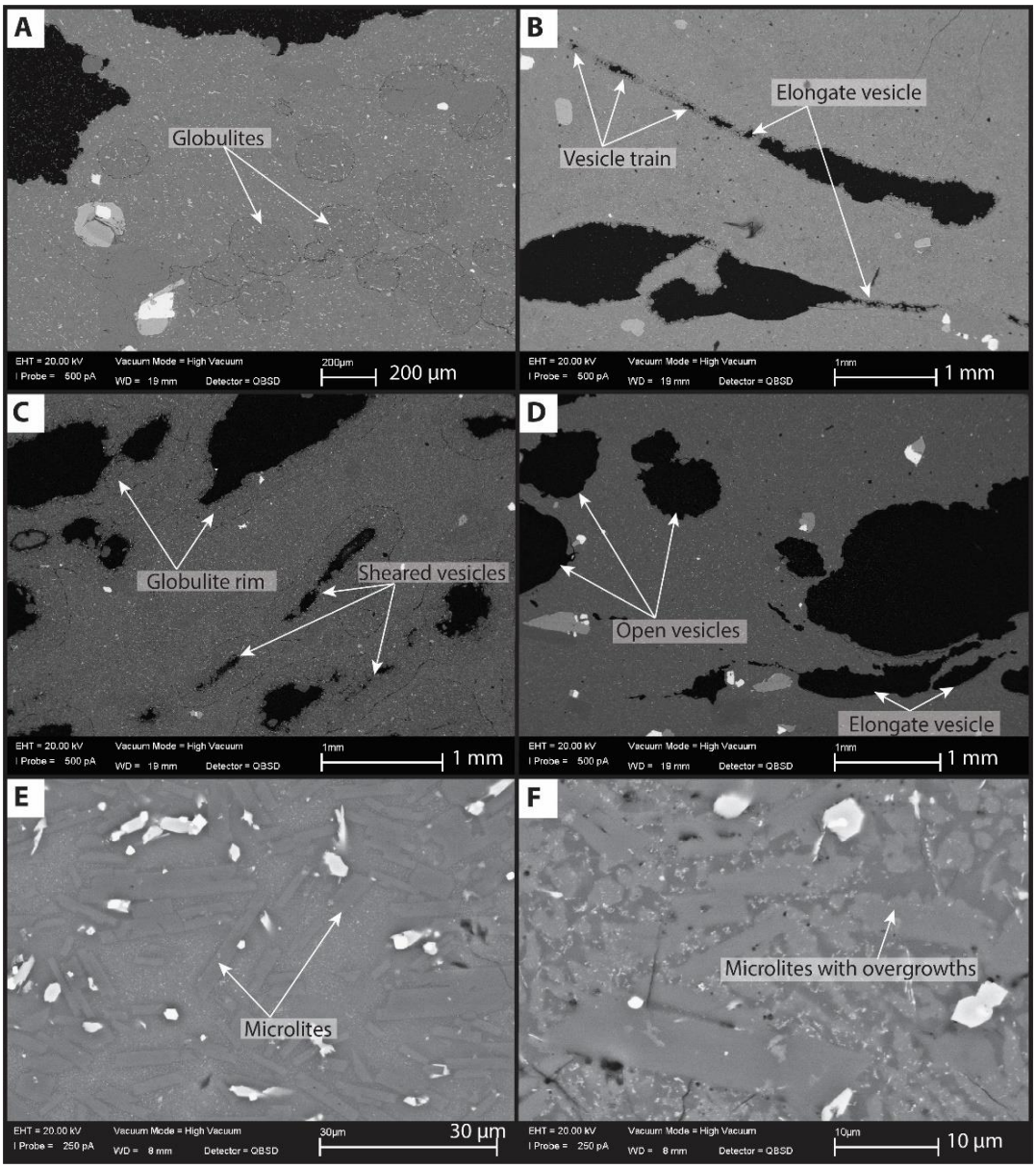


Figure 4.10: SEM images of breakout samples. (**A**) Globulites in glassy rhyolite. (**B**) Partially collapsed and elongate bubble trains in the quenched surface of a breakout. (**C**) Sheared vesicles with a rim of globulites material surrounding the vesicles. (**D)** More open and undeformed vesicles from the surface samples of a breakout, the vesicles lack the globulites rims. (**E**) Typical microlites in a glassy matrix of a breakout sample, some of these microlites have growth rims. (**F**) Microlites in the globulites have distinctive uneven overgrowths. The globulites are almost entirely crystalline and the space between the crystals is occupied with cristobalite.

The two vesicle populations comprise 1) sheared, partially collapsed vesicles and 2) spherical and relatively undeformed vesicles, both of which can be observed in hand specimen (Fig. 9C), thin section (Fig. 4.10B-D) and CT renderings (Fig. 4.11). Sheared vesicles are elongate (Table 4.1) and many are pinched at one end, suggesting partial collapse. Some form vesicle trails (Fig. 4.10B), but many are found in isolation (Fig. 4.10C). Sheared and collapsed vesicles are more abundant in samples from deeper in breakouts than at the surface. In contrast, spherical (Table 4.1) and undeformed vesicles (Fig.4. 9C, 4.10D, 4.11) are found throughout most breakouts but are more common near the surface and in flow-bands (Fig. 4.11A).

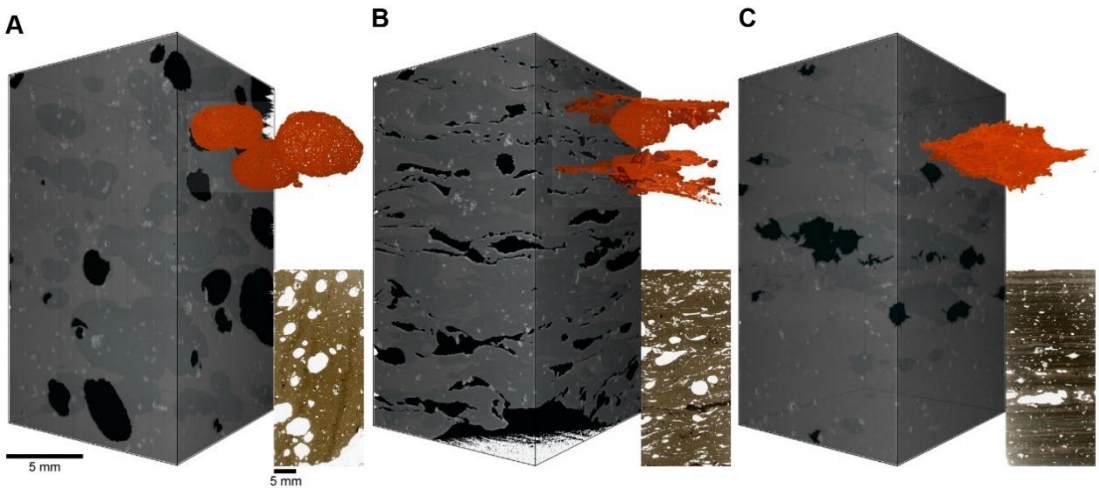


Figure 4.11. 3-D cT renderings and associated thin section scans of representative breakout samples. For each sample, main volume is rendered with solid lava in grey, with slight transparency to show internal pores within the volume. Red images show expanded view of selected pores. Subjacent frames show standard petrographic thin sections for each sample. (**A**) Breakout with little indication of shear or compaction, relatively glassy groundmass, and sub-spherical pores. (**B**) Moderately compacted breakout, with moderately crystalline and flow-banded groundmass. There are sub-spherical vesicles within this sample. (**C**) Highly compacted and crystallised core of a mature lobe. Note that despite nearly complete compaction/densification, the sample maintains a few vesicles. The ragged appearance of these surviving vesicles (red pore in **C**) is not an analytical artefact, but represents the actual roughness of the surviving pores.

Many of the vesicles located deeper within the breakouts have uneven walls (Fig. 4.11C) that have undergone partial preferential dissolution of interstitial groundmass glass due to gas flux through the vesicle network (Schipper et al., 2015). Dissolution leads to the formation of a diktytaxitic halo (0.05 – 0.22 mm wide) that results in their white-walled appearance in hand specimen (Fig. 4.10D). However, haloes are absent from vesicles in the uppermost (upper tens of centimetres) glassy carapace.

## 4.8 Discussion

With breakouts constituting ~12% of the final lava flow volume at Cordón Caulle, they represent an important component of the emplacement process. Furthermore, evidence from satellite images, field observations (Tuffen et al., 2013) and numerical modelling (Farquharson et al., 2015) indicate that they can remain active, and hence hazardous, many months after effusion ended.

### *4.8.1 Conditions for breakout formation*

For breakouts to form, the local conditions must evolve to favour the initiation of a new path for lava advance rather than continuing with the current scenario. This usually arises when flow front advance slows or ceases, despite continued lava supply from the vent, and can result in a change in the direction of lava propagation. More specifically, breakouts form when the internal pressure within the lava flow exceeds the local confining force, due to increased core pressure and/or decreased carapace strength. Carapace weakening is enhanced by lateral spreading of lava flow front lobes and higher effusion rates at the vent can increase core pressure by propagating an increased supply rate to the lava flow front, even if the front is still advancing. Within-flow crystallization (e.g. second boiling) can also pressurize the core by increasing the melt vapour pressure, leading to vesicle growth.

### *4.8.2 Breakout initiation*

At Cordón Caulle, both internal pressure increase and crustal weakening are likely to have contributed to breakout formation (Fig. 4.12). The internal pressure increase may also have weakened the surface crust due to inflation thinning the crust. The breakouts that formed from the completely stalled lava flow margins, in areas without clear crustal weakening such as the static margin of the southern channel (e.g. Fig. 4.6A, 4.7), suggest that the core pressure exceeded the yield strength of the surface crust, which, based on previous work is likely between $10^6$ and $10^8$ Pa (Griffiths and Fink, 1993; Bridges, 1997; Fink and Griffiths, 1998; DeGroat-Nelson et al., 2001; Magnall et al., 2017). Such pressure increases could have resulted from the continued supply of lava through preferential thermal pathways (or 'fluid pathways') beneath the static surface crust, representing Saffman-Taylor fluid instabilities between low and high-viscosity lava in the flow core (Anderson et al., 2005). Alternatively, smaller breakouts formed from static portions of the lava flow margins, where thermal pathways were likely absent or potentially only locally developed (Fig. 4.1), suggesting that more localised processes, such as margin collapse or late stage core vesiculation, could also have been important.

Late-stage vesiculation is suggested within most breakouts by the presence of a relatively undeformed vesicle population (Fig. 4.9C, 4.10, 4.11), with the limited deformation interpreted to reflect a short distance of flow, e.g. from breakout advance only. Consequently, these vesicles probably result from volatile exsolution either due to a pressure decrease during breakout extrusion, or potentially initiated by crystallisation occurring between the vent and lava flow front. Lava crystallinity increases from <25 volume% at the vent (as low as <5 volume% in some flow-top-pumice samples), to ~30 – 40 volume% in breakout samples. The increase in crystallinity as lava moved towards breakouts will have increased the volatile

concentration in the melt and potentially driven second boiling (Manley and Fink, 1987) or enhanced vesicle nucleation and growth, if the melt was already at volatile saturation. Some support for distal volatile exsolution from the lava flow core is provided by the observations of degassing plumes at the stalled lava flow front (Fig. 4.6C, 4.13) but, strictly, this is proof only of gas migration and escape, and concurrent vesicle growth for contributing to pressure increase can only be inferred. Nevertheless, this gas remobilization likely contributed to the precipitation of cristobalite throughout the lava flow (Schipper et al., 2015) and late-stage volatile exsolution, driven by in-flow

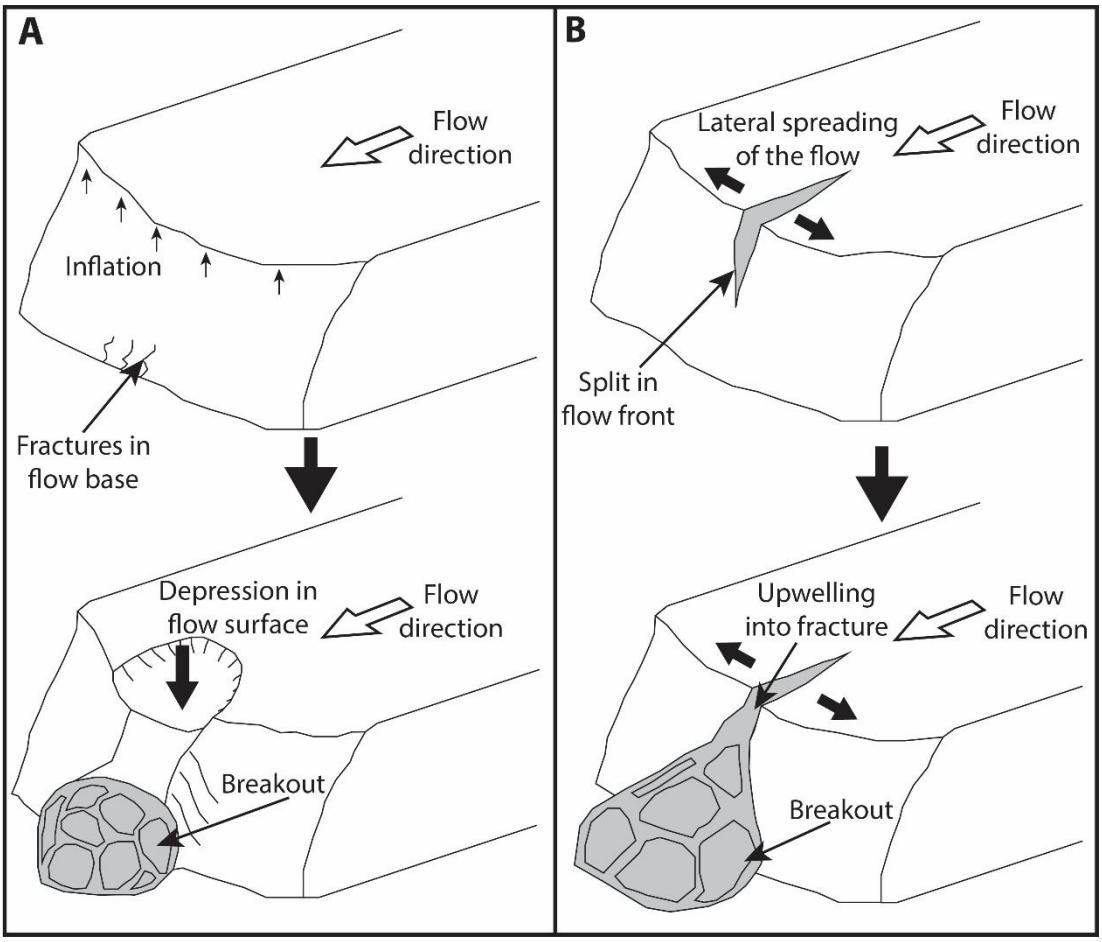


Figure 4.12: (**A**) Development of breakouts from the flow base or midway up the flow front, such as the breakout in Figure 5.6A. As the breakout emerges the main flow can become drained to form an amphitheatre-like structure. (**B**) The development of split fed breakouts such as in Figure 5.6B. A split forms in the flow surface related to flow front spreading or inflation of the flow front, the breakout emerges from the fracture.

crystallization, has also been inferred to form the vesicular layers observed in many prehistoric rhyolite lava flows (e.g. Fink, 1980b; Fink and Manley, 1987; Manley and Fink, 1987).

The large extensional fractures associated with lobe formation at the lava flow front were often preferential regions of breakout formation, with breakouts appearing to exploit the weakened crust (Fig. 4.6B, 4.12B). A similar process has been observed in laboratory experiments, where tensile surface fractures in a spreading and lobate analogue lava flow front enabled upwelling of the viscous core (Applegarth et al., 2010a).

### *4.8.3 Breakout evolution*

The growth and inflation of breakouts is inferred to have occurred through a combination of continued magma supply and vesiculation, with the smaller, morphologically simpler breakouts forming from less mobile areas of the lava flow (i.e. the lateral margins rather than the fronts; Fig. 4.1, 4.8). Small dome-like breakouts, some with a drained amphitheatre structure in the adjacent leveé (Fig. 4.6A, 4.12A, 4.13D) indicate a limited, locally-sourced magma supply. In these breakouts, vesiculation caused by decompression after extrusion from the main channel could have played a significant role in the overall inflation, with the observed vesicularities (15 – 30 volume%, Table 4.1) representing a potential contribution of order metres to inflation (or a lateral advance of order tens of metres). Decompression-driven vesiculation of breakout lava likely contributed to the formation of their scoriaceous and glassy surfaces (Fig. 4.9), which are similar to the surface carapaces observed at lava domes (Anderson and Fink, 1990). At Cordón Caulle, this glassy surface grades into the lighter, grey, breakout interior that contains abundant globulites (Fig. 4.10 A). Given that globulites form due to devitrification below the glass transition temperature

(Schipper et al., 2015), their growth is unlikely to have driven vesiculation within breakouts and they probably had negligible influence on breakout development.

As breakout inflation progresses, causing increased fracturing and upturning of surface slabs (Tuffen et al., 2013), we infer an evolution from domed to petaloid, rubbly then cleft-split morphologies (Fig. 4.8, 4.13). The striated surfaces of the resulting clefts mark repeated transitions from brittle fracturing to ductile tearing during the cleft opening (Forbes et al., 2012; Forbes et al., 2014). However, clefts do not have the centimetre-scale striations and convex sides typical of crease structures commonly observed at other silicic lava flows and domes, which suggests that the simultaneous upwelling and deformation of core lava associated with crease structure formation did not occur (c.f. Anderson and Fink, 1990; Anderson and Fink, 1992). We therefore propose that the formation of clefts within cleft-split breakouts is similar to that of “lava-inflation clefts” observed in basaltic pahoehoe tumuli, where a surface crust is buckled upwards by an increased core pressure (Walker, 1991). Nevertheless, in contrast to basaltic systems, we consider that late-stage vesiculation at Cordón Caulle provided an important contribution to this inflation.

The sustained advance of breakouts further promotes carapace brecciation, and breakouts that are active over timescales of up to months require the establishment of extended preferential thermal pathways to maintain a continued lava supply. In one of the longer rubbly breakouts, the observation of platy fractures suggests that sustained breakouts may begin to develop microstructure characteristics comparable with those of the main channel. With such characteristics not observed in smaller breakouts, it is likely that the presence of platy fractures reflects processes that occur only towards the end of the emplacement of long breakouts or substantial channels.

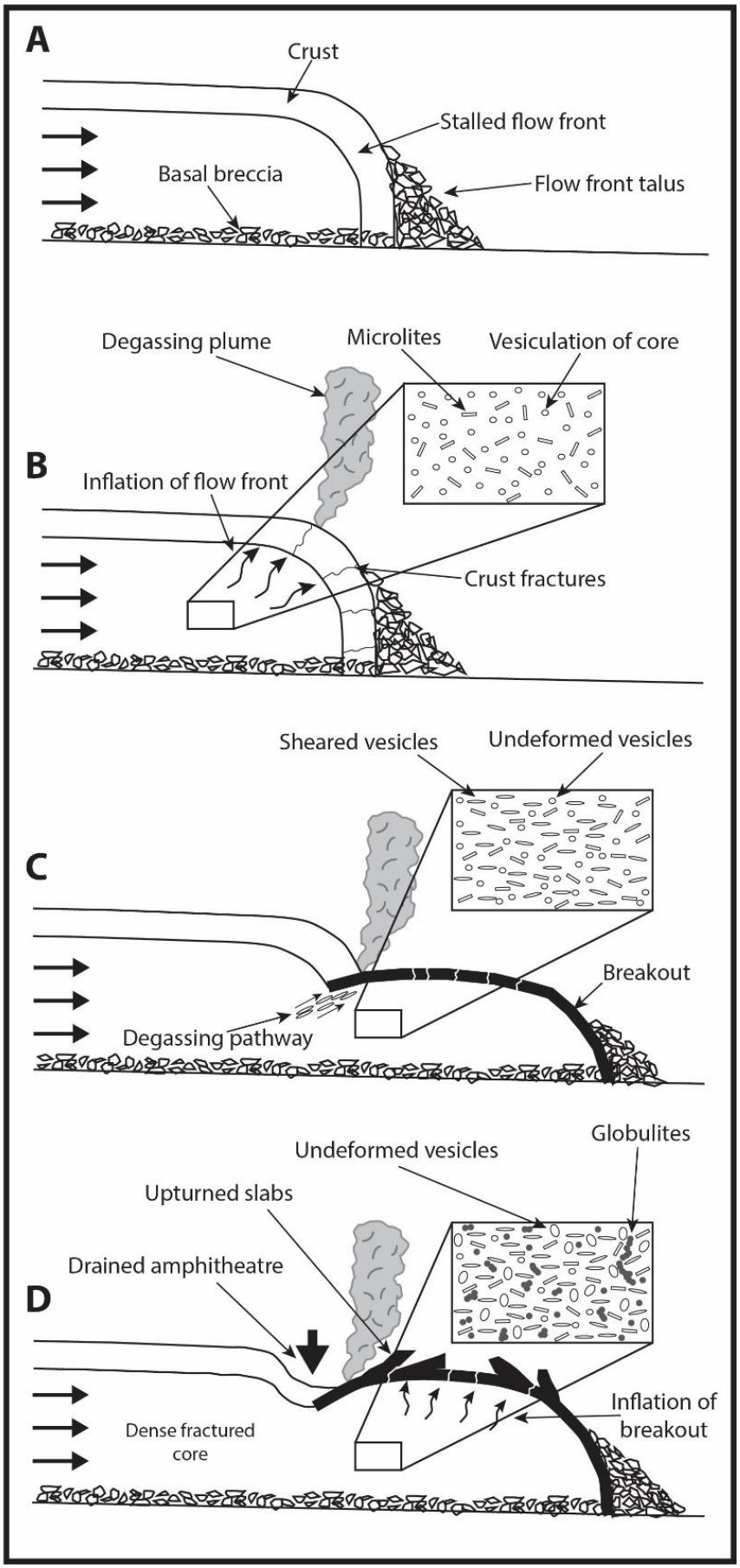
A
Crust
Stalled flow front
Basal breccia
Flow front talus
Degassing plume
Microlites
Vesiculation of core
B
Inflation of flow front
Crust fractures
Sheared vesicles
Undeformed vesicles
C
Breakout
Degassing pathway
Undeformed vesicles
Globulites
Upturned slabs
Drained amphitheatre
D
Inflation of breakout
Dense fractured core

← Figure 4.13: Cross section schematic of breakout formation. (**A**) The flow front stalls due to the strength of the cooled surface crust. (**B**) Material continues to be supplied to the flow front leading to inflation. Vesiculation of the flow core, partly driven by ongoing anhydrous crystallisation, applies pressure to the flow crust, causing it to fracture. (**C**) The crust fails and a breakout forms. As the breakout extrudes, some vesicles are sheared and partially collapse as volatiles escape from the lava. The drop in pressure during breakout formation leads to further vesiculation of the breakout surface. (**D**) As the breakout extrudes, sections of the main channel surface drained to form an amphitheatre behind the breakout. Continued supply to the breakout, coupled with core vesiculation, leads to inflation and upturning of surface slabs. Globulites form in the breakout core below the quenched surface crust, these have limited impact on the breakout development. The crystallisation history of the lava flow is shown in Appendix 8C.

The surface morphology of a breakout may also reflect the rate at which it grows, just as the transition from pahoehoe to 'a'ā lava can be driven by increased effusion and strain rates (Pinkerton and Sparks, 1976; Rowland and Walker, 1990; Cashman et al., 1999; Hon, 2003). In analogue experiments of silicic lava dome formation, low effusion rates (relative to cooling rate) aided surface crust formation and favoured of spiny or platy morphologies (Fink and Griffiths, 1998), whereas higher effusion rates created smoother and lower profiles (Fink and Griffiths, 1998). Thus, we propose that the larger volume rubbly and brecciated breakouts (Table 4.2) formed at higher supply rates than domed and petaloid breakouts, with higher supply rates facilitated by efficient preferential thermal pathways. Future work should attempt to systematically relate breakout properties (i.e. volume, effusion rate, rheology) to breakout morphologies and the transitions between different morphological types. Such work would likely combine analysis of breakout types, and comparisons to features generated in analogue experiments (e.g. Griffiths and Fink, 1993; Griffiths and Fink, 1997; Fink and Griffiths, 1998).

Finally, it is likely that breakouts did not all evolve independently, particularly those linked by preferential thermal pathways. For example, the onset of the formation of the large northeast breakout coincided with a decreased rate of new breakout initiation from the main northern lava flow (Fig. 4.1, Appendix 8A.18). This suggests that the supply of lava towards the northeast breakout reduced lava supply to the northern lava flow. Nevertheless, the drainage (or partial drainage) of preferential thermal pathways enabled continued formation and evolution (e.g. fracture growth) of some breakouts even after vent effusion had ceased (Fig. 4.3). The rubbly northeast breakout ultimately attained a final length of ~2 km and it represents an example of the challenge for hazard forecasting that late-stage breakouts present.

### *4.8.4 Breakout formation at other lava flows*

Breakouts are widespread in basaltic lava flow fields (e.g. Self et al., 1996; Anderson et al., 1999; Vye-Brown et al., 2013) where the process of continued flow beneath a static surface crust is a fundamental aspect of the inflation and growth of pahoehoe flow fields (e.g. Anderson et al., 1999; Vye-Brown et al., 2013) and is a recognized process in lengthening 'a'ā flow fields (e.g. Calvari and Pinkerton, 1998). In both basaltic and silicic lava flows, the continued supply of lava to a stalled lava flow front can generate breakout formation through driving a pressure increase and eventual rupturing of the surface crust (Pinkerton and Sparks, 1976; Blake and Bruno, 2000). However, in silicic lava flows, crystallization-driven late-stage vesiculation or vesicle growth is also likely to provide an important contribution to pressurisation. This process will not be as important in basaltic lava flows, where lower lava viscosities allow faster bubble migration (e.g. Vergniolle and Jaupart, 1986) and substantial vesicle loss can be measured with increasing distance from the vent (Cashman et al., 1994). However, vesiculation-driven inflation may play a minor role in the observed inflation of some

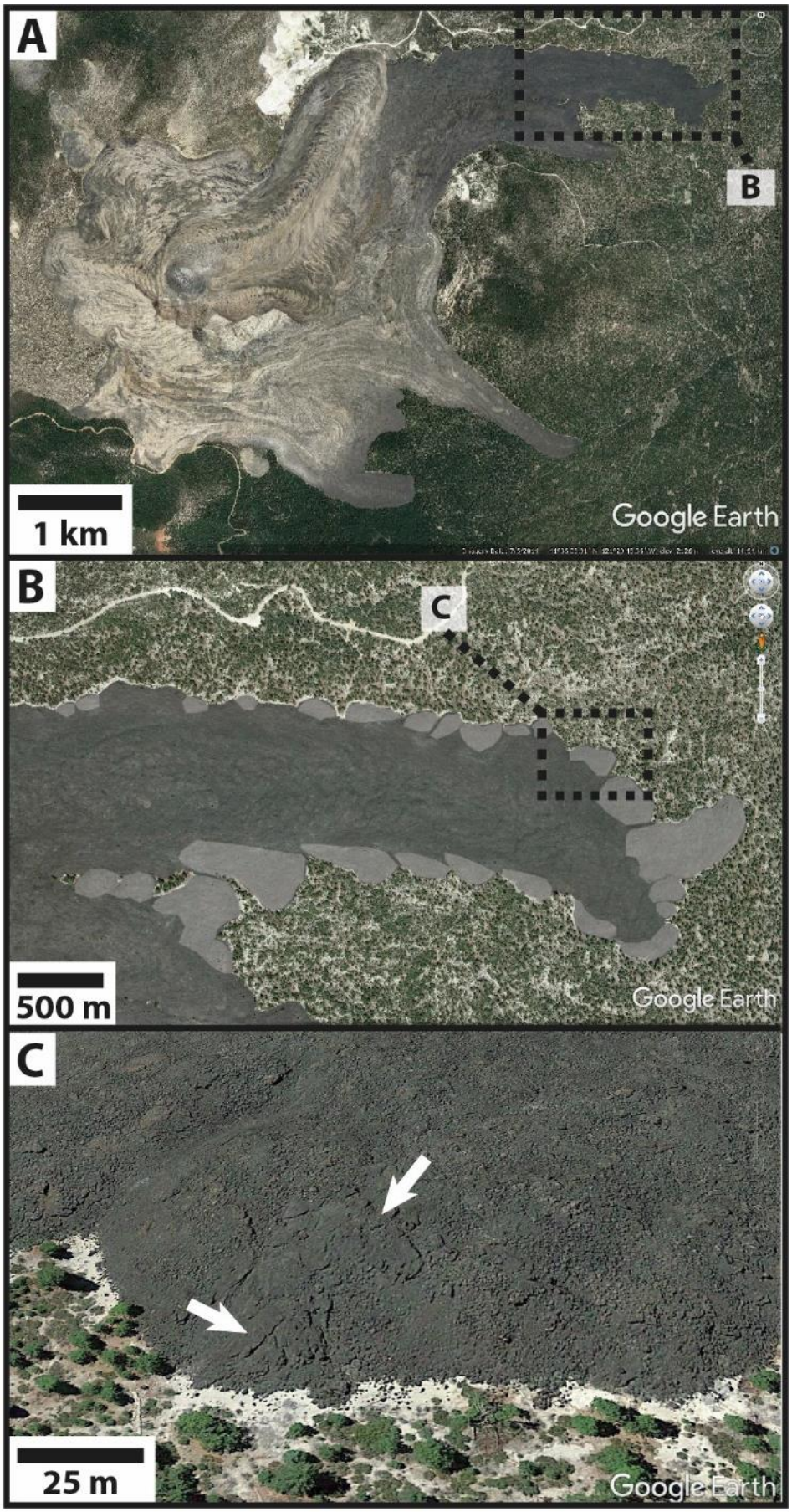
A
B
1 km
Google Earth
B
C
500 m
Google Earth
C
25 m
Google Earth

← Figure 4.14: Google Earth images of potential breakouts in the Big Glass Mountain Dacite-Rhyolite lava flow (Medicine Lake Volcano, California). (**B**) Shaded areas show potential breakouts from one lobe of the lava flow. (**C**) Arrows highlight a slabby and fractured area of the flow front that is similar in appearance to the breakouts at the Cordón Caulle lava flow.

mafic lava flows and lava lakes (e.g. Peck, 1978; Stevens et al., 2001). Due to the higher viscosities of silica-rich lavas preventing easy gas loss, pressure can rise with important hazard considerations. Not only can it enhance the potential for breakouts, it can lead to explosions from the surface of a lava flow (Jensen, 1993; Castro et al., 2002a), and has the potential to drive collapse of the front of a silicic lava (Baum et al., 1989; Calder et al., 2002), rapid core decompression, and the possible generation of pyroclastic density currents (Fink and Kieffer, 1993).

The prevalence of breakouts in silicic lava flows may be currently underestimated, and other likely candidates are also observed in an earlier eruption at Cordón Caulle (1960). One of the 1960 lava flows has a thin lobe (800 m long and 80 m wide, Lat: 40.542765° S, Long: 72.235110° W) with an overall morphology similar to the northeast breakout (Fig. 4.1). At the front of this rubbly lobe, a domed and slabby secondary breakout (~50 m in diameter) is observed and appears similar to the domed and petaloid breakouts of the 2011-2012 lava (Fig. 4.8). In some of the large rhyolite lava flows in the western USA, lobes have also been identified at lava flow fronts and lateral margins (Bonnichsen and Kauffman, 1987; Manley, 1992, 1996) but they have not been discussed in terms of breakout processes. The margin of the dacitic portion of Glass Mountain at Medicine Lake Volcano (California) has a particularly pronounced lobate flow front, and satellite images show that some lobe surfaces are partially comprised of large fractured slabs, similar to the domed and petaloid breakouts at Cordón Caulle (Fig. 4.8, 4.13). Unfortunately, the age of the Glass Mountain lava (several thousand years) makes definitive identification of breakouts challenging in remotely sensed data

but, similarly, over the five years following emplacement at Cordón Caulle, ash removal from the main channels has reduced their contrast with breakouts in satellite imagery, making some breakouts almost indistinguishable (Fig. 4.3). Although the Cordón Caulle lava flow has a similar lobate morphology to the dacitic portion of Big Glass Mountain (61.3 – 67.3% $SiO_2$, Donnelly-Nolan et al., 2016), it is substantially different from the rhyolitic portion (70 – 75% $SiO_2$, Donnelly-Nolan et al., 2016), which lacks such a lobate margin (Fig. 4.12). This difference could suggest that emplacement processes for the Cordón Caulle lava flow have more in common with those of glassy dacitic flows than some higher silica rhyolite flows.

Although breakouts are not readily identifiable at most other rhyolite lava flows, other emplacement features have been linked to late stage vesiculation. In many higher silica (>70% $SiO_2$) rhyolites, diapirs of coarsely vesicular pumice (Fink, 1980b, 1983; Fink and Manley, 1987) are thought to form due to bubble growth in the core of the lava flow (Manley and Fink, 1987; Furukawa and Uno, 2015) and could represent a vertically-orientated equivalent of lateral breakouts. Similarly, the formation of large gas cavities capable of triggering small explosions (DeGroat-Nelson et al., 2001; Castro et al., 2002a), is thought to be caused by the accumulation of gas in a layer directly beneath the surface crust (Jensen, 1993; Castro et al., 2002a). The late stage vesiculation inferred at Cordón Caulle did not lead to any observed pumice diapirs or substantial gas cavities, and further work could explore whether the small compositional differences between Cordón Caulle and more silica-rich rhyolites are responsible for observed differences in late-stage evolution.

## 4.9 Conclusions

The 2011-2012 rhyolite lava flow at Cordón Caulle generated ~90 breakouts and provided the first observations of breakout processes during such an eruption. Our

multi-scale analyses have enabled a morphological classification of rhyolite breakouts and given insight into their importance as part of the emplacement of silicic lava flows:

- Breakouts are likely initiated by a combination of pressure build-up in the core of the lava (due to continued lava supply and vesiculation, partly driven by in-flow crystal growth), and fracturing of the surface crust (due to spreading of the lava flow front and lobe formation).
- At Cordón Caulle, breakouts developed into a sequence of morphologies from domed, petaloid, rubbly, to cleft-split, which reflected their evolving stages of growth and inflation. Inflation is inferred to be driven by both lava supply and vesiculation within the core of a breakout, and was responsible for the breakup of surface slabs and the formation of inflation clefts. Breakout morphology may also reflect the rate of extrusion.
- The presence of active preferential thermal pathways, supplying fresh lava beneath a stationary lava crust, was indicated by continued formation and growth of breakouts after advance of the main flow had ceased. The potential presence of such pathways should be considered in the interpretation of emplacement processes at other laterally extensive rhyolite lavas.
- The evidence for late-stage vesiculation in breakouts has substantial hazard implications, with volatile accumulation potentially leading to surface explosions or flow front collapse and possible pyroclastic density currents.

The processes of breakout formation and lava supply through preferential thermal pathways, that we have showed for a rhyolite lava, are well-studied in mafic lava flows, and direct comparisons can be made across the compositions. However, in rhyolites the driving effects of late-stage vesiculation is likely to be strongly enhanced with respect to in basalts, due to the high-viscosity inhibiting pressure release and vesicle migration.

## 4.10 Acknowledgements

NM is supported by a NERC ENVISION studentship and a BUFI grant from the British Geological Survey. HT is supported by a Royal Society University Research Fellowship. CV-B publishes with the express permission of the executive director of the British Geological Survey. CIS acknowledges access to the Australian Synchrotron's IMBL granted under proposals 2014/1-M7574 and 2017/1-M11688, with travel support from the New Zealand Synchrotron Group Ltd. JMC is supported by the VAMOS research centre, University of Mainz. We gratefully acknowledge the assistance of Gren Turner (British Geological Survey) with SEM imaging of the thin sections. We also wish to thank the BBC Earth team for assistance with aerial photography of the lava flow. EO-1 data were obtained via NASA's Volcano Sensor Web at the Jet Propulsion Laboratory – California Institute of Technology, Pasadena, CA. EO-1 was managed by the NASA Goddard Space Flight Center, Greenbelt, MD. We gratefully acknowledge editorial handling and helpful comments from Brad S. Singer and Jocelyn McPhie, and constructive reviews from Jonathan Fink and an anonymous reviewer.

# 5 Lateral breakouts or core upwelling? Contrasting late-stage evolution of silicic lava flows

N. Magnall[1], M.R. James[1], H. Tuffen[1], J. Fink[2], S. Anderson[3], E. Lev[4], C. Vye-Brown[5]

*[1]Lancaster Environment Centre, Lancaster University, Lancaster, UK*

*[2]Department of Geology, Portland State University, Portland, USA*

*[3]Mathematics and Science Teaching Institute and Earth Science Department, The University of Northern Colorado, Greeley, USA*

*[4]Lamont-Doherty Earth Observatory, Palisades, USA*

*[5]British Geological Survey, The Lyell Centre, Edinburgh, UK*

The following paper, at the time of writing, is currently in preparation for submission to Journal of Volcanology and Geothermal Research. Processing and analysis of remote sensing data, field data, microstructural characterisation, and quantitative modelling, as well as the bulk of the writing of the manuscript, was conducted by myself. All authors aided in the conception of the project and with writing and editing of the manuscript. Mike James and Hugh Tuffen aided with fieldwork as well as the interpretation of remote sensing and microstructural data. Jon Fink and Steve Anderson aided with fieldwork in the USA as well as the interpretation of the observed features, Einat Lev assisted with collection of the UAV survey data of lava flows in the USA, and Charlotte Vye-Brown aided with SEM imaging of samples. The detailed methodology for this paper can be found in the appendices: Appendix 8A details the remote sensing techniques used, Appendix 8B expands on the data gathered in the field, and Appendix 8C outlines the microstructural analysis techniques used.

The paper aims to understand the conditions that may favour the formation of breakouts in some rhyolite lava flows, and core upwelling to the surface of the lava in others. The study contrasts observations of Cordón Caulle and Medicine Lake

(California) silicic lavas to determine the processes that contribute to core upwelling in many rhyolitic lava flows. We further assess the timescales of diapir upwelling to demonstrate the influence that lava rheology may have on the ability of lava to upwell to the surface of a lava flow.

The approach taken yielded insights into the conditions that may favour, or prohibit, core upwelling in silicic lava flows:

- Pumice diapirs form in crystal-poor, high-silica rhyolite lavas (>70% $SiO_2$), in response to the opening of a crease structure, buoyant rise of a vesicular body, or a pressure increase within the flow core.
- In contrast to previously studied rhyolites in the USA, limited core upwelling was documented at Cordón Caulle. This upwelling was associated with the formation of large surface fractures at a spreading portion of the flow, suggesting that the surface crust of the Cordón Caulle lava flow was, for the most part, sufficiently strong to inhibit upwelling.
- The crystal content of the Cordón Caulle lava flow, and the consequent effect on lava rheology, may have impeded the formation of pumice diapirs. The associated higher viscosity may have acted to limit vesicle growth, as well as slowing the ascent rate of vesicular core lava to timescales greater than flow emplacement and cooling.
- Where core upwelling is impeded, vesiculation of the flow may be more likely to contribute to a pressure increase in the flow core, forming breakouts if the flow front has stalled or slowed.

## 5.1 Abstract

The complexity of emplacement processes in silica-rich lava flows results in cascading hazards that can augment the hazards of lava inundation with events such as surface explosions and pyroclastic flows from collapsing flow fronts. However, our understanding of emplacement processes and the controls on associated hazards is based on feature interpretations from a limited number of ancient rhyolites (e.g. crease structures and pumice diapirs at Medicine Lake Volcano, California). Here, we integrate new observations of breakouts from the 2011-2012 Puyehue-Cordón Caulle rhyolite with observations of classic features on US silicic flows, to provide new insights into the emplacement dynamics and associated hazards of silicic lava flows.

We use a combination of aerial and satellite imagery, field studies, and microstructural characterisation to assess the factors controlling crease structure and pumice diapir formation. Field observations suggest that pumice diapirs form only in crystal-poor rhyolite lavas, driven by either passive upwelling into opening extensional crease structures, or by buoyant diapiric upwelling of a vesicular layer from the flow core. We identified only two sites of fracture-associated upwelling at Cordón Caulle, and propose that the formation of crease structures and pumice diapirs may have been locally inhibited by a strong and continuous surface crust. We further suggest that the crystallinity, and consequent greater viscosity (~$10^9$ – $10^{10}$ Pa s), of the Cordón Caulle lava flow compared to the crystal-poor rhyolites at Medicine Lake (~$10^8$ Pa s) could slow and impede bubble growth rates and, thus, the development of pumice diapirs. Models of diapir rise give expected upwelling rates that are one to two orders of magnitude slower at Cordón Caulle compared to crystal-poor rhyolites. Breakout formation or flow front collapse will be promoted when pressure increases within the flow core, either due to volatile exsolution or continued lava supply to a stalled flow

front, cannot be mitigated by upwelling. This leads to increased potential for pyroclastic density current generation.

## 5.2 Introduction

The emplacement of rhyolitic lava flows is typically modelled as the slow spread and collapse of crystal-poor domes, without the complexities of cooling-limited behaviour such as breakout formation (e.g. Fink, 1983; Manley, 1992; Castro et al., 2002b). However, observations of the 2011-2012 eruption of Cordón Caulle, Chile (Fig. 5.1), show the potential importance of such complexities, with ~12% of the flow ultimately comprised of flow margin breakouts (Tuffen et al., 2013; Farquharson et al., 2015; Magnall et al., 2018), and likely more had the eruption continued. Such breakouts contribute a significant hazard, complicating estimates of lava inundation area, as well as contributing to collapse of the front of the lava flow (Tuffen et al., 2013; Magnall et al., 2018). Further hazards associated with emplacement of silicic lava flows relate to pressurisation of the flow interior, driven by gas accumulation (Fink and Manley, 1987; Baum et al., 1989; Fink and Kieffer, 1993). In some cases this pressurisation can lead to flow front collapse, explosive decompression of the flow core, and the generation of a pyroclastic density current (Fink and Kieffer, 1993). Similar late stage vesiculation and pressurisation of the flow core was also inferred for Cordón Caulle but, in this case, instead contributed the initiation of breakouts (Magnall et al., 2018).

The accumulation of gases in a rhyolite lava flow can also lead to localised buoyant upwelling of vesicular core lava, and extrusion of a diapir onto the surface of the lava flow. Such diapirs, formed of coarsely vesicular pumice (CVP), are believed to be common in these lavas (Fink, 1980b; Baum et al., 1989; Anderson and Fink, 1990, 1992; Fink, 1993). However, CVP diapirs are not observed at the Cordón Caulle lava flow, suggesting that the core of the lava did not vesiculate to the same degree as in other rhyolite lava flows, potentially limiting the hazards posed from explosive decompression.

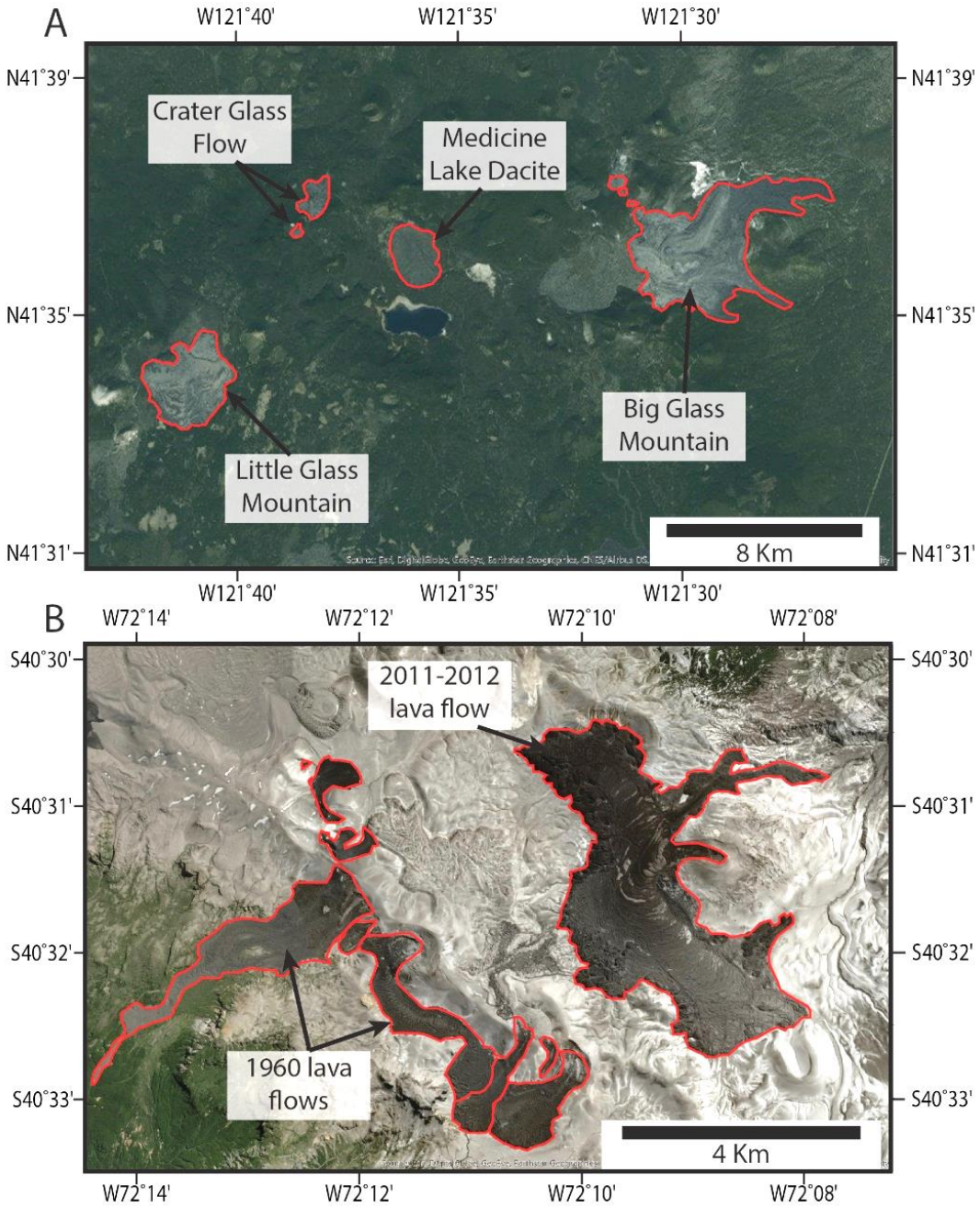


Figure 5.1: (**A**) Location of lava flows at Medicine Lake Volcano, Northern California, USA. (**B**) Rhyolitic lava flows from the 1960 and 2011-2012 eruption of Puyehue-Cordón Caulle, Chile. Images derived from ArcGIS base map imagery.

The relationship between core upwelling and breakout processes in rhyolitic lavas should be better understood to ensure these processes can be considered

appropriately within hazard assessments. Here, we review the existing understanding of core upwelling in silicic lava flows and, through structural analysis and quantitative modelling, we propose that lava rheology, including the development of a strong surface crust, is a key factor in determining whether a flow will form breakouts or develop surface features such as CVP diapirs.

Previous studies on Holocene silicic lavas in the USA (Fig. 5.1, 5.2) have used observations of crease structures (Anderson and Fink, 1990, 1992) and CVP diapirs (Fink, 1980b, 1983) as evidence for core upwelling, as well as for the spreading and fracturing of a surface crust. Crease structures are common across the surface of many silicic lava flows, but CVP diapirs are found exclusively at the most silica-rich and crystal-poor rhyolite flows and domes, such as those found at Medicine Lake Volcano in California (Fink, 1980b, 1983; Fink and Manley, 1987). Large gas cavities are also observed at the surface of many of these flows and form due to gas accumulation in association with a buckling surface crust. Gas cavities can vent explosively from the surface of a lava flow, presenting a considerable hazard (Jensen, 1993; Castro et al., 2002a), but these features have not been observed at Cordón Caulle.

In contrast, observations at the 2011-2012 Puyehue-Cordón Caulle rhyolite flow have revealed few crease structures, no pumice diapirs, and no gas cavities. Furthermore, the prevalence of breakouts at Cordón Caulle raises the possibility that the generation of breakouts or CVP diapirs could be mutually exclusive and compositionally dependent. Given that breakouts can attain substantial lengths (e.g. 2 km, Magnall et al., 2018), determining the conditions that favour breakout formation, rather than core upwelling to the surface, is important for improving our understanding of silicic lava

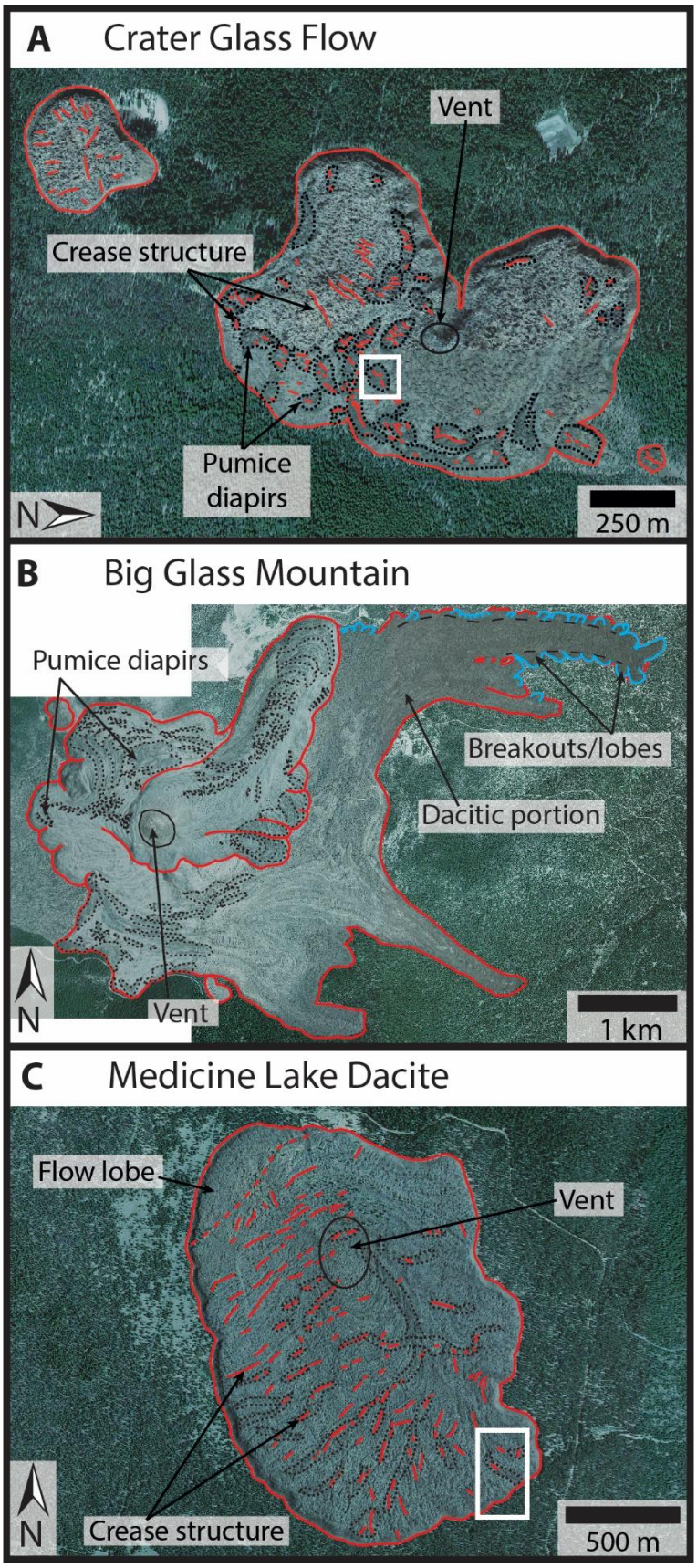
A
Crater Glass Flow
Vent
Crease structure
Pumice diapirs
N
250 m
B
Big Glass Mountain
Pumice diapirs
Breakouts/lobes
Dacitic portion
N
Vent
1 km
C
Medicine Lake Dacite
Flow lobe
Vent
N
Crease structure
500 m

← Figure 5.2: Aerial images of the dacite and rhyolite lava flows from Medicine Lake Volcano, California. (**A**) The crater Glass Flow. Black dashed lines highlight pumice diapirs, red lines show crease structures and the white box shows the location of Figure 5.7. (**B**) Big Glass Mountain dacite-rhyolite lava flow. Black dashed lines highlight pumice diapirs and blue lines highlight possible breakout lobes in the dacitic portion. (**C**) Medicine Lake dacite lava flow. Black dashed lines highlight the coherent surfaces around crease structures, red lines highlight the crease structures and the white box shows the location of Figure 5.6. Imagery from the National Agriculture Imagery Program (NAIP).

emplacement processes and their associated hazards. Furthermore, given the potential for vesiculation-driven pressurisation of the core of a rhyolite lava flow, it is important to examine the processes that may favour or hinder core vesiculation. Here, we build on previous work (Fink, 1980b, 1983; Fink and Manley, 1987; Manley and Fink, 1987; Baum et al., 1989; Anderson and Fink, 1990, 1992), by first describing the geological settings of the silicic flows studied and giving an overview of their lithologies and structural features (i.e. pumice diapirs and crease structures). We then describe the methods used to characterise such features on flows at Medicine Lake Volcano, and identify comparable examples at Cordón Caulle. Finally, we discuss the conditions that either favour or inhibit core upwelling, and explore the hazard implications of these processes.

## 5.3 Geological settings and lithological overview

We focus on silicic lava flows from Medicine Lake Volcano (California), and Puyehue-Cordón Caulle (Chile), but also provide some additional data on flows from South Sister volcano, Newberry Caldera (both Oregon), and Mono-Inyo domes (California) in Table 5.1 for comparison.

### *5.3.1 Medicine Lake, USA*

Medicine Lake Volcano is a broad shield volcano located on the eastern edge of the southern Cascades, in northern California (Donnelly-Nolan et al., 2016). The volcano has produced numerous lava flows ranging in composition from basaltic to rhyolitic (Fig. 5.1A). Three main Late Holocene eruptive episodes occurred at ~1 ka, ~3 ka, and ~5 ka (Donnelly-Nolan et al., 2016). We focus on the Glass Mountain dacitic-rhyolitic lava flows and domes, and the Little Glass Mountain and Crater Glass lava flows, all erupted between 950 and 1230 years ago; and the Medicine Lake Glass Flow, erupted during the ~5 ka episode (Donnelly-Nolan et al., 2016).

The complex Glass Mountain eruption began with a rhyolitic Plinian tephra fall from a 5 km long, NNW-trending fissure (Heiken, 1978), followed by emplacement of ~1 $km^3$ of lava (Donnelly-Nolan et al., 2016). The first lavas to appear were rhyolite domes along the fissure. The eruption soon consolidated to a single point source under what is now Glass Mountain. The first lobes of Glass Mountain were dacitic (61 – 69% $SiO_2$) in composition and had a substantial crystal population (Eichelberger, 1975; Donnelly-Nolan et al., 2016). The lava flow is multi-lobed, up to ~6 km long, and ~40 m thick (Fig. 5.1A, 5.2B). Later erupted lava was rhyolitic in composition (70 – 74.6% $SiO_2$) and the youngest lava lobe is ~3 km long and 70 – 100 m thick.

The Little Glass Mountain and Crater Glass rhyolite flows (72.6 – 74.3% $SiO_2$) erupted ~50 years prior to the Glass Mountain eruption. The eruptive episode initiated as a NNE-trending fissure eruption and produced ~0.4 $km^3$ of lava (Donnelly-Nolan et al., 2016). Little Glass Mountain comprises two overlapping flows (Fink, 1983), the larger of which is ~50 m thick and ~2.5 km across. The Crater Glass flows comprise three distinct domes, the largest of which is ~40 m thick and ~1 km across (Fig. 5.2A), which

is associated with an underlying dyke that fed these three domes. The domes are co-linear with, and overlap, two or three much smaller domes. The older, dacitic Medicine Lake Glass Flow (68.2 – 68.8% $SiO_2$) was erupted ~5200 years ago (Nathenson et al., 2007), and is pancake-shaped (Fig. 5.2C), ~2 km long, 30 m thick, with a total volume of ~0.08 $km^3$ (Donnelly-Nolan et al., 2016).

#### 5.3.1.1 Lithologies

Rhyolite lava flows in the western USA have been described in terms of textural components (Fig. 5.3, 5.4) of finely vesicular pumice (FVP), coarsely vesicular pumice (CVP), and obsidian (OBS; Fink, 1983; Fink and Manley, 1987; Manley and Fink, 1987).

FVP is dominant at the flow surface and light brown to grey in colour. Vesicularity is heterogeneous and comprises variably deformed small (<1 mm) vesicles (Fig. 3A). The FVP may also include microcrystalline lava (MCL) that is associated with the last extruded lava and is typically found close to the inferred vent position (Bonnichsen, 1982; Manley and Fink, 1987). MCL is similar in appearance at hand specimen scale to FVP but has a higher crystal content, a lower vesicularity, and with vesicles typically homogeneous, isolated, and showing little deformation.

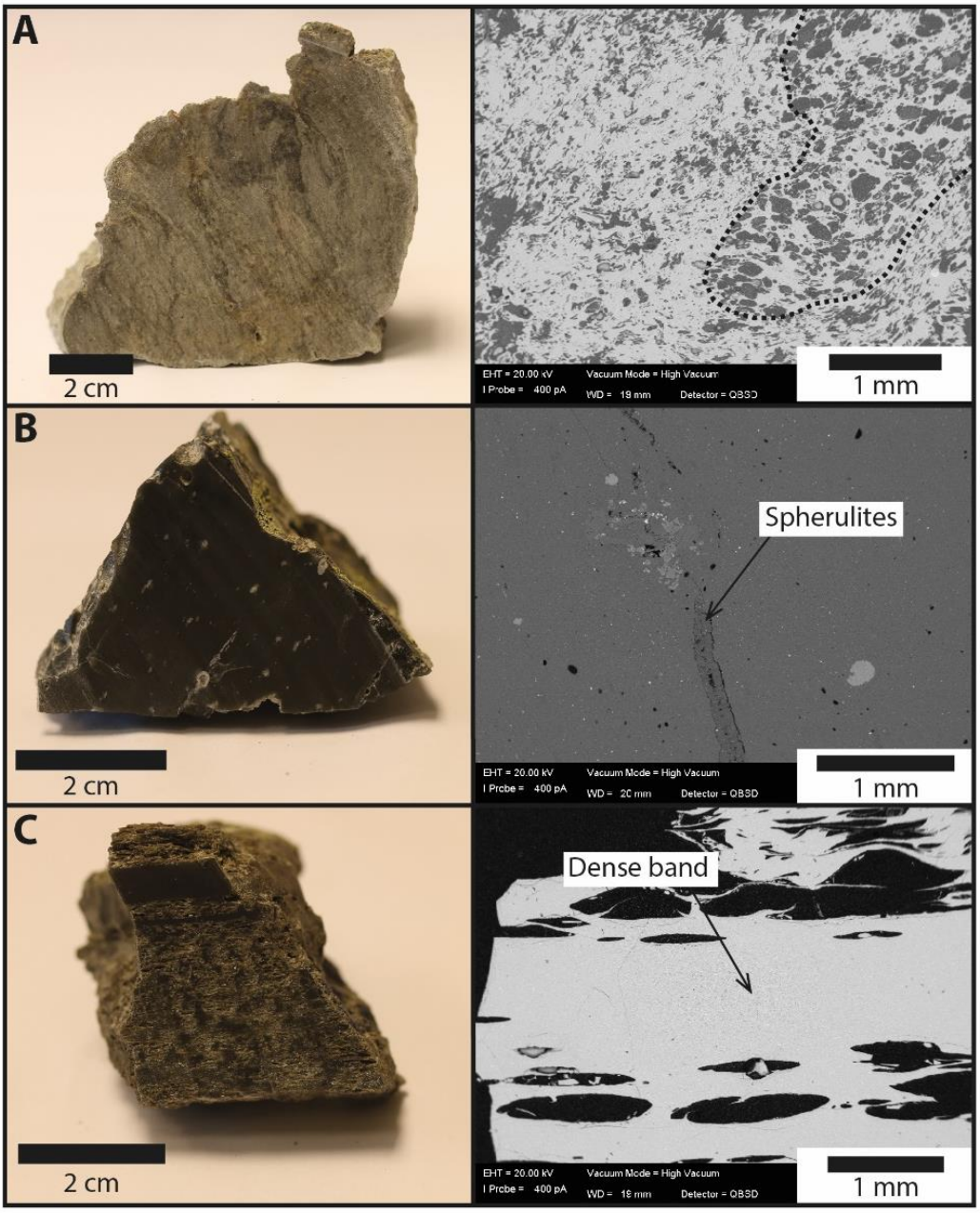


Figure 5.3: Hand specimen photos and associated SEM images of the main lithologies of the Medicine Lake rhyolite lava flows. (**A**) Finely vesicular pumice (FVP), variably vesicular sample with the dashed line highlighting a marked change in vesicularity. (**B**) Obsidian (OBS), glassy and crystal-poor except for some isolated spherulites. (**C**) Coarsely vesicular pumice (CVP) with a dense obsidian band.

CVP is dark brown in colour (Fig. 5.3C) and forms isolated patches on the lava flow surface that are elliptical to linear in shape. CVP is not uniformly vesicular and commonly includes variably-folded bands of dense OBS (Fink, 1983; Castro and Cashman, 1999). Vesicles range from relatively undeformed to highly deformed with pinched ends, indicative of vesicle collapse (Fig. 5.3C). OBS comprises dense rhyolitic glass, which can form a coherent layer up to several metres thick. OBS is crystal-poor except where spherulites have formed (Fig. 5.3B). Isolated and centimetre-sized vesicles can be found, and are most likely lithophysae, typically having a white surface coating relating to vapour-phase cristobalite formation (Schipper et al., 2015; Schipper et al., 2017). The vitrophyre (Fig. 5.4) is an old and hydrated obsidian not observed at the flows discussed here.

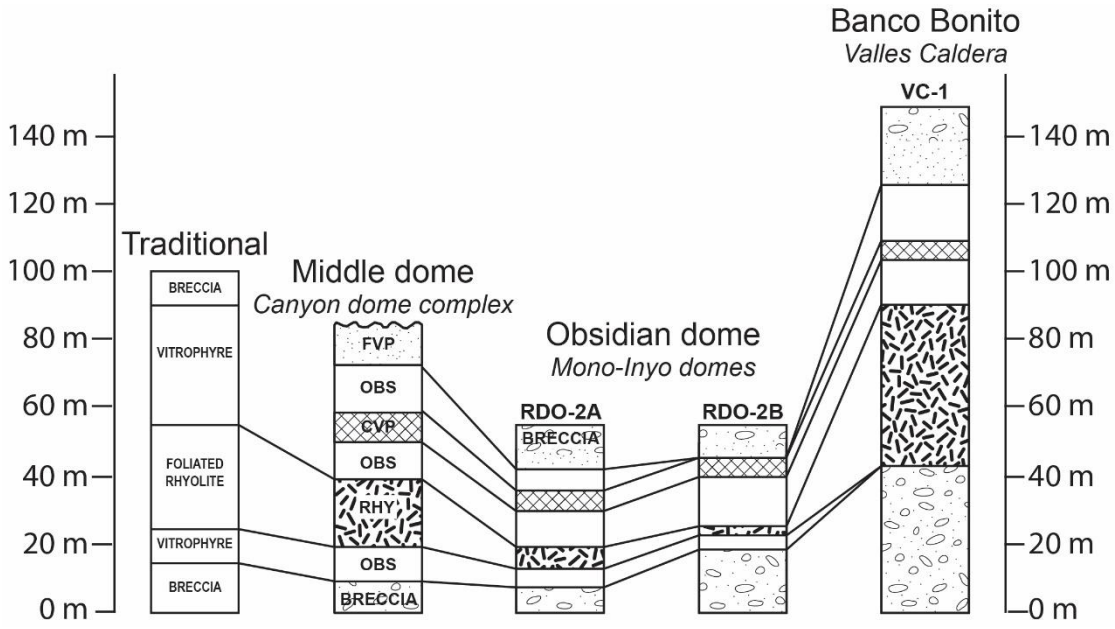


Figure 5.4: Textural stratigraphy of obsidian rhyolite lava flows as determined by drill cores. The upper breccia in cores from Obsidian dome and Banco Bonito composes FVP. From Manley and Fink (1987).

The dacitic lava flows (Medicine Lake Glass Flow, and the dacitic portion of Glass Mountain) lack the abundant textural variations of the rhyolitic lava flows. The dacites

are richer in phenocrysts and microlites than the rhyolites, resulting in a duller appearance than the glassy rhyolitic obsidian (Donnelly-Nolan et al., 2016).

### *5.3.2 Puyehue-Cordón Caulle*

Puyehue-Cordón Caulle is a basaltic to rhyolitic volcanic complex in the southern volcanic zone of the Chilean Andes (Lara et al., 2004; Singer et al., 2008). The 2011-2012 eruption (Fig. 5.1B) initiated on 4 Jun 2011, producing a 15 km high Plinian ash column (Castro et al., 2013). This activity subsided into a coupled effusive-explosive eruption, with simultaneous emission of a 30 – 40 m thick rhyolite lava flow and pyroclastic rhyolite (Schipper et al., 2013; Tuffen et al., 2013). The lava is at the lower silica end of rhyolitic composition at 69.8 – 70.1 wt% $SiO_2$ (Castro et al., 2013) and was first identified from CosmoSkyMed SAR images on 19 Jun 2011 (Bignami et al., 2014). The lava diverged into two directions due to the underlying topography; advance of the northern flow was stopped by a ~40 – 150 m high topographic barrier 60 days into the eruption, while a southern flow advanced more freely but began to be impeded by topography after ~200 days (Magnall et al., 2017). The lava was also impeded by lateral barriers (ridges and old lava flows), which limited lateral spreading of the northern flow and, to a lesser extent, the southern flow (Magnall et al., 2017; Magnall et al., 2018).

Breakouts in the northern flow were first observed 153 days into the eruption (Magnall et al., 2018). These breakouts have a range of morphologies and their size varied from tens of metres to two kilometres in length, and some of the longer breakouts were supplied by preferential thermal pathways within the lava (Magnall et al., 2018). The breakouts initiated and evolved due to the continued supply of lava to the stalled flow front, as well as late stage vesiculation of the main flow interior and the breakout cores

(Magnall et al., 2018). Both continued lava supply and breakout vesiculation contributed to their observed inflation (Tuffen et al., 2013).

Effusion ended on 15 March 2012, as indicated by the ceasing of seismicity at the vent (Global Volcanism Program, 2012; Tuffen et al., 2013). Despite this, a number of breakouts subsequently formed and some were observed advancing in January 2013 (Tuffen et al., 2013), indicative of an effective thermal insulation of the core of the lava flow by the surface crust (Farquharson et al., 2015), which dominated the latter phases of emplacement (Magnall et al., 2017). Ultimately, ~0.4 $km^3$ of lava was erupted with a total length of ~6 km (Tuffen et al., 2013).

#### 5.3.2.1 Lithologies

The Cordón Caulle lava flow shows some textural variation, but not to the same degree as many of the rhyolite lava flows located in the western USA. Magnall et al. (2018) examined the lithologies of the Cordón Caulle lava flow and identified that the bulk of the main flow surface comprises blocks of dark vesicular rhyolite and glassy flow-top-pumice, which is crystal-poor (<5 volume%). Lava at the vent is less vesicular and more crystalline (up to 25 volume%) than the flow-top-pumice and the flow core is grey in colour, highly fractured and crystalline (~70 – 80 volume%). Breakouts are texturally distinct from the main channel of the flow. The breakout lava is dark in colour (black to grey), vesicular, and has microlite crystallinities of ~30 – 40 volume%; the vesicles within the breakouts have variable morphologies, ranging from highly sheared and collapsed to relatively open and undeformed (Schipper et al., 2015; Magnall et al., 2018).

#### 5.3.2.2 Crease structures and pumice diapirs

Crease structures have been documented in numerous ancient silicic lava flows, and were observed forming during the extrusion of the Mount St. Helens lava dome in the 1980s (Anderson and Fink, 1990, 1992). They have a range of morphologies, but are characterised by a central valley (several metres long) with outwardly convex walls that become increasingly blocky away from the central axis (Fig. 5.5; Anderson and Fink, 1992). The walls are striated with “chisel marks” (millimetre to centimetre high ridges) that can extend the full length of the structure (Anderson and Fink, 1992) and indicate the incremental downward fracture advance into a more ductile flow interior during crease structure opening (Degraff and Aydin, 1993).

In some rhyolitic lava flows (e.g. Crater Glass Flow), crease structures are associated with the CVP diapirs (Fink, 1980b, 1983; Fink and Manley, 1987) that punctuate the surface of the flow, either in isolation or as clusters of up to ~30, some with a regular spacing (Fink, 1980b, 1983). Diapirs are domal in shape, commonly split by a central fracture (Fink, 1983), similar in morphology to a crease structure, and range from equant to highly elongate in plan view. Diapirs become more elongate towards the flow front (Fink, 1980b), and many are ringed by outcrops of dense obsidian. In general, the flow stratigraphy (Fig. 5.4) shows that the FVP surface is separated from an interior zone of coarsely vesicular pumice by a layer of OBS (Fink, 1983; Manley and Fink, 1987). The CVP required to generate a pumice diapir has been inferred to form due to anhydrous crystal growth within an aphyric flow core, causing an increase in volatile concentration, which can then migrate along vesicle and fracture networks to a layer beneath the surface crust (Fink and Manley, 1987; Manley and Fink, 1987; Furukawa and Uno, 2015). This forms a vesicle-rich layer at shallower depths (lower pressure) in

the lava, the resulting low-density lava then buoyantly rises to the surface of the lava flow (Fig. 5.5B), potentially aided by the formation of a crease structure (Fink, 1980b).

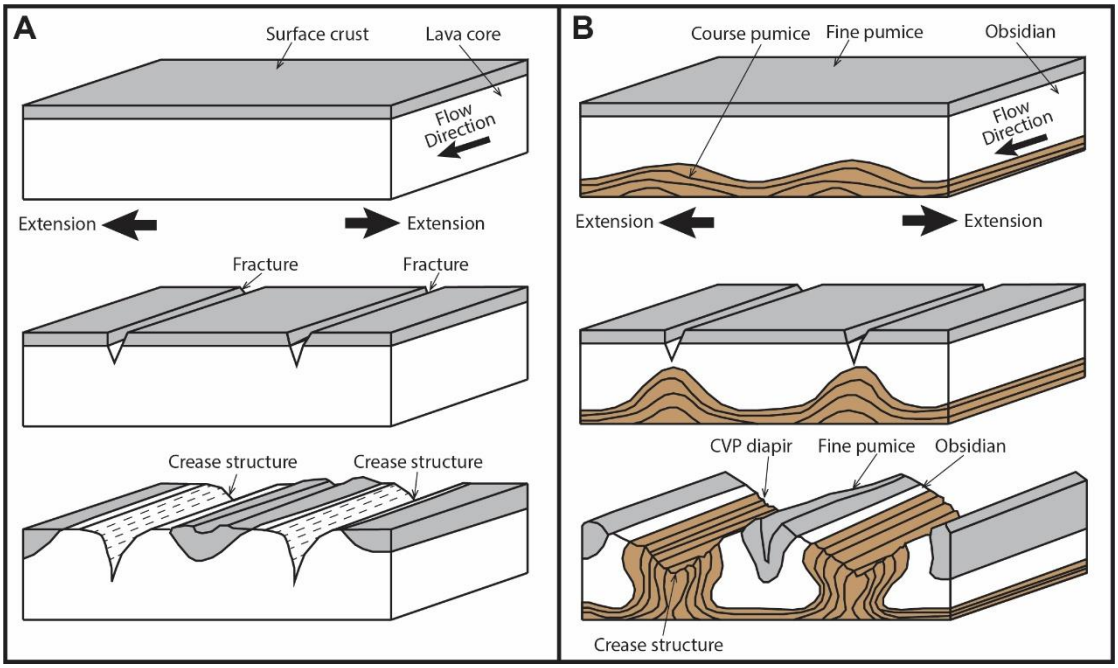


Figure 5.5: **A**. The formation of crease structures in a silicic lava flow. The crease structures open due to spreading of the lava flow surface, typically perpendicular to the advance direction. **B**. The formation of CVP diapirs in rhyolite lava flows. A low-density layer upwells into an opening and fracturing surface crust. Adapted from Fink (1983).

## 5.4 Methods

To understand the processes that contribute to core upwelling in silicic lava flows, we use a combination of fieldwork, remote sensing, and microstructural characterisation of samples via petrographic and scanning electron microscopy (SEM). Fieldwork was conducted at Puyehue-Cordón Caulle in January 2015, to characterise the flow structures and collect representative samples. The work was supplemented by aerial imaging of the lava using a continuously recording GoPro camera attached to the front of a helicopter during repeated overflights, and a DSLR used manually from the

helicopter window. Full details of the methodologies used can be found in Appendix 8A, 8B and 8C.

Fieldwork at Medicine Lake Volcano, California, was conducted in August 2016 and August 2017 and focussed on the emplacement processes of the Crater Glass and Glass Mountain lava flows, with visits to the Medicine Lake Glass Flow and Little Glass Mountain. Representative samples were gathered from different flow facies for microstructural characterisation and the work was supplemented by aerial imaging using a small unmanned aerial vehicle (UAV).

### *5.4.1 Remote sensing*

Satellite images of the lava flow evolution at Cordón Caulle were obtained from EarthObserving 1 (EO-1) ALI (Digenis et al., 1998), Landsat 7 ETM+, as well as from GoogleEarth (Worldview 2 images). EO-1 and Landsat 7 ETM+ bands (30 m resolution, data available from the U.S. Geological Survey) were combined into true or false colour VNIR or SWIR images in ENVI, then pansharpened using their corresponding panchromatic images (15 m resolution). Landsat 7 ETM+ thermal data (Band 6, 30 m resolution) were stretched in ArcGIS to highlight variations across the surface of the lava flow. Maps of the Medicine Lake lava flows originated from the one meter resolution NAIP JPG 2000 aerial imagery data set (data available from the U.S. Geological Survey).

#### 5.4.1.1 UAV Structure-from-Motion (SfM) photogrammetry

To determine the detailed structure of regions of interest on the surface of the Crater Glass lava flow and the Medicine Lake Glass Flow, 3-D models were generated using structure-from-motion (SfM) photogrammetry (e.g. James and Robson, 2012). UAV

aerial photography was conducted using a DJI Phantom drone equipped with a DJI FC300X camera. The georeferenced photos were processed in Agisoft Photoscan Professional (v. 1.3.4) to produce a dense point cloud from which a scaled orthophoto (2 cm resolution) and digital elevation model (DEM, 5 cm resolution) were generated. Given that these were for visual interpretation only, detailed georeferencing and photogrammetric analyses were not required.

### *5.4.2 Microstructural characterisation*

Analysis of petrographic thin sections was conducted using a petrographic microscope fitted with a digital camera. A more detailed microstructural characterisation of key representative flow facies was carried out by SEM analysis using a LEO 435VP variable pressure digital scanning electron microscope at the British Geological Survey. Phase/mineral identification was aided by qualitative observation of energy-dispersive X-ray spectra recorded simultaneously during SEM observation, using an Oxford Instruments INCA energy-dispersive X-ray microanalysis (EDXA) system. Images were captured from thin sections in BSE mode.

## 5.5 Results

### *5.5.1 Crease structures and pumice diapirs at Medicine Lake Volcano*

Crease structures are common on the surface of the dacitic Medicine Lake Glass Flow. Aerial photographs show that most are oriented parallel to the inferred flow direction, in some cases forming en-echelon arrays (Fig. 5.6A). Coarsely vesicular pumice diapirs are found across the surfaces of Glass Mountain and the Crater Glass flows (Fig. 5.2A, B). In both cases the pumice diapir outcrops are concentrated closer to the

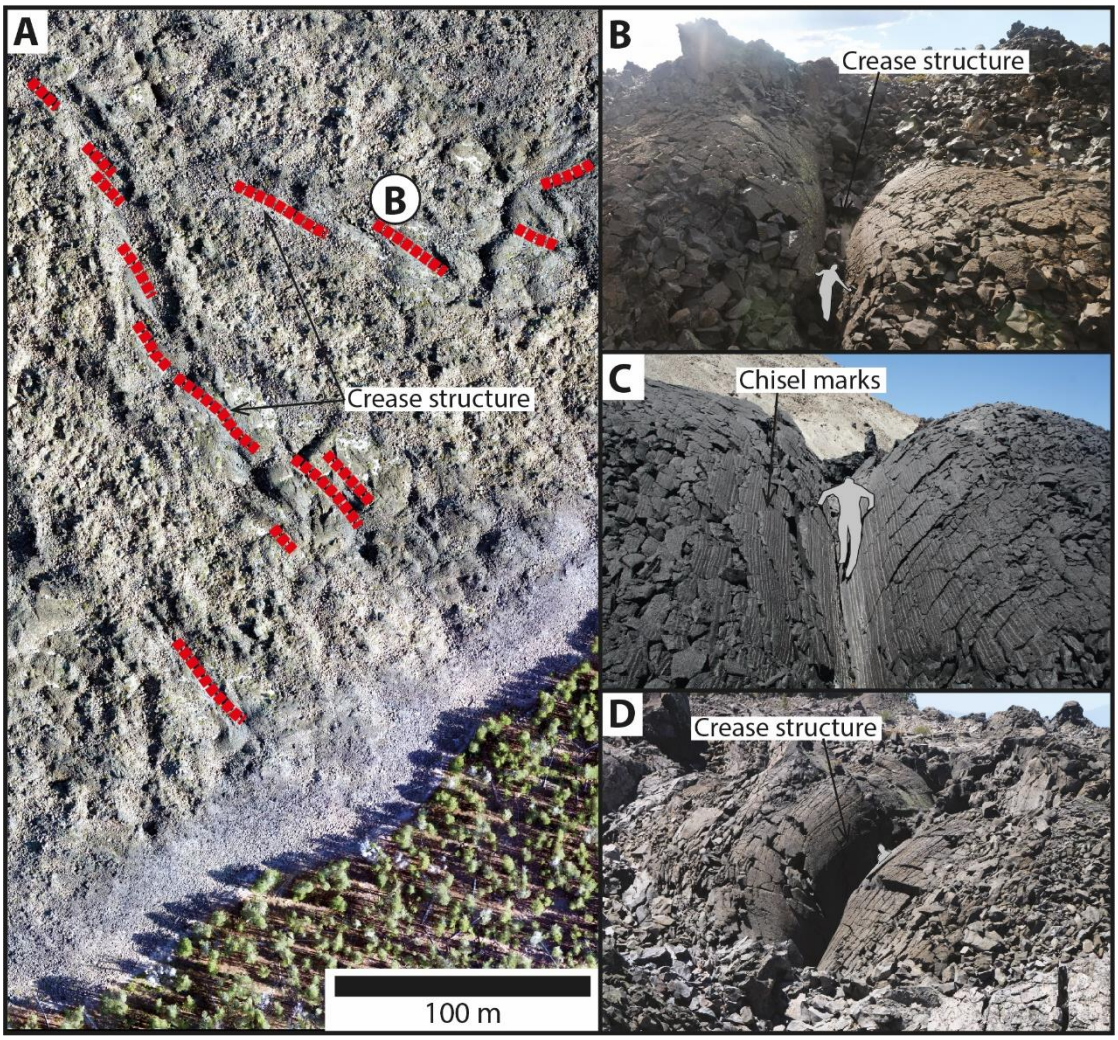


Figure 5.6: Crease structures on rhyolite and dacite lava flows. (**A**) UAV-derived orthophoto of a portion of the Medicine Lake Glass Flow (Appendix 8A.31); red dashed lines highlight crease structures. Crease structures on (**B**) the Medicine Lake Glass Flow, (**C**) at the vent of the 2011-2012 Cordón Caulle rhyolite lava flow, with “chisel marks” clearly visible, and (**D**) on a pumice diapir of the Crater Glass Flow.

flow front than to the vent (Fig. 5.2A). At Glass Mountain, CVP diapirs are only observed in the rhyolitic portions of the lava flows (Fig. 5.2). The diapirs either form circular features, typically 10 – 150 m across or are elongate, up to ~800 m long and 10 – 150 m wide, and oriented parallel to flow surface ogives. The circular diapirs are

typically associated with large (metres to tens of metres long) crease structures (Fig. 5.6D), but crease structures are not as obvious in many of the elongate diapirs.

We broadly divide circular diapirs into simple and compound types. Simple diapirs have a single central crease structure, with the sides of the fracture curving outwards onto the horizontal surface of the lava flow (Fig. 5.6). Where simple diapirs are close to the lava flow front, the crease structure is typically oriented perpendicular to the flow front (and therefore perpendicular to ogives).

The sub-decimetre-resolution of the UAV DEM (Fig. 5.7A) clearly resolves the multiple, differently orientated, fractures in a typical compound diapir (Fig. 5.7). Individual fractures are similar to crease structures but they variably merge and cross-cut one another. Between the fractures are jointed slabs of CVP, separated by small (tens of centimetres high) ridges (Fig. 5.7). Fractures and coherent surface slabs of CVP are most easily seen in the smaller (tens of metre) diapirs, such as those on the Crater Glass flows. The top surface of some diapirs can be elevated several metres above the surrounding flow surface (Fig. 5.7B) but, for larger and highly elongate diapirs such as those at Glass Mountain, it can be very difficult to discern crease structures and surface fractures in coarser resolution (1 m) aerial imagery.

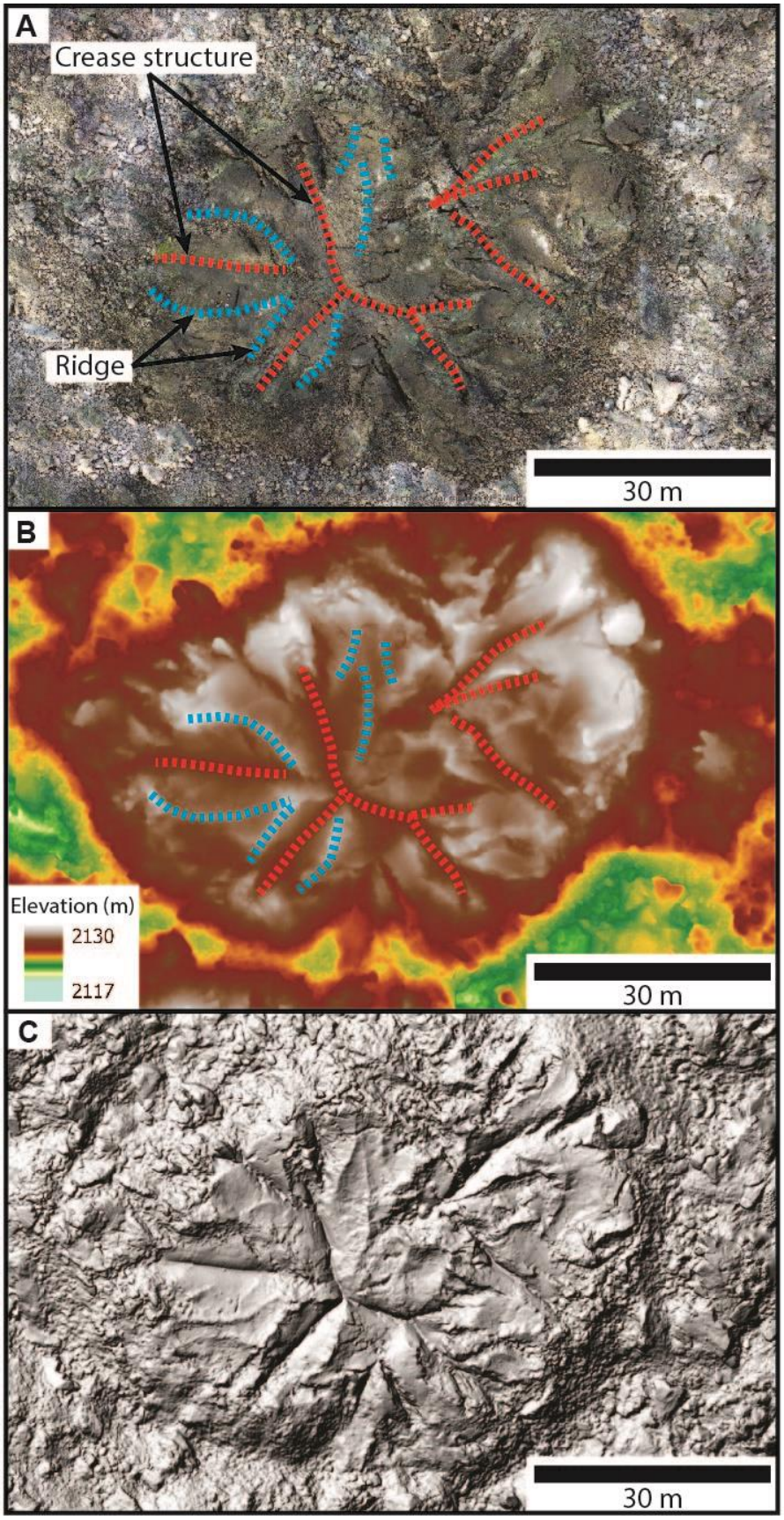
A
Crease structure
Ridge
30 m
B
Elevation (m)
2130
2117
30 m
C
30 m

← Figure 5.7: (**A**) UAV derived orthophoto of a complex diapir on the surface of the Crater Glass lava flow. Red dashed lines highlight crease structures, blue dashed lines highlight the ridges between converging slabs. (**B**) Digital elevation model (DEM) of the same pumice diapir. The pumice diapir is up to 5 m higher than the surrounding lava.

#### 5.5.1.1 Microstructural characterisation

There is a high degree of variability in the CVP samples in terms of vesicularity, with substantial variability within a diapir. Dense bands of obsidian are common within the CVP (Fig. 5.3C), either representing areas that have not vesiculated, or that have partially collapsed. Diapiric CVP displays further vesicularity changes with depth (Fig. 5.8). The surface of a diapir is the most vesicular, with open, millimetre sized vesicles

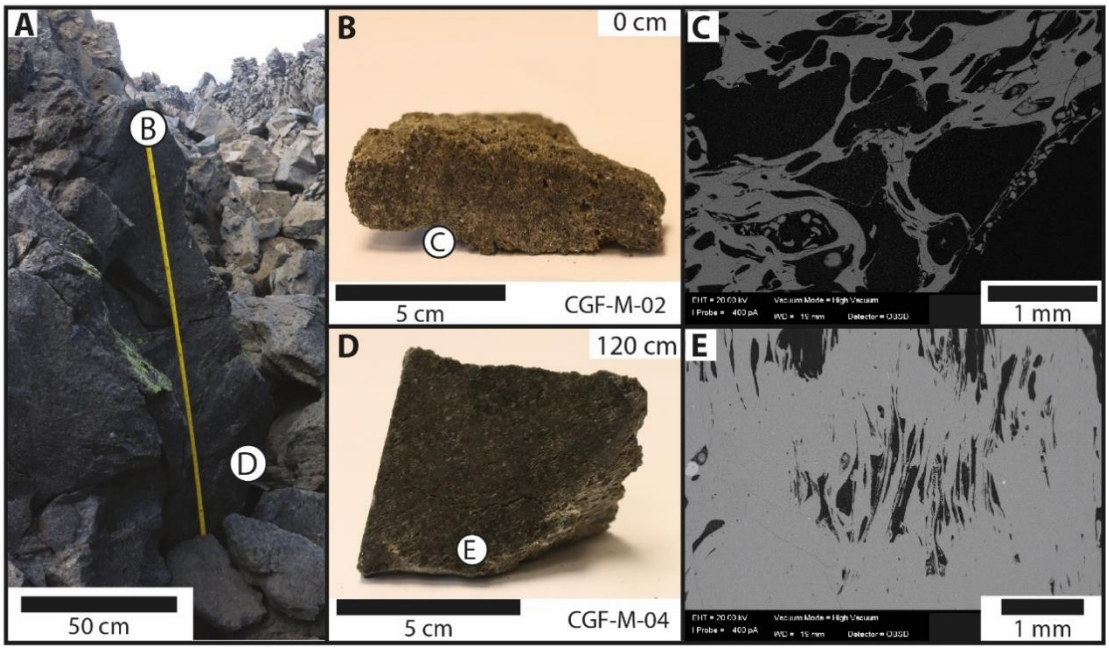


Figure 5.8: (**A**) Outcrop of the pumice diapir in Fig. 5.7 on the Crater Glass Flow. (**B**) Hand specimen from the surface of the diapir. (**C**) SEM image of **B**, the surface is more vesicular with a large number of open and partially coalesced vesicles. (**D**) Hand specimen from deeper in the breakout. (**E**) SEM image of D, there is an increased number of collapsed and partially collapsed vesicles, these are typically flattened at either end.

that are variably deformed and exhibit varying stages of coalescence (Fig. 5.8B, C). Below the diapir surface the vesicularity decreases, with vesicles isolated to discreet patches (Fig. 5.8D). These vesicles are typically elongate and pinch-out at either end, suggesting vesicle collapse or elongation (Fig. 5.8E).

### *5.5.2 Crease structures and core upwelling at Cordón Caulle*

Crease structures are not common on the Cordón Caulle rhyolite, with the only two identified within 100 m of the vent (Fig. 5.6C). These are comparable in morphology and scale to those observed at the Medicine Lake Glass Flow (Anderson and Fink, 1992) and each include a central fracture that can be several metres long and deep (Fig. 5.6C). Smooth, “chisel-marked”, curved sides merge with the horizontal surface of the lava flow, leading to a relatively rubble-free surface for several metres either side of the central fracture. While crease structures are rare at Cordón Caulle, breakouts are common and are often split by an inflationary cleft. However, unlike crease structures, clefts have straight sides that lack a outwardly convex morphology, and are associated with inflation rather than upwelling of core lava (Magnall et al., 2018) Thus, the principle stress is orientated vertically, rather than horizontally.

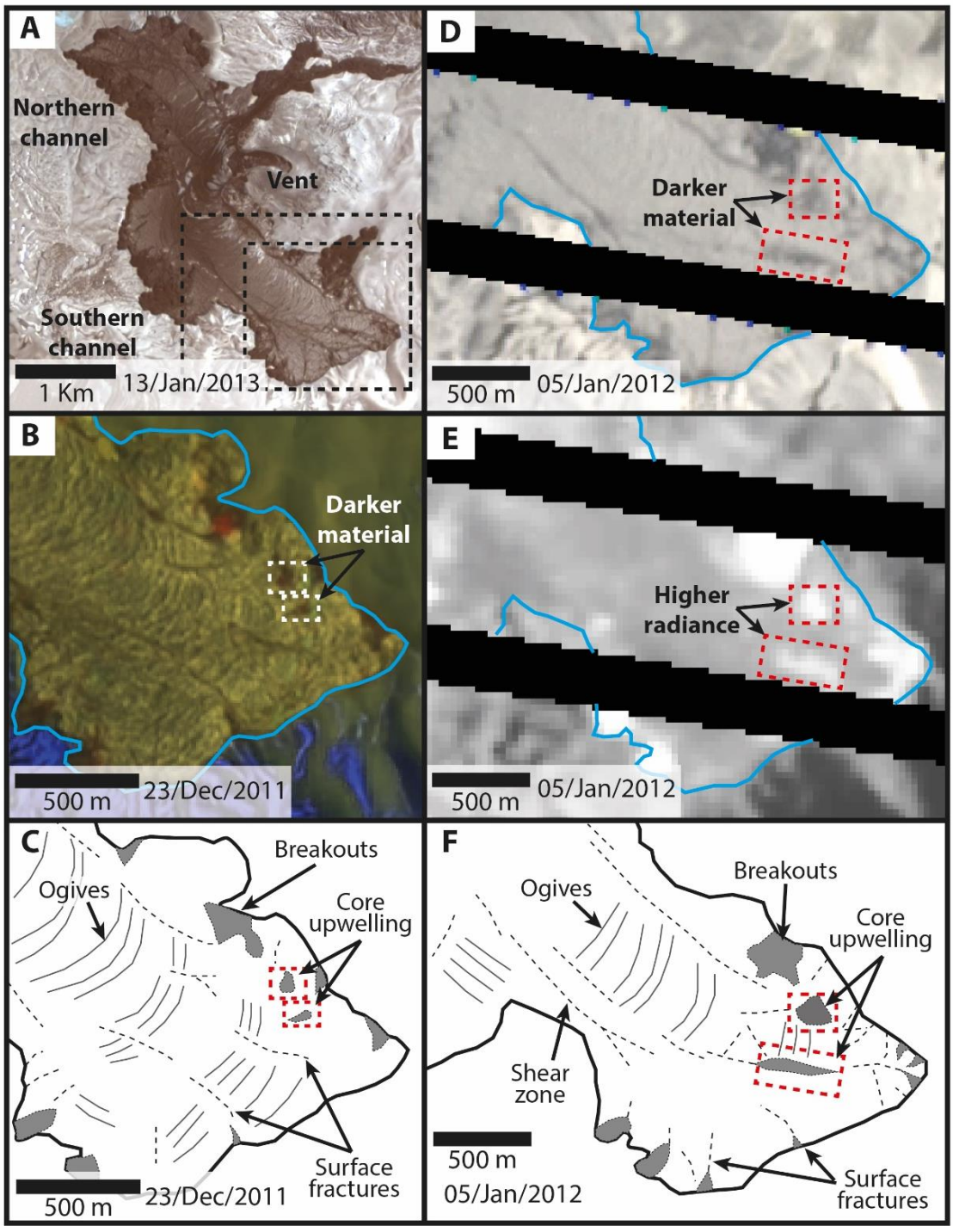
A
Northern channel
Vent
Southern channel
1 Km
13/Jan/2013
D
Darker material
500 m
05/Jan/2012
B
Darker material
500 m
23/Dec/2011
E
Higher radiance
500 m
05/Jan/2012
C
Breakouts
Ogives
Core upwelling
Surface fractures
500 m
23/Dec/2011
F
Ogives
Breakouts
Core upwelling
Shear zone
500 m
05/Jan/2012
Surface fractures

← Figure 5.9: Satellite images of the Cordón Caulle lava flow. (**A**) EO-1 satellite image of the lava flow post eruption (NASA, 2013). Black boxes show the extent of **B**/**C** and **D**/**E**/**F**. B. EO-1 satellite image of the lava flow showing breakouts (NASA, 2011e). The two white boxes show darker areas on the flow surface similar in appearance to the breakouts. (**C**) Interpretive sketch of image **B**. (**D**) Landsat 7 image of the lava flow (NASA, 2012b), the red boxes highlight a dark area near the flow front (same as those in **B**) and a dark area in a large fracture. (**E**) Corresponding TIR image to **B** showing brighter areas associated with the darker areas in image **B**. (**F**) Interpretive sketch of image **D**/**E**.

Some evidence for core upwelling at Cordón Caulle is provided by two features observed in satellite imagery on 23 Dec 2011 (~200 days from the eruption onset). These are similar in colour to dark breakouts and occur 100-200 m behind the stalled southern flow front (Fig. 5.9B, C). The features had a higher TIR radiance than the surrounding main channel lava (Fig. 5.9D) and, although they appeared to form at a similar time, they show differing morphologies. The northern feature (Fig. 5.9C, D, 5.10A, B) is rounded in appearance, approximately 100 m wide, and has a central slabbed region, cross-cut by a number of fractures and surrounded by a heavily fractured area of rubble (Fig. 5.10A, B). The southern feature (Fig. 5.9C, 5.10C) is elongate, 200 m long and 30 m wide, and appears to be associated with a large (~400 m long) fracture that extends back from the flow front into the main channel. The lava that fills this fracture comprises intact and larger (several metres across) blocks and slabs compared to the surrounding main channel rubble (Fig. 5.10C).

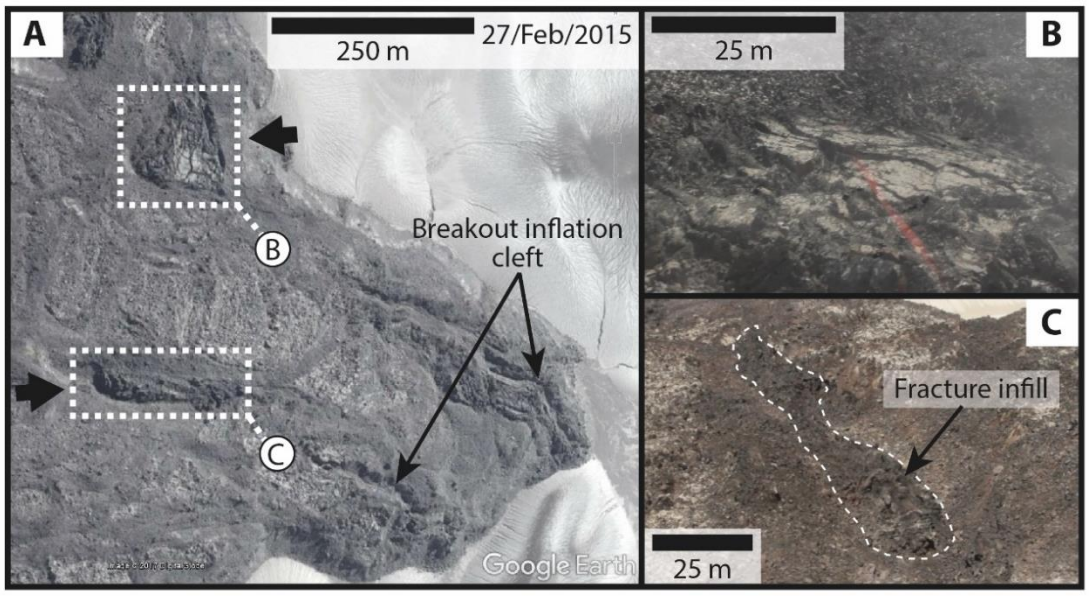


Figure 5.10: Post eruption images of the features highlighted in Figure 5.9. (**A**) Google Earth image of a large slabbed area at the location of the dark patch in Figure 5.9 as well as the large fracture in Figure 5.9C (DigitalGlobe, 2015). The dark arrows show the orientation of the photos in **B** and **C**. Oblique aerial images of (**B**) the large slabbed area near the flow front, and (**C**) the large fracture with apparent infill. Details of field data gathered can be found in Appendix 8B.

Although extensive CVP diapirs are not observed at Cordón Caulle, some flow-top pumice is observed in the field and in satellite images. This flow-top-pumice is golden in colour and forms isolated spines up to 2 m tall (Fig. 5.11). The vesicularity of the pumice decreased with depth (Fig. 5.11B), with vesicles becoming sheared and typically pinched at one end deeper within the flow (Fig. 5.11C). The abundance of pinched, partially collapsed vesicles increases with depth, and is associated with a colour change in hand specimen from golden to black (Fig. 5.11), likely due to the reduction in vesicularity. The flow-top-pumice represents some of the most crystal-poor rhyolite erupted during the Cordón Caulle eruption, with microlite contents <5 volume% (Magnall et al., 2018).

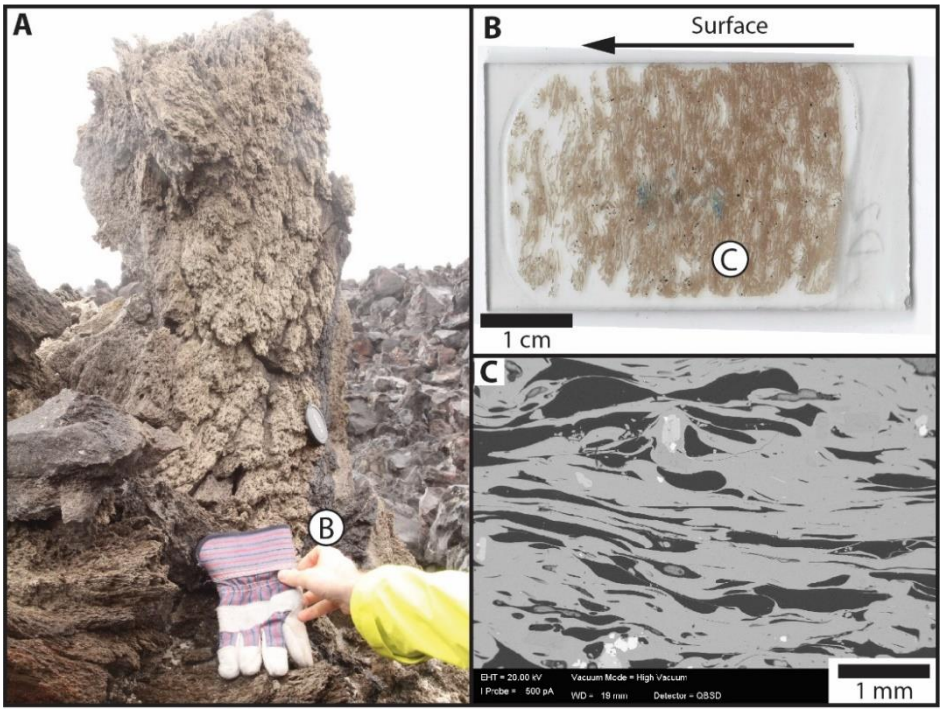


Figure 5.11: (**A**) Pumice from the surface of the Cordón Caulle lava flow. (**B**) Scan of thin section from base of the pumice, vesicles are highly deformed and become increasingly collapsed with depth into the base of the pumice spine. Label C on panel **B** shows the approximate location of panel **C**. (**C**) SEM image of collapsed and elongate vesicles in microlite-poor glass.

## 5.6 Discussion

Previous work has indicated that crease structures form due to the opening of an extensional fracture at the surface of a lava flow or dome (Anderson and Fink, 1990, 1992), with the upwelling of core lava to a the surface of a flow requiring one or more of the following: a spreading surface crust, buoyant rise of core lava, or a pressure increase in the core of the flow. Observations of the surface of rhyolite lava flows indicate that many of the simpler CVP diapirs are associated with a single dominant crease structure that splits the entire diapir (Fig. 5.6D, 5.12); such a fracture may precede the upwelled CVP diapir and continue to form in the diapir, splitting the diapir. Many of the crease structures are orientated perpendicular to the flow front, indicating

that their formation was driven by lateral spreading of the flow. The southern elongate feature in the Cordón Caulle lava flow (Fig. 5.10C) is associated with a substantial surface fracture oriented perpendicular to the flow front, suggesting that this feature may also have formed by upwelling into a spreading fracture that formed due to lateral spreading of the flow. The association of crease structures with CVP diapirs could suggest that the fracture intercepts a vesicular body at depth (Fink et al., 1992),

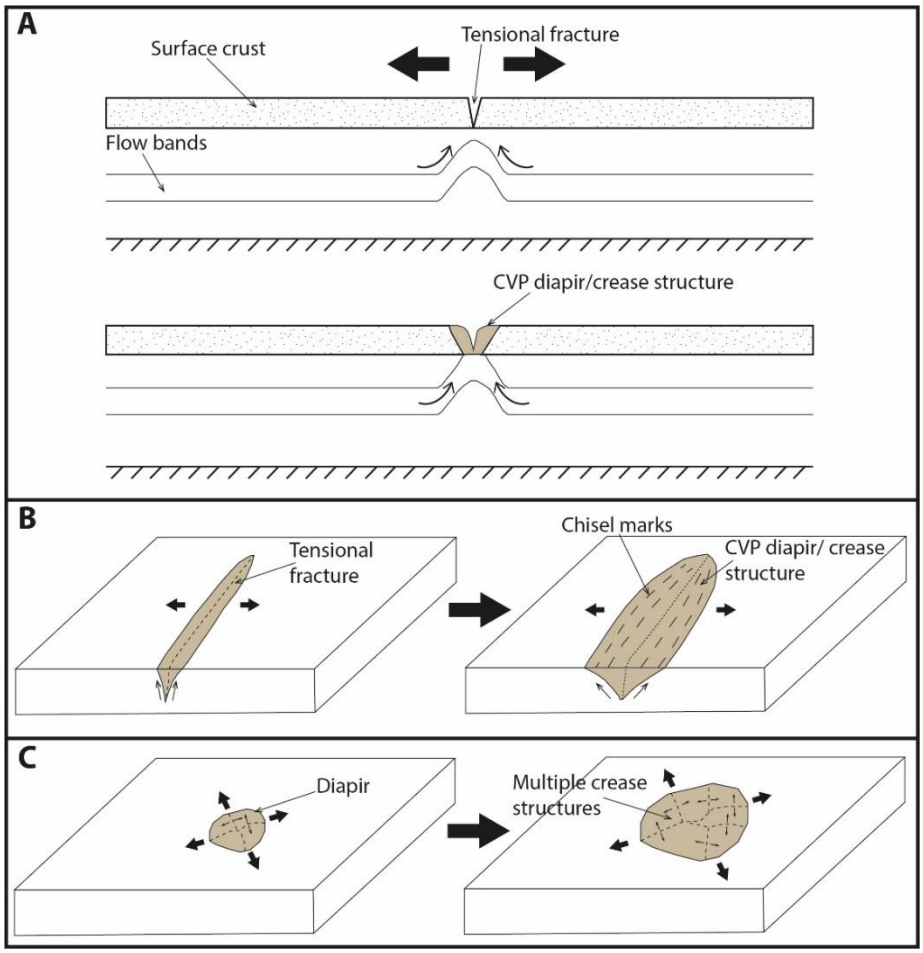


Figure 5.12: (**A**) Formation of pumice diapirs in a lava flow. Either vesiculation of the flow core leads to the buoyant ascent of lava capable of rupturing the surface crust, or a crease structure opens, leading to a drop in pressure in the lava directly below it. Core lava upwells into the new space. (**B**) In some cases, a simple diapir forms where lava upwells into an already opening crease structure. (**C**) If this continues to be supplied, a complex of multiple, differently oriented crease structures is formed.

promoting its rise to the surface (Fig. 5.12). Alternatively, the associated reduction in pressure at the fracture tip may promote vesiculation, and initiate diapiric rise.

Many diapirs have complex morphologies, with multiple slabs and variably oriented crease structures suggestive of multiple spreading centres (Fig. 5.7, 5.12C). Where the flat surfaces of adjacent crease structures meet, they are separated by small ridges, which likely form as the two crease structures spread towards one another (Fig. 5.7). These multiple spreading centres suggest that these diapirs are emplaced over longer periods of time, potentially due to buoyant rise of a vesicular body (Fink, 1980b), rather than being primarily driven by upwelling associated with spreading and fracturing of the lava flow surface.

Some diapirs are not associated with crease structures, suggesting that they do not form in an actively spreading portion of the flow. In this case, they may form due to a pressure increase in the flow core, in a process comparable to localised inflation and subsequent formation of squeeze-ups (Applegarth et al., 2010c) and tumuli (Rossi and Gudmundsson, 1996) in basaltic lava flows. In this scenario, pressurised core lava could be exposed to a sudden pressure reduction on rupturing the surface, leading to vesiculation of the extruded lava prior to quenching (Fig. 5.8). The pressure required to drive core lava through the surface could be generated by continued lava supply to a static or stalled front, or to ongoing vesiculation of the flow core, provided that the flow surface crust was sufficiently strong to prevent flow inflation. If a diapir forcefully ruptures the surface crust and extrudes, it might be considered as conceptually comparable to the formation of a vertically oriented breakout. This feature then contributes to localised exogenous growth of the flow surface. Similarly, during emplacement of the Mount St. Helens lava dome, the formation of a large crease structure was thought to reflect the stalling of the advancing dome front, and indicate

the transition to vertical lava movement above the vent (Anderson and Fink, 1990, 1992). As well as diapirs and crease structures, localised inflation of breakouts in silicic flows can lead to the formation of inflationary clefts, which lack associated core upwelling (Magnall et al., 2018).

The northern upwelling site at the Cordón Caulle lava flow (Fig. 5.10B) has a more rounded morphology compared to the southern upwelling site (Fig. 5.10C). This site is more similar to the pumice diapirs observed in other rhyolite lava flows. Due to low resolution syn-eruptive imaging, and the difficulty of sampling this site, it is not clear whether this feature formed from the diapiric rise of vesicular lava, upwelling into a fracture, or the extrusion of pressurised core lava. Given the extensive number of breakouts at the Cordón Caulle lava flow, the latter seems the most likely.

### *5.6.1 Influence of the surface crust*

Rising core lava must overcome any crustal strength before being extruded onto the surface, unless upwelling occurs into an actively opening fracture. The strength and continuity of the lava crust may therefore control the surface expression of upwelling. The limited number of observed sites of core extrusion at Cordón Caulle could reflect a relatively coherent crust due to a generally compressional regime resulting from the lava being emplaced on relatively shallow topography, and parts of the flow being constrained by topographic barriers (Magnall et al., 2017). This would limit lateral flow spreading and the formation of associated surface fractures. It is noteworthy that the two sites of upward extrusion observed at Cordón Caulle are located in the southern channel, which was relatively unconstrained by topographic barriers for most of its emplacement (Magnall et al., 2017), allowing the formation of large surface fractures due to lateral flow spreading (Fig. 5.9, 5.10). Surface fracturing driven by lateral

spreading may be a pre-requisite for core extrusion onto the surface of the flow. Furthermore, the strength and coherence of the surface crust at Cordón Caulle is thought to have controlled the latter stages of the eruption, slowing flow advance and promoting the transition to a cooling-limited flow (Magnall et al., 2017). This transition produced surface fractures at the northern flow front of the Cordón Caulle lava, but these were preferential sites of breakout formation (Magnall et al., 2018), instead of core upwelling to the surface of the lava.

At Medicine Lake Volcano, the rhyolitic and dacitic lavas are typically unconstrained by natural topographic features or flow levées, and pumice diapirs and numerous crease structures are observed (Fig. 5.2). Some portions of Glass Mountain emplaced on steeper slopes (e.g. the SE lobes) and do form levées, but no obvious diapirs are observed in these portions of the flow (Fig. 5.2). The general lack of topographic constraints enabled greater lateral spreading than at Cordón Caulle, which is consistent with conditions that promoted fracturing of the surface crust, and facilitate core upwelling. Localised advance down steep slopes may also promote extension and disruption of the surface crust, potentially favouring upwelling rather than breakouts from the flow front. The surface crust could be further weakened by hydration from the accumulation of volatiles in a layer underlying the surface crust (0.3-0.5 wt%, Fink and Manley, 1987; Manley and Fink, 1987), acting to decrease the viscosity of the ductile portion of the crust. Water contents of CVP could support this hypothesis, as these are often elevated, 0.3-0.5 wt% compared to 0.1-0.2 wt% in the bulk of the flow (Manley and Fink, 1987), it is unclear whether this was the same for Cordón Caulle as measured water contents are normally between 0.1-0.2 wt% (Castro et al., 2013).

### *5.6.2 Influence of lava rheology*

While the continuity of a surface crust may control whether core lava will upwell or move laterally to form a breakout, it does not explain the lack of pumice diapirs in the dacitic Medicine Lake Glass Flow (despite abundant crease structures, Fig. 5.6A) and the dacitic NE lobe of Glass Mountain. Thus, the presence of diapirs in most rhyolites (e.g. Fig. 5.2) suggests a compositional control, with the threshold for diapir formation lying within the rhyolite composition. Composition, including volatile content, is an important factor in determining the lava rheology, as are the temperature, and proportions of vesicles and crystals (e.g. Llewellin et al., 2002; Mueller et al., 2011; Mader et al., 2013; Truby et al., 2015). Composition further controls the crystal growth rate, with crystals growing faster in lower silica melts. Lava rheology is likely to be a primary control on diapir formation, with high apparent viscosities expected to hinder vesiculation, and reduce flow rates, including buoyant rise, although they may not all be affected to the same degree. Considering only bulk compositions, viscosities of the most silica-rich rhyolite flows would be expected to be highest (Table 5.1), at comparable temperatures, and thus lower viscosities could be inferred to limit diapir formation. However, given the higher crystallinities of many lower-silica rhyolites and dacites, due to their shorter diffusion timescales, any inference should consider the substantial impact of the crystal population on rheology (e.g. Costa, 2005; Mueller et al., 2011; Mader et al., 2013).

Microlite crystallinities at Cordón Caulle range from up to ≤20 volume% at the vent to 30 – 40 volume% in breakouts and mature parts of the lava flow due to in-flow crystal growth (Schipper et al., 2015; Magnall et al., 2018), and are substantially greater than in the diapir-rich rhyolites (e.g. crystallinities of <2 volume% for the Glass Mountain and Crater Glass flows, Donnelly-Nolan et al., 2016). The Medicine Lake Glass Flow was

also likely more crystalline compared to the Crater Glass Flow and Glass Mountain rhyolites. The effects of crystallinity on the viscosity of the Cordón Caulle lava has been previously considered using the Einstein-Roscoe equation (Farquharson et al., 2015; Magnall et al., 2017):

$$\eta = \eta_0(1 - R\phi)^{-Q}, \qquad [Eq. 5.1]$$

where $\eta$ is the apparent viscosity, $\eta_0$ is the melt viscosity, $\phi$ is the crystal volume and $R$ and $Q$ are constants equal to 1.67 and 2.5 respectively. However, this approach assumes crystals are isotropic, and neglects the additional effects that elongate forms (such as microlites) can have on increasing bulk viscosity (Kerr and Lister, 1991; Mueller et al., 2011). To account for crystal anisotropy, we use the Maron and Pierce (1956) equation (Mueller et al., 2010, 2011), valid for intermediate strain rates (1 $s^{-1}$), and crystal packing fractions of $\emptyset/\emptyset_m < 0.7$ (where $\emptyset$ is the crystal volume and $\emptyset_m$ is the maximum packing fraction):

$$\eta = \eta_0 \left(1 - \frac{\phi}{\phi_m}\right)^{-2}, \qquad [Eq. 5.2]$$

where the maximum packing fraction ($\phi_m$) for crystals of a given aspect ratio ($r_p$) is calculated from:

$$\phi_m = \phi_{mi} exp\left[-\frac{\left(log_{10} r_p\right)^2}{2b^2}\right], \qquad [Eq. 5.3]$$

and $\phi_{mi}$ is the maximum packing fraction for particles with $r_p$ = 1, and $b$ is a fitting parameter, we use values of $\phi_{mi}$ = 0.656 and $b$ = 1.08 (Mueller et al., 2011). Using this approach, the bulk viscosity of the Cordón Caulle lava flow would be one to two orders of magnitude greater than the predicted viscosities of the crystal-poor rhyolites of the Crater Glass flow and Glass Mountain rhyolite (Fig. 5.13, Table 5.1). Furthermore, the Medicine Lake Glass Flow, and dacitic portion of Glass Mountain, could have up to an order of magnitude greater viscosity than crystal-poor rhyolitic flows (Table 5.1). It is worth noting that viscosity calculations for the Medicine Lake Glass Flow and dacitic portion of Glass Mountain use the bulk composition, including crystals, so such

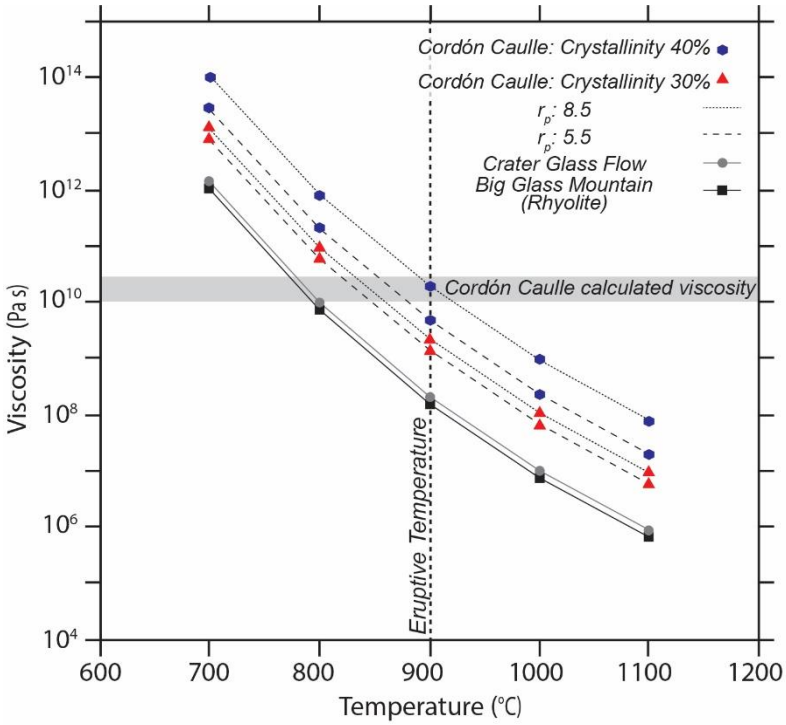


Figure 5.13: Estimated viscosity of crystal-poor rhyolite lavas (Crater Glass flow and Big Glass Mountain) and the crystalline Cordón Caulle rhyolite lava flow. $r_p$ is the crystal aspect ratio, derived from analysis of SEM imagery in Magnall et al. (2018), Appendix 8C. The grey bar shows the apparent viscosity range previously derived for Cordón Caulle from flow observations (Farquharson et al., 2015; Magnall et al., 2017). The eruptive temperature for Cordón Caulle is given by the dashed line (Castro et al., 2013), which is comparable to the magmatic temperature of Medicine Lake lava flows (Grove and Donnelly-Nolan, 1986).

estimates may represent a minimum, as the melt component would be expected to be more silicic. The viscosity estimates for Cordón Caulle here are greater than those in Section 4, but are comparable to the viscosity determined from flow observations (Section 4), demonstrating the importance of accounting for crystal shape when estimating viscosity.

The higher estimated bulk viscosity values for the Cordón Caulle lava flow (Table 5.1) and, by extension, of silicic lavas with a significant microlite content, such as the dacitic portion of the Glass Mountain lava (Eichelberger, 1975), could control whether a lava can form pumice diapirs. While crystallisation may promote vesicle nucleation, the inferred high bulk viscosities of more crystalline silicic lavas would act to impede the growth, migration and buoyant rise of vesicles and vesicular lava. Indeed, the only flow pumice at Cordón Caulle is observed in crystal-poor rhyolite (Fig. 5.11). The flow-alignment of elongate microlites in the Cordón Caulle lava (Magnall et al., 2018) may have also created more resistance to upward flow than to horizontal motion due to the influence of crystal alignment on effective viscosity (Smith, 2002; Mueller et al., 2011), provided they formed prior to breakouts. The greater crystallinity of the Cordón Caulle lava could also have increased the yield strength of the crust, inhibiting the ability of buoyant core lava to rupture the surface.

The presence of a pre-effusion microlite population could also limit the amount of in-flow crystal growth. Given that the concentration of volatiles required to drive vesiculation of the core of a silicic lava is thought to result from anhydrous crystallisation of an aphyric flow core (Fink and Manley, 1987; Furukawa and Uno, 2015), if the lava were erupted with an existing microlite population, then the volume of syn-emplacement crystallisation, and therefore vesiculation, may be reduced. Conversely, the presence of crystals could provide nucleation sights for new crystals,

allowing more rapid crystallisation. The presence of a crystal population could also indicate that the magma was already volatile-poor, particularly if crystallisation was driven by degassing in the conduit (Simakin et al., 2000; Applegarth et al., 2013a). While late stage vesiculation of the Cordón Caulle lava flow was likely stifled by its rheology, some limited core vesiculation has been inferred (Magnall et al., 2018). This may have contributed some of the pressure required to initiate breakouts from this flow, particularly from marginal portions of the flow that were unlikely to have been fed by preferential thermal pathways (Magnall et al., 2018).

Higher viscosities could also impede the formation of large gas cavities that are observed at the surface of some rhyolitic lava flows (Bonnichsen, 1982; Jensen, 1993; Castro et al., 2002a). These cavities form from the coalescence of bubbles beneath the surface crust into a single cavity, which then vent explosively if the gas pressure exceeds the surface strength (Jensen, 1993; Castro et al., 2002a). The generation of these features may also be influenced by enhanced volatile exsolution in regions of reduced pressure created during buckling of the surface crust and ogive formation, being preferentially found in the anticline of ogives (Castro et al., 2002a). Thus far, such features have not been observed at Cordón Caulle, or in dacitic lava flows (Table 5.1), suggesting that the high-viscosity may have inhibited vesicle growth, migration, and coalescence required for the formation of large gas cavities. Alternatively, the lack of such features could simply reflect an insufficient volatile content. It is interesting that most rhyolite flows display these features except for the Crater Glass Flow (Table 5.1) and that a visual inspection of the Crater Glass Flow shows a relatively high number density of diapirs compared to others (Fig. 5.2). Therefore, as well as indicating the accumulation of volatiles within the flow core, it is possible that the diapirs helped to facilitate the degassing of this flow, and limited the potential for gas cavity formation.

*Table 5.1: Flow properties and features; all calculations assume 900 °C and a water content of 0.1%. Data from other comparable flows at other volcanoes are provided for comparison.*

| Property | Medicine Lake - Glass Mountain *(Dacite)* | Medicine Lake Glass Flow *(Dacite)* | 2011-2012 Cordón Caulle *(Rhyolite)* | Mono-Inyo Domes – Obsidian Dome *(Rhyolite)* | South Sister - Rock Mesa *(Rhyolite)* | Newberry Caldera – Big Obsidian Flow *(Rhyolite)* | Medicine Lake - Little Glass Mountain *(Rhyolite)* | Medicine Lake - Crater Glass Flow *(Rhyolite)* | Medicine Lake - Glass Mountain *(Rhyolite)* |
|---|---|---|---|---|---|---|---|---|---|
| Bulk $SiO_2$, wt% | 61.3-67.3 [a,b] | 68.2-68.8 [a,b] | 69.8-70.1 [c] | 70.2-72.6 [d] | 73.3-73.5 [e] | 71.8-73.7 [f,g] | 71.4-74.2 [b] | 72.6-74.3 [a] | 70-74.6 [a,b] |
| Crystallinity, volume% | ~3 phenocryst, microlite matrix [b] | ~6 phenocryst, microlite matrix [b] | <5 phenocryst, 30%-40% microlites [h] | 5-10 [d] | 5-8 [e] | <1 [g] | 1-2 [b] | <2 [b] | <2 [b] |
| Microlite aspect ratio ($r_p$) | N/A | N/A | 5.5 to 8.5 [i] | 3.1 to 5.4 [j] | N/A | N/A | N/A | N/A | N/A |
| Density ($\rho$), kg $m^{-3}$ | 2400 [k] | 2400 [k] | 2300 [c] | 2350 [k] | 2350 [k] | 2350 [k] | 2350 [k] | 2350 [k] | 2350 [k] |
| Melt viscosity ($\eta_0$), Pa s | $3.1\times10^7$ [l] | $4.6\times10^7$ [l] | $3.5\times10^7$ [m] | $1.1\times10^8$ [n] | $2.3\times10^8$ [o] | $9.3\times10^7$ [p] | $1.7\times10^8$ [l] | $2.0\times10^8$ [l] | $1.6\times10^8$ [l] |
| Bulk viscosity ($\eta$), Pa s | $1.7\times10^8$ to $2.3\times10^9$ [q] | $2.6\times10^8$ to $3.4\times10^9$ [q] | $1.4\times10^9$ to $1.8\times10^{10}$ [r] | $1.7\times10^8$ [s] | $3.2\times10^8$ [s] | As above | As above | As above | As above |
| Breakouts [t] | Potentially [u] | x | ✓ | x | x | x | x | x | x |
| Crease structures [t] | ✓ | ✓ | ✓ | ✓ | ✓ | ✓ | ✓ | ✓ | ✓ |
| Pumice diapirs [t] | x | x | x (potentially in 2 places) | ✓ | ✓ | ✓ | ✓ | ✓ | ✓ |
| Large gas cavities [t] | x | x | x | x (potentially in places) [v] | ✓ | ✓ | ✓ | x | ✓ |

[a] Grove and Donnelly-Nolan (1986)
[b] Donnelly-Nolan et al. (2016)
[c] Castro et al. (2013)
[d] Westrich et al. (1988)
[e] Fierstein et al. (2011)
[f] Laidley and McKay (1971)
[g] Kolzenburg et al. (2013)
[h] Schipper et al. (2015), Magnall et al. (2018)
[i] Measured from SEM images in Magnall et al. (2018)
[j] Castro et al. (2002b)
[k] Glass-Density-Calc_v3 (Lange and Carmichael, 1990; Ochs and Lange, 1999)
[l] Determined from Giordano et al. (2008) using a composition from Grove and Donnelly-Nolan (1986)
[m] Determined from Giordano et al. (2008) using a bulk composition from Castro et al. (2013)
[n] Determined from Giordano et al. (2008) using a composition from Westrich et al. (1988)
[o] Determined from Giordano et al. (2008) using a composition from Scott (1987)
[p] Determined from Giordano et al. (2008) using a composition from Kolzenburg et al. (2013)
[q] Determined from Mueller et al. (2011) using a bulk composition (melt composition not available) from Grove and Donnelly-Nolan (1986), note that this assumes similar microlite crystallinity to Cordón Caulle
[r] Determined from Mueller et al. (2011) using a melt composition from Schipper et al. (2015)
[s] Determined from Eq. 1
[t] Based on observations of GoogleEarth imagery
[u] Magnall et al. (2018)
[v] Observations inconclusive from GoogleEarth imagery

#### 5.6.2.1 Models of buoyant upwelling

Previous work has explored the formation of pumice diapirs as growing Rayleigh-Taylor (R-T) instabilities (Fink, 1980b; Baum et al., 1989), from which diapir spacing (Fink, 1980b), as well as the potential viscosity contrast between CVP and the surrounding flow can be inferred (Baum et al., 1989). However, an R-T model ignores the potential influence of surface fractures on diapir spacing. Using both this approach and the simple ascent of a buoyant sphere, we can consider the influence of lava viscosity on upwelling times for different flow compositions (Fig. 5.13).

Given the circular appearance of many diapirs at the surface of a rhyolite lava flow, a first order estimate of ascent time can be derived using Stokes' law to provide a terminal velocity for an ascending sphere (u):

$$u = \frac{1}{18}\frac{g d_e^2 \Delta\rho}{\eta_l}, \qquad [Eq. 5.4]$$

where $g$ is the acceleration due to gravity (9.81 $ms^{-2}$), $d_e$ is the sphere diameter, $\Delta\rho$ is the density contrast, and $\eta_l$ is the viscosity of the host fluid with Stokes' law assuming a rigid spherical body in an infinite static Newtonian fluid (Fig. 5.14A). Interpretations here must be limited, as diapirs were deformable. Nevertheless, plausible first order insight into the effect of different viscosities on diapir ascent can be gained. Furthermore, given the low Reynolds number ($10^{-10}$ – $10^{-4}$) of silicic lava flows (Griffiths, 2000), the assumption of a static flow is reasonable.

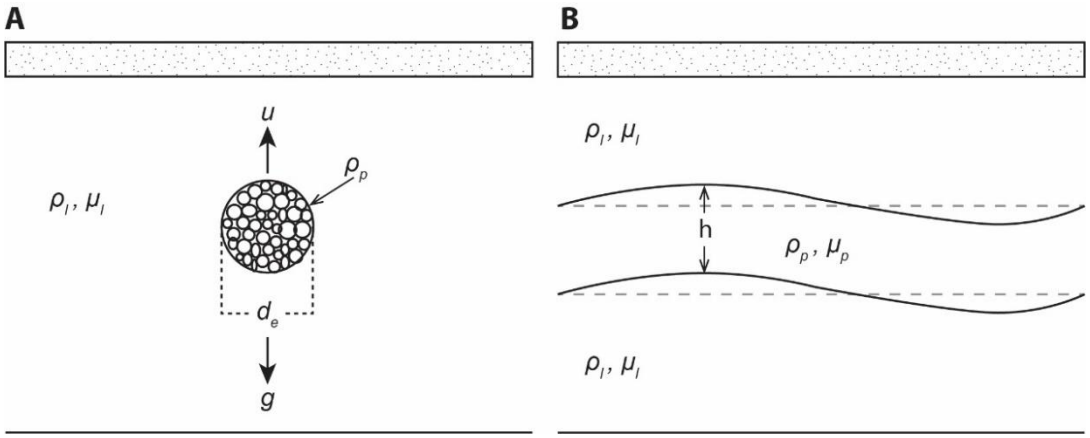


Figure 5.14: First order models for diapiric rise. (**A**) Representing a pumice diapir as a buoyantly rising low-density sphere, for using Stokes' law. u is the terminal velocity, $\rho_l$ is the ambient fluid density, $\rho_p$ is the density of the sphere, $\mu_l$ is the viscosity of the ambient fluid, $d_e$ is the sphere diameter, and g is the acceleration due to gravity. (**B**) The development of a diapir as a Rayleigh-Taylor instability in a low-density layer sandwiched between two higher density layers. h is the layer thickness and $\mu_p$ is the viscosity of the low-density layer, after Wilcock and Whitehead (1991).

The Rayleigh-Taylor approach assumes a lower density CVP layer is located within a lava of higher density, and in this case viscosity (Fig. 5.14B), in an inherently unstable configuration (Fink, 1980b; Baum et al., 1989). Such a layer must derive from the accumulation of gases in a layer beneath the surface crust (Fink and Manley, 1987; Manley and Fink, 1987). The growth rate (*n*) of the resulting instabilities can be expressed by (Wilcock and Whitehead, 1991):

$$n = \frac{1}{3^{1/2}2^{5/3}} \frac{g\Delta\rho h}{\eta_l} \varepsilon^{1/3}, \qquad [Eq. 5.5],$$

where h is the layer thickness, $\eta_l$ is the viscosity of the high-density lava, and ε is the viscosity ratio between the lava and the low-density layer ($\eta_l/\eta_p$). This approach is

typically applied to systems with high values of $\varepsilon$ (~350, Wilcock and Whitehead, 1991), but here we necessarily assume it is also suitable for lower values of $\varepsilon$ (1 – 10).

The low-density layer may have an order of magnitude lower viscosity due to elevated $H_2O$ contents (0.2 – 0.5 wt%, as measured in CVP samples; Manley and Fink, 1987), in turn leading to a value of $\varepsilon = 10$. Given that the vesicles within the pumice diapirs are sheared and elongate (Fig. 5.3C), the vesicles may also act to reduce viscosity (e.g. Mader et al., 2013) as described by:

$$\eta = \eta_0 \left(\frac{1}{1 + B\phi_b}\right), \qquad [Eq. 5.6]$$

where B is an empirically-adjustable parameter, equal to 24, and $\phi_b$ is the proportion of vesicles (Bagdassarov and Dingwell, 1992). Therefore, vesicularities of 20 – 60 volume% could reduce viscosity by up to an order of magnitude, leading to corresponding values of $\varepsilon$ of ~10 – 100, which agree with the range previously determined from diapir spacing ($\varepsilon$ = 10 – 100; Baum et al., 1989). For bubbles to decrease viscosity, they must be sheared prior to or early on during buoyant rise of CVP. However, if the vesicles were undeformable (i.e. a low capillary number) they would increase the bulk viscosity (e.g. Llewellin et al., 2002; Mader et al., 2013), and volatile exsolution would also increase the melt viscosity. Thus, vesiculation could potentially increase or decrease the6 apparent viscosity.

The R-T approach can be used to estimates of the dominant wavelength ($\lambda$) of the instability (Wilcock and Whitehead, 1991):

$$\lambda = \pi(2\varepsilon)^{1/3}h. \qquad [Eq. 6.7]$$

However, such analyses cannot consider more complex effects such as viscous anisotropy due to crystal alignment and, in tectonic-scale systems, isotropy has been shown to have effects on parameters such as diapir spacing (Lev and Hager, 2008).

#### *5.6.2.1.1 Upwelling modelling results*

Crease structures formed during extrusion of the Mount St. Helens lava dome on the order of days (Anderson and Fink, 1992) and, with the 2011-2012 Cordón Caulle lava flow active for over 10 months (Tuffen et al., 2013), this provides broad upper and lower bounds on the possible timescales of core upwelling. Using Crater Glass to typify the bulk viscosity of rhyolites with pumice diapirs (Table 5.1) the rate of ascent of low-density bodies 1m and 10 m in diameter or thickness, and porosities of 20 – 60 volume% (Manley and Fink, 1987), can be estimated. Under these conditions, the ascent of a low-density body would be one to two orders of magnitude faster than in the Cordón Caulle lava flow (Fig. 5.15). The corresponding timescales for 10 m of ascent, a depth at which CVP has been found within some rhyolitic lava flows ( Manley and Fink, 1987), are of order a day to tens of days for the Crater Glass flow (Fig. 5.15). In the Rayleigh-Taylor model, increasing $\varepsilon$ from 1 to 10 (Eq. 5.5) reduces the ascent time by half; to attain an order of magnitude reduction in ascent time requires $\varepsilon \approx 100$. Such upwelling timescales would be of order hours, which seems too fast given the emplacement timescales of these lavas. Given that these diapirs likely upwell over timescales of days, based on the timescale of crease structure formation (Anderson and Fink, 1990), their absence in many smaller rhyolite lava domes (Fink and Manley, 1987) could suggest that the dome emplacement occurred over timescales shorter than those required for volatile accumulation, exsolution and buoyant rise.

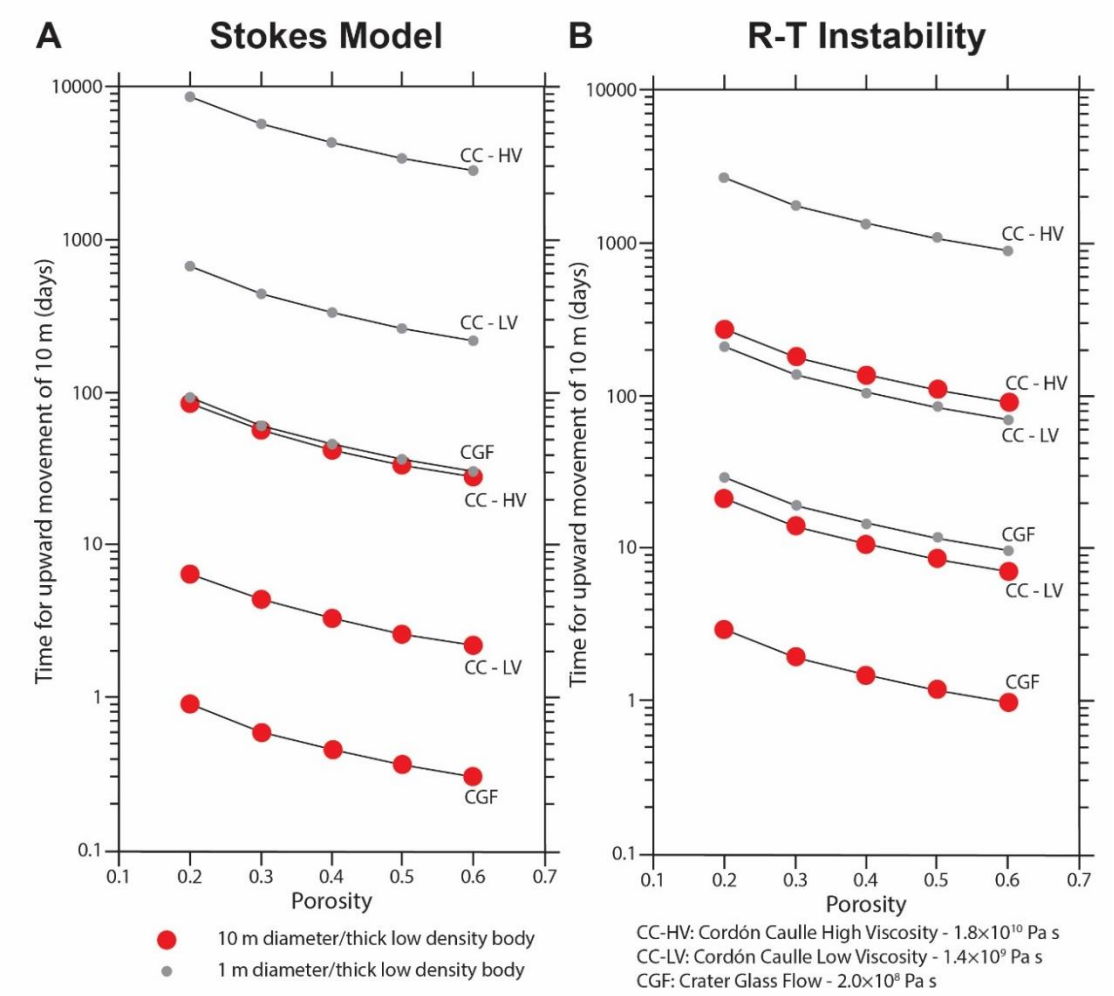


Figure 5.15: The viscosities of the rhyolite lava flows derive from Figure 5.14. Spherical bodies with diameters of 1 m and 10 m are modelled rising through the Cordón Caulle lava flow (CC-HV high-viscosity, CC-LV low-viscosity), as well as the Crater Glass flow (CGF). The bulk density used is found in Table 5.1. (**A**) Theoretical time for a lower density spherical body to rise 10 m through a rhyolite lava flow, based on Stokes' law. (**B**) Theoretical time for a 10 m R-T instability to develop in a rhyolite lava flow, based on Wilcock and Whitehead (1991). The Cordón Caulle lava flow emplaced over ~300 days (Tuffen et al., 2013) giving an upper bound to diapir formation timescales.

Diapirs at the surface of rhyolite lava flows such as Glass Mountain and the Crater Glass Flow have spacings of tens of metres (Fig. 5.2). Considering the wavelength of a Raleigh-Taylor instability (Eq. 5.7), gives ~40 m and ~4 m for a 10 m and 1 m thick

layer respectively ($\varepsilon = 1$). For $\varepsilon = 10$ or 100 wavelengths are estimated at ~85 m and ~180 m respectively for a 10 m thick layer and ~8.5 m and ~18 m for a 1 m thick layer. This indicates that the CVP layer thickness required to generate CVP diapirs is likely of order 10 m.

### *5.6.3 Hazard implications*

Given that rhyolite lava flows are typically emplaced over timescales of order months (Manley, 1992; Tuffen et al., 2013; Farquharson et al., 2015), knowledge of whether a flow will form breakouts would aid syn-eruptive estimations of lava flow inundation hazards. The difficulty that breakouts pose in predicting lava flow inundation was particularly evident during emplacement of the Cordón Caulle lava flow, where some breakouts attained substantial lengths, contributed to the redistribution of preferential thermal pathways within the lava flow, and facilitated drainage of the lava core after the eruption ended (Magnall et al., 2018). Breakouts are difficult to incorporate into flow models, and models of lava advance have only examined advance of the main channel of the Cordón Caulle lava flow (Magnall et al., 2017). The formation of a breakout is dependent on a pressure increase within the flow core. However, if a diapir extrudes forcefully through the surface crust, its formation could act to reduce the pressure within the flow core, thus contributing to localised exogenous growth of the flow surface, rather than lengthening (Fig. 5.16). Thus, the ability of a lava flow to form pumice diapirs may act as a primary control on the lava advance processes.

The formation of pumice diapirs indicates that vesicles are growing within the lava core, which can produce surface explosions when large gas cavities rupture (Fink and Manley, 1987; Jensen, 1993; Castro et al., 2002a). Vesiculation, as well as continued lava supply to the flow front can also contribute to an internal pressure capable of

causing flow front collapse (Fink and Manley, 1987; Baum et al., 1989), which could comprise a considerable volume given flow thicknesses often >30 m. Such flow front collapse could be particularly hazardous where slopes are steep, potentially leading to the generation of pyroclastic density currents (Malin and Sheridan, 1982; Fink and Kieffer, 1993). This may be especially prevalent where volatile concentrations exceed equilibrium, as collapse of a flow front could lead to rapid decompression of the core of a lava body (Fink and Kieffer, 1993).

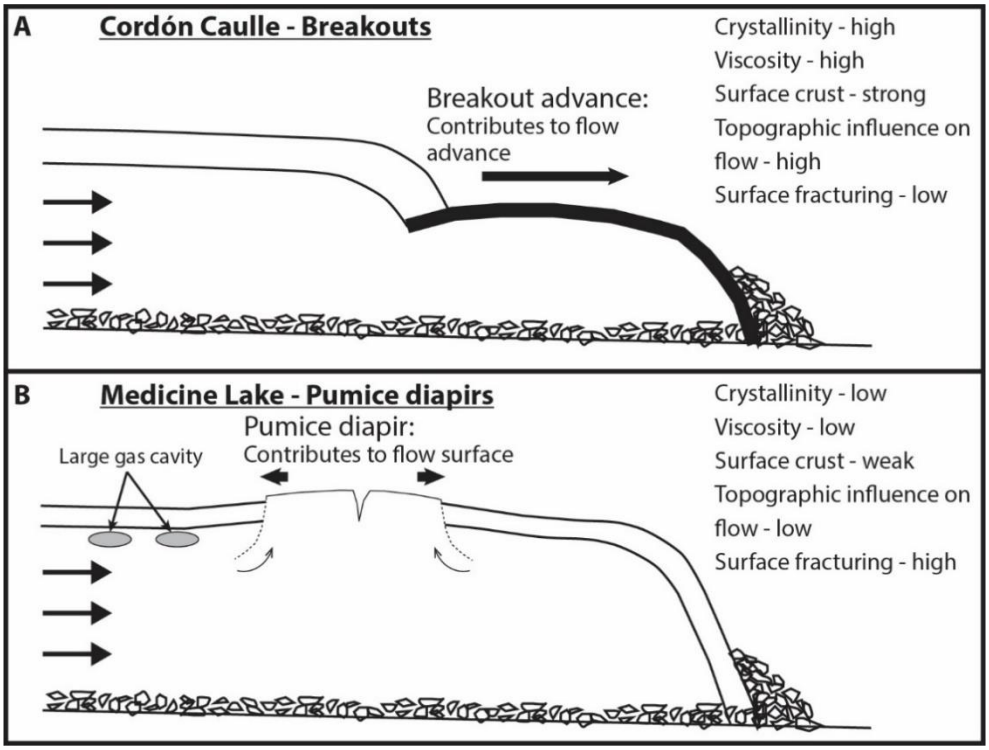


Figure 5.16: (**A**) The formation of a strong pervasive surface crust and/or the presence of a substantial crystal population (and associated higher viscosity) inhibits the formation of pumice diapirs. As a result, pressurised flow core lava is more likely to push through the flow front, leading to flow front collapse and breakout formation, which consequently increases the footprint of the lava flow. (**B**) A weaker fractured surface crust and/or a low crystallinity (and consequently lower viscosity) promoted the formation of pumice diapirs. Diapir formation contributes to the surface crust of the flow and may act to limit the possibility for breakouts to form, as they could act to relieve pressure in the flow core.

The hazards presented by these flows do not lend themselves to direct interventions. The slow advance rate could make it possible to divert a rhyolite lava flow through the building of barriers, but the thickness of these lavas would mean that such barriers would need to be of order tens of metres high. Furthermore, the hazards posed by explosions from the surface or collapses of the front of the lava flow would be very difficult to mitigate, and should be considered for future similar eruptions.

## 5.7 Conclusions

In contrast to many previously studied Holocene rhyolite flows, the 2011-2012 Cordón Caulle rhyolite underwent little upwelling of its core to the surface. We identify rheology as a primary control on the generation of such features, with pumice diapirs appearing to be absent in dacites and lavas at the low-silica end of the rhyolite composition, but common in higher-silica rhyolites. This trend reflects that, with decreasing silica content in the studied lavas, bulk viscosity counter-intuitively increases, due to increasing microlite contents. Consequently, diapirs are associated with lavas of sufficiently low-viscosity (~$9\times10^7$ – $2\times10^8$ Pa s) that upwelling can occur over the timescales of lava emplacement, or even more rapidly. The presence of microlites, e.g. at Cordón Caulle, hinder syn-flow vesiculation and slow buoyant ascent to timescales of, or greater than, lava cooling and solidification. The viscosity of many dacitic and lower-silica rhyolite lavas may have also limited the migration and accumulation of volatiles required for the formation of large gas cavities. Such features are more common in higher-silica rhyolite lavas, and these could pose a significant hazard due to their association with surface explosions.

We further suggest that during emplacement of the Cordón Caulle lava flow, topographic barriers inhibited lateral spreading of the lava for some of the emplacement

(Section 4). This reduced the degree to which the coherent portion of the surface crust fragmented (Section 4) and, consequently, restricted the locations where upwelling lava could have easily reached the surface. In this case, the upwelling of core lava necessitates the opening of a surface fracture, not just diapiric rise of a low-density body. Inhibited upwelling is likely to have promoted formation of the observed breakouts at the flow margins, due to pressurised and vesicular core lava preferentially moving laterally rather than vertically, presenting an increased inundation hazard. Lavas that are less laterally constrained by topography, such as the Medicine Lake Glass Flow, have a surface crust that is more pervasively compromised by fractures, facilitating the upwelling of core lava to the surface, and reducing the likelihood of breakout formation. Finally, the vesiculation of the flow core, prior to the development of a pumice diapir, presents a considerable hazard, with the associated pressure increase potentially promoting flow front collapse, rapid decompression of the flow core, and potentially the generation of pyroclastic density currents.

## 5.8 Acknowledgements

NM is supported by a NERC ENVISION studentship and a BUFI grant from the British Geological Survey. HT is supported by a Royal Society University Research Fellowship. CV-B publishes with the express permission of the executive director of the British Geological Survey. We gratefully acknowledge the assistance of Gren Turner (British Geological Survey) with SEM imaging of the thin sections. We also wish to thank the BBC Earth team for assistance with aerial photography of the lava flow.

# 6 Discussion and Conclusions

The three papers presented in this thesis provide an analysis of some of the processes that occurred during the emplacement of the Cordón Caulle rhyolite lava flow. This work has also attempted to identify commonalities and differences between the emplacement of cooling-limited mafic and silicic lavas.

The first paper (Section 3) used a combination of field and remote sensing observations to infer the presence of a strong surface crust in the emplacement of the 2001 Mt Etna lava flow and the 2011-2012 Cordón Caulle lava flow. These observations informed the application of quantitative models of lava advance to these two lava flows, and the results suggest that advance of both lava flows was initially controlled by a Newtonian viscosity and then by the influence of a cooled surface crust. This cooled surface crust, as well as surrounding topography, ultimately halted the advance of the Cordón Caulle lava flow, breakouts then formed from the stalled flow front and margins. The second paper (Section 4) indicated that breakouts formed due to the continued supply of lava to the stalled flow front and margins along preferential thermal pathways. This continued lava supply, coupled with possible vesiculation of the main channel core, contributed to a pressure increase at the flow front, this ultimately led to the fracturing of the surface crust and breakout formation. The morphological evolution of the breakouts was further controlled by the volume of lava supply to the breakout, leading to advance and inflation.

The formation of breakouts during the emplacement of the 2011-2012 Cordón Caulle lava flow is a unique observation, with such features not being previously documented at other rhyolitic lava flows. However, pumice diapirs and crease structures are characteristic of many ancient, crystal-poor, rhyolite lava flows in the western USA. The third paper (Section 5) indicates that these features are scarce at the Cordón Caulle

lava flow, but identifies two sites of potential core lava upwelling into large surface fractures. I suggest that pumice diapir formation in a rhyolite may be inhibited by the formation of a pervasive surface crust, which would limit the formation of crease structures that pumice diapirs could upwell into. Conversely, a lack of low-density layers within a flow could limit upwelling and the associated rupturing of the surface crust. Furthermore, the potentially greater viscosity of the Cordón Caulle lava flow (due to the crystallinity of the lava), compared to its crystal-poor rhyolitic counterparts (e.g. the rhyolite lava flows at Medicine Lake Volcano, California), could inhibit lava vesiculation, and the ability of a low-density layer to buoyantly rise to the surface of a lava. If core lava is inhibited from rising to the surface of the lava flow, then it may be more likely to form breakouts from the flow front. Breakout formation poses a challenge when predicting lava advance patterns due to the inherent randomness of their locations, as well as their ability to shift the propagation direction.

The Cordón Caulle eruption has provided a unique opportunity to study the emplacement of a rhyolitic lava flow. The processes observed, and subsequent features produced during emplacement, show commonalties with other lava flows, particularly mafic lavas. The following sections discuss similarities in features and processes in the emplacement of low-silica lava flows and the emplacement of the Cordón Caulle rhyolite flow. Contrasts with the emplacement of more crystalline silicic lavas are also discussed, as well as the implication of this work for the interpretation of volcanic facies.

## 6.1 Discussion

### *6.1.1 Similarities between features of mafic and silicic lava flows*

The advance of a cooling-limited lava flow can be controlled in the latter phases of emplacement by the lavas surface crust (Castruccio et al., 2013). As was shown in Section 4, the surface crust controlled the latter advance of both the 2001 Mt Etna basaltic lava flow, and the 2011-2012 Cordón Caulle rhyolitic lava flow, generating the characteristic features that formed during emplacement. There are many examples of a surface crust influencing the latter emplacement of mafic lava flows (e.g. Kilburn, 1993; Dance et al., 2001; Hon, 2003; Kerr and Lyman, 2007; Castruccio et al., 2013; Castruccio and Contreras, 2016), but similar observations are rare for rhyolitic lava flows. In rhyolitic lava flows, the features formed include ogives, breakouts, pumice diapirs and surface spines. Mafic lavas show similar or comparable breakouts, ogives, and surface spines. However, pumice diapirs are not found, and instead, lava rising to the surface of 'a'ā lava flows forms squeeze-ups and tumuli (Walker, 1991; Applegarth et al., 2010c; Sheth et al., 2011). The following sections outline the possible similarities in the processes that lead to the formation of features of mafic and silicic lava flows.

#### 6.1.1.1 Breakouts

The breakouts from the Mt Etna lava show some similarities in formation process to the breakouts at Cordón Caulle. In both cases, the formation of breakouts is, in part, due to the continued supply of lava to stalled portions of the flow front, leading to a pressure increase and eventual rupturing of the surface crust, and for the case of Cordón Caulle this partly relates to post-effusion core lava drainage (Tuffen et al., 2013; Farquharson et al., 2015). The longest breakouts on the 2001 Mt Etna lava flow form a similar surface morphology to the original main channel, comprising 'a'ā clinker (Applegarth et al., 2010c). This is similar to the NE lobe of the Cordón Caulle lava flow,

which evolved into a 2 km long channel with a rubbly and blocky surface due to continued disruption of the surface crust. The formation of such lengthy breakouts at

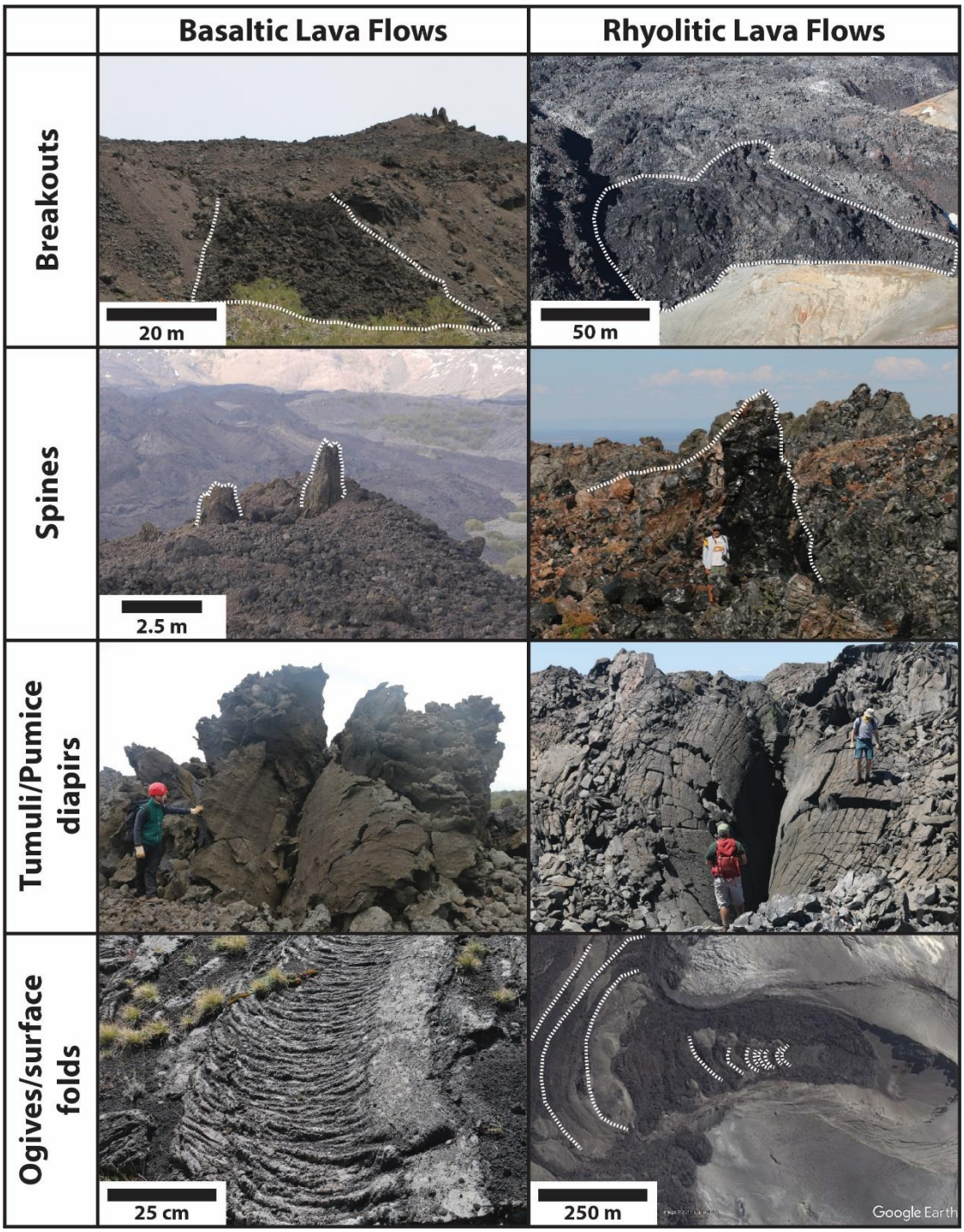


Figure 6.1: Common features in basaltic and silicic lava flows. Basaltic features are from the 2001 Mt Etna lava flow and the 1792-93 lava flow. Rhyolitic features are from the 2011-2012 Cordón Caulle lava flow, Big Glass Mountain and the Crater Glass flow.

Cordón Caulle and the 2001 Mt Etna lava flow, is likely reflective of the availability of fresh lava and supply to the breakout by a preferential thermal pathway, or lava tube, in the main flow.

#### 6.1.1.2 Core upwelling: spines, squeeze-ups and segregation structures

The surfaces of ancient lava flows are used to determine the processes that occurred during their emplacement; here I outline the processes that contribute to the formation of surface features in mafic and silicic lava flows. Spines are occasionally found at the surface of basaltic 'a'ā flows (e.g. Applegarth et al., 2010c) and are common on silicic blocky lava flows (Fig. 6.1), these spines are typically a few metres tall in both mafic and silicic lava flows (e.g. Fink, 1983; Latutrie et al., 2016). The spines form due to the ramping of lava with a yield strength to the surface of the flow along inclined shear planes (Christiansen and Lipman, 1966; Lockwood and Lipman, 1980; Harris et al., 2016; Latutrie et al., 2016). The deformation associated with spine extrusion results in a highly fractured zone adjacent to the spine (Latutrie et al., 2016).

The size of a spine does not seem to differ substantially depending on composition, with spines on the 2001 Mt Etna flow and the 2011-2012 Cordón Caulle flow rarely exceeding ~2 m in height. Spines observed on other silicic lava flows, such as the Glass Mountain rhyolite lava flow (Medicine Lake Volcano) and the Medicine Lake Dacite lava flow, are typically of a similar scale (i.e. a few metres tall). This similarity in spine scale could suggest that the size of a spine is controlled by the yield strength of the lava, a property that does not differ substantially between basalts and rhyolites, ~$10^4$ – $10^5$ Pa (Moore et al., 1978; Blake, 1990), as yield strength is based on the crystal network, rather than the viscosity.

Squeeze-ups and toothpaste lavas are found at numerous basaltic lava flows (Applegarth et al., 2010c; Sheth et al., 2011). Their morphology varies, but in the case

of the 2001 Mt Etna lava flow the squeeze-ups stand up from the surface of the flow and have an uneven spiny and blade-like morphology (Fig. 6.1), suggesting development of a yield strength (Applegarth et al., 2010c). In some cases these squeeze-ups can pile-up on top of a bocca to form what is termed a tumuli in Applegarth et al. (2010c). Their formation is similar to breakouts, whereby a pressure increase in the flow core leads to the extrusion of lava with a yield strength at the surface, forming a squeeze-up. In silicic lava flows the upwelling of core lava to the surface of a lava flow is associated with crease structure formation (Fig. 6.1), likely driven by extensional fracturing (Anderson and Fink, 1992), but also contributed to by buoyant rise of a vesicular core to form a pumice diapir in rhyolitic lava flows (Fink, 1983). Fracturing of the surface and buoyant upwelling are likely linked, with crease structures promoting buoyant upwelling, and vice versa.

Pumice diapirs in rhyolitic lavas form due to vesiculation of a layer and buoyant upwelling to the lavas surface (Fink, 1980b, 1983; Manley and Fink, 1987). Comparable features in the form of vesicle sheets, cylinders and pods (a.k.a. segregation pipes/veins) are observed within some basaltic lava flows, vesicle sheets are typically centimetre up to one metre in thickness/width (Goff, 1996; Caroff et al., 2000; Merle et al., 2005). Segregation structures form due to the separation of more evolved basalt from the cooling lava, this evolved lava typically vesiculates and is then able to diapirically rise towards the surface of a lava flow (Helz et al., 1989; Goff, 1996). The vesicle cylinders are then trapped by the lavas surface crust and do not reach the surface of the flow (Caroff et al., 2000). Unlike rhyolitic pumice diapirs, segregation structures form during cooling of the lava flow and the features themselves comprise more evolved basalt compared to the rest of the lava. Whether pumice diapirs in rhyolitic lava flows comprise more evolved lava than the surrounding flow is currently unclear.

### *6.1.2 Similarities between crystalline dacite and rhyolite lava flows*

Many silicic lavas are erupted with a high crystal content (Nakada et al., 1995; Blundy and Cashman, 2001; Cichy et al., 2011; Latutrie et al., 2016); therefore, it is worth drawing comparisons between the emplacement of crystalline lava flows and the crystal-poor Cordón Caulle lava flow. The Cordón Caulle lava flow advanced in a caterpillar track-like motion, whereby a flow core advanced and overrode the lavas collapsed flow front talus. Such advance styles have been observed during the emplacement of a dacitic lava flow at Santiaguito Volcano, Guatemala (Harris and Flynn, 2002). However, not all silicic lavas advance in this style; some lavas advance on a thin (~1 m thick) basal shear zone, with very little strain elsewhere in the lava flow (Smith, 1996; Latutrie et al., 2016). This basal shear zone would then migrate upwards as the lava cooled (Smith, 1996). As yet, there is no evidence that the Cordón Caulle lava flow advanced in this style, and the observations of thick layers of platy-fractured core lava at the flow front (Fig. 5.4), as well as the shear arrays in these fractures (Fig. 5.5), suggests that shear was accommodated throughout the lava flow. However, it is currently unclear whether such platy fractures relate to large-scale (hundreds of metres) of displacement, or small-scale (millimetre) displacement in the final stages of advance. The millimetre scale of the shear arrays within the platy fractures could indicate that the latter is more likely. The change in advance style from a caterpillar track advance to one in which the flow advances over a basal shear zone, similar to the advance of a glacier (Latutrie et al., 2016), could indicate that there is a critical threshold where the style of flow will change. This threshold could relate to the yield strength of the lava, which is in turn influenced by the lava crystallinity. Indeed, the alignment of elongate crystals, and subsequent shear-thinning behaviour, could promote the onset of basal shearing (Smith, 1996). Understanding such rheological

changes, and transitions in advance style, are important for predicting likely lava advance rates.

Ramping structures are observed in dissected silicic lava flows and are thought to form due to the ramping of core lava to the surface of the lava (Christiansen and Lipman, 1966; Manley, 1996; Smith, 1996; Latutrie et al., 2016). Whilst such features cannot be directly observed in the Cordón Caulle lava flow, until such time as the lava is eroded, their presence can be inferred from the formation of spines at the surface of a lava flow. Such ramps may be caused by the continued forward movement of lava behind a stalling and slowing flow front, thus they form under comparable conditions to ogives and breakouts.

### *6.1.3 Implications for the interpretation of volcanic facies*

Numerous studies have examined the emplacement dynamics of rhyolitic lava flows, suggesting the emplacement of some rhyolitic lava flows as a slowly spreading and collapsing, crystal-poor dome (e.g. Fink, 1983). While this may certainly be the case for some examples, observations from Cordón Caulle suggest that others may undergo more complex emplacement processes, more comparable to cooling-limited mafic lava flows and leading to the formation of breakouts from a stalled main flow. Such breakouts would have been supplied by preferential thermal pathways within the flow core, and similar thermal pathways could have been important in the development of some long-lived rhyolitic flows (e.g. Christiansen and Lipman, 1966; Bonnichsen, 1982; Bonnichsen and Kauffman, 1987; Manley, 1992, 1996). The observation of lobes at the margin of some extensive rhyolitic lava flows (Bonnichsen, 1982; Bonnichsen and Kauffman, 1987) could also suggest that these lavas formed breakouts from their margin. Distinguishing lobes from breakouts is important for understanding lava evolution. Lobes can form as a result of the splitting of the flow front (Applegarth et al.,

2010a) or due to the emplacement of multiple small flows. Breakouts, on the other hand, initiate an entirely new flow from an otherwise stalled or slowing lava flow (e.g. Blake and Bruno, 2000), sometimes changing the advance direction. Breakouts can also indicate endogenous flow to the front of the lava (Section 4), and pose a challenge when predicting areas of inundation.

Observations of the Cordón Caulle lava flow also inform the potential origin of the flow facies commonly observed in rhyolitic lava flows (Fink, 1980b; Fink and Manley, 1987; Manley and Fink, 1987). The origin of finely vesicular pumice (FVP) is somewhat controversial, being linked to eruption of a permeable foam (Eichelberger et al., 1986) or vesiculation after extrusion (Fink and Manley, 1987; Fink et al., 1992). However, observations of the recent Cordón Caulle eruption suggest a different hypothesis. Here, continuous explosions and ash emission at the vent acted to allow volatile escape (Schipper et al., 2013). This continued fracture and rehealing, typical of tuffisite vein formation (e.g. Stasiuk et al., 1996; Tuffen et al., 2003), could mean that the FVP represents a fractured and partially welded upper-conduit pumice breccia, similar to some tuffisite vein filling pyroclasts (Saubin et al., 2016). Analysis of the Cordón Caulle lava flow indicates that this lava lacks much of the textural complexity observed in some rhyolite lava flows (Schipper et al., 2015), which could relate to the slightly lower silica content of Cordon Caulle, 69 – 70 wt% $SiO_2$ (Castro et al., 2013), compared to other rhyolite lavas, up to 74% $SiO_2$ (Grove and Donnelly-Nolan, 1986; Donnelly-Nolan et al., 2016).

The work conducted here also raises questions about the origin of the coarsely vesicular pumice (CVP) observed in many rhyolite lava flows (Fink, 1983; Fink and Manley, 1987; Manley and Fink, 1987; Baum et al., 1989). The proposed model for CVP formation is slightly counter intuitive in that the volatiles required to drive vesiculation are thought to derive from a crystallising flow core (Fink and Manley, 1987;

Manley and Fink, 1987; Furukawa and Uno, 2015), but it would be expected that cooling and crystallisation would preferentially occur from the surface of the lava and propagate downwards. Thus, this model requires the upper OBS layer to be sufficiently cooled that crystals will not grow, yet sufficiently hot that vesicles can grow or migrate. The model further requires the migration of gases from the flow core, towards the surface. However, given bubble rise times in these flows are likely longer than the timescale of emplacement (of order months), gas migration must be along interconnected pores or fractures (Furukawa and Uno, 2015), these gases must then be halted by the upper OBS layer. It is difficult to imagine such fractures or pores remaining open during emplacement. Future work could further examine the origin of the CVP.

As well as aiding in the interpretation of ancient subaerial lavas, the observations presented here could aid in the interpretation of the recently erupted Havre submarine rhyolite lava flows (Carey et al., 2014; Jutzeler et al., 2014; Carey et al., 2018). Observations of these flows indicate similarities in lava morphology to the Cordón Caulle lava flow, despite a vast difference in the erupted water contents, 0.1 – 0.2% Cordón Caulle (Castro et al., 2013) and 0.9% Havre (Mundana and Carey, 2016). The flows at both Cordón Caulle and Havre show a tendency to form a narrower, more channelized, flow on steeper topography, and a broader, more fanned flow on shallower topography (Ikegami et al., 2017; Carey et al., 2018). Similar observations have been made of basaltic flows from Mt Etna (e.g. Kilburn and Lopes, 1988).

As well as considering the emplacement of silicic lavas on Earth, exploring the composition of lavas on other celestial bodies is vital to understanding planetary crustal evolution. Studies have attempted to determine the presence of silicic lava flows and domes on other planets (Fig. 6.2) based on flow morphology (Fink et al., 1993; Gregg et al., 1998; Stofan et al., 2000; Hawke et al., 2003; Warner and Gregg, 2003; Wilson

and Head, 2003), as well as infrared remote sensing (Christensen et al., 2005; Hagerty et al., 2006). Studies based on measurements of lava surface folds have proved relatively controversial, with some studies inferring high viscosities, and thus high-silica, lava flows on Mars (Fink, 1980a; Gregg et al., 1998). However, others have suggested these surface folds relate to the emplacement of a cool, viscous, basaltic lava flow (Theilig and Greeley, 1986; Warner and Gregg, 2003). It is further unclear whether the emplacement of pancake domes on Venus related to episodic emplacement of a silicic lava (Fink et al., 1993), or the prolonged eruption of a basaltic lava (Stofan et al., 2000).

The morphological observations at Cordón Caulle may aid with the identification of silicic lava flows. The identification, and morphology, of breakouts for example may aid in distinguishing a viscous basaltic lava from a silicic lava on mars, through morphological comparisons to lobes and breakouts at terrestrial mafic and silicic lava flows (Fig. 6.2A). Furthermore, the steep flow sides and fractured surface crusts observed on pancake domes on Venus, as well as the inference of a mobile, endogenously growing, interior after emplacement (Stofan et al., 2000) show similarities to the Cordón Caulle lava flow (Fig. 6.2). Such similarities could confirm that these lavas are silicic in composition (Fink et al., 1993), rather than basaltic (Stofan et al., 2000).

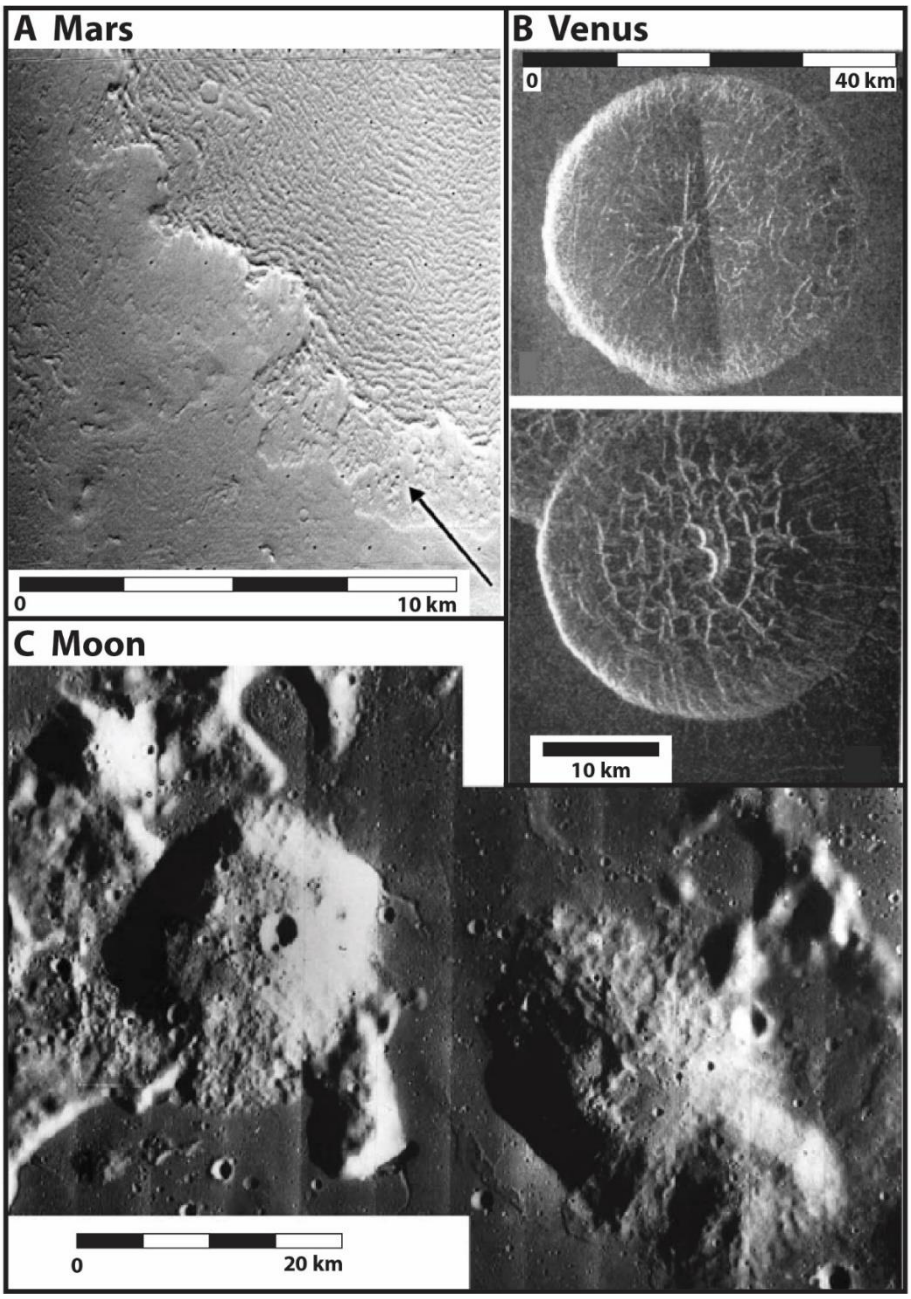


Figure 6.2: (**A**) Viscous lava flow on Mars, southwest of Arsia Mons, large-scale (~100m wavelength) ogives can be seen on the lavas surface in the top right of the image. Image centred at 1.91°S, 140.53°W. (VO F731A38.). The arrow points towards potential flow front lobes. From Warner and Gregg (2003). (**B**) Pancake domes on Venus, note the large fractures on the surface of the dome as well as the pits at the domes centre. Top: Magellan radar image centred at 2.9°S, 150.9° (F-MIDR 05S149, radar illumination from the left). Bottom: Magellan radar image centred at 29.7°S, 11.8° (F-MIDR 30S009, radar illumination from the left). Images from Stofan et al. (2000). (**C**) The Gruithuisen lava domes on the Moon. Portion of Lunar Orbiter IV 145 H1. From Wilson and Head (2003).

### *6.1.4 Commonalities in the emplacement of lava flows*

This work has demonstrated that there are, in many cases, controlling processes in the emplacement of lava flows at opposing ends of the compositional spectrum, which, in turn, generate comparable features. The formation of an effective cooled surface crust is evidently important in the development of both silicic and mafic lava flows. In both cases, the formation of the surface crust leads to an evident slowing in the lava advance rate that can ultimately lead to stalling. Furthermore, the formation of a surface crust influences the features generated, leading to the development of breakouts. The formation of a surface crust may further influence the ability of core lava to upwell to the surface of a lava to form squeeze-ups and tumuli in mafic lavas, and pumice diapirs in silicic lava flows.

The emplacement of both low and high-silica lava flows is highly dependent on the lava rheology, with an evident dependency on the lava crystallinity. Increased crystallinity within a lava changes its advance style, due to the associated onset of a yield strength. In the case of mafic lavas an increase in crystallinity can drive the transition from pahoehoe to 'a'ā (e.g. Cashman et al., 1999). In silicic lavas, high crystallinities lead to an advance style in which the bulk of the flow moves on a relatively thin basal shear zone (Latutrie et al., 2016), as opposed to a caterpillar track style of advance. Furthermore, the development of a crystal body in a rhyolite lava flow may inhibit vesicle growth in the flow core and diapiric rise to the lavas surface to form a pumice diapir.

The Cordón Caulle lava flow displayed varying morphologies depending on the slope that the flow was emplaced onto. The majority of the flow emplaced onto relatively shallow topography, and developed a complex morphology with multiple breakouts. However, the large NE breakout that advanced over steeper topography developed a

channelized morphology. Similarly, in mafic lava flows, those lavas that emplace on steeper topography tend to develop highly channelized flows (e.g. Kilburn and Guest, 1993; Applegarth et al., 2010c; Guest et al., 2012; Dietterich and Cashman, 2014) . Mafic lava flows that emplace on shallower gradients develop more complex flow field morphologies, e.g. the Holuhraun lava flow (Pedersen et al., 2017), leading to the formation of multiple channels, and promoting the stalling of flow lobes, consequently leading to breakout formation.

## 6.2 Summary

The overall aim of this work has been to improve upon our understanding of the emplacement of silicic lava flows through a detailed, multiscale analysis of the 2011-2012 Cordón Caulle rhyolitic lava flow. The findings from this work, outlined in the following section, have raised a number of questions that are pertinent to the study of lava flow emplacement, as well as the broader dynamics of silicic eruptions.

1. *What was the rheological control on the development of the Cordón Caulle lava flow, and how did it compare to other cooling-limited lava flows?*

Observations of the emplacement of the Cordón Caulle lava flow suggested that, in common with many basaltic lava flows, the lava formed a retarding surface crust that led to the stalling of flow advance; this was followed by breakout formation ~150 days from the eruption onset. Quantitative models of lava flow lengthening supported these observations by best-fitting flow advance data when crustal control was assumed (where the flow was topographically unconstrained). The application of these models further demonstrated the importance of considering flow observations, such as the presence of ogives and surface fractures, to help constrain model parameters and structure.

2. *What processes contributed to the formation and evolution of breakouts from the Cordón Caulle lava flow?*

Observations of the lava emplacement, as well as detailed analysis of the lava flow facies, revealed the processes that contributed to breakout formation, and evolution, at the Cordón Caulle lava flow. Continued supply of lava to the flow front along preferential thermal pathways resulted in a pressure increase and eventual rupturing of the surface crust, which was followed by the formation of breakouts. This pressure increase was likely compounded by limited vesicle growth in the lava core, possibly driven by post-effusion anhydrous crystal growth. Extensional fractures, associated with the spreading of flow front lobes, were also preferential sites of breakout formation.

Analysis of the morphology of breakouts at the Cordón Caulle lava flow indicated that breakouts can be classified into four types: domed, petaloid, rubbly and cleft-split. These are indicative of the degree to which a breakout has been supplied with lava and has advanced and inflated. Breakout advance and inflation was primarily controlled by the availability of lava supply, with the largest breakouts associated with supply from a preferential thermal pathway. The cessation of flow within a preferential thermal pathway may also end supply to breakouts in one portion of the flow. These observations suggest that not only can substantial endogenous flow occur within silicic lava flows, but it was instrumental in the flow development at Cordón Caulle.

3. *What conditions favour core upwelling to the surface of a silicic lava flow, instead of breakout formation?*

Studies of silicic lava flows have revealed that, rather than forming breakouts, some silicic flows develop crease structures and pumice diapirs at their surface, which is indicative of core lava upwelling to the surface of a lava. Only two sites of core

upwelling were identified during the development of the Cordón Caulle lava flow, suggesting that conditions at this flow were not favourable for core upwelling.

The formation of crease structures and pumice diapirs may be inhibited by the development of a pervasive surface crust capable of restricting buoyant rise to the surface of a lava flow. Furthermore, the crystallinity of lower silica rhyolites (68 – 69 wt% $SiO_2$), and dacites, may act to inhibit the formation of pumice diapirs, which are only observed in crystal-poor and silica-rich rhyolitic lava flows. The higher crystallinities could give viscosities one to two orders of magnitude higher than crystal-poor silicic lavas, potentially impeding vesicle growth, and extending buoyant upwelling timescales to greater than those of flow emplacement and cooling. Where pressurised core lava is unable to extrude through the surface of the lava flow, the flow may be more likely to form breakouts from the flow front. As such, whether a silicic flow develops diapirs at its surface may indicate whether breakouts could form.

4. *What commonalities exist in the emplacement of mafic and silicic lava flows?*

The observations of silicic lava flows presented here have demonstrated the complexity of their emplacement, with the evident transition from a volume-limited to a cooling-limited lava flow. The inferred emplacement processes, and the resulting flow structures formed, show remarkable similarities to those in mafic lava flows. The stalling of a lava flow and subsequent development of breakouts appears to be a process that can occur in both basaltic and rhyolitic lava flows. Furthermore, a controlling surface crust can dominate the latter emplacement stages of flows at either end of the compositional spectrum. The locations of breakouts in mafic and silicic flows appears dependent on the internal distribution of preferential thermal pathways or lava tubes, as well as weaknesses in the confining surface crust. Lava in the flow core is also clearly able to upwell to the surface of both mafic and silicic lava flows, with the

location of upwelling dependent on the strength of the surface crust as well as the internal driving pressure.

### 6.3 Future directions

While considerable syneruptive data were gathered during the 2011-2012 Cordón Caulle eruption, some potentially informative data were not gathered due to logistical, monetary, and safety constraints. In the event of a future, comparable, eruption attempts should be made to gather more syneruptive data to aid our understanding of silicic lava emplacement. Time-lapse photography of the lava flow would have proved useful for showing how the lava flow evolved, potentially exposing the processes involved in the moments just prior to breakout formation, such as flow inflation and fracture formation. High resolution thermal imagery could have also aided estimates of lava cooling and crust formation, as well as highlighting hot regions on the lava flow that could relate to fracture opening, breakout extrusion, or the upwelling of core lava to the surface of a lava flow. Repeat topographic surveys could also have proved useful for understanding flow evolution, potentially revealing patterns of inflation and drainage during emplacement. Such surveys could be conducted using terrestrial/aerial laser scanning, or using UAV based structure-from-motion (SfM) photogrammetry. Limited ground based SfM photogrammetry was conducted during the emplacement of the Cordón Caulle lava flow, and these data proved useful for identifying lava inflation (Tuffen et al., 2013; Farquharson et al., 2015). A good time series of satellite data was available for the Cordón Caulle eruption, but few high resolution (<10 m per pixel) satellite images were available. Since this eruption, a number of higher resolution satellite imaging platforms are now available, such as Planet Labs imagery (3 m resolution, near daily repeat time). Such imagery could prove invaluable for future monitoring of the emplacement of long-lived lava flows.

A primary aim of studying the processes inherent in lava flow emplacement is to contribute to robust hazard models capable of predicting the extent of future events. While numerous sophisticated models have been applied to the emplacement of basaltic lava flows (e.g. Crisci et al., 1986; Hidaka et al., 2005; Vicari et al., 2007; Hérault et al., 2011), few have been extended to the emplacement of silicic lava flows. Such models could be extended to the emplacement of silicic lava flows. However, given the infrequency of these eruptions, complex modelling of silicic lava flow emplacement may prove to be somewhat unnecessary.

Numerical models of lava emplacement cannot currently forecast breakout location. It may be that the inherent uncertainty of breakout formation may be impossible to incorporate into numerical models. However, given that breakouts can act to substantially increase the footprint of a lava flow, attempts could be made to predict locations of breakout formation during lava advance. Observations of a stalling flow front, partly due to topographic barriers, followed by substantial surface crust fracturing and lobe formation at Cordón Caulle could provide a useful indicator of breakout formation. Furthermore, advances in precision structure-from-motion photogrammetry, to generate high resolution (cm scale) DEMs, could be used to monitor inflation at a stalled flow front, an expected precursor to breakout formation. Such observations could help to predict syneruptive lava flow advance patterns.

A further difficulty with modelling the advance of a lava flow is the development of preferential thermal pathways and lava tubes, with some limited success in incorporating tube formation into the advance of basaltic lava flows (Hidaka et al., 2005). It is well documented that lava tubes are dominant in the emplacement of mafic lava flows (e.g. Guest et al., 1980; Polacci and Papale, 1997; Calvari and Pinkerton, 1998; Sakimoto and Zuber, 1998). Preferential thermal pathways certainly played an important role in the evolution of the Cordón Caulle lava flow, but it is unclear how

ubiquitous the role of preferential thermal pathways are in the development of other silicic lava flows. Detailed structural analysis of ancient, dissected silicic lava flows could reveal whether the formation of preferential thermal pathways in these flows is commonplace. Furthermore, the use of relaxation geospeedometry (e.g. Gottsmann and Dingwell, 2001; Gottsmann et al., 2004) could determine the cooling rate through a lava, which could reveal whether there was continued lava supply beneath a static surface crust, as this may contribute to slower than expected cooling rates in the lava.

## 6.4 Conclusions

The work presented within this thesis has aimed to compare the emplacement of mafic and rhyolitic cooling-limited lava flows, focussing on the emplacement of the Cordón Caulle rhyolite lava. A cooled surface crust was evidently dominant during the latter phases of emplacement at Cordón Caulle. This surface crust was capable of slowing flow advance and, ultimately, controlled the production of flow features such as breakouts, which formed because of the continued supply of lava to the stalled flow front along preferential thermal pathways. Furthermore, the formation of a coherent surface crust within a silicic lava flow can act to inhibit the upwelling of core lava to the surface of the lava, potentially increasing the likelihood of lateral breakout production. Breakouts can extend the flows footprint, facilitate drainage of the main channel, and present a challenge when assessing likely areas of inundation.

The growth of a crystal population within a silicic lava can also have a substantial impact on the development of a lava flow. Growth of anhydrous crystals within the flow can act to concentrate volatiles within the melt, promoting vesiculation. At Cordón Caulle, limited late stage vesiculation of the flow core likely contributed some of the pressure required to trigger breakouts, providing a possible mechanism by which breakouts formed in regions located away from preferential thermal pathways. The

crystallinity of the Cordón Caulle lava, as well as other lower-silica rhyolites and dacites, may have contributed to a higher than expected viscosity, potentially limiting the extensive pumice formation observed within some rhyolite lava flows, and slowing upwelling of core lava to the surface of a flow.

Finally, there are many similarities in the emplacement of mafic and silicic lava flows, such as the formation of breakouts, the influence of a surface crust, and the importance of preferential thermal pathways. However, the elevated viscosity in high-silica lava flows increases the importance of some processes, such as the influence of late stage vesiculation of the flow core, which can drive breakout formation and inflation, as well as the formation of pumice diapirs and large gas cavities in some silicic flows. The accumulation of pressure within the core of a silicic lava flow, either due to continued lava supply or volatile exsolution, has substantial hazard implications, potentially contributing to flow front collapse, rapid decompression of the flow interior, and the generation of a pyroclastic density current.

# “So long, and thanks for all the fish”

*– Douglas Adams, The Hitchhikers Guide to the Galaxy –*

# 7 References

Anderson, S. W., and Fink, J. H., 1990, The development and distribution of surface textures at the Mount St-Helens dome, *in* Fink, J. H., ed., Lava Flows and Domes: Emplacement Mechanisms and Hazard Implications, Volume 2, p. 25-46. doi:10.1007/978-3-642-74379-5_2.

-, 1992, Crease structures - indicators of emplacement rates and surface stress regimes of lava flows: Geological Society of America Bulletin, v. 104, no. 5, p. 615-625. doi:10.1130/0016-7606(1992)104<0615:csioer>2.3.co;2.

Anderson, S. W., Fink, J. H., and Rose, W. I., 1995, Mount St Helens and Santiaguito lava domes: The effect of short-term eruption rate on surface texture and degassing processes: Journal of Volcanology and Geothermal Research, v. 69, no. 1-2, p. 105-116. doi:10.1016/0377-0273(95)00022-4.

Anderson, S. W., McColley, S. M., Fink, J. H., and Hudson, R. K., 2005, The development of fluid instabilities and preferred pathways in lava flow interiors: Insights from analog experiments and fractal analysis: Geological Society of America Special Papers, v. 396, p. 147-161. doi:10.1130/0-8137-2396-5.147.

Anderson, S. W., Stofan, E. R., Smrekar, S. E., Guest, J. E., and Wood, B., 1999, Pulsed inflation of pahoehoe lava flows: implications for flood basalt emplacement: Earth and Planetary Science Letters, v. 168, no. 1-2, p. 7-18. doi:10.1016/s0012-821x(99)00044-8.

Applegarth, L. J., 2008, Complexity in lava flows : surface features and structural morphology: Thesis (PhD) Lancaster University, 451 p.

Applegarth, L. J., James, M. R., de Vries, B. V., and Pinkerton, H., 2010a, Influence of surface clinker on the crustal structures and dynamics of 'a'ā lava flows: Journal of Geophysical Research-Solid Earth, v. 115, p. 15. doi:10.1029/2009jb006965.

Applegarth, L. J., Pinkerton, H., James, M. R., and Calvari, S., 2010b, Lava flow superposition: The reactivation of flow units in compound 'a'ā flows: Journal of Volcanology and Geothermal Research, v. 194, no. 4, p. 100-106. doi:10.1016/j.jvolgeores.2010.05.001.

-, 2010c, Morphological complexities and hazards during the emplacement of channel-fed 'a'ā lava flow fields: A study of the 2001 lower flow field on Etna: Bulletin of Volcanology, v. 72, no. 6, p. 641-656. doi:10.1007/s00445-010-0351-1.

Applegarth, L. J., Tuffen, H., James, M. R., and Pinkerton, H., 2013a, Degassing-driven crystallisation in basalts: Earth-Science Reviews, v. 116, p. 1-16. doi:10.1016/j.earscirev.2012.10.007.

Applegarth, L. J., Tuffen, H., James, M. R., Pinkerton, H., and Cashman, K. V., 2013b, Direct observations of degassing-induced crystallization in basalts: Geology, v. 41, no. 2, p. 243-246. doi:10.1130/g33641.1.

Bagdassarov, N. S., and Dingwell, D. B., 1992, A rheological investigation of vesicular rhyolite: Journal of Volcanology and Geothermal Research, v. 50, no. 3, p. 307-322. doi:10.1016/0377-0273(92)90099-Y.

Barberi, F., Carapezza, M. L., Valenza, M., and Villari, L., 1993, The control of lava flow during the 1991–1992 eruption of Mt. Etna: Journal of Volcanology and Geothermal Research, v. 56, no. 1, p. 1-34. doi:10.1016/0377-0273(93)90048-V.

Baum, B. A., Krantz, W. B., Fink, J. H., and Dickinson, R. E., 1989, Taylor instability in rhyolite lava flows: Journal of Geophysical Research: Solid Earth, v. 94, no. B5, p. 5815-5828. doi:10.1029/JB094iB05p05815.

Befus, K. S., Manga, M., Gardner, J. E., and Williams, M., 2015, Ascent and emplacement dynamics of obsidian lavas inferred from microlite textures: Bulletin of Volcanology, v. 77, no. 10. doi:10.1007/s00445-015-0971-6.

Behncke, B., and Neri, M., 2003, The July–August 2001 eruption of Mt. Etna (Sicily): Bulletin of Volcanology, v. 65, no. 7, p. 461-476. doi:10.1007/s00445-003-0274-1.

Benn, D., and Evans, D. J., 2014, Glaciers and glaciation, Abingdon, UK, Routledge.

Bernstein, M., Pavez, A., Varley, N., Whelley, P., and Calder, E. S., 2013, Rhyolite lava dome growth styles at Chaiten Volcano, Chile (2008-2009): Interpretation of thermal imagery: Andean Geology, v. 40, no. 2, p. 295-309. doi:10.5027/andgeoV40n2-a07.

Bertin, D., Lara, L. E., Basualto, D., Amigo, Á., Cardona, C., Franco, L., Gil, F., and Lazo, J., 2015, High effusion rates of the Cordón Caulle 2011-12 eruption (Southern Andes) and their relation with the quasi-harmonic tremor: Geophysical Research Letters, v. 42, no. 17, p. 7054-7063. doi:10.1002/2015gl064624.

Bignami, C., Corradini, S., Merucci, L., de Michele, M., Raucoules, D., De Astis, G., Stramondo, S., and Piedra, J., 2014, Multisensor Satellite Monitoring of the 2011 Puyehue-Cordon Caulle Eruption: Ieee Journal of Selected Topics in

Applied Earth Observations and Remote Sensing, v. 7, no. 7, p. 2786-2796. doi:10.1109/jstars.2014.2320638.

Blake, S., 1990, Viscoplastic Models of Lava Domes, Lava Flows and Domes: Emplacement Mechanisms and Hazard Implication: Berlin, Heidelberg: Springer Berlin Heidelberg, p. 88-126. doi:10.1007/978-3-642-74379-5.

Blake, S., and Bruno, B. C., 2000, Modelling the emplacement of compound lava flows: Earth and Planetary Science Letters, v. 184, no. 1, p. 181-197. doi:10.1016/s0012-821x(00)00278-8.

Blundy, J., and Cashman, K., 2001, Ascent-driven crystallisation of dacite magmas at Mount St Helens, 1980-1986: Contributions to Mineralogy and Petrology, v. 140, no. 6, p. 631-650.

Blundy, J., Cashman, K., and Humphreys, M., 2006, Magma heating by decompression-driven crystallization beneath andesite volcanoes: Nature, v. 443, p. 76. doi:10.1038/nature05100.

Bonnichsen, B., 1982, Rhyolite lava flows in the Bruneau-Jarbidge eruptive center, southwestern Idaho: Cenozoic Geology of Idaho: Idaho Bureau of Mines and Geology Bulletin, v. 26, p. 283-320.

Bonnichsen, B., and Kauffman, D. F., 1987, Physical features of rhyolite lava flows in the Snake River Plain volcanic province, southwestern Idaho: Geological Society of America Special Papers, v. 212, p. 119-145. doi:10.1130/SPE212-p119.

Bottinga, Y., and Weill, D. F., 1972, The viscosity of magmatic silicate liquids; a model calculation: American Journal of Science, v. 272, no. 5, p. 438-475. doi:10.2475/ajs.272.5.438.

Breitkreuz, C., 2013, Spherulites and lithophysae-200 years of investigation on high-temperature crystallization domains in silica-rich volcanic rocks: Bulletin of Volcanology, v. 75, no. 4. doi:10.1007/s00445-013-0705-6.

Bridges, N. T., 1997, Ambient effects on basalt and rhyolite lavas under Venusian, subaerial, and subaqueous conditions: Journal of Geophysical Research: Planets (1991–2012), v. 102, no. E4, p. 9243-9255. doi:10.1029/97JE00390.

Calder, E. S., Luckett, R., Sparks, R. S. J., and Voight, B., 2002, Mechanisms of lava dome instability and generation of rockfalls and pyroclastic flows at Soufrière Hills Volcano, Montserrat: Geological Society, London, Memoirs, v. 21, no. 1, p. 173-190. doi:10.1144/gsl.mem.2002.021.01.08.

Calvari, S., and Pinkerton, H., 1998, Formation of lava tubes and extensive flow field during the 1991–1993 eruption of Mount Etna: Journal of Geophysical Research: Solid Earth, v. 103, no. B11, p. 27291-27301. doi:10.1029/97JB03388.

Campbell, J. B., and Wynne, R. H., 2011, Introduction to remote sensing, New York, USA, Guilford Press.

Carey, R., Soule, S. A., Manga, M., White, J., McPhie, J., Wysoczanski, R., Jutzeler, M., Tani, K., Yoerger, D., Fornari, D., Caratori-Tontini, F., Houghton, B., Mitchell, S., Ikegami, F., Conway, C., Murch, A., Fauria, K., Jones, M., Cahalan, R., and McKenzie, W., 2018, The largest deep-ocean silicic volcanic eruption

of the past century: Science Advances, v. 4, no. 1. doi:10.1126/sciadv.1701121.

Carey, R. J., Wysoczanski, R., Wunderman, R., and Jutzeler, M., 2014, Discovery of the Largest Historic Silicic Submarine Eruption: Eos, Transactions American Geophysical Union, v. 95, no. 19, p. 157-159. doi:10.1002/2014EO190001.

Caricchi, L., Burlini, L., Ulmer, P., Gerya, T., Vassalli, M., and Papale, P., 2007, Non-Newtonian rheology of crystal-bearing magmas and implications for magma ascent dynamics: Earth and Planetary Science Letters, v. 264, no. 3, p. 402-419. doi:10.1016/j.epsl.2007.09.032.

Caroff, M., Maury, R. C., Cotten, J., and Clément, J.-P., 2000, Segregation structures in vapor-differentiated basaltic flows: Bulletin of Volcanology, v. 62, no. 3, p. 171-187. doi:10.1007/s004450000077.

Cas, R., and Wright, J. V., 1987, Volcanic successions - modern and ancient : a geological approach to processes, products and successions, London; Sydney, Allen & Unwin.

Cashman, K., and Blundy, J., 2000, Degassing and crystallization of ascending andesite and dacite: Philosophical Transactions of the Royal Society of London Series a-Mathematical Physical and Engineering Sciences, v. 358, no. 1770, p. 1487-1513. doi:10.1098/rsta.2000.0600.

Cashman, K., Pinkerton, H., and Stephenson, J., 1998, Introduction to special section: Long lava flows: Journal of Geophysical Research-Solid Earth, v. 103, no. B11, p. 27281-27289. doi:10.1029/98jb01820.

Cashman, K. V., 1992, Groundmass crystallization of Mount St Helens dacite, 1980-1986 - a tool for interpreting shallow magmatic processes: Contributions to Mineralogy and Petrology, v. 109, no. 4, p. 431-449. doi:10.1007/bf00306547.

Cashman, K. V., Kerr, R. C., and Griffiths, R. W., 2006, A laboratory model of surface crust formation and disruption on lava flows through non-uniform channels: Bulletin of Volcanology, v. 68, no. 7-8, p. 753-770. doi:10.1007/s00445-005-0048-z.

Cashman, K. V., Mangan, M. T., and Newman, S., 1994, Surface degassing and modifications to vesicle size distributions in active basalt flows: Journal of Volcanology and Geothermal Research, v. 61, no. 1, p. 45-68. doi:10.1016/0377-0273(94)00015-8.

Cashman, K. V., Thornber, C., and Kauahikaua, J. P., 1999, Cooling and crystallization of lava in open channels, and the transition of Pahoehoe Lava to 'a'ā: Bulletin of Volcanology, v. 61, no. 5, p. 306-323. doi:10.1007/s004450050299.

Castro, J., Cashman, K., Joslin, N., and Olmsted, B., 2002a, Structural origin of large gas cavities in the Big Obsidian Flow, Newberry Volcano: Journal of Volcanology and Geothermal Research, v. 114, no. 3-4, p. 313-330. doi:10.1016/s0377-0273(01)00296-7.

Castro, J., and Cashman, K. V., 1999, Constraints on rheology of obsidian lavas based on mesoscopic folds: Journal of Structural Geology, v. 21, no. 7, p. 807-819. doi:10.1016/s0191-8141(99)00070-x.

Castro, J., Manga, M., and Cashman, K., 2002b, Dynamics of obsidian flows inferred from microstructures: insights from microlite preferred orientations: Earth and

Planetary Science Letters, v. 199, no. 1, p. 211-226. doi:10.1016/S0012-821X(02)00559-9.

Castro, J. M., Beck, P., Tuffen, H., Nichols, A. R. L., Dingwell, D. B., and Martin, M. C., 2008, Timescales of spherulite crystallization in obsidian inferred from water concentration profiles: American Mineralogist, v. 93, no. 11-12, p. 1816-1822. doi:10.2138/am.2008.2904.

Castro, J. M., Cordonnier, B., Schipper, C. I., Tuffen, H., Baumann, T. S., and Feisel, Y., 2016, Rapid laccolith intrusion driven by explosive volcanic eruption: Nature Communications, v. 7. doi:10.1038/ncomms13585.

Castro, J. M., Schipper, C. I., Mueller, S. P., Militzer, A. S., Amigo, A., Silva Parejas, C., and Jacob, D., 2013, Storage and eruption of near-liquidus rhyolite magma at Cordon Caulle, Chile: Bulletin of Volcanology, v. 75, no. 4, p. 1 - 17. doi:10.1007/s00445-013-0702-9.

Castruccio, A., and Contreras, M. A., 2016, The influence of effusion rate and rheology on lava flow dynamics and morphology: A case study from the 1971 and 1988–1990 eruptions at Villarrica and Lonquimay volcanoes, Southern Andes of Chile: Journal of Volcanology and Geothermal Research, v. 327, no. Supplement C, p. 469-483. doi:10.1016/j.jvolgeores.2016.09.015.

Castruccio, A., Rust, A. C., and Sparks, R. S. J., 2010, Rheology and flow of crystal-bearing lavas: Insights from analogue gravity currents: Earth and Planetary Science Letters, v. 297, no. 3-4, p. 471-480. doi:10.1016/j.epsl.2010.06.051.

-, 2013, Evolution of crust- and core-dominated lava flows using scaling analysis: Bulletin of Volcanology, v. 75, no. 1. doi:10.1007/s00445-012-0681-2.

Chevrel, M. O., Labroquère, J., Harris, A. J. L., and Rowland, S. K., 2018, PyFLOWGO: An open-source platform for simulation of channelized lava thermo-rheological properties: Computers & Geosciences, v. 111, no. Supplement C, p. 167-180. doi:10.1016/j.cageo.2017.11.009.

Chien, S., Cichy, B., Davies, A., Tran, D., Rabideau, G., Castano, R., Sherwood, R., Mandl, D., Frye, S., Shulman, S., Jones, J., and Grosvenor, S., 2005, An autonomous earth-observing sensorWeb: IEEE Intelligent Systems, v. 20, no. 3, p. 16-24. doi:10.1109/MIS.2005.40.

Christensen, P. R., McSween, H. Y., Bandfield, J. L., Ruff, S. W., Rogers, A. D., Hamilton, V. E., Gorelick, N., Wyatt, M. B., Jakosky, B. M., Kieffer, H. H., Malin, M. C., and Moersch, J. E., 2005, Evidence for magmatic evolution and diversity on Mars from infrared observations: Nature, v. 436, no. 7050, p. 504-509. doi:10.1038/nature03639.

Christiansen, R. L., and Lipman, P. W., 1966, Emplacement and thermal history of a rhyolite lava flow near Fortymile Canyon Southern Nevada: Geological Society of America Bulletin, v. 77, no. 7, p. 671-684. doi:10.1130/0016-7606(1966)77[671:eathoa]2.0.co;2.

Cichy, S. B., Botcharnikov, R. E., Holtz, F., and Behrens, H., 2011, Vesiculation and Microlite Crystallization Induced by Decompression: a Case Study of the 1991-1995 Mt Unzen Eruption (Japan): Journal of Petrology, v. 52, no. 7-8, p. 1469-1492. doi:10.1093/petrology/egq072.

Coltelli, M., Proietti, C., Branca, S., Marsella, M., Andronico, D., and Lodato, L., 2007, Analysis of the 2001 lava flow eruption of Mt. Etna from three-dimensional

mapping: Journal of Geophysical Research: Earth Surface, v. 112, no. F2, p. F02029. doi:10.1029/2006jf000598.

Connor, L. J., Connor, C. B., Meliksetian, K., and Savov, I., 2012, Probabilistic approach to modeling lava flow inundation: a lava flow hazard assessment for a nuclear facility in Armenia: Journal of Applied Volcanology, v. 1, no. 1, p. 3. doi:10.1186/2191-5040-1-3.

Coppola, D., Laiolo, M., Franchi, A., Massimetti, F., Cigolini, C., and Lara, L. E., 2017, Measuring effusion rates of obsidian lava flows by means of satellite thermal data: Journal of Volcanology and Geothermal Research. doi:10.1016/j.jvolgeores.2017.09.003.

Costa, A., 2005, Viscosity of high crystal content melts: Dependence on solid fraction: Geophysical Research Letters, v. 32, no. 22. doi:10.1029/2005gl024303.

Costa, A., Caricchi, L., and Bagdassarov, N., 2009, A model for the rheology of particle-bearing suspensions and partially molten rocks: Geochemistry Geophysics Geosystems, v. 10. doi:10.1029/2008gc002138.

Crisci, G. M., Gregorio, D., Pindaro, O., and Ranieri, G. A., 1986, Lava Flow Simulation Bv A Discrete Cellular Model: First Implementation: International Journal of Modelling and Simulation, v. 6, no. 4, p. 137-140. doi:10.1080/02286203.1986.11759975.

Dadd, K. A., 1992, Structures within large volume rhyolite lava flows of the Devonian Comerong volcanics, Southeastern Australia, and the Pleistocene Ngongotaha lava dome, New-Zealand: Journal of Volcanology and Geothermal Research, v. 54, no. 1-2, p. 33-51. doi:10.1016/0377-0273(92)90113-r.

Dance, M., Hancock, P. L., Sparks, R. S. J., and Wallman, A., 2001, Fracture and surface crust development in a Holocene pahoehoe lava flow on the Island of Tenerife, Canaries: Journal of Structural Geology, v. 23, no. 2-3, p. 165-182. doi:10.1016/s0191-8141(00)00089-4.

Davies, A. G., Chien, S., Wright, R., Miklius, A., Kyle, P. R., Welsh, M., Johnson, J. B., Tran, D., Schaffer, S. R., and Sherwood, R., 2006, Sensor web enables rapid response to volcanic activity: Eos, Transactions American Geophysical Union, v. 87, no. 1, p. 1-5. doi:10.1029/2006EO010002.

de Silva, S. L., Self, S., Francis, P. W., Drake, R. E., and Carlos, R. R., 1994, Effusive silicic volcanism in the Central Andes: The Chao dacite and other young lavas of the Altiplano-Puna Volcanic Complex: Journal of Geophysical Research: Solid Earth, v. 99, no. B9, p. 17805-17825. doi:10.1029/94JB00652.

Degraff, J. M., and Aydin, A., 1993, Effect of thermal regime on growth increment and spacing of contraction joints in basaltic lava: Journal of Geophysical Research-Solid Earth, v. 98, no. B4, p. 6411-6430. doi:10.1029/92jb01709.

DeGroat-Nelson, P. J., Cameron, B. I., Fink, J. H., and Holloway, J. R., 2001, Hydrogen isotope analysis of rehydrated silicic lavas: implications for eruption mechanisms: Earth and Planetary Science Letters, v. 185, no. 3-4, p. 331-341. doi:10.1016/s0012-821x(00)00379-4.

Dietterich, H. R., and Cashman, K. V., 2014, Channel networks within lava flows: Formation, evolution, and implications for flow behavior: Journal of Geophysical Research-Earth Surface, v. 119, no. 8, p. 1704-1724. doi:10.1002/2014jf003103.

Dietterich, H. R., Cashman, K. V., Rust, A. C., and Lev, E., 2015, Diverting lava flows in the lab: Nature Geoscience, v. 8, no. 7, p. 494-496. doi:10.1038/ngeo2470.

Dietterich, H. R., Lev, E., Chen, J., Richardson, J. A., and Cashman, K. V., 2017, Benchmarking computational fluid dynamics models of lava flow simulation for hazard assessment, forecasting, and risk management: Journal of Applied Volcanology, v. 6, no. 1, p. 9. doi:10.1186/s13617-017-0061-x.

Dietterich, H. R., Poland, M. P., Schmidt, D. A., Cashman, K. V., Sherrod, D. R., and Espinosa, A. T., 2012, Tracking lava flow emplacement on the east rift zone of Kīlauea, Hawai'i, with synthetic aperture radar coherence: Geochemistry, Geophysics, Geosystems, v. 13, no. 5, p. Q05001. doi:10.1029/2011GC004016.

Digenis, C. J., Lencioni, D. E., and Bicknell, W. E., New Millennium EO-1 Advanced Land Imager, *in* Proceedings SPIE Conference on Earth Observing Systems III1998, p. 49-55. doi:10.1117/12.325668.

DigitalGlobe, 2012, WorldView-2 Pan_MS1_MS2 scene 103001001234BC00, 10/04/2012: Accessed from Google Earth.

-, 2015, WorldView-2 Pan_MS1_MS2 scene 103001003D539F00, 27/02/2015: Accessed from Google Earth.

Dingwell, D. B., 1989, Effect of fluorine on the viscosity of diopside liquid: American Mineralogist, v. 74, no. 3-4, p. 333-338.

Dingwell, D. B., and Hess, K. U., 1998, Melt viscosities in the system Na-Fe-Si-O-F-Cl: Contrasting effects of F and Cl in alkaline melts: American Mineralogist, v. 83, no. 9-10, p. 1016-1021.

Dingwell, D. B., Scarfe, C. M., and Cronin, D. J., 1985, The effect of fluorine on viscosities in the system Na2O-Al2O3-SiO2 - implications for phonolites, trachytes and rhyolites: American Mineralogist, v. 70, no. 1-2, p. 80-87.

Donaldson, C. H., 1979, An experimental investigation of the delay in nucleation of olivine in Mafic Magmas: Contributions to Mineralogy and Petrology, v. 69, no. 1, p. 21-32. doi:10.1007/bf00375191.

Donnelly-Nolan, J. M., Champion, D. E., and Grove, T. L., 2016, Late Holocene volcanism at Medicine Lake Volcano, northern California Cascades: US Geological Survey, 2330-7102.

Duraiswami, R. A., Dole, G., and Bondre, N., 2003, Slabby pahoehoe from the western Deccan Volcanic Province: evidence for incipient pahoehoe-aa transitions: Journal of Volcanology and Geothermal Research, v. 121, no. 3-4, p. 195-217. doi:10.1016/s0377-0273(02)00411-0.

Durham, W., Mirkovich, V., and Heard, H., 1987, Thermal diffusivity of igneous rocks at elevated pressure and temperature: Journal of Geophysical Research: Solid Earth (1978–2012), v. 92, no. B11, p. 11615-11634.

Eichelberger, J. C., 1975, Origin of andesite and dacite: Evidence of mixing at Glass Mountain in California and at other circum-Pacific volcanoes: GSA Bulletin, v. 86, no. 10, p. 1381-1391. doi:10.1130/0016-7606(1975)86<1381:OOAADE>2.0.CO;2.

Eichelberger, J. C., 1995, Silicic volcanism - ascent of viscous magmas from crustal reservoirs: Annual Review of Earth and Planetary Sciences, v. 23, p. 41-63. doi:10.1146/annurev.earth.23.1.41.

Eichelberger, J. C., Carrigan, C. R., Westrich, H. R., and Price, R. H., 1986, Non-explosive silicic volcanism: Nature, v. 323, no. 6089, p. 598-602. doi:10.1038/323598a0.

Eichelberger, J. C., Lysne, P. C., and Younker, L. W., 1984, Research drilling at Inyo Domes, Long Valley Caldera, California: Eos, Transactions American Geophysical Union, v. 65, no. 39, p. 721-725. doi:10.1029/EO065i039p00721.

Elkhrachy, I., 2017, Vertical accuracy assessment for SRTM and ASTER Digital Elevation Models: A case study of Najran city, Saudi Arabia: Ain Shams Engineering Journal. doi:10.1016/j.asej.2017.01.007.

Fagents, S. A., and Thordarson, T., 2007, Rootless volcanic cones in Iceland and on Mars, *in* Chapman, M., ed., The Geology of Mars: Evidence from Earth-Based Analogs: Cambridge, Cambridge University Press, p. 151-177. doi:DOI: 10.1017/CBO9780511536014.007.

Farquharson, J. I., James, M. R., and Tuffen, H., 2015, Examining rhyolite lava flow dynamics through photo-based 3D reconstructions of the 2011–2012 lava flowfield at Cordón-Caulle, Chile: Journal of Volcanology and Geothermal Research, v. 304, p. 336-348. doi:10.1016/j.jvolgeores.2015.09.004.

Favalli, M., Harris, A. J. L., Fornaciai, A., Pareschi, M. T., and Mazzarini, F., 2010, The distal segment of Etna's 2001 basaltic lava flow: Bulletin of Volcanology, v. 72, no. 1, p. 119-127. doi:10.1007/s00445-009-0300-z.

Fiege, A., and Cichy, S. B., 2015, Experimental constraints on bubble formation and growth during magma ascent: A review, American Mineralogist, Volume 100, p. 2426. doi:10.2138/am-2015-5296.

Fierstein, J., and Hildreth, W., 1992, The plinian eruptions of 1912 at Novarupta, Katmai National Park, Alaska: Bulletin of Volcanology, v. 54, no. 8, p. 646-684. doi:10.1007/bf00430778.

Fierstein, J., Hildreth, W., and Calvert, A. T., 2011, Eruptive history of South Sister, Oregon Cascades: Journal of Volcanology and Geothermal Research, v. 207, no. 3, p. 145-179. doi:10.1016/j.jvolgeores.2011.06.003.

Fink, J., 1980a, Surface folding and viscosity of rhyolite flows: Geology, v. 8, no. 5, p. 250-254. doi:10.1130/0091-7613(1980)8<250:sfavor>2.0.co;2.

Fink, J. H., 1980b, Gravity instability in the Holocene Big and Little Glass Mountain rhyolitic obsidian flows, northern California: Tectonophysics, v. 66, no. 1-3, p. 147-166. doi:10.1016/0040-1951(80)90043-8.

-, 1983, Structure and emplacement of a rhyolitic obsidian flow - Little Glass Mountain, Medicine Lake Highland, northern California: Geological Society of America Bulletin, v. 94, no. 3, p. 362-380. doi:10.1130/0016-7606(1983)94<362:saeoar>2.0.co;2.

Fink, J. H., 1993, The emplacement of silicic lava flows and associated hazards, *in* Kilburn, C. R. J., and Luongo, G., eds., Active lavas: monitoring and modelling, UCL Press, p. 5-21.

Fink, J. H., and Anderson, S. W., 2000, Lava domes and coulees: Encyclopedia of volcanoes, p. 307-319.

Fink, J. H., Anderson, S. W., and Manley, C. R., 1992, Textural constraints on effusive silicic volcanism - beyond the permeable foam model: Journal of Geophysical Research-Solid Earth, v. 97, no. B6, p. 9073-9083. doi:10.1029/92jb00416.

Fink, J. H., Bridges, N. T., and Grimm, R. E., 1993, Shapes of Venusian “pancake” domes imply episodic emplacement and silicic composition: Geophysical Research Letters, v. 20, no. 4, p. 261-264. doi:10.1029/92GL03010.

Fink, J. H., and Fletcher, R. C., 1978, Ropy pahoehoe: Surface folding of a viscous fluid: Journal of Volcanology and Geothermal Research, v. 4, no. 1–2, p. 151-170. doi:10.1016/0377-0273(78)90034-3.

Fink, J. H., and Griffiths, R. W., 1990, Radial spreading of viscous gravity currents with solidifying crust: Journal of Fluid Mechanics, v. 221, p. 485-509. doi:10.1017/s0022112090003640.

Fink, J. H., and Griffiths, R. W., 1998, Morphology, eruption rates, and rheology of lava domes: Insights from laboratory models: Journal of Geophysical Research: Solid Earth, v. 103, no. B1, p. 527-545. doi:10.1029/97jb02838.

Fink, J. H., and Kieffer, S. W., 1993, Estimate of pyroclastic flow velocities resulting from explosive decompression of lava domes: Nature, v. 363, p. 612. doi:10.1038/363612a0.

Fink, J. H., and Manley, C. R., 1987, Origin of pumiceous and glassy textures in rhyolite flows and domes: Geological Society of America Special Papers, v. 212, p. 77-88. doi:10.1130/SPE212-p77.

Fonstad, M. A., Dietrich, J. T., Courville, B. C., Jensen, J. L., and Carbonneau, P. E., 2013, Topographic structure from motion: a new development in photogrammetric measurement: Earth Surface Processes and Landforms, v. 38, no. 4, p. 421-430. doi:10.1002/esp.3366.

Forbes, A. E. S., Blake, S., McGarvie, D. W., and Tuffen, H., 2012, Pseudopillow fracture systems in lavas: Insights into cooling mechanisms and environments from lava flow fractures: Journal of Volcanology and Geothermal Research, v. 245, p. 68-80. doi:10.1016/j.jvolgeores.2012.07.007.

Forbes, A. E. S., Blake, S., Tuffen, H., and Wilson, A., 2014, Fractures in a trachyandesitic lava at Öræfajökull, Iceland, used to infer subglacial emplacement in 1727–8 eruption: Journal of Volcanology and Geothermal Research, v. 288, no. 0, p. 8-18. doi:10.1016/j.jvolgeores.2014.10.004.

Friedman, I., Long, W., and Smith, R. L., 1963, Viscosity and water content of rhyolite glass: Journal of Geophysical Research, v. 68, no. 24, p. 6523-6535. doi:10.1029/JZ068i024p06523.

Furukawa, K., and Uno, K., 2015, Origin and deformation of high porosity bands in the Takanoobane Rhyolite lava of Aso volcano, Japan: Journal of Volcanology and Geothermal Research, v. 305, p. 76-83. doi:10.1016/j.jvolgeores.2015.09.021.

Furukawa, K., Uno, K., and Miyagi, I., 2010, Mechanisms of oxidation and degassing in the Takanoobane rhyolite lava of Aso Volcano, Japan: Journal of Volcanology and Geothermal Research, v. 198, no. 3–4, p. 348-354. doi:10.1016/j.jvolgeores.2010.09.015.

Ginibre, C., Kronz, A., and Wörner, G., 2002, High-resolution quantitative imaging of plagioclase composition using accumulated backscattered electron images: new constraints on oscillatory zoning: Contributions to Mineralogy and Petrology, v. 142, no. 4, p. 436-448. doi:10.1007/s004100100298.

Giordano, D., Romano, C., Dingwell, D. B., Poe, B., and Behrens, H., 2004, The combined effects of water and fluorine on the viscosity of silicic magmas: Geochimica Et Cosmochimica Acta, v. 68, no. 24, p. 5159-5168. doi:10.1016/j.gca.2004.08.012.

Giordano, D., Russell, J. K., and Dingwell, D. B., 2008, Viscosity of magmatic liquids: A model: Earth and Planetary Science Letters, v. 271, no. 1-4, p. 123-134. doi:10.1016/j.epsl.2008.03.038.

Global Volcanism Program, 2012, Report on Puyehue-Cordón Caulle (Chile), Weekly Volcanic Activity Report, 18 April-24 April 2012: Smithsonian Institution and US Geological Survey.

Goff, F., 1996, Vesicle cylinders in vapor-differentiated basalt flows: Journal of Volcanology and Geothermal Research, v. 71, no. 2, p. 167-185. doi:10.1016/0377-0273(95)00073-9.

Gottsmann, J., and Dingwell, D. B., 2001, The cooling of frontal flow ramps: a calorimetric study on the Rocche Rosse rhyolite flow, Lipari, Aeolian Islands, Italy: Terra Nova, v. 13, no. 3, p. 157-164. doi:10.1046/j.1365-3121.2001.00332.x.

Gottsmann, J., Harris, A. J. L., and Dingwell, D. B., 2004, Thermal history of Hawaiian pahoehoe lava crusts at the cylass transition: implications for flow rheology and emplacement: Earth and Planetary Science Letters, v. 228, no. 3-4, p. 343-353. doi:10.1016/j.epsl.2004.09.038.

Gregg, T. K. P., and Fink, J. H., 2000, A laboratory investigation into the effects of slope on lava flow morphology: Journal of Volcanology and Geothermal Research, v. 96, no. 3-4, p. 145-159. doi:10.1016/s0377-0273(99)00148-1.

Gregg, T. K. P., Fink, J. H., and Griffiths, R. W., 1998, Formation of multiple fold generations on lava flow surfaces: Influence of strain rate, cooling rate, and lava composition: Journal of Volcanology and Geothermal Research, v. 80, no. 3, p. 281-292. doi:10.1016/S0377-0273(97)00048-6.

Griffiths, R. W., 2000, The dynamics of lava flows: Annual Review of Fluid Mechanics, v. 32, p. 477-518. doi:10.1146/annurev.fluid.32.1.477.

Griffiths, R. W., and Fink, J. H., 1993, Effects of surface cooling on the spreading of lava flows and domes: Journal of Fluid Mechanics, v. 252, p. 667-702. doi:10.1017/s0022112093003933.

Griffiths, R. W., and Fink, J. H., 1997, Solidifying Bingham extrusions: a model for the growth of silicic lava domes: Journal of Fluid Mechanics, v. 347, p. 13-36.

Grove, T., and Donnelly-Nolan, J., 1986, The evolution of young silicic lavas at Medicine Lake Volcano, California: implications for the origin of compositional gaps in calc-alkaline series lavas: Contributions to Mineralogy and Petrology, v. 92, no. 3, p. 281-302.

Guest, J. E., Duncan, A. M., Stofan, E. R., and Anderson, S. W., 2012, Effect of slope on development of pahoehoe flow fields: Evidence from Mount Etna: Journal of Volcanology and Geothermal Research, v. 219, p. 52-62. doi:10.1016/j.jvolgeores.2012.01.006.

Guest, J. E., and Stofan, E. R., 2005, The significance of slab-crusted lava flows for understanding controls on flow emplacement at Mount Etna, Sicily: Journal of Volcanology and Geothermal Research, v. 142, no. 3-4, p. 193-205. doi:10.1016/j.jvolgeores.2004.09.003.

Guest, J. E., Underwood, J. R., and Greeley, R., 1980, Role of lava tubes in flows from the observatory-vent, 1971 eruption on Mount Etna: Geological Magazine, v. 117, no. 6, p. 601-606. doi:10.1017/S0016756800028946.

Guest, J. E., Wood, C., and Greeley, R., 1984, Lava tubes, terraces and megatumuli on the 1614–24 pahoehoe lava flow field, Mount Etna, sicily: Bulletin Volcanologique, v. 47, no. 3, p. 635-648. doi:10.1007/bf01961232.

Hagerty, J. J., Lawrence, D. J., Hawke, B. R., Vaniman, D. T., Elphic, R. C., and Feldman, W. C., 2006, Refined thorium abundances for lunar red spots: Implications for evolved, nonmare volcanism on the Moon: Journal of Geophysical Research: Planets, v. 111, no. E6. doi:10.1029/2005JE002592.

Hale, A. J., and Wadge, G., 2008, The transition from endogenous to exogenous growth of lava domes with the development of shear bands: Journal of Volcanology and Geothermal Research, v. 171, no. 3-4, p. 237-257. doi:10.1016/j.jvolgeores.2007.12.016.

Hamilton, C. W., Glaze, L. S., James, M. R., and Baloga, S. M., 2013, Topographic and stochastic influences on pahoehoe lava lobe emplacement: Bulletin of Volcanology, v. 75, no. 11. doi:10.1007/s00445-013-0756-8.

Harris, A., and Rowland, S., 2001, FLOWGO: a kinematic thermo-rheological model for lava flowing in a channel: Bulletin of Volcanology, v. 63, no. 1, p. 20-44. doi:10.1007/s004450000120.

Harris, A. J. L., Favalli, M., Mazzarini, F., and Hamilton, C. W., 2009, Construction dynamics of a lava channel: Bulletin of Volcanology, v. 71, no. 4, p. 459. doi:10.1007/s00445-008-0238-6.

Harris, A. J. L., and Flynn, L. P., 2002, The thermal stealth flows of Santiaguito dome, Guatemala: Implications for the cooling and emplacement of dacitic block-lava flows: Geological Society of America Bulletin, v. 114, no. 5, p. 533-546. doi:10.1130/0016-7606(2002)114<0533:ttsfos>2.0.co;2.

Harris, A. J. L., Flynn, L. P., Matias, O., Rose, W. I., and Cornejo, J., 2004, The evolution of an active silicic lava flow field: an ETM+ perspective: Journal of Volcanology and Geothermal Research, v. 135, no. 1-2, p. 147-168. doi:10.1016/j.jvolgeores.2003.12.011.

Harris, A. J. L., Rose, W. I., and Flynn, L. P., 2003, Temporal trends in lava dome extrusion at Santiaguito 1922-2000: Bulletin of Volcanology, v. 65, no. 2-3, p. 77-89. doi:10.1007/s00445-002-0243-0.

Harris, A. J. L., Rowland, S. K., Villeneuve, N., and Thordarson, T., 2016, Pāhoehoe, ʻaʻā, and block lava: an illustrated history of the nomenclature: Bulletin of Volcanology, v. 79, no. 1, p. 7. doi:10.1007/s00445-016-1075-7.

Hawke, B. R., Lawrence, D. J., Blewett, D. T., Lucey, P. G., Smith, G. A., Spudis, P. D., and Taylor, G. J., 2003, Hansteen Alpha: A volcanic construct in the lunar

highlands: Journal of Geophysical Research: Planets, v. 108, no. E7. doi:10.1029/2002JE002013.

Heiken, G., 1978, Plinian-type eruptions in the medicine lake highland, california, and the nature of the underlying magma: Journal of Volcanology and Geothermal Research, v. 4, no. 3, p. 375-402. doi:10.1016/0377-0273(78)90023-9.

Helz, R. T., Kirschenbaum, H., and Marinenko, J. W., 1989, Diapiric transfer of melt in Kilauea Iki lava lake, Hawaii: A quick, efficient process of igneous differentiation: Geological Society of America Bulletin, v. 101, no. 4, p. 578-594. doi:10.1130/0016-7606(1989)101<0578:DTOMIK>2.3.CO;2.

Hérault, A., Bilotta, G., Vicari, A., Rustico, E., and Del Negro, C., 2011, Numerical simulation of lava flow using a GPU SPH model: Annals of Geophysics, v. 54, no. 5, p. 600-620. doi:10.4401/ag-5343.

Hess, K. U., Dingweil, D. B., and Webb, S. L., 1995, The influence of excess alkalis on the viscosity of a haplogranitic melt, American Mineralogist, Volume 80, p. 297. doi:10.2138/am-1995-3-412.

Hidaka, M., Goto, A., Umino, S., and Fujita, E., 2005, VTFS project: Development of the lava flow simulation code LavaSIM with a model for three-dimensional convection, spreading, and solidification: Geochemistry, Geophysics, Geosystems, v. 6, no. 7, p. Q07008. doi:10.1029/2004GC000869.

Higgins, M. D., 2000, Measurement of crystal size distributions: American Mineralogist, v. 85, no. 9, p. 1105-1116. doi:10.2138/am-2000-8-901.

-, 2002, Closure in crystal size distributions (CSD), verification of CSD calculations, and the significance of CSD fans: American Mineralogist, v. 87, no. 1, p. 171-175. doi:10.2138/am-2002-0118.

Hildreth, W., and Fierstein, J., 2012, The Novarupta-Katmai eruption of 1912—largest eruption of the twentieth century; centennial perspectives: U.S. Geological Survey Professional Paper, v. 1791, p. 259 p.

Ho, A. M., and Cashman, K., 1997, Temperature constraints on the Ginkgo flow of the Columbia River Basalt Group: Geology, v. 25, no. 5, p. 403-406. doi:10.1130/0091-7613(1997)025<0403:TCOTGF>2.3.CO;2.

Holland, A. S. P., Watson, I. M., Phillips, J. C., Caricchi, L., and Dalton, M. P., 2011, Degassing processes during lava dome growth: Insights from Santiaguito lava dome, Guatemala: Journal of Volcanology and Geothermal Research, v. 202, no. 1–2, p. 153-166. doi:10.1016/j.jvolgeores.2011.02.004.

Hon, K., 2003, The transition from 'A'ā to Pāhoehoe crust on flows emplaced during the Pu'u 'Ō'ō-Kūpaianaha eruption: U.S. Geological Survey Professional Paper, v. 1676, p. 89-103.

Hon, K., Kauahikaua, J., Denlinger, R., and Mackay, K., 1994, Emplacement and inflation of pahoehoe sheet flows - observations and measurements of active lava flows on Kilauea Volcano, Hawaii: Geological Society of America Bulletin, v. 106, no. 3, p. 351-370. doi:10.1130/0016-7606(1994)106<0351:eaiops>2.3.co;2.

Hulme, G., 1974, The Interpretation of Lava Flow Morphology: Geophysical Journal of the Royal Astronomical Society, v. 39, no. 2, p. 361-383. doi:10.1111/j.1365-246X.1974.tb05460.x.

Huppert, H. E., 1982, Flow and instability of a viscous current down a slope: Nature, v. 300, no. 5891, p. 427-429. doi:10.1038/300427a0.

Ikegami, F., Carey, R. J., and McPhie, J., 2017, Topographical and structural controls on the Havre 2012 submarine rhyolitic lavas, IAVCEI 2017: Portland, OR.

INGV, C., 2001, Multidisciplinary approach yields insight into Mt. Etna eruption: Eos, Transactions American Geophysical Union, v. 82, no. 52, p. 653-656. doi:10.1029/01eo00376.

Ives, J. D., Sugden, D. E., and John, B. S., 1976, Glaciers and Landscape: A Geomorphological Approach, JSTOR.

James, M. R., and Robson, S., 2012, Straightforward reconstruction of 3D surfaces and topography with a camera: Accuracy and geoscience application: Journal of Geophysical Research: Earth Surface, v. 117, no. F3, p. 1 - 17. doi:10.1029/2011JF002289.

-, 2014, Sequential digital elevation models of active lava flows from ground-based stereo time-lapse imagery: ISPRS Journal of Photogrammetry and Remote Sensing, v. 97, no. Supplement C, p. 160-170. doi:10.1016/j.isprsjprs.2014.08.011.

James, M. R., and Varley, N., 2012, Identification of structural controls in an active lava dome with high resolution DEMs: Volcan de Colima, Mexico: Geophysical Research Letters, v. 39. doi:10.1029/2012gl054245.

Jeffreys, H., 1925, The flow of water in an inclined channel of rectangular section: Philosophical Magazine Series 6, v. 49, no. 293, p. 793-807. doi:10.1080/14786442508634662.

Jensen, R. A., 1993, Explosion craters and giant gas bubbles on Holocene rhyolite flows at Newberry Crater, Oregon: Oregon Geology, v. 55, no. 1, p. 13-19.

Johnson, R. W., and Smith, I. E., 1974, Volcanoes and rocks of St Andrew Strait, Papua New Guinea: Journal of the Geological Society of Australia, v. 21, no. 3, p. 333-351. doi:10.1080/00167617408728855.

Jutzeler, M., Marsh, R., Carey, R. J., White, J. D. L., Talling, P. J., and Karlstrom, L., 2014, On the fate of pumice rafts formed during the 2012 Havre submarine eruption: Nature Communications, v. 5, p. 3660. doi:10.1038/ncomms4660.

Katsui, Y., and Katz, H. R., 1967, Lateral fissure eruptions in the southern Andes of Chile: Journal of the Faculty of Science, Hokkaido University. Series 4, Geology and mineralogy, v. 13, no. 4, p. 433-448.

Kendrick, J. E., Lavallee, Y., Ferk, A., Perugini, D., Leonhardt, R., and Dingwell, D. B., 2012, Extreme frictional processes in the volcanic conduit of Mount St. Helens (USA) during the 2004-2008 eruption: Journal of Structural Geology, v. 38, p. 61-76. doi:10.1016/j.jsg.2011.10.003.

Kerr, R. C., and Lister, J. R., 1991, The effects of shape on crystal settling and on the rheology of magmas: Journal of Geology, v. 99, no. 3, p. 457-467. doi:10.1086/629506.

Kerr, R. C., and Lyman, A. W., 2007, Importance of surface crust strength during the flow of the 1988-1990 andesite lava of Lonquimay Volcano, Chile: Journal of

Geophysical Research-Solid Earth, v. 112, no. B3, p. B03209. doi:10.1029/2006jb004522.

Kilburn, C. R. J., 1981, Pahoehoe and AA-lavas - a discussion and continuation of the model of Peterson and Tilling: Journal of Volcanology and Geothermal Research, v. 11, no. 2-4, p. 373-382. doi:10.1016/0377-0273(81)90033-0.

-, 1993, Lava crusts, aa flow lengthening and the pahoehoe-aa transition, *in* Kilburn, C. R. J., and Luongo, G., eds., Active lava flows: monitoring and modelling, UCL Press, p. 263-277.

-, 2004, Fracturing as a quantitative indicator of lava flow dynamics: Journal of Volcanology and Geothermal Research, v. 132, no. 2-3, p. 209-224. doi:10.1016/s0377-0273(03)00346-9.

Kilburn, C. R. J., and Guest, J. E., 1993, Aa lavas of Mount Etna, Sicily, *in* Kilburn, C. R. J., and Luongo, G., eds., Active lavas: monitoring and modelling: London, UCL Press, p. 73-101.

Kilburn, C. R. J., and Lopes, R. M. C., 1988, The growth of AA lava flow-fields on Mount Etna, Sicily: Journal of Geophysical Research-Solid Earth and Planets, v. 93, no. B12, p. 14759-14772. doi:10.1029/JB093iB12p14759.

-, 1991, General patterns of flow field growth - aa and blocky lavas: Journal of Geophysical Research-Solid Earth, v. 96, no. B12, p. 19721-19732. doi:10.1029/91jb01924.

Klemetti, E. W., and Grunder, A. L., 2008, Volcanic evolution of Volcan Aucanquilcha: a long-lived dacite volcano in the Central Andes of northern Chile: Bulletin of Volcanology, v. 70, no. 5, p. 633-650. doi:10.1007/s00445-007-0158-x.

Kolzenburg, S., Favalli, M., Fornaciai, A., Isola, I., Harris, A. J. L., Nannipieri, L., and Giordano, D., 2016, Rapid Updating and Improvement of Airborne LIDAR DEMs Through Ground-Based SfM 3-D Modeling of Volcanic Features: IEEE Transactions on Geoscience and Remote Sensing, v. 54, no. 11, p. 6687-6699. doi:10.1109/TGRS.2016.2587798.

Kolzenburg, S., Russell, J. K., and Kennedy, L. A., 2013, Energetics of glass fragmentation: Experiments on synthetic and natural glasses: Geochemistry, Geophysics, Geosystems, v. 14, no. 11, p. 4936-4951. doi:10.1002/2013GC004819.

Laidley, R. A., and McKay, D. S., 1971, Geochemical examination of obsidians from Newberry Caldera, Oregon: Contributions to Mineralogy and Petrology, v. 30, no. 4, p. 336-342. doi:10.1007/bf00404728.

Lange, R. L., and Carmichael, I. S. E., 1990, Thermodynamic properties of silicate liquids with emphasis on density, thermal expansion and compressibility: Reviews in Mineralogy and Geochemistry, v. 24, no. 1, p. 25-64.

Lanzafame, G., Neri, M., Acocella, V., Billi, A., Funiciello, R., and Giordano, G., 2003, Structural features of the July–August 2001 Mount Etna eruption: evidence for a complex magma supply system: Journal of the Geological Society, v. 160, no. 4, p. 531-544. doi:10.1144/0016-764902-151.

Lara, L. E., Moreno, H., Naranjo, J. A., Matthews, S., and de Arce, C. P., 2006, Magmatic evolution of the Puyehue-Cordon Caulle volcanic complex (40 degrees S), Southern Andean Volcanic Zone: From shield to unusual rhyolitic fissure volcanism: Journal of Volcanology and Geothermal Research, v. 157, no. 4, p. 343-366. doi:10.1016/j.jvolgeores.2006.04.010.

Lara, L. E., Naranjo, J. A., and Moreno, H., 2004, Rhyodcacitic fissure eruption in Southern Andes (Cordon Caulle; 40.5 degrees S) after the 1960 (Mw : 9.5) Chilean earthquake: a structural interpretation: Journal of Volcanology and Geothermal Research, v. 138, no. 1-2, p. 127-138. doi:10.1016/j.jvolgeores.2004.06.009.

Latutrie, B., Harris, A., Médard, E., and Gurioli, L., 2016, Eruption and emplacement dynamics of a thick trachytic lava flow of the Sancy volcano (France): Bulletin of Volcanology, v. 79, no. 1, p. 4. doi:10.1007/s00445-016-1084-6.

Lavallée, Y., Dingwell, D. B., Johnson, J. B., Cimarelli, C., Hornby, A. J., Kendrick, J. E., von Aulock, F. W., Kennedy, B., Andrews, B. J., Wadsworth, F. B., Rhodes, E., and Chigna, G., 2015, Thermal vesiculation during volcanic eruptions: Nature, v. 528, no. 7583, p. 544-547. doi:10.1038/nature16153.

Lavallée, Y., Hess, K.-U., Cordonnier, B., and Bruce Dingwell, D., 2007, Non-Newtonian rheological law for highly crystalline dome lavas: Geology, v. 35, no. 9, p. 843-846. doi:10.1130/g23594a.1.

Lescinsky, D. T., and Fink, J. H., 2000, Lava and ice interaction at stratovolcanoes: Use of characteristic features to determine past glacial extents and future volcanic hazards: Journal of Geophysical Research: Solid Earth, v. 105, no. B10, p. 23711-23726. doi:10.1029/2000JB900214.

Lescinsky, D. T., and Merle, O., 2005, Extensional and compressional strain in lava flows and the formation of fractures in surface crust: Geological Society of America Special Papers, v. 396, p. 163-179. doi:10.1130/0-8137-2396-5.163.

Lev, E., and Hager, B. H., 2008, Rayleigh–Taylor instabilities with anisotropic lithospheric viscosity: Geophysical Journal International, v. 173, no. 3, p. 806-814. doi:10.1111/j.1365-246X.2008.03731.x.

Limaye, A., Drishti: a volume exploration and presentation tool, *in* Proceedings Proc Spie2012, Volume 8506, p. 85060X-85060X. doi:doi:10.1117/12.935640.

Linneman, S., and Borgia, A., 1993, The blocky andesitic lava flows of Arenal volcano, Costa Rica, *in* Fink, C. R. J., and Luongo, G., eds., Active lava flows: modelling and monitoring, UCL Press, p. 25-70.

Lipman, P. W., and Banks, N. G., 1987, Aa flow dynamics, Mauna Loa 1984: U.S. Geological Survey Professional Paper, v. 1350, p. 1527-1567.

Lister, J. R., 1992, Viscous flows down an inclined plane from point and line sources: Journal of Fluid Mechanics, v. 242, p. 631-653. doi:10.1017/s0022112092002520.

Llewellin, E. W., Mader, H. M., and Wilson, S. D. R., 2002, The rheology of a bubbly liquid: Proceedings of the Royal Society a-Mathematical Physical and Engineering Sciences, v. 458, no. 2020, p. 987-1016. doi:10.1098/rspa.2001.0924.

Lockwood, J. P., and Lipman, P. W., 1980, Recovery of datable charcoal beneath young lavas: Lessons from Hawaii: Bulletin Volcanologique, v. 43, no. 3, p. 609-615. doi:10.1007/bf02597697.

Loewen, M. W., Bindeman, I. N., and Melnik, O. E., 2017, Eruption mechanisms and short duration of large rhyolitic lava flows of Yellowstone: Earth and Planetary Science Letters, v. 458, p. 80-91. doi:doi.org/10.1016/j.epsl.2016.10.034.

Lofgren, G., 1971a, Experimentally Produced Devitrification Textures in Natural Rhyolitic Glass: Geological Society of America Bulletin, v. 82, no. 1, p. 111-124. doi:10.1130/0016-7606(1971)82[111:epdtin]2.0.co;2.

Lofgren, G., 1971b, Spherulitic textures in glassy and crystalline rocks: Journal of Geophysical Research, v. 76, no. 23, p. 5635-5648. doi:10.1029/JB076i023p05635.

Lyman, A. W., and Kerr, R. C., 2006, Effect of surface solidification on the emplacement of lava flows on a slope: Journal of Geophysical Research: Solid Earth, v. 111, no. B5, p. B05206. doi:10.1029/2005JB004133.

Lyman, A. W., Kerr, R. C., and Griffiths, R. W., 2005a, Effects of internal rheology and surface cooling on the emplacement of lava flows: Journal of Geophysical Research: Solid Earth, v. 110, no. B8. doi:10.1029/2005JB003643.

-, 2005b, Effects of internal rheology and surface cooling on the emplacement of lava flows: Journal of Geophysical Research-Solid Earth, v. 110, no. B8, p. B08207. doi:10.1029/2005jb003643.

Macdonald, G. A., 1953, Pahoehoe, AA, and block lava: American Journal of Science, v. 251, no. 3, p. 169-191. doi:10.2475/ajs.251.3.169.

Mader, H. M., Llewellin, E. W., and Mueller, S. P., 2013, The rheology of two-phase magmas: A review and analysis: Journal of Volcanology and Geothermal Research, v. 257, p. 135-158. doi:10.1016/j.jvolgeores.2013.02.014.

Magnall, N., James, M. R., Tuffen, H., and Vye-Brown, C., 2017, Emplacing a Cooling-Limited Rhyolite Lava Flow: Similarities with Basaltic Lava Flows: Frontiers in Earth Science, v. 5, no. 44. doi:10.3389/feart.2017.00044.

Magnall, N., James, M. R., Tuffen, H., Vye-Brown, C., Schipper, C. I., Castro, J., and Davies, A. G., 2018, The origin and evolution of breakouts in a cooling-limited rhyolite lava flow: Geological Society of America Bulletin, p. (submitted).

Major, J. J., and Lara, L. E., 2013, Overview of Chaiten Volcano, Chile, and its 2008-2009 eruption: Andean Geology, v. 40, no. 2, p. 196-215. doi:10.5027/andgeoV40n2-a01.

Malin, M. C., and Sheridan, M. F., 1982, Computer-Assisted Mapping of Pyroclastic Surges: Science, v. 217, no. 4560, p. 637-640. doi:10.1126/science.217.4560.637.

Manley, C. R., 1992, Extended cooling and viscous-flow of large, hot rhyolite lavas - implications of numerical modeling results: Journal of Volcanology and Geothermal Research, v. 53, no. 1-4, p. 27-46. doi:10.1016/0377-0273(92)90072-l.

-, 1996, Physical volcanology of a voluminous rhyolite lava flow: The Badlands lava, Owyhee plateau, southwestern Idaho: Journal of Volcanology and Geothermal Research, v. 71, no. 2-4, p. 129-153. doi:10.1016/0377-0273(95)00066-6.

Manley, C. R., and Fink, J. H., 1987, Internal textures of rhyolite flows as revealed by research drilling: Geology, v. 15, no. 6, p. 549-552. doi:10.1130/0091-7613(1987)15<549:itorfa>2.0.co;2.

Maron, S. H., and Pierce, P. E., 1956, Application of ree-eyring generalized flow theory to suspensions of spherical particles: Journal of Colloid Science, v. 11, no. 1, p. 80-95. doi:10.1016/0095-8522(56)90023-X.

Marsh, B. D., 1981, On the crystallinity, probability of occurrence, and rheology of lava and magma: Contributions to Mineralogy and Petrology, v. 78, no. 1, p. 85-98. doi:10.1007/bf00371146.

Mattox, T. N., Heliker, C., Kauahikaua, J., and Hon, K., 1993, Development of the 1990 Kalapana Flow Field, Kilauea Volcano, Hawaii: Bulletin of Volcanology, v. 55, no. 6, p. 407-413. doi:10.1007/bf00302000.

Merle, R., Caroff, M., Girardeau, J., Cotten, J., and Guivel, C., 2005, Segregation vesicles, cylinders, and sheets in vapor-differentiated pillow lavas: examples from Tore-Madeira Rise and Chile Triple Junction: Journal of Volcanology and Geothermal Research, v. 141, no. 1–2, p. 109-122. doi:10.1016/j.jvolgeores.2004.09.007.

Moore, H., Arthur, D., and Schaber, G., 1978, Yield strengths of flows on the Earth, Mars, and Moon, *in* Proceedings Lunar and planetary science conference proceedings, Houston, Tex, 1978, Volume 3: New York, p. 3351-3378.

Mueller, S., Llewellin, E. W., and Mader, H. M., 2010, The rheology of suspensions of solid particles: Proceedings of the Royal Society A: Mathematical, Physical and Engineering Science, v. 466, no. 2116, p. 1201-1228. doi:10.1098/rspa.2009.0445.

-, 2011, The effect of particle shape on suspension viscosity and implications for magmatic flows: Geophysical Research Letters, v. 38, p. L13316. doi:10.1029/2011gl047167.

Mundana, R., and Carey, R. J., 2016, Havre 2012 Submarine Eruption: The Role of Hydrostatic Pressure on the Morphology of a Silicic Lava Flow, AGU Chapman Conference: Hobart, Tasmania, Australia.

Nakada, S., 2000, Hazards from pyroclastic flows and surges, *in* Sigurdsson, H., ed., Encyclopedia of Volcanoes, editado por Haraldur Sigurdsson, p. 945-956.

Nakada, S., Miyake, Y., Sato, H., Oshima, O., and Fujinawa, A., 1995, Endogenous growth of dacite dome at Unzen volcano (Japan), 1993-1994: Geology, v. 23, no. 2, p. 157-160. doi:10.1130/0091-7613(1995)023<0157:egodda>2.3.co;2.

Naranjo, J. A., Sparks, R. S. J., Stasiuk, M. V., Moreno, H., and Ablay, G. J., 1992, Morphological, structural and textural variations in the 1988-1990 andesite lava of Lonquimay volcano, Chile: Geological Magazine, v. 129, no. 6, p. 657-678. doi:10.1017/S0016756800008426.

NASA, 2011a, EO-1 ALI scene EO1A2330882011212110KF_1T: Image Courtesy of U.S. Geological Survey. 31/07/2011.

-, 2011b, EO-1 ALI scene EO1A2330882011230110KF_1T: Image Courtesy of U.S. Geological Survey. 18/08/2011.

-, 2011c, EO-1 ALI scene EO1A2330882011282110KF_1T: Image Courtesy of U.S. Geological Survey. 09/10/2011.

-, 2011d, EO-1 ALI scene EO1A2330882011308110KF_1T: Image Courtesy of U.S. Geological Survey. 04/11/2011.

-, 2011e, EO-1 ALI scene EO1A2330882011357110PF_1T: Image Courtesy of U.S. Geological Survey. 23/12/2011.

-, 2011f, Landsat 5 TM scene LT52330882011177COA00: Image Courtesy of U.S. Geological Survey. 26/06/2011.

-, 2012a, EO-1 ALI scene EO1A2330882012026110KF_1T: Image Courtesy of U.S. Geological Survey. 26/01/2012.

-, 2012b, Landsat 7 scene LE72320882012005EDC00: Image courtesy of the U.S. Geological Survey. 05/12/2012.

-, 2013, EO-1 ALI scene EO1A2330882013013110PF_1T: Image Courtesy of U.S. Geological Survey. 13/01/2013.

NASA/METI, 2011a, ASTER scene AST_L1T_00312272011145305_20150608212959: Image courtesy of the NASA Land Processes Distributed Active Archive Center (LP DAAC), USGS Earth Resources Observation and Science (EROS) Center. 27/12/2011. doi:10.5067/ASTER/AST_L1T.003.

-, 2011b, ASTER scene AST_L1T_00306272011034130_20150606124151: Image courtesy of the NASA Land Processes Distributed Active Archive Center (LP DAAC), USGS Earth Resources Observation and Science (EROS) Center. 27/06/2011. doi:10.5067/ASTER/AST_L1T.003.

-, 2011c, ASTER scene AST_L1T_00310242011145240_20150608034435: Image courtesy of the NASA Land Processes Distributed Active Archive Center (LP DAAC), USGS Earth Resources Observation and Science (EROS) Center. 24/10/2011. doi:10.5067/ASTER/AST_L1T.003.

-, 2012a, ASTER scene AST_L1T_00311272012145258_20150613151154: Image courtesy of the NASA Land Processes Distributed Active Archive Center (LP

DAAC), USGS Earth Resources Observation and Science (EROS) Center. 27/11/2012. doi:10.5067/ASTER/AST_L1T.003.

-, 2012b, ASTER scene AST_L1T_00306042012034740_20150611051208: Image courtesy of the NASA Land Processes Distributed Active Archive Center (LP DAAC), USGS Earth Resources Observation and Science (EROS) Center. 04/06/2012. doi:10.5067/ASTER/AST_L1T.003.

-, 2012c, ASTER scene AST_L1T_00302132012145257_20150609123045: Image courtesy of the NASA Land Processes Distributed Active Archive Center (LP DAAC), USGS Earth Resources Observation and Science (EROS) Center. 13/02/2012. doi:10.5067/ASTER/AST_L1T.003.

Nathenson, M., Donnelly-Nolan, J. M., Champion, D. E., and Lowenstern, J. B., 2007, Chronology of postglacial eruptive activity and calculation of eruption probabilities for Medicine Lake volcano, Northern California: US Geol. Surv. Sci. Inv. Rept, v. 5174.

Newman, S., and Lowenstern, J. B., 2002, VOLATILECALC: a silicate melt-H2O-CO2 solution model written in Visual Basic for excel: Computers & Geosciences, v. 28, no. 5, p. 597-604. doi:10.1016/s0098-3004(01)00081-4.

Nichols, R. L., 1939, Viscosity of Lava: The Journal of Geology, v. 47, no. 3, p. 290-302. doi:10.1086/624778.

Niethammer, U., Rothmund, S., Schwaderer, U., Zeman, J., and Joswig, M., 2010, Open source image-processing tools for low-cost UAV-based landslide investigations, International Archives of the Photogrammetry, Remote Sensing

and Spatial Information Sciences, Volume XXXVIII-1/C22: Zurich, Switzerland, p. 161-166.

Nikolakopoulos, K. G., Kamaratakis, E. K., and Chrysoulakis, N., 2006, SRTM vs ASTER elevation products. Comparison for two regions in Crete, Greece: International Journal of Remote Sensing, v. 27, no. 21, p. 4819-4838. doi:10.1080/01431160600835853.

Ochs, F. A., and Lange, R. A., 1999, The Density of Hydrous Magmatic Liquids: Science, v. 283, no. 5406, p. 1314-1317. doi:10.1126/science.283.5406.1314.

Pallister, J. S., Diefenbach, A. K., Burton, W. C., Munoz, J., Griswold, J. P., Lara, L. E., Lowenstern, J. B., and Valenzuela, C. E., 2013, The Chaiten rhyolite lava dome: Eruption sequence, lava dome volumes, rapid effusion rates and source of the rhyolite magma: Andean Geology, v. 40, no. 2, p. 277-294. doi:10.5027/andgeoV40n2-a06.

Peck, D. L., 1978, Cooling and vesiculation of Alae lava lake, Hawaii, Geological Survey professional paper, Volume 935, Government Printing Office.

Pedersen, G. B. M., Höskuldsson, A., Dürig, T., Thordarson, T., Jónsdóttir, I., Riishuus, M. S., Óskarsson, B. V., Dumont, S., Magnusson, E., Gudmundsson, M. T., Sigmundsson, F., Drouin, V. J. P. B., Gallagher, C., Askew, R., Gudnason, J., Moreland, W. M., Nikkola, P., Reynolds, H. I., and Schmith, J., 2017, Lava field evolution and emplacement dynamics of the 2014–2015 basaltic fissure eruption at Holuhraun, Iceland: Journal of Volcanology and Geothermal Research, v. 340, p. 155-169. doi:10.1016/j.jvolgeores.2017.02.027.

Peterson, D. W., and Tilling, R. I., 1980, Transition of basaltic lava from pahoehoe to AA, Kilauea Volcano, Hawaii - field observations and key factors: Journal of Volcanology and Geothermal Research, v. 7, no. 3-4, p. 271-293. doi:10.1016/0377-0273(80)90033-5.

Peterson, D. W., and Tilling, R. I., 2000, Lava flow hazards, *in* Sigurdsson, H., ed., Encyclopedia of Volcanoes, editado por Haraldur Sigurdsson, p. 957-972.

Pinkerton, H., 1987, Factors affecting the morphology of lava flows: Endeavour, v. 11, no. 2, p. 73-79. doi:10.1016/0160-9327(87)90241-9.

Pinkerton, H., and Sparks, R. S. J., 1976, The 1975 sub-terminal lavas, Mount Etna - case history of formation of a compound lava field: Journal of Volcanology and Geothermal Research, v. 1, no. 2, p. 167-182. doi:10.1016/0377-0273(76)90005-6.

-, 1978, Field-measurements of rheology of lava: Nature, v. 276, no. 5686, p. 383-385. doi:10.1038/276383a0.

Pinkerton, H., and Stevenson, R. J., 1992, Methods of determining the rheological properties of magmas at sub-liquidus temperatures: Journal of Volcanology and Geothermal Research, v. 53, no. 1, p. 47-66. doi:10.1016/0377-0273(92)90073-M.

Pinkerton, H., and Wilson, L., 1994, Factors controlling the lengths of channel-fed lava flows: Bulletin of Volcanology, v. 56, no. 2, p. 108-120. doi:10.1007/bf00304106.

Pistolesi, M., Cioni, R., Bonadonna, C., Elissondo, M., Baumann, V., Bertagnini, A., Chiari, L., Gonzales, R., Rosi, M., and Francalanci, L., 2015, Complex

dynamics of small-moderate volcanic events: the example of the 2011 rhyolitic Cordon Caulle eruption, Chile: Bulletin of Volcanology, v. 77, no. 1. doi:10.1007/s00445-014-0898-3.

Pistone, M., Caricchi, L., Ulmer, P., Burlini, L., Ardia, P., Reusser, E., Marone, F., and Arbaret, L., 2012, Deformation experiments of bubble- and crystal-bearing magmas: Rheological and microstructural analysis: Journal of Geophysical Research-Solid Earth, v. 117. doi:10.1029/2011jb008986.

Pistone, M., Whittington, A. G., Andrews, B. J., and Cottrell, E., 2017, Crystal-rich lava dome extrusion during vesiculation: An experimental study: Journal of Volcanology and Geothermal Research, v. 347, p. 1-14. doi:10.1016/j.jvolgeores.2017.06.018.

Polacci, M., and Papale, P., 1997, The evolution of lava flows from ephemeral vents at Mount Etna: Insights from vesicle distribution and morphological studies: Journal of Volcanology and Geothermal Research, v. 76, no. 1–2, p. 1-17. doi:10.1016/S0377-0273(96)00070-4.

Prata, A., and Rose, W. I., 2000, Volcanic ash hazards to aviation, *in* Sigurdsson, H., ed., Encyclopedia of Volcanoes, p. 915-930.

Reed, S. J. B., 2005, Electron microprobe analysis and scanning electron microscopy in geology, Cambridge, UK, Cambridge University Press.

Reynolds, M. A., Best, J., and Johnson, R. W., 1980, 1953-57 Eruption of Tuluman Volcano: Rhyolitic Volcanic Activity in the Northern Bismarck Sea, Geological Survey of Papua New Guinea.

Richardson, J. A., Connor, L., Connor, C., and Gallant, E., 2017, Probabilistically modeling lava flows with MOLASSES, V41B-02, presented at 2017 Fall Meeting, AGU, New Orleans, LA, 11-15 Dec.

Richet, P., Hovis, G., and Whittington, A., 2006, Water and magmas: Thermal effects of exsolution: Earth and Planetary Science Letters, v. 241, no. 3, p. 972-977. doi:10.1016/j.epsl.2005.10.015.

Romine, W., Whittington, A., Nabelek, P., and Hofmeister, A., 2012, Thermal diffusivity of rhyolitic glasses and melts: effects of temperature, crystals and dissolved water: Bulletin of Volcanology, v. 74, no. 10, p. 2273-2287. doi:10.1007/s00445-012-0661-6.

Romine, W. L., and Whittington, A. G., 2015, A simple model for the viscosity of rhyolites as a function of temperature, pressure and water content: Geochimica et Cosmochimica Acta, v. 170, no. Supplement C, p. 281-300. doi:10.1016/j.gca.2015.08.009.

Rose, W. I., 1987, Santa María, Guatemala: Bimodal soda-rich calc-alkalic stratovolcano: Journal of Volcanology and Geothermal Research, v. 33, no. 1-3, p. 109-129. doi:10.1016/0377-0273(87)90056-4.

Rossi, M. J., and Gudmundsson, A., 1996, The morphology and formation of flow-lobe tumuli on Icelandic shield volcanoes: Journal of Volcanology and Geothermal Research, v. 72, no. 3, p. 291-308. doi:10.1016/0377-0273(96)00014-5.

Rowland, S. K., and Walker, G. P. L., 1987, Toothpaste lava: Characteristics and origin of a lava structural type transitional between pahoehoe and aa: Bulletin of Volcanology, v. 49, no. 4, p. 631-641. doi:10.1007/bf01079968.

-, 1990, Pahoehoe and AA in Hawaii - volumetric flow-rate controls the lava structure: Bulletin of Volcanology, v. 52, no. 8, p. 615-628. doi:10.1007/bf00301212.

Rust, A. C., and Manga, M., 2002, Effects of bubble deformation on the viscosity of dilute suspensions: Journal of Non-Newtonian Fluid Mechanics, v. 104, no. 1, p. 53-63. doi:10.1016/S0377-0257(02)00013-7.

Ryan, G. A., Loughlin, S. C., James, M. R., Jones, L. D., Calder, E. S., Christopher, T., Strutt, M. H., and Wadge, G., 2010, Growth of the lava dome and extrusion rates at Soufrière Hills Volcano, Montserrat, West Indies: 2005–2008: Geophysical Research Letters, v. 37, no. 19. doi:10.1029/2009GL041477.

Saar, M. O., Manga, M., Cashman, K. V., and Fremouw, S., 2001, Numerical models of the onset of yield strength in crystal–melt suspensions: Earth and Planetary Science Letters, v. 187, no. 3–4, p. 367-379. doi:10.1016/S0012-821X(01)00289-8.

Sakimoto, S. E. H., and Zuber, M. T., 1998, Flow and convective cooling in lava tubes: Journal of Geophysical Research: Solid Earth, v. 103, no. B11, p. 27465-27487. doi:10.1029/97JB03108.

Saubin, E., Tuffen, H., Gurioli, L., Owen, J., Castro, J. M., Berlo, K., McGowan, E. M., Schipper, C. I., and Wehbe, K., 2016, Conduit Dynamics in Transitional Rhyolitic Activity Recorded by Tuffisite Vein Textures from the 2008–2009 Chaitén Eruption: Frontiers in Earth Science, v. 4, no. 59. doi:10.3389/feart.2016.00059.

Schipper, C. I., Castro, J., Tuffen, H., Wadsworth, F., Chappell, D., Pantoja, A., Simpson, M., and Le Ru, E., 2015, Cristobalite in the 2011–2012 Cordón Caulle

eruption (Chile): Bulletin of Volcanology, v. 77, no. 5, p. 1-19. doi:10.1007/s00445-015-0925-z.

Schipper, C. I., Castro, J. M., Tuffen, H., James, M. R., and How, P., 2013, Shallow vent architecture during hybrid explosive-effusive activity at Cordon Caulle (Chile, 2011-12): Evidence from direct observations and pyroclast textures: Journal of Volcanology and Geothermal Research, v. 262, p. 25-37. doi:10.1016/j.jvolgeores.2013.06.005.

Schipper, C. I., Mandon, C., Maksimenko, A., Castro, J. M., Conway, C. E., Hauer, P., Kirilova, M., and Kilgour, G., 2017, Vapor-phase cristobalite as a durable indicator of magmatic pore structure and halogen degassing: an example from White Island volcano (New Zealand): Bulletin of Volcanology, v. 79, no. 10, p. 74. doi:10.1007/s00445-017-1157-1.

Schneider, C. A., Rasband, W. S., and Eliceiri, K. W., 2012, NIH Image to ImageJ: 25 years of image analysis: Nature methods, v. 9, no. 7, p. 671-675. doi:doi:10.1038/nmeth.2089.

Schulze, F., Behrens, H., Holtz, F., Roux, J., and Johannes, W., 1996, The influence of H2O on the viscosity of a haplogranitic melt: American Mineralogist, v. 81, no. 9-10, p. 1155-1165. doi:10.2138/am-1996-9-1014.

Scott, W. E., 1987, Holocene rhyodacite eruptions on the flanks of South Sister volcano, Oregon, *in* Fink, J. H., ed., The Emplacement of Silicic Domes and Lava Flows, Geological Society of America.

Seaman, S. J., Dyar, M. D., and Marinkovic, N., 2009, The effects of heterogeneity in magma water concentration on the development of flow banding and

spherulites in rhyolitic lava: Journal of Volcanology and Geothermal Research, v. 183, no. 3–4, p. 157-169. doi:10.1016/j.jvolgeores.2009.03.001.

Sehlke, A., Whittington, A., Robert, B., Harris, A., Gurioli, L., and Médard, E., 2014, Pahoehoe to `a`a transition of Hawaiian lavas: an experimental study: Bulletin of Volcanology, v. 76, no. 11, p. 876. doi:10.1007/s00445-014-0876-9.

Seitz, S. M., Curless, B., Diebel, J., Scharstein, D., and Szeliski, R., A comparison and evaluation of multi-view stereo reconstruction algorithms, *in* Proceedings Computer vision and pattern recognition, 2006 IEEE Computer Society Conference on2006, Volume 1, IEEE, p. 519-528.

Self, S., Thordarson, T., Keszthelyi, L., Walker, G. P. L., Hon, K., Murphy, M. T., Long, P., and Finnemore, S., 1996, A new model for the emplacement of Columbia River basalts as large, inflated pahoehoe lava flow fields: Geophysical Research Letters, v. 23, no. 19, p. 2689-2692. doi:10.1029/96GL02450.

Sepulveda, F., Dorsch, K., Lahsen, A., Bender, S., and Palacios, C., 2004, Chemical and isotopic composition of geothermal discharges from the Puyehue-Cordon Caulle area (40.5 degrees S), Southern Chile: Geothermics, v. 33, no. 5, p. 655-673. doi:10.1016/j.geothermics.2003.10.005.

Sharp, T. G., Stevenson, R. J., and Dingwell, D. B., 1996, Microlites and "nanolites" in rhyolitic glass: microstructural and chemical characterization: Bulletin of Volcanology, v. 57, no. 8, p. 631-640. doi:10.1007/s004450050116.

Shaw, H. R., 1963, Obsidian-H2O viscosities at 100 and 200 bars in temperature range 700 to 900 °C: Journal of Geophysical Research, v. 68, no. 23, p. 6337-6343. doi:10.1029/JZ068i023p06337.

-, 1972, Viscosities of magmatic silicate liquids - empitical method of prediction: American Journal of Science, v. 272, no. 9, p. 870-893. doi:10.2475/ajs.272.9.870.

Shaw, H. R., Wright, T. L., Peck, D. L., and Okamura, R., 1968, The viscosity of basaltic magma - an analysis of field measurements in Makaopuhi Lava Lake Hawaii: American Journal of Science, v. 266, no. 4, p. 225-264. doi:10.2475/ajs.266.4.225.

Sheth, H. C., Ray, J. S., Kumar, A., Bhutani, R., and Awasthi, N., 2011, Toothpaste lava from the Barren Island volcano (Andaman Sea): Journal of Volcanology and Geothermal Research, v. 202, no. 1-2, p. 73-82. doi:10.1016/j.jvolgeores.2011.01.006.

Silva Parejas, C., Lara, L., Bertin, D., Amigo, A., and Orozco, G., 2012, The 2011-2012 eruption of Cordón Caulle volcano (Southern Andes): Evolution, crisis management and current hazards, EGU General Assembly Conference Abstracts, Volume 14: Vienna, Austria, p. 9382.

Simakin, A. G., Armienti, P., and Salova, T. P., 2000, Joint degassing and crystallization: Experimental study with a gradual pressure release: Geochemistry International, v. 38, no. 6, p. 523-534.

Singer, B. S., Jicha, B. R., Harper, M. A., Naranjo, J. A., Lara, L. E., and Moreno-Roa, H., 2008, Eruptive history, geochronology, and magmatic evolution of the Puyehue-Cordon Caulle volcanic complex, Chile: Geological Society of America Bulletin, v. 120, no. 5-6, p. 599-618. doi:10.1130/b26276.1.

Smets, B., d'Oreye, N., Kervyn, M., and Kervyn, F., 2017, Gas piston activity of the Nyiragongo lava lake: First insights from a Stereographic Time-Lapse Camera system: Journal of African Earth Sciences, v. 134, no. Supplement C, p. 874-887. doi:10.1016/j.jafrearsci.2016.04.010.

Smith, J. V., 1996, Ductile-brittle transition structures in the basal shear zone of a rhyolite lava flow, eastern Australia: Journal of Volcanology and Geothermal Research, v. 72, no. 3-4, p. 217-223. doi:10.1016/0377-0273(96)00009-1.

-, 2000, Textural evidence for dilatant (shear thickening) rheology of magma at high crystal concentrations: Journal of Volcanology and Geothermal Research, v. 99, no. 1, p. 1-7. doi:10.1016/S0377-0273(99)00191-2.

-, 2002, Structural analysis of flow-related textures in lavas: Earth-Science Reviews, v. 57, no. 3-4, p. 279-297. doi:10.1016/s0012-8252(01)00081-2.

Smith, J. V., and Houston, E. C., 1995, Structure of lava flows of the Nimbin rhyolite, Northeast New-South-Wales: Australian Journal of Earth Sciences, v. 42, no. 1, p. 69-74. doi:10.1080/08120099508728179.

Snavely, N., Seitz, S. M., and Szeliski, R., Photo tourism: exploring photo collections in 3D, *in* Proceedings ACM transactions on graphics (TOG)2006, Volume 25, ACM, p. 835-846.

-, 2008, Modeling the world from internet photo collections: International Journal of Computer Vision, v. 80, no. 2, p. 189-210. doi:10.1007/s11263-007-0107-3.

Soule, S. A., and Cashman, K. V., 2005, Shear rate dependence of the pahoehoe-to-'a'a transition: Analog experiments: Geology, v. 33, no. 5, p. 361-364. doi:10.1130/g21269.1.

Sparks, R. S. J., Barclay, J., Jaupart, C., Mader, H. M., and Phillips, J. C., 1994, Physical aspects of magma degassing; 1, Experimental and theoretical constraints on vesiculation: Reviews in Mineralogy and Geochemistry, v. 30, no. 1, p. 413-445.

Sparks, R. S. J., Murphy, M. D., Lejeune, A. M., Watts, R. B., Barclay, J., and Young, S. R., 2000, Control on the emplacement of the andesite lava dome of the Soufriere Hills volcano, Montserrat by degassing-induced crystallization: Terra Nova, v. 12, no. 1, p. 14-20. doi:10.1046/j.1365-3121.2000.00267.x.

Sparks, R. S. J., Pinkerton, H., and Hulme, G., 1976, Classification and formation of lava levees on Mount Etna, Sicily: Geology, v. 4, no. 5, p. 269-271. doi:10.1130/0091-7613(1976)4<269:cafoll>2.0.co;2.

Spera, F. J., 2000, Physical Properties of Magmas, *in* Sigurdsson, H., ed., *Encyclopedia of Volcanoes*, San Diego, Calif. ; Academic, 2000., p. 171-190.

Spera, F. J., Borgia, A., Strimple, J., and Feigenson, M., 1988, Rheology of melts and magmatic suspensions: 1. Design and calibration of concentric cylinder viscometer with application to rhyolitic magma: Journal of Geophysical Research: Solid Earth, v. 93, no. B9, p. 10273-10294. doi:10.1029/JB093iB09p10273.

Spieler, O., Kennedy, B., Kueppers, U., Dingwell, D. B., Scheu, B., and Taddeucci, J., 2004, The fragmentation threshold of pyroclastic rocks: Earth and Planetary Science Letters, v. 226, no. 1-2, p. 139-148. doi:10.1016/j.epsl.2004.07.016.

Stasiuk, M. V., Barclay, J., Carroll, M. R., Jaupart, C., Ratte, J. C., Sparks, R. S. J., and Tait, S. R., 1996, Degassing during magma ascent in the Mule Creek vent

(USA): Bulletin of Volcanology, v. 58, no. 2-3, p. 117-130. doi:10.1007/s004450050130.

Stasiuk, M. V., Jaupart, C., and Sparks, R. S. J., 1993, Influence of cooling on lava-flow dynamics: Geology, v. 21, no. 4, p. 335-338. doi:10.1130/0091-7613(1993)021<0335:iocolf>2.3.co;2.

Stevens, N. F., Wadge, G., Williams, C. A., Morley, J. G., Muller, J. P., Murray, J. B., and Upton, M., 2001, Surface movements of emplaced lava flows measured by synthetic aperture radar interferometry: Journal of Geophysical Research: Solid Earth, v. 106, no. B6, p. 11293-11313. doi:10.1029/2000JB900425.

Stevenson, R. J., Bagdassarov, N. S., Dingwell, D. B., and Romano, C., 1998, The influence of trace amounts of water on the viscosity of rhyolites: Bulletin of Volcanology, v. 60, no. 2, p. 89-97. doi:10.1007/s004450050218.

Stevenson, R. J., Briggs, R. M., and Hodder, A. P. W., 1994a, Physical volcanology and emplacement history of the Ben-Lomond rhyolite lava flow, Taupo volcanic center, New-Zealand: New Zealand Journal of Geology and Geophysics, v. 37, no. 3, p. 345-358. doi:10.1080/00288306.1994.9514625.

Stevenson, R. J., Dingwell, D. B., Bagdassarov, N. S., and Manley, C. R., 2001, Measurement and implication of "effective" viscosity for rhyolite flow emplacement: Bulletin of Volcanology, v. 63, no. 4, p. 227-237. doi:10.1007/s004450100137.

Stevenson, R. J., Hodder, A. P. W., and Briggs, R. M., 1994b, Rheological estimates of rhyolite lava flows from the Okataina volcanic center, New-Zealand: New

Zealand Journal of Geology and Geophysics, v. 37, no. 2, p. 211-221. doi:10.1080/00288306.1994.9514616.

Stofan, E. R., Anderson, S. W., Crown, D. A., and Plaut, J. J., 2000, Emplacement and composition of steep-sided domes on Venus: Journal of Geophysical Research: Planets, v. 105, no. E11, p. 26757-26771. doi:10.1029/1999JE001206.

Swanson, D., Dzurisin, D., Holcomb, R., Iwatsubo, E., Chadwick, W., Casadevall, T., Ewert, J., and Heliker, C., 1987, Growth of the lava dome at Mount St. Helens, Washington,(USA), 1981–1983: Geological Society of America Special Papers, v. 212, p. 1-16. doi:10.1130/SPE212-p1.

Swanson, D. A., 1973, Pahoehoe flows from 1969-1971 Mauna Ulu eruption, Kilauea volcano, Hawaii: Geological Society of America Bulletin, v. 84, no. 2, p. 615-626. doi:10.1130/0016-7606(1973)84<615:pfftmu>2.0.co;2.

Swanson, S., Naney, M., Westrich, H. R., and Eichelberger, J. C., 1989, Crystallization history of Obsidian Dome, Inyo Domes, California: Bulletin of Volcanology, v. 51, no. 3, p. 161-176. doi:10.1007/bf01067953.

Tachikawa, T., Kaku, M., Iwasaki, A., Gesch, D. B., Oimoen, M. J., Zhang, Z., Danielson, J. J., Krieger, T., Curtis, B., Haase, J., Abrams, M., and Carabajal, C., 2011, ASTER Global Digital Elevation Model Version 2 - summary of validation results.

Theilig, E., and Greeley, R., 1986, Lava flows on Mars: Analysis of small surface features and comparisons with terrestrial analogs: Journal of Geophysical

Research: Solid Earth, v. 91, no. B13, p. E193-E206. doi:10.1029/JB091iB13p0E193.

Thorarinsson, S., 1953, The crater groups in Iceland: Bulletin Volcanologique, v. 14, no. 1, p. 3-44. doi:10.1007/bf02596003.

Truby, J. M., Mueller, S. P., Llewellin, E. W., and Mader, H. M., 2015, The rheology of three-phase suspensions at low bubble capillary number: Proceedings of the Royal Society A: Mathematical, Physical and Engineering Science, v. 471, no. 2173. doi:10.1098/rspa.2014.0557.

Tuffen, H., Dingwell, D. B., and Pinkerton, H., 2003, Repeated fracture and healing of silicic magma generate flow banding and earthquakes?: Geology, v. 31, no. 12, p. 1089-1092. doi:10.1130/g19777.1.

Tuffen, H., James, M. R., Castro, J. M., and Schipper, C. I., 2013, Exceptional mobility of an advancing rhyolitic obsidian flow at Cordon Caulle volcano in Chile: Nature Communications, v. 4. doi:10.1038/ncomms3709.

Ullman, S., 1979, The interpretation of structure from motion: Proceedings of the Royal Society of London B: Biological Sciences, v. 203, no. 1153, p. 405-426. doi:10.1098/rspb.1979.0006.

Vergniolle, S., and Jaupart, C., 1986, Separated two-phase flow and basaltic eruptions: Journal of Geophysical Research: Solid Earth, v. 91, no. B12, p. 12842-12860. doi:10.1029/JB091iB12p12842.

Vicari, A., Alexis, H., Del Negro, C., Coltelli, M., Marsella, M., and Proietti, C., 2007, Modeling of the 2001 lava flow at Etna volcano by a Cellular Automata

approach: Environmental Modelling & Software, v. 22, no. 10, p. 1465-1471. doi:10.1016/j.envsoft.2006.10.005.

von Aulock, F. W., Nichols, A. R. L., Kennedy, B. M., and Oze, C., 2013, Timescales of texture development in a cooling lava dome: Geochimica Et Cosmochimica Acta, v. 114, p. 72-80. doi:10.1016/j.gca.2013.03.012.

Vye-Brown, C., Self, S., and Barry, T. L., 2013, Architecture and emplacement of flood basalt flow fields: case studies from the Columbia River Basalt Group, NW USA: Bulletin of Volcanology, v. 75, no. 3, p. 1-21. doi:10.1007/s00445-013-0697-2.

Wadge, G., Voight, B., Sparks, R. S. J., Cole, P. D., Loughlin, S. C., and Robertson, R. E. A., 2014, Chapter 1 An overview of the eruption of Soufrière Hills Volcano, Montserrat from 2000 to 2010: Geological Society, London, Memoirs, v. 39, no. 1, p. 1-40. doi:10.1144/m39.1.

Walker, G. P. L., 1971, Compound and simple lava flows and flood basalts: Bulletin Volcanologique, v. 35, no. 3, p. 579-590. doi:10.1007/bf02596829.

Walker, G. P. L., 1991, Structure, and origin by injection of lava under surface crust, of tumuli, “lava rises”, “lava-rise pits”, and “lava-inflation clefts” in Hawaii: Bulletin of Volcanology, v. 53, no. 7, p. 546-558. doi:10.1007/bf00298155.

Warner, N. H., and Gregg, T. K. P., 2003, Evolved lavas on Mars? Observations from southwest Arsia Mons and Sabancaya volcano, Peru: Journal of Geophysical Research: Planets, v. 108, no. E10. doi:10.1029/2002JE001969.

Watts, R. B., Herd, R. A., Sparks, R. S. J., and Young, S. R., 2002, Growth patterns and emplacement of the andesitic lava dome at Soufrière Hills Volcano,

Montserrat: Geological Society, London, Memoirs, v. 21, no. 1, p. 115-152. doi:10.1144/gsl.mem.2002.021.01.06.

Wells, O. C., 1974, Scanning electron microscopy, McGraw-Hill.

Westrich, H. R., Stockman, H. W., and Eichelberger, J. C., 1988, Degassing of rhyoliticmagma during ascent and emplacement: Journal of Geophysical Research-Solid Earth and Planets, v. 93, no. B6, p. 6503-6511. doi:10.1029/JB093iB06p06503.

Wilcock, W. S. D., and Whitehead, J. A., 1991, The Rayleigh-Taylor instability of an embedded layer of low-viscosity fluid: Journal of Geophysical Research: Solid Earth, v. 96, no. B7, p. 12193-12200. doi:10.1029/91JB00339.

Williams, R. S., 1997, Lava-cooling operations during the 1973 eruption of Eldfell Volcano, Heimaey, Vestmannaeyjar, Iceland: US Geological Survey Open-file Report, v. 97-724.

Williams, R. S., Jr., and Moore, J. G., 1983, Man against volcano : the eruption on Heimaey, Vestmannaeyjar, Iceland.

Wilson, L., and Head, J. W., 2003, Lunar Gruithuisen and Mairan domes: Rheology and mode of emplacement: Journal of Geophysical Research: Planets, v. 108, no. E2. doi:10.1029/2002JE001909.

Yamaguchi, Y., Kahle, A. B., Tsu, H., Kawakami, T., and Pniel, M., 1998, Overview of advanced spaceborne thermal emission and reflection radiometer (ASTER): IEEE Transactions on geoscience and remote sensing, v. 36, no. 4, p. 1062-1071. doi:10.1109/36.700991.

Zimova, M., and Webb, S. L., 2007, The combined effects of chlorine and fluorine on the viscosity of aluminosilicate melts: Geochimica Et Cosmochimica Acta, v. 71, no. 6, p. 1553-1562. doi:10.1016/j.gca.2006.12.002.

# 8 Appendices

The following appendices provide the detailed methodologies, and their associated data, that expand on the brief methods provided with each of the paper format sections. Appendix A details the remote sensing methodologies, associated products and processing techniques. Appendix B provides information on the field data gathered, including samples and breakout types. Appendix C expands on the microstructural techniques utilised in the thesis and the associated data. Finally, Appendix D outlines the methodology for the quantitative modelling in Section 3.

## 8.1 Appendix A: Remote Sensing

Remote sensing data, associated products, and processing techniques, used in this thesis include satellite imagery (true colour, false colour and thermal), digital elevation models, and structure-from-motion photogrammetry. Satellite imagery is used throughout the results sections and thermal data are used in Section 4 and 5. DEMs were used for the numerical modelling in Section 3, and a high resolution (1 m) DEM was used to assess lava morphology in Section 4. Structure-from-motion photogrammetry was used to determine changes in lava flow morphology in Section 4 and 5.3.

The satellite data used in this thesis are from freely available open sources. Earth Observing-1, Landsat, and the ASTER Global DEM are available from the U.S. Geological Survey (EarthExplorer database), ASTER data are distributed by the Land Processes Distributed Active Archive Center (LP DAAC), located at USGS/EROS, Sioux Falls, SD. http://lpdaac.usgs.gov. These data were used to examine the emplacement dynamics of the Cordón Caulle rhyolite lava during the eruption.

### *8.1.1 Satellite Imagery*

For the purpose of this study, I used data from imaging satellites to observe morphological changes of the lava flow. Some flow outlines from radar satellite data are also used; these were provided by Bignami et al. (2014). The flow outlines were particularly useful for tracking the lava in the early phases of emplacement when the lava was partly or wholly obscured by the eruptive ash plume and clouds at visible or infrared wavelengths, as radar is able to penetrate clouds and, to more limited effect, volcanic ash plumes.

Table 8A.1: Satellite sensors

| Satellite | Sensor | Spectral range (µm) | Resolution | Lifespan | Access site |
|---|---|---|---|---|---|
| Earth Observing 1 (EO-1) | Advanced Land Imager (ALI) | 0.48-2.35 (10 bands) | 10 m (Pan)<br>30 m (VNIR / SWIR) | November 2000 – March 2017 | USGS Earth Explorer |
| | Hyperion | 0.4 – 2.5 (220 bands) | 30 m (all bands) | " | " |
| Terra | Advanced Spaceborne Thermal Emission and Reflection Radiometer (ASTER) | VNIR: 0.520-0.860 (3 bands)<br>SWIR: 1.60-2.360 (6 bands)<br>TIR: 8.125-11.650 (5 bands) | 15 m (VNIR)<br>30 m (SWIR)<br>90 m (TIR) | December 1999 - Present | Land Processes Distributed Active Archive Center (LP DAAC) |
| Landsat 5 | Thematic Mapper (TM) | VNIR: 0.45-0.90 (4 bands)<br>SWIR: 1.55-1.75 (2 bands)<br>TIR 10.40-12.50 (1 band) | 30 m (all bands) | March 1984 – June 2013 | USGS Earth Explorer |
| Landsat 7 | Enhanced Thematic Mapper (ETM+) | VNIR: 0.45-0.90 (4 bands)<br>SWIR: 1.55-2.35 (2 bands)<br>TIR: 10.40-12.50 (1 band) | 15 m (Pan),<br>30 m (VNIR, SWIR, TIR) | April 1999 – Present | USGS Earth Explorer |
| Worldview 2 | Not applicable | VNIR: 0.45-0.9 (9 bands) | 0.46 m (Pan)<br>1.84 m (VNIR) | October 2009 – Present | Google Earth |
| GeoEye-1 | Not applicable | VNIR: 0.45-0.92 (5 bands) | 0.41 m (Pan)<br>1.84 m (VNIR) | September 2008 – Present | GeoEye Foundation |

With the lava flow at Cordón Caulle being emplaced over ~10 months, over a spatial extent of kilometres, satellites that image at the spatial resolutions <100 m in the

panchromatic/VNIR bands and with moderate repeat times (of order weeks), such as Landsat, ASTER (on the TERRA satellite) and EO-1 (Digenis et al., 1998; Yamaguchi et al., 1998) proved the most useful. These sensors have a resolution of 10 – 90 m, depending on the spectral band in question (Table 8A.1), with thermal infrared bands typically having the coarsest resolution (Table 8A.1). The data from these sensors are also freely available with no limits on usage. Furthermore, the role of EO-1 in the Volcano Sensorweb (Digenis et al., 1998; Chien et al., 2005; Davies et al., 2006) meant that higher resolution (10 m) images were regularly captured throughout the eruption as the satellite was tasked to focus on the eruption.

The utility of the satellite images, was limited primarily by cloud cover or obscuring of the lava flow by the ash plume. Despite these limitations, a good quality time series of images was available for the 2011-2012 Cordón Caulle rhyolite lava flow emplacement (Table 8A.2). The time series was supplemented by several images (Table 8A.2) from high resolution (0.5 – 1 m) commercial imaging satellites, such as GeoEye and WorldView, which offer high resolutions but are hampered by poor spatial extents, long repeat times and high costs to the end user.

#### 8.1.1.1 Application of true and false colour imagery

For the 2011-2012 Cordón Caulle eruption images in the visible light, near infrared (NIR), and shortwave infrared (SWIR) spectrum were obtained from Earth Observing-1 (EO-1, ALI and Hyperion sensors), Landsat 4/5, Landsat 7 ETM+, and ASTER (Table 8A.1). All images are in a GeoTiff or hdf format. Images from Google Earth were also used, these are from WorldView 2 (1 m resolution), and one GeoEye image (1 m resolution) from the early phases of the eruption. For the EO-1, Landsat and ASTER data three bands were combined in ENVI to create a true colour image, or a false colour image in the NIR and SWIR bands These images have a resolution of 30 m for EO-1

and Landsat and 15 m for ASTER. EO-1 ALI and Landsat 7 ETM+ colour images were combined with their corresponding higher resolution panchromatic band using the NNDiffusePanSharpening tool in ENVI to generate higher resolution (10 m for EO-1 ALI and 15 m for Landsat 7 ETM+) colour imagery. This technique was not applied to EO-1 Hyperion, Landsat 4/5, and ASTER images as these sensors do not include a panchromatic band (Table 8A.1).

The images generated in ENVI were exported into ArcGIS, where images were manually co-registered using fixed points, such as roads, lakes, and older lava flows that were assumed to be stationary throughout the eruption. This typically left RMS errors of ~10 m and up to 100 m. Larger errors are associated with images where large areas are obscured by the eruptive plume, clouds, or where the area of interest lies at the edge of the satellite image, limiting locations for fixed points to use. A timeline of lava flow development was generated from the satellite imagery (approximately two images per month, Section 3 and 4). It is worth noting that the Landsat 7 ETM+ images were obtained with the Scan Line Corrector (SLC) turned off (as the SLC malfunctioned in 2003), and so these images have large data gaps running across the images in all bands. Despite these data gaps, the images provide useful information on the lava flow evolution.

Images were exported to Adobe Illustrator to generate detailed structural maps of the Cordón Caulle lava flow at different times (e.g. Section 4). These maps were further used to determine the position of the flow front throughout the eruption, and were supplemented by flow outlines derived from COSMO-SkyMED radar images of the lava from Bignami et al. (2014). The satellite images were used to determine the surface velocity of the lava flow by tracking surface features (such as pumice rafts, crust fractures and ogives) between two georeferenced images. Tracking was carried out manually in ArcGIS. Images of rhyolite lavas of the western USA (Section 5) were

sourced from Google Earth as well as the NAIP JPEG aerial photograph series (true colour, 1 m resolution), data available from the U.S. Geological Survey. These images were annotated in Adobe Illustrator to generate detailed maps of the lava flows.

Table 8A.2: Satellite images available for the Cordón Caulle eruption

| Satellite | Sensor | Number syn-eruption | Number post-eruption |
|---|---|---|---|
| Earth Observing 1 (EO-1) | Advanced Land Imager (ALI) | 8 | 1 |
| | Hyperion | 4 | 0 |
| Terra | Advanced Spaceborne Thermal Emission and Reflection Radiometer (ASTER) | 3 (VNIR)<br>4 (TIR) | 1 (VNIR)<br>2 (TIR) |
| Landsat 5 | Thematic Mapper (TM) | 2<br>2 (TIR) | 0 |
| Landsat 7 | Enhanced Thematic Mapper (ETM+) | 21 | 4 |
| Worldview 2 | Not applicable | 0 | 2 |
| GeoEye-1 | Not applicable | 1 | N/A |

#### 8.1.1.2 Application of thermal imagery

Satellite images in the thermal infrared (TIR) spectrum were obtained from Landsat 4/5 (band 6), Landsat 7 ETM+ (band 6), and ASTER (bands 10 – 14) for the Cordón Caulle lava flow. The TIR images are single band, in which the qualitative thermal evolution of the lava flow could be tracked as a time series (Section 4 and 5). The TIR images of the lava flow have a lower resolution (Landsat 30 m, ASTER 90 m) compared to their true colour, NIR and SWIR counterparts and, as a result, the thermal evolution of some of the smallest features cannot be observed. For visualisation, the stretch on the TIR images was adjusted in ArcGIS to enhance differences across the lava flow at the expense of detail at the highest temperature.

#### 8.1.1.3 Satellite imagery provided

The following pages (260-276) provide enlarged versions of the GeoEye, EO-1, ASTER and Landsat data used in the thesis. Page 277 is a series of outline maps showing the development of key lava flow features.

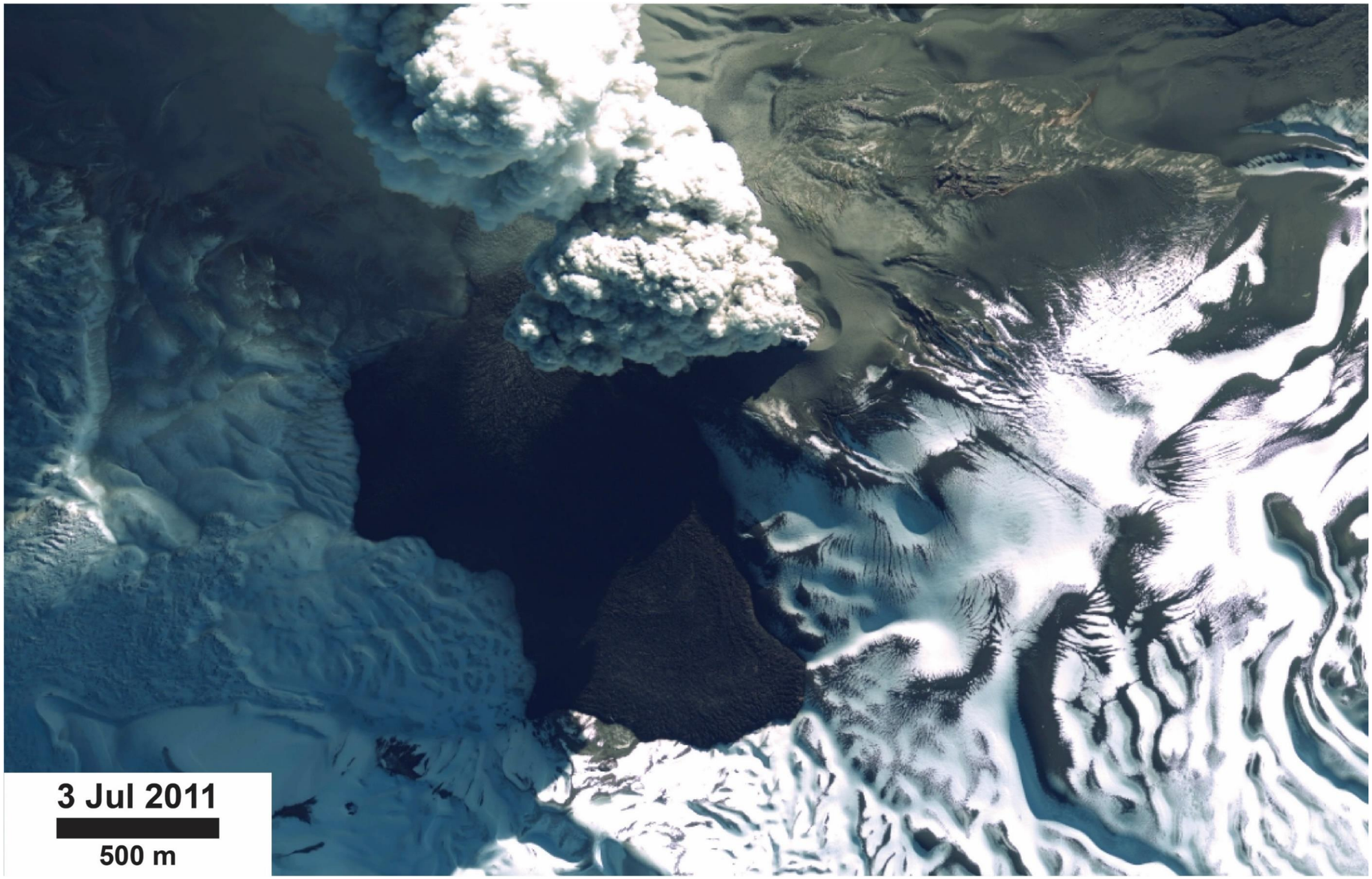


Figure 8A.1: GeoEye image of the Cordón Caulle lava flow. Courtesy of the GeoEye foundation.

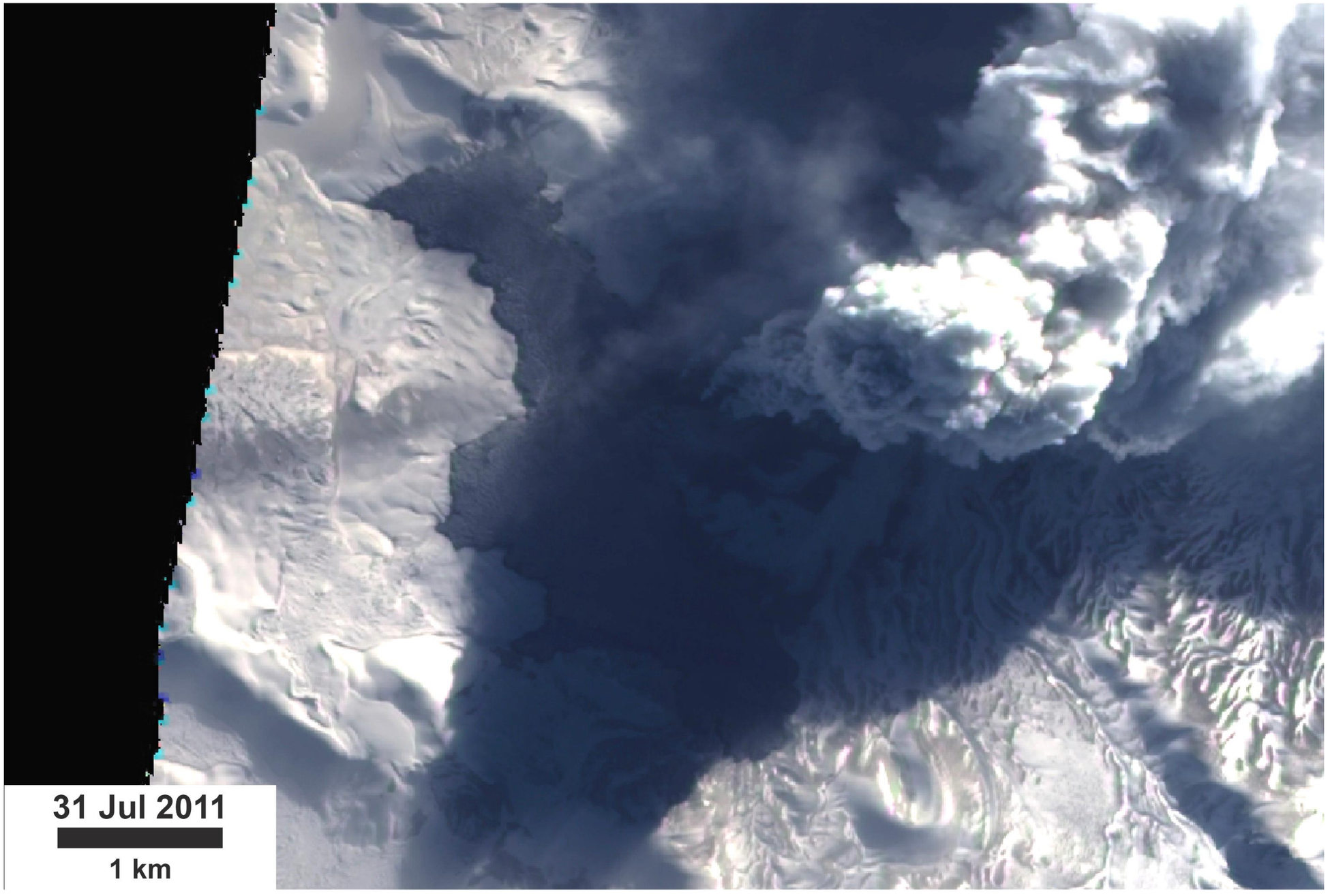


Figure 8A.2: EO-1 ALI image – Scene EO1A2330882011212110KF_1T

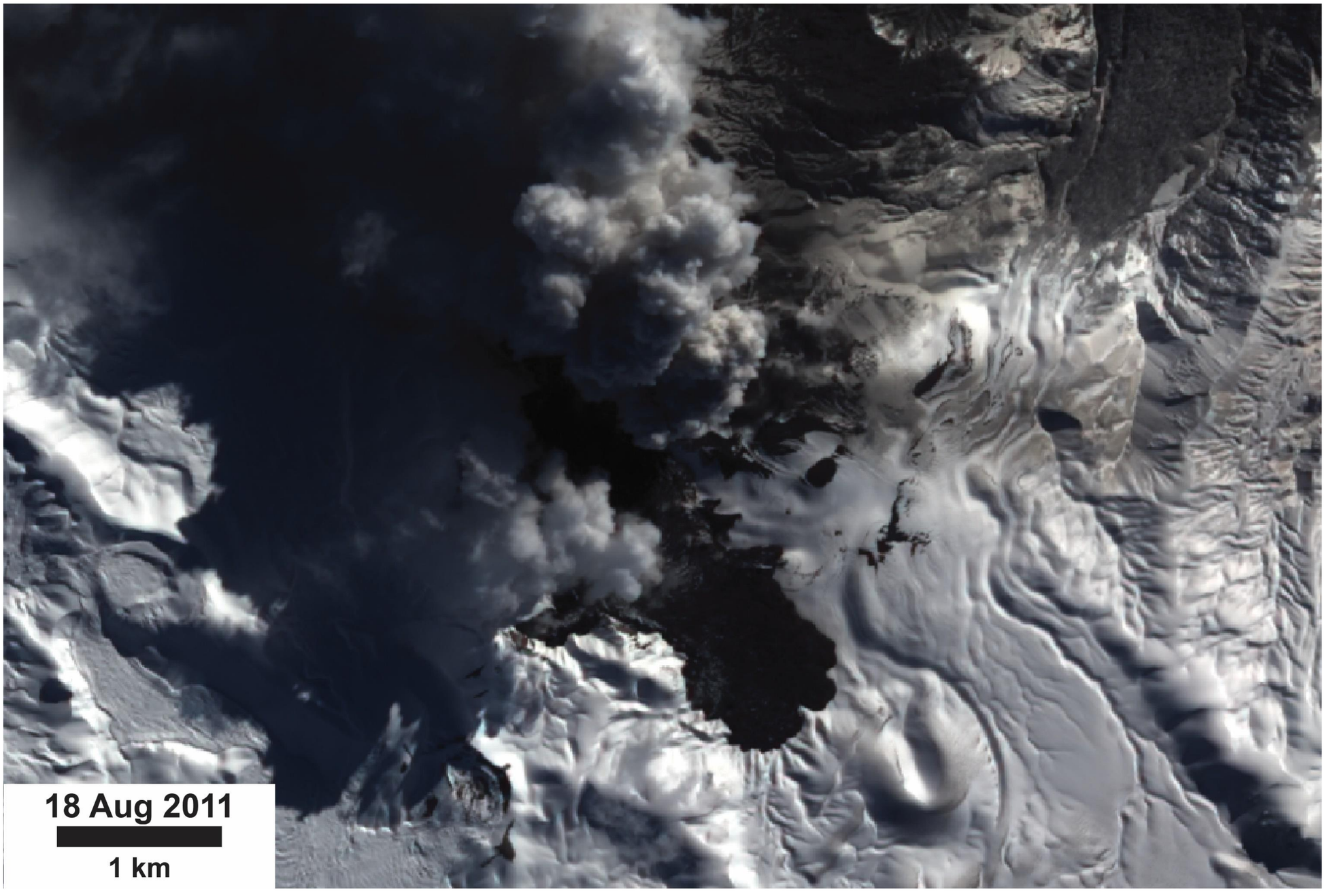


Figure 8A.3: EO-1 ALI image – Scene EO1A2330882011230110KF_1T

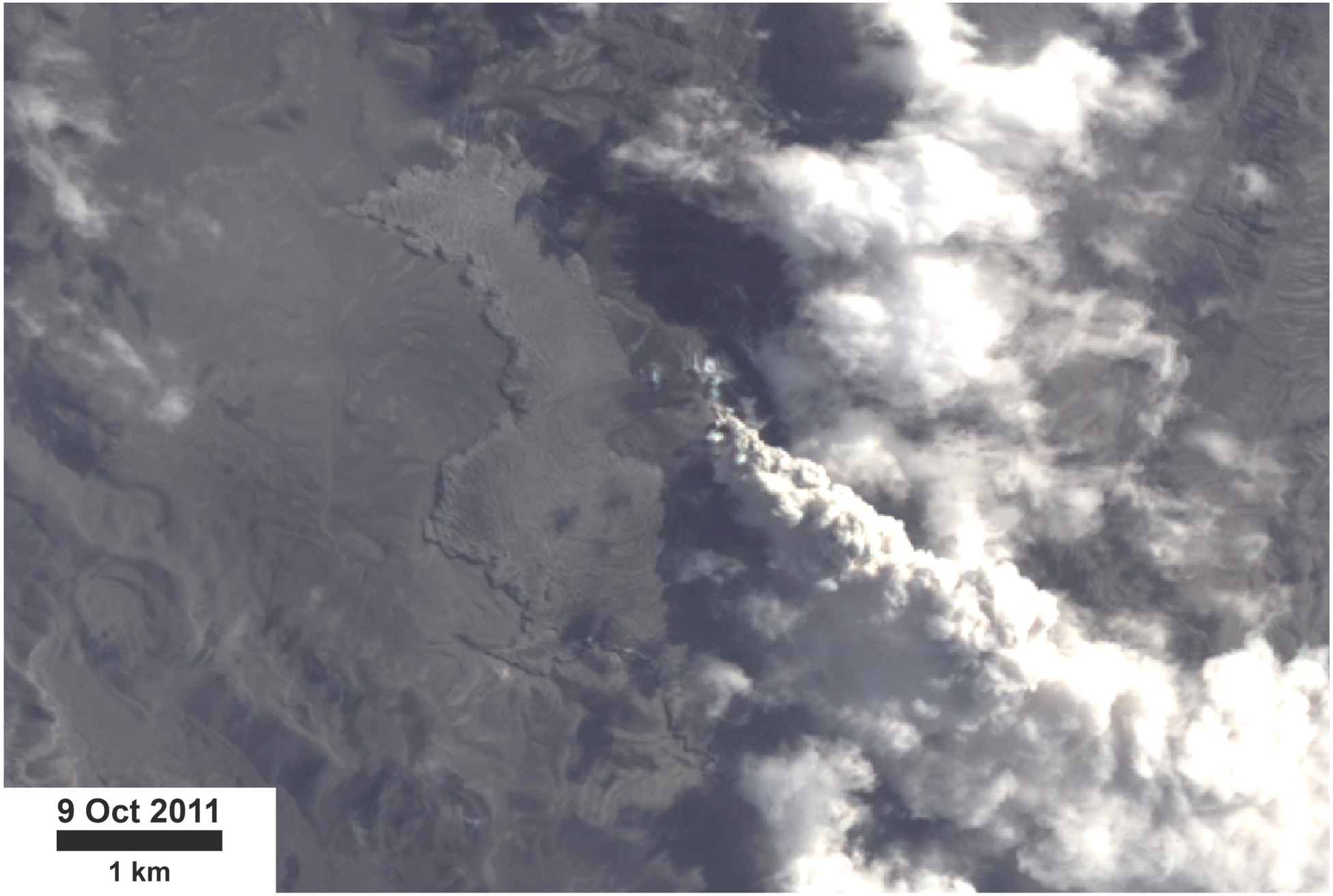


Figure 8A.4: EO-1 ALI image – Scene EO1A2330882011282110KF_1T

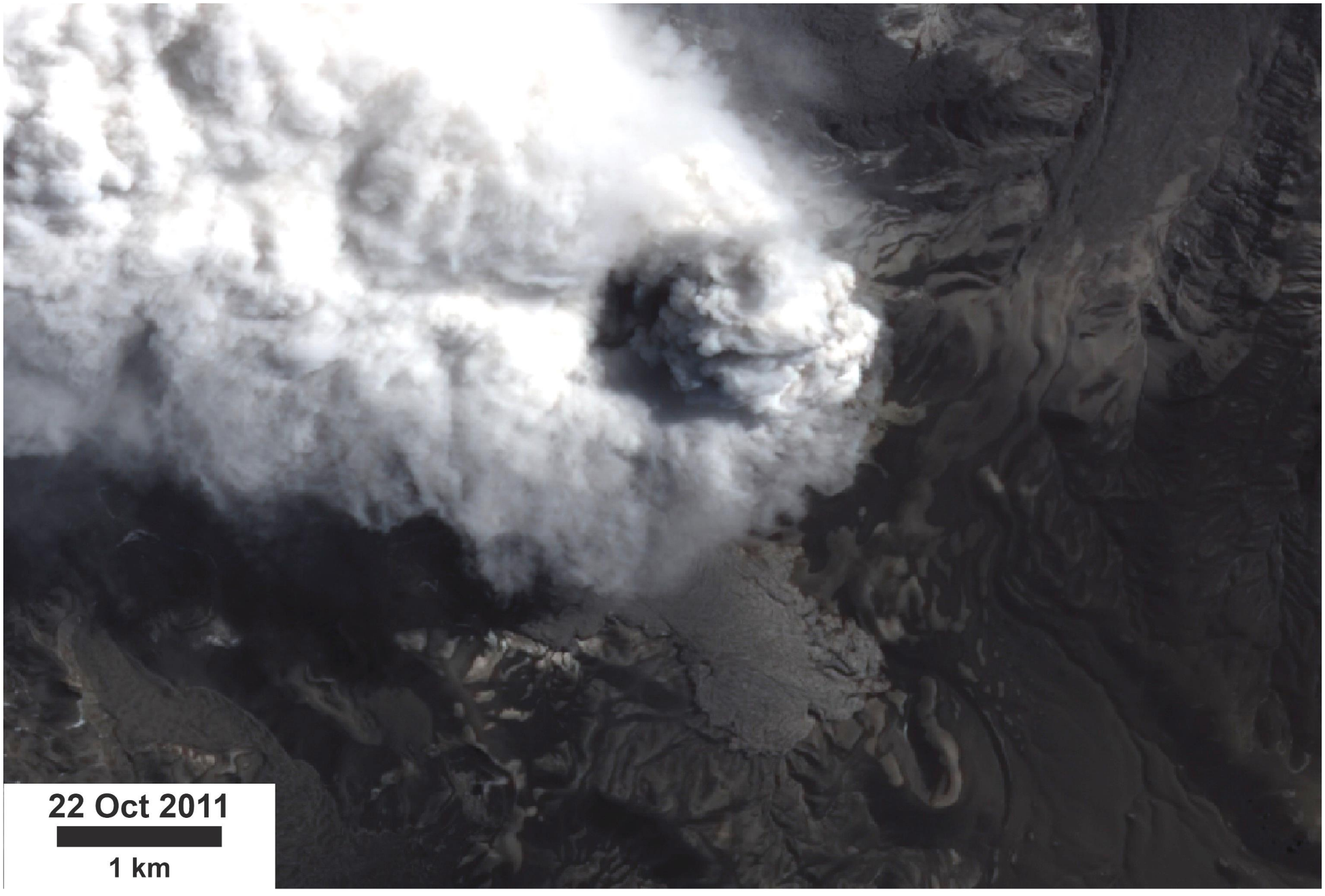


Figure 8A.5: EO-1 ALI image – Scene EO1A2330882011295110KF_1T

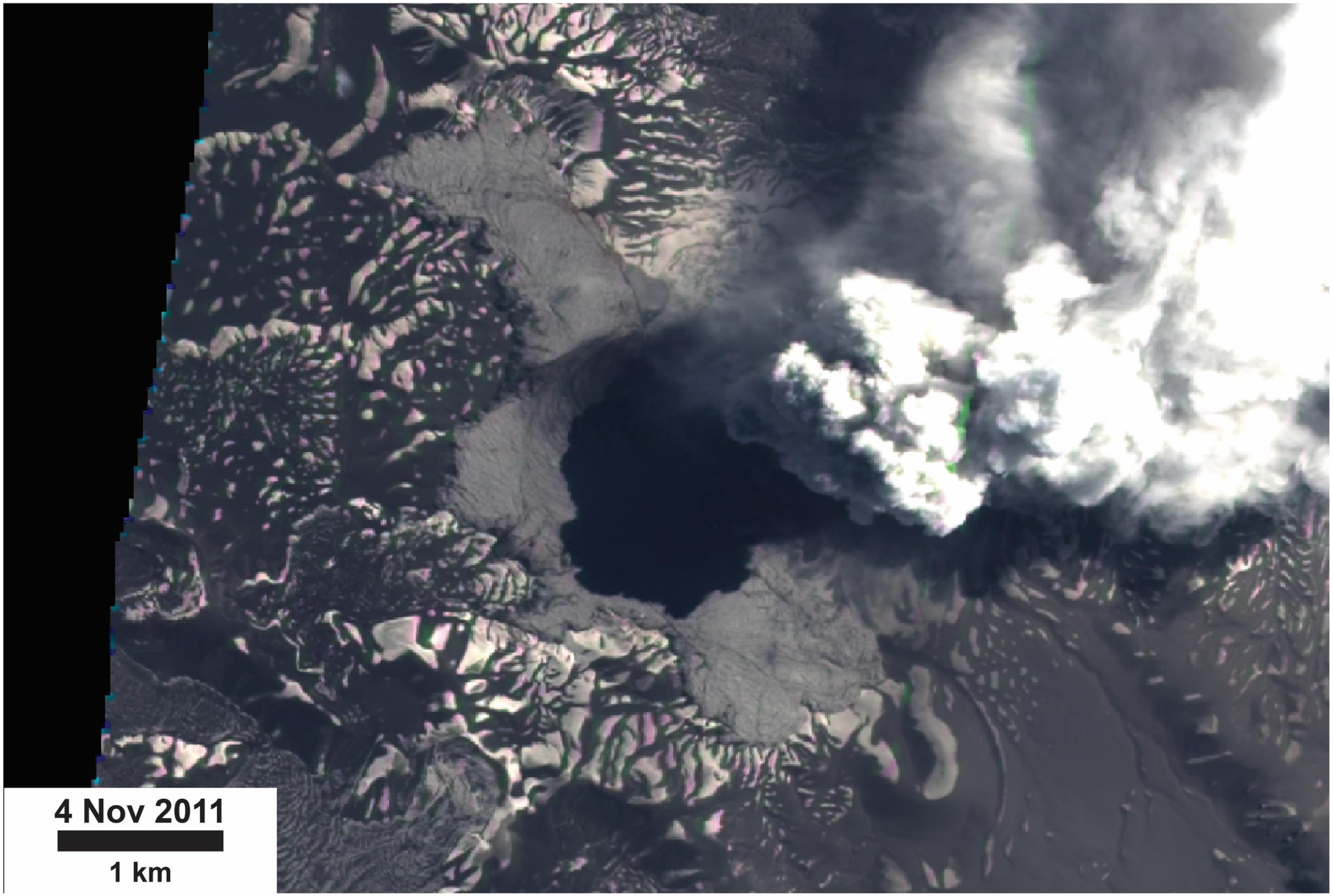


Figure 8A.6: EO-1 ALI image – Scene EO1A2330882011308110KF_1T

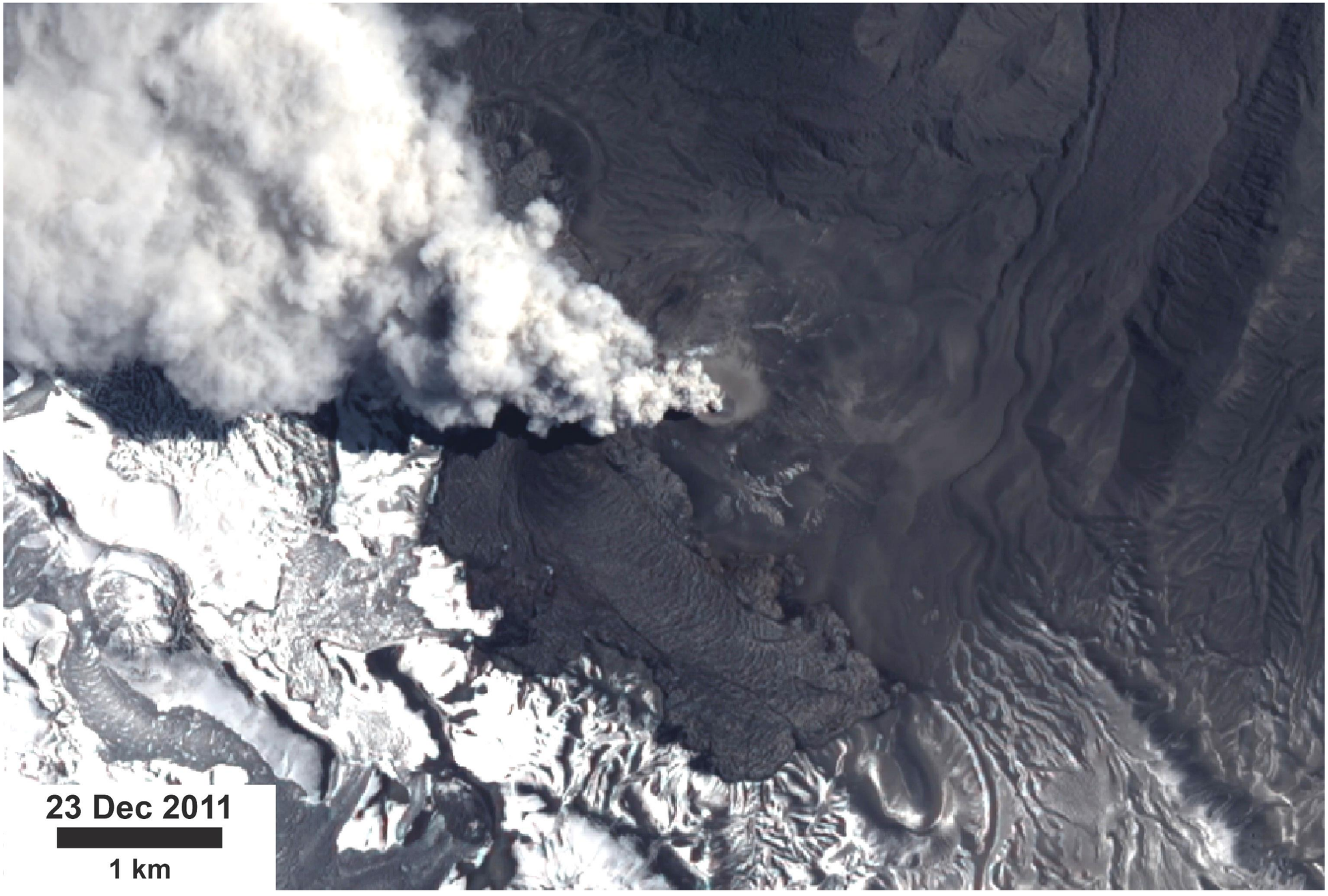


Figure 8A.7: EO-1 ALI image – Scene EO1A2330882011357110PF_1T

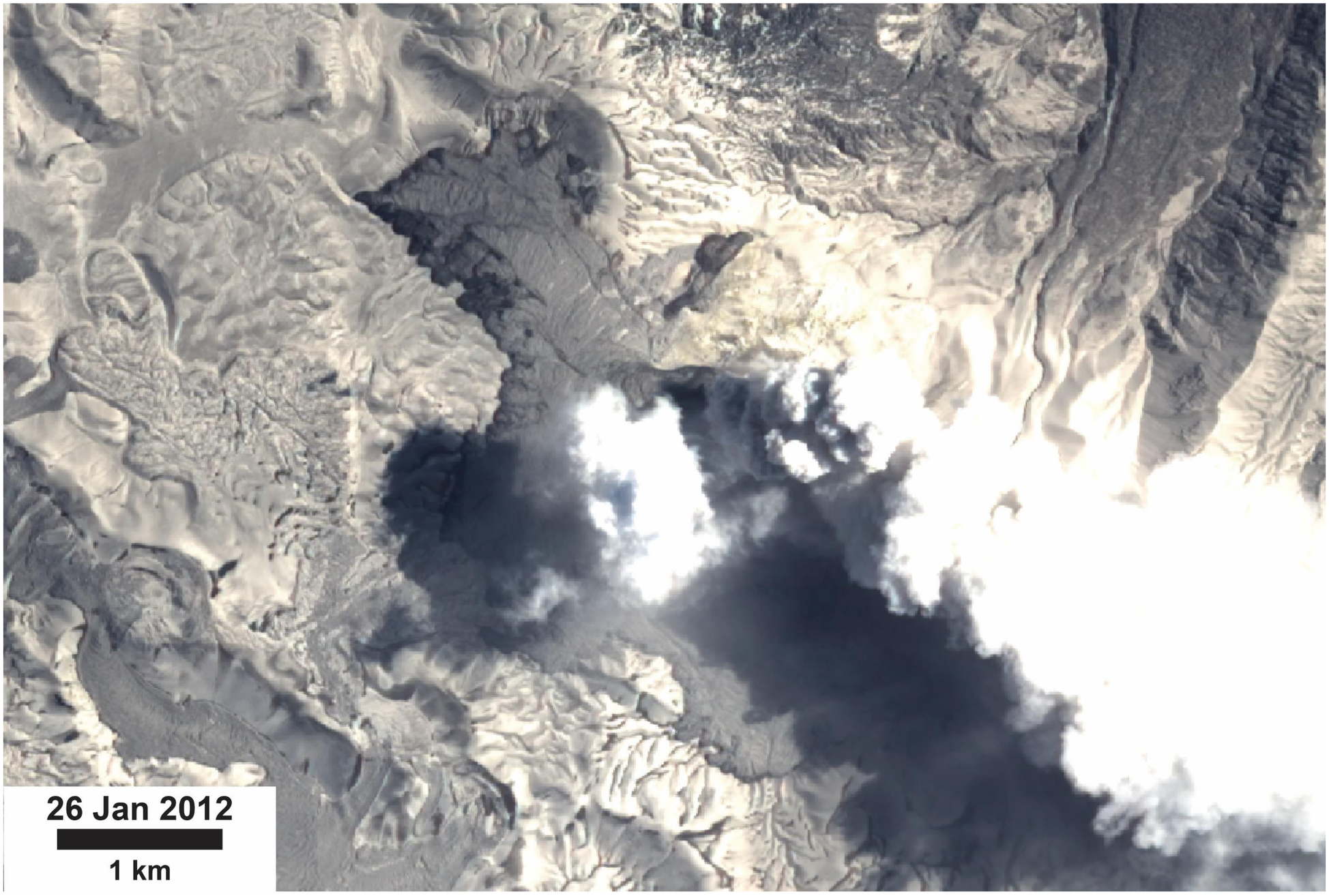


Figure 8A.8: EO-1 ALI image – Scene EO1A2330882012026110KF_1T

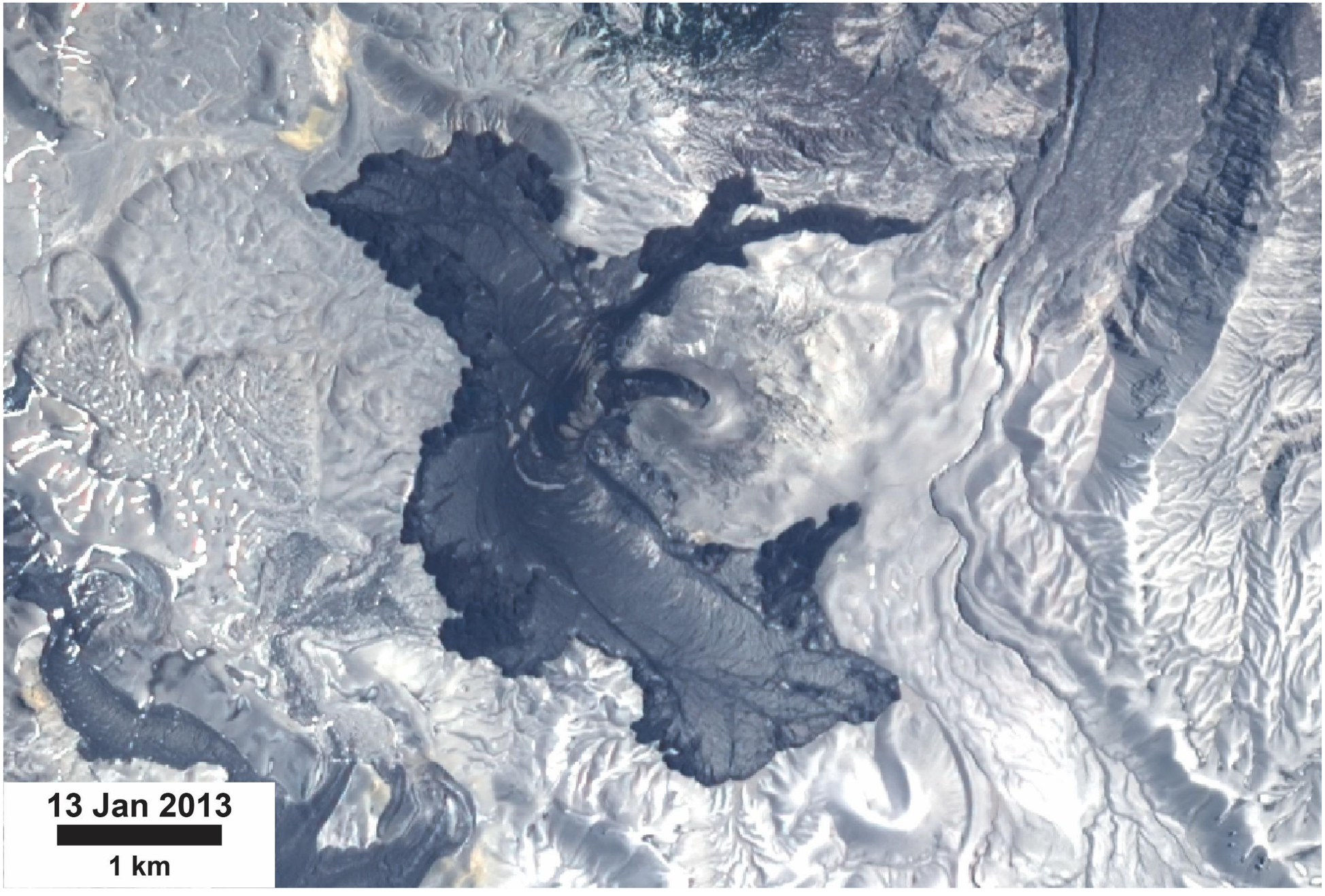


Figure 8A.9: EO-1 ALI image – Scene EO1A2330882013013110PF_1T

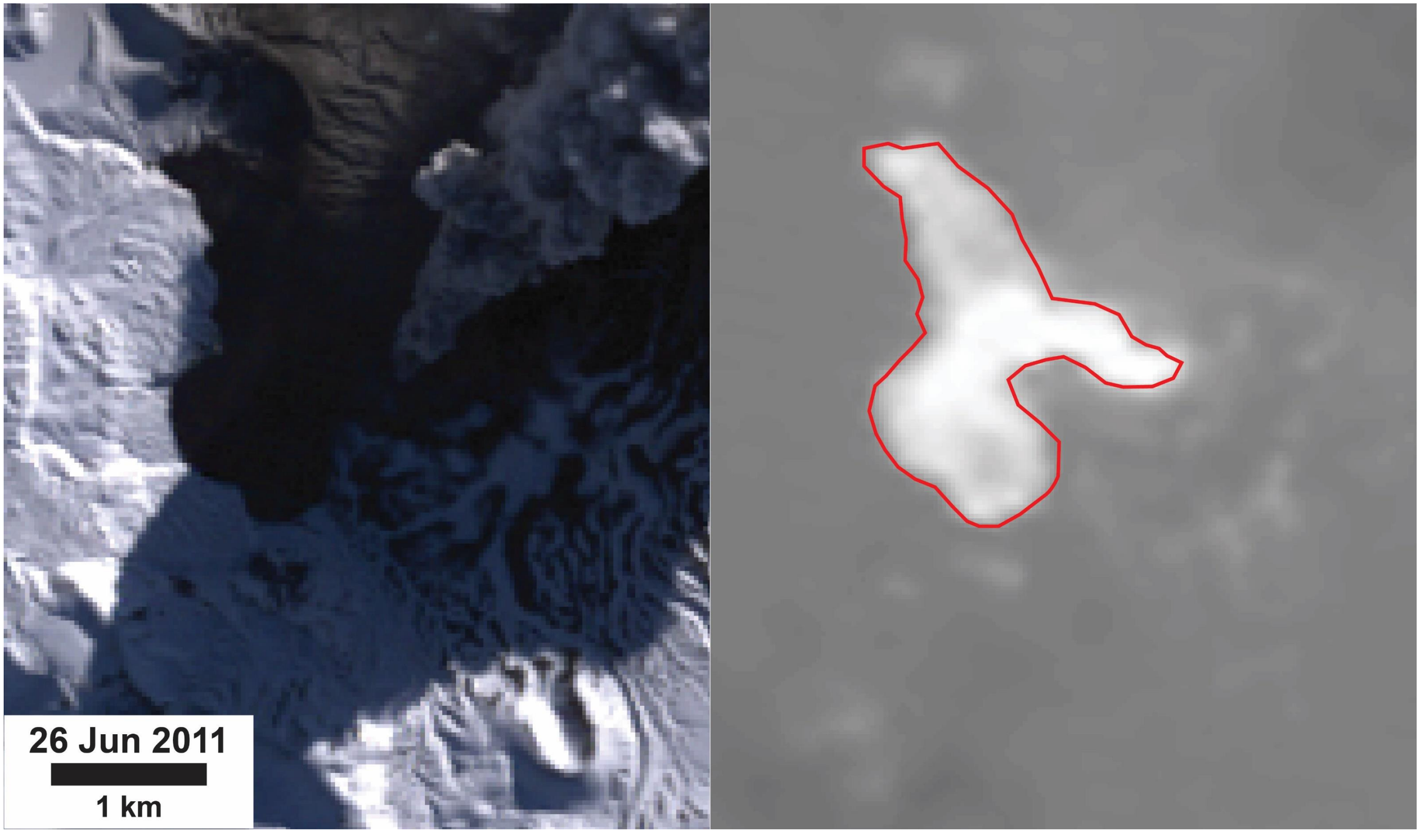


Figure 8A.10: Landsat 5 optical and thermal image - Scene LT52330882011177COA00

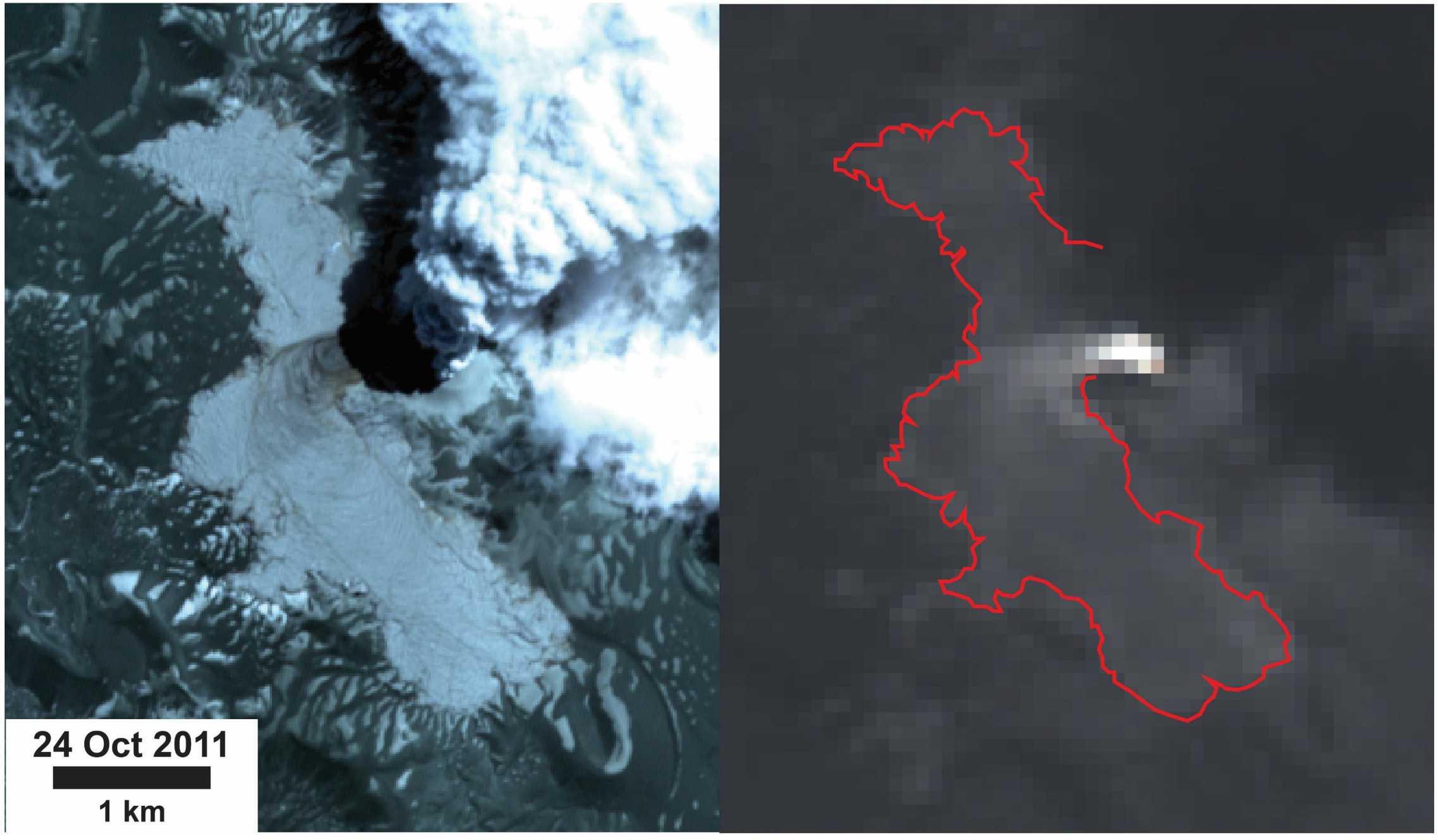


Figure 8A.11: ASTER optical and thermal image – Scene AST_L1T_00310242011145240_20150608034435

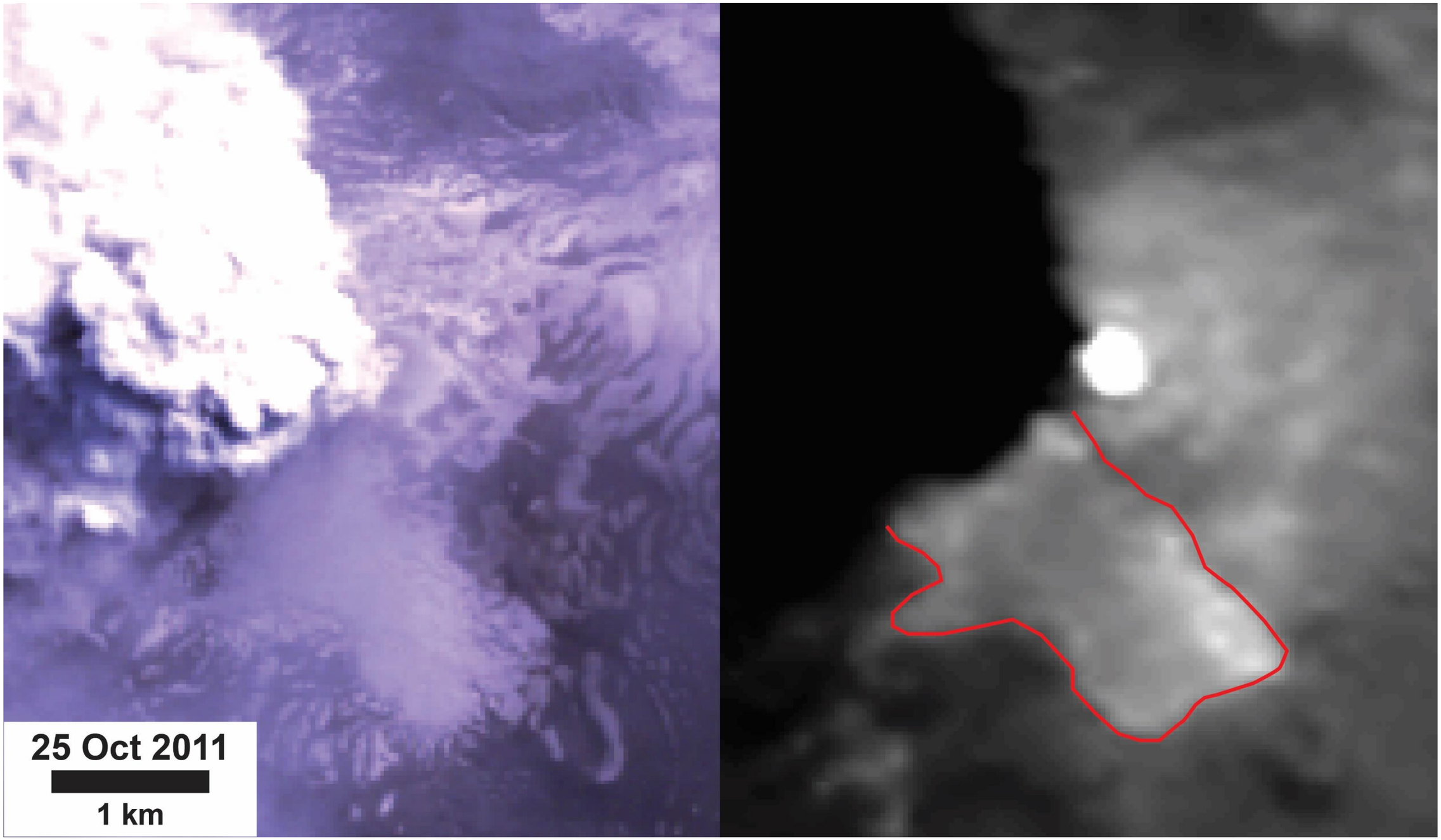


Figure 8A.12: Landsat 5 optical and thermal image – Scene LT52320882011298COA00

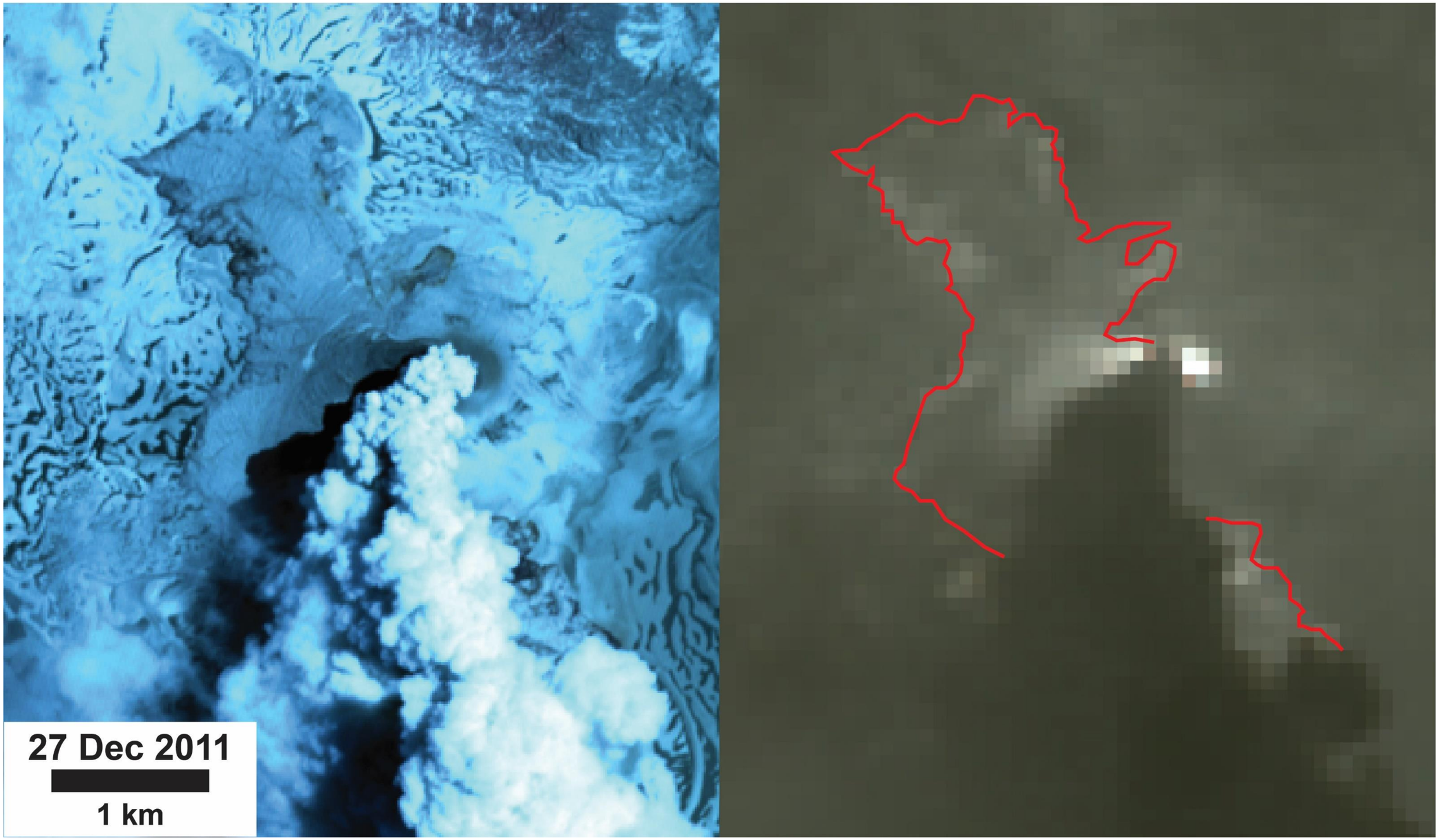


Figure 8A.13: ASTER optical and thermal image – Scene AST_L1T_00312272011145305_20150608212959

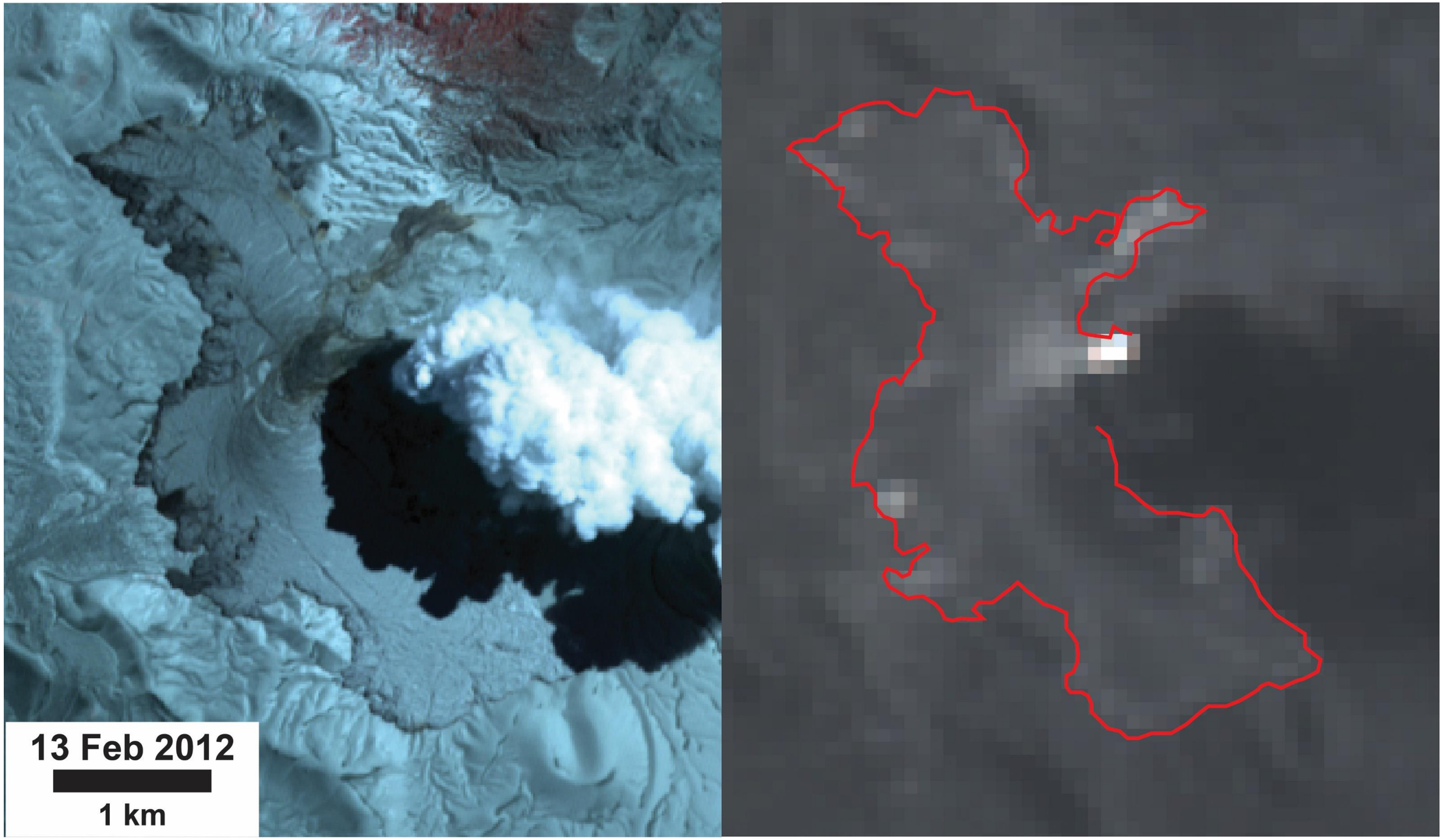


Figure 8A.14: ASTER optical and thermal image – Scene AST_L1T_00302132012145257_20150609123045

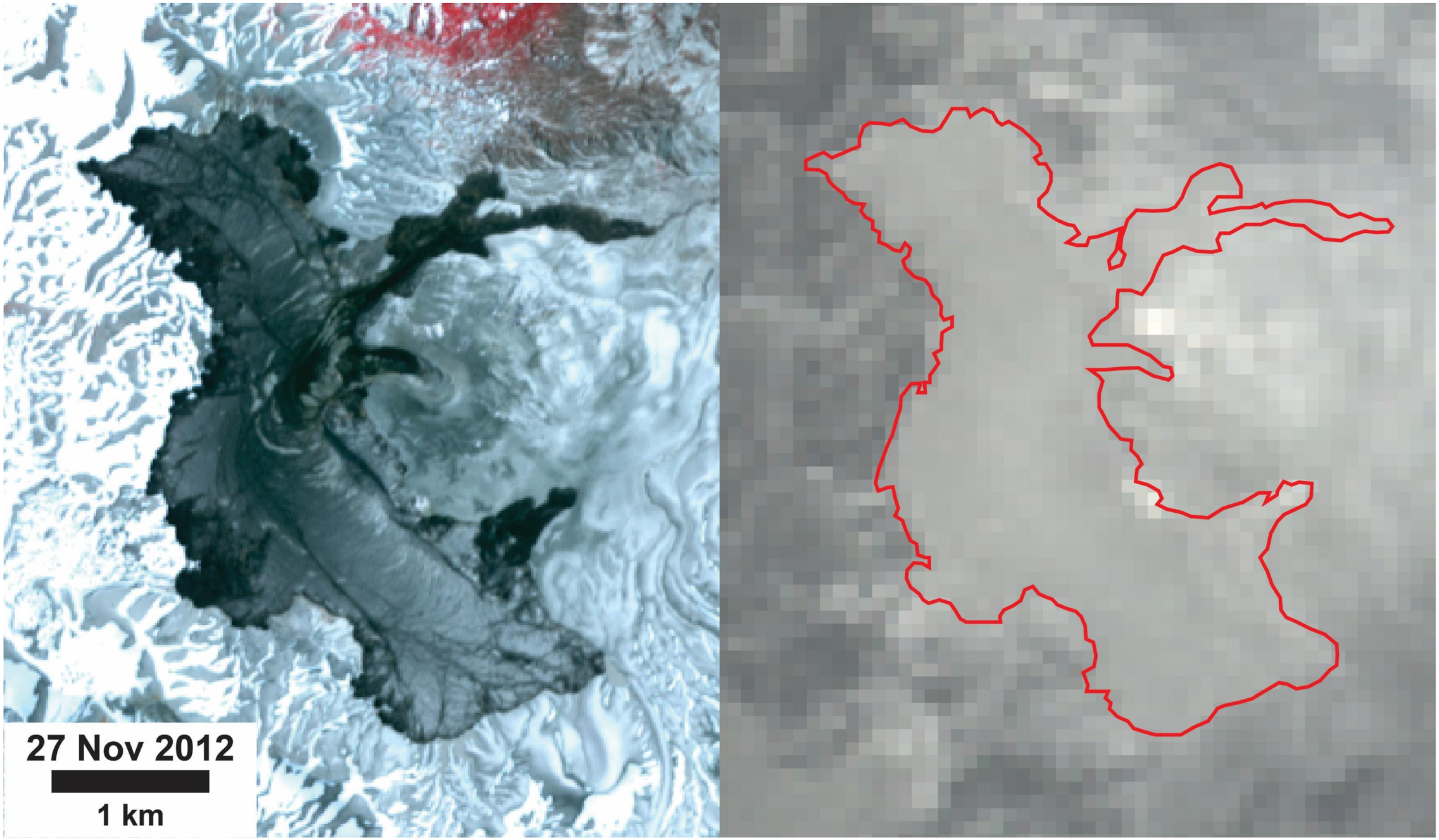


Figure 8A.15: ASTER optical and thermal image – Scene AST_L1T_00311272012145258_20150613151154

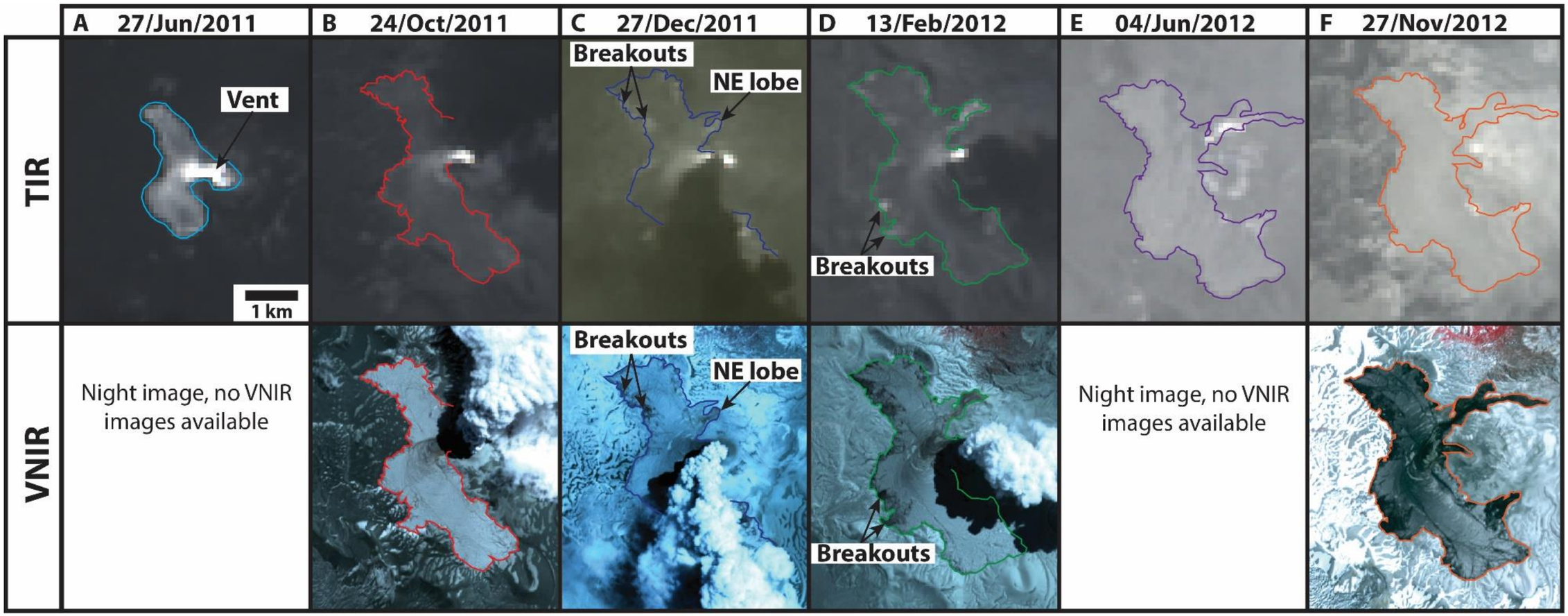


Figure 8A.16: ASTER VNIR and corresponding TIR images of the 2011-2012 Cordón Caulle flow (NASA/METI, 2011b, c, a, 2012c, b, a), these data are distributed by the Land Processes Distributed Active Archive Center (LP DAAC), located at USGS/EROS, Sioux Falls, SD. http://lpdaac.usgs.gov. Breakouts correspond to bright spots at the flow front in the TIR images. The NE flow lobe is visible in images **C-F**, when this is active it appears as a brighter lobe. The eruption ended at the end of March 2012 but for several months after this hot spots were observed at the flow front, particularly at the SE breakouts and NE flow (**F**).

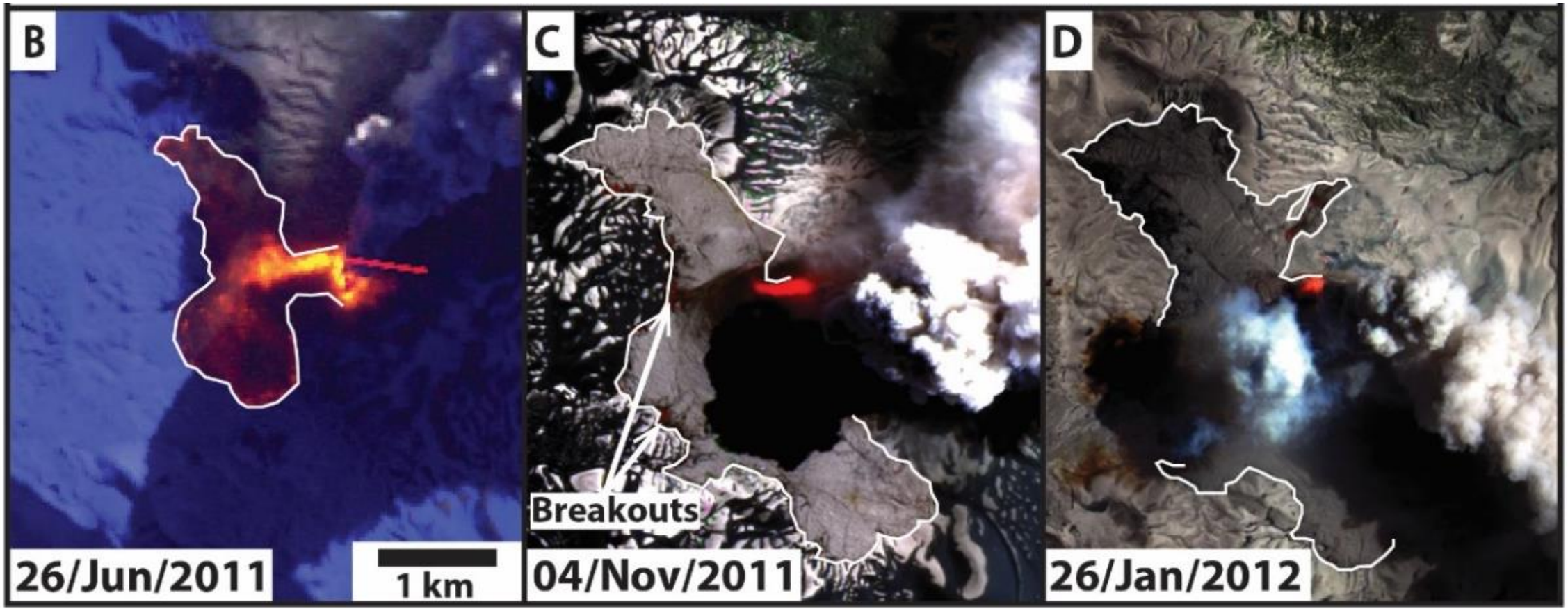


Figure 8A.17: Enlarged version of parts B-D of Figure 5.1 (**B**) Landsat 5 image of the initial lava effusion, with collapse related hot spots at the flow front. The red line trending E-W is likely a saturation effect/anomaly. (**C)** EO-1 ALI image of the initial breakout formation after a lobate flow front developed and the surface crust had extensively fractured. (**D**) EO-1 ALI image showing the continued breakout formation with the initial effusion of the NE lobe.

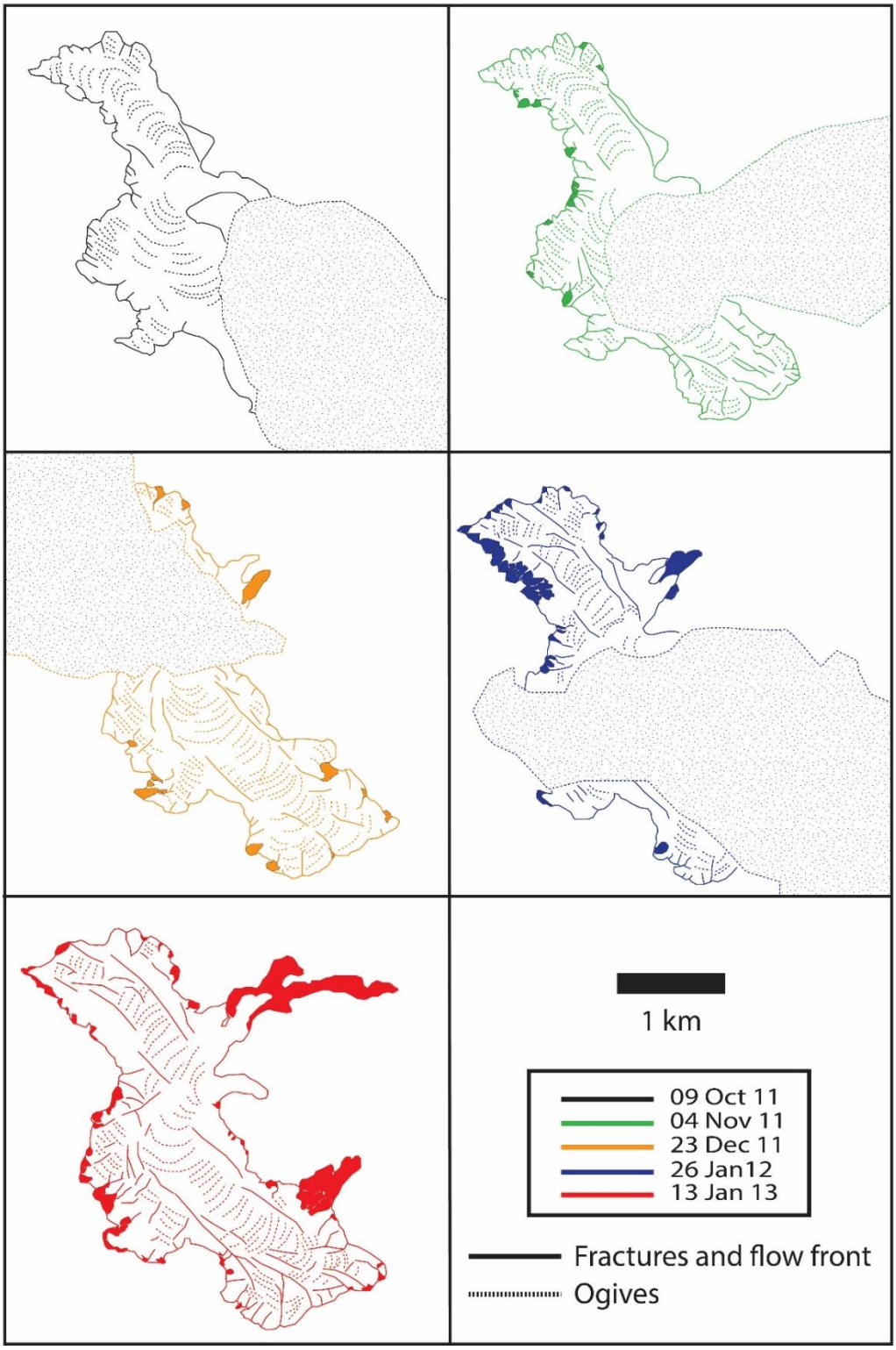


Figure 8A.18: Separated maps of the Cordón Caulle lava flow during emplacement showing the locations of breakouts, ogives and surface fractures throughout the flow emplacement.

### *8.1.2 Digital elevation models (DEMs)*

The DEM data used in this thesis includes a pre-eruption ASTER DEM of Cordón Caulle (Page 280), from which a slope angle map was derived (Page 281), an ASTER DEM of the 2001 Mt Etna lava flow (Page 283), and topographic profiles of the Cordón Caulle lava flow obtained from a Pléiades DEM (Pages 290-293). DEMs can be generated from satellite or aerial images using stereo parallax for an array of points in a region (Campbell and Wynne, 2011). DEMs from satellite imagery stereo pairs were first derived from SPOT images. These images were taken on different days so changes in illumination and weather presented challenges when deriving the DEM (Nikolakopoulos et al., 2006). The ASTER sensor built upon the use of stereo pairs by enabling the use of images taken from its two near infrared telescopes, one nadir-looking and the other backward-looking (27.7° off-nadir). This eliminated the effects of varying illumination and weather conditions between different days and allowed for the production of a global DEM (Nikolakopoulos et al., 2006).

Detailed topographic models have, in the past, been reliant on DEMs derived from satellites, airborne photogrammetry, airborne LiDAR, and terrestrial laser scanning (TLS). These methods have different limitations; as they can produce lower resolution DEMs (e.g. tens of metres from satellites), entail a high cost to conduct the survey (as is the case for airborne LiDAR), or are limited by accessibility to the area of interest (as is the case with TLS, where the equipment can be heavy and difficult to move to a remote area). Camera-based approaches therefore provide considerable advantages over such techniques for generating high resolution 3-D topographic models, due to their ease of use, low cost and reduced bulk. The camera-based techniques used to generate high resolution DEMs are outlined in Section 8.1.3.

#### 8.1.2.1 Application of DEMs

Pre-eruption and post-eruption DEMs were available for the Puyehue-Cordón Caulle lava flow. The pre-eruption DEM used is the 30 m resolution ASTER Global DEM v2 (released in mid-October 2011 and supplied in GeoTiff format), ASTER GDEM is a product of METI and NASA. This DEM is thought to have a vertical accuracy ±17 m at 95% confidence (Tachikawa et al., 2011; Elkhrachy, 2017). A slope angle map was derived using the slope function in ArcGIS Pro. Slope angles at a number of points along the path of the Cordón Caulle lava flow were determined from this DEM using trigonometry (Section 3), this was done to average the slope angle along the path of the lava flow. However, Castro et al. (2016) identified substantial (20 – 240 m) uplift of the terrain in the region surrounding the vent and underlying the lava flow, limiting the usefulness of the pre-eruptive DEM. Even with these topographic changes, slope angles beneath the lava flow likely only increase by ~3° (Section 3).

A post eruption DEM is available from the Pléiades Elevation 1 dataset, a 1 m resolution DEM produced from stereo-pairs from two Pléiades images (Section 4). The dataset has a horizontal and vertical accuracy of 1.5 m. Transects of relevant portions of the lava flow were provided by Castro. These transects were sampled at 2 m horizontal intervals to reduce noise from the highly uneven lava surface. As this DEM was produced from stereo-pairs, the true depths of some deep and narrow features (i.e. fractures) may be under-estimated due to being occluded in one or both images.

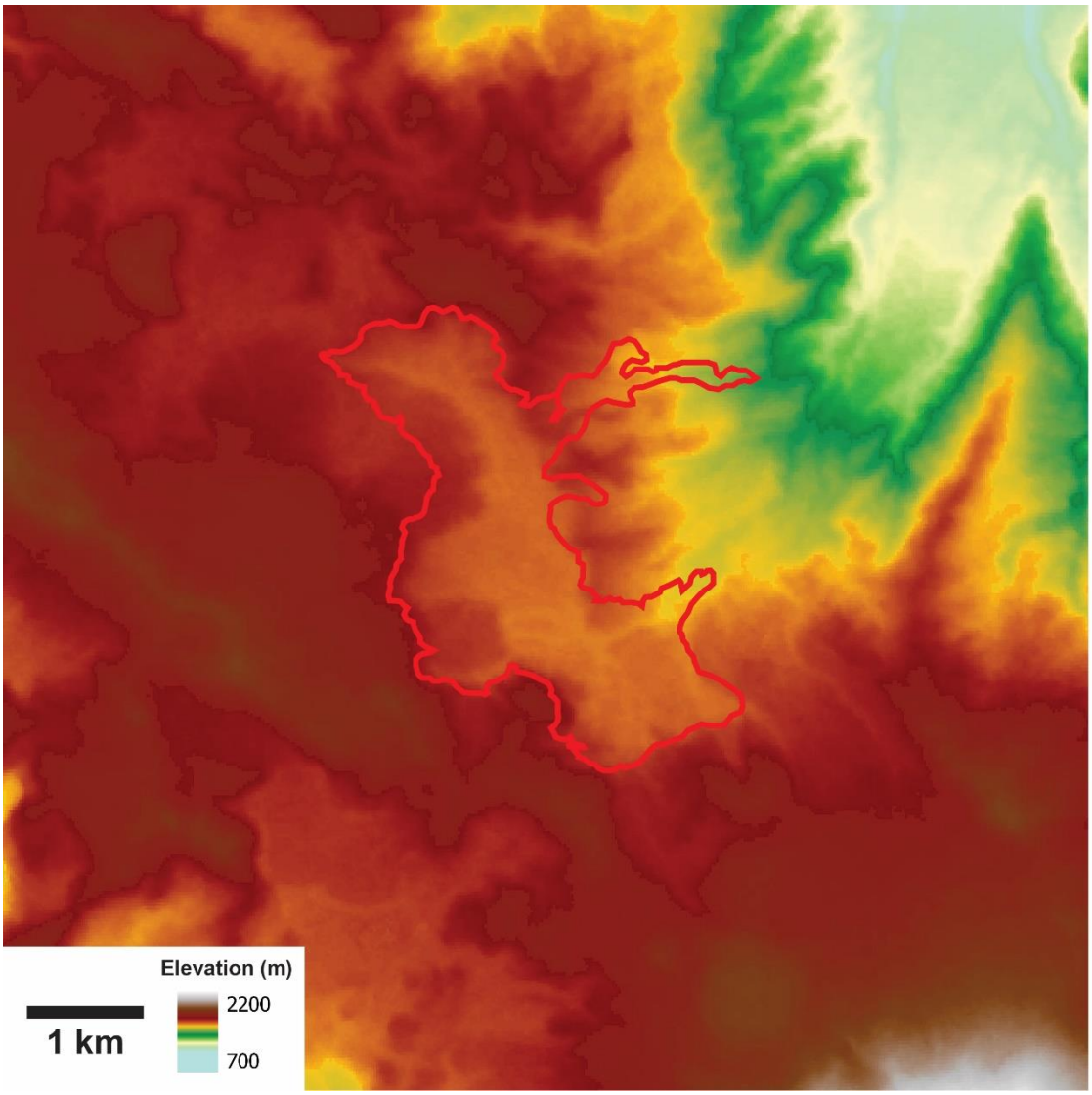


Figure 8A.19: Pre-eruption DEM of Cordón Caulle from the ASTER GDEM. The red line shows the extent of the 2011-2012 Cordón Caulle lava flow.

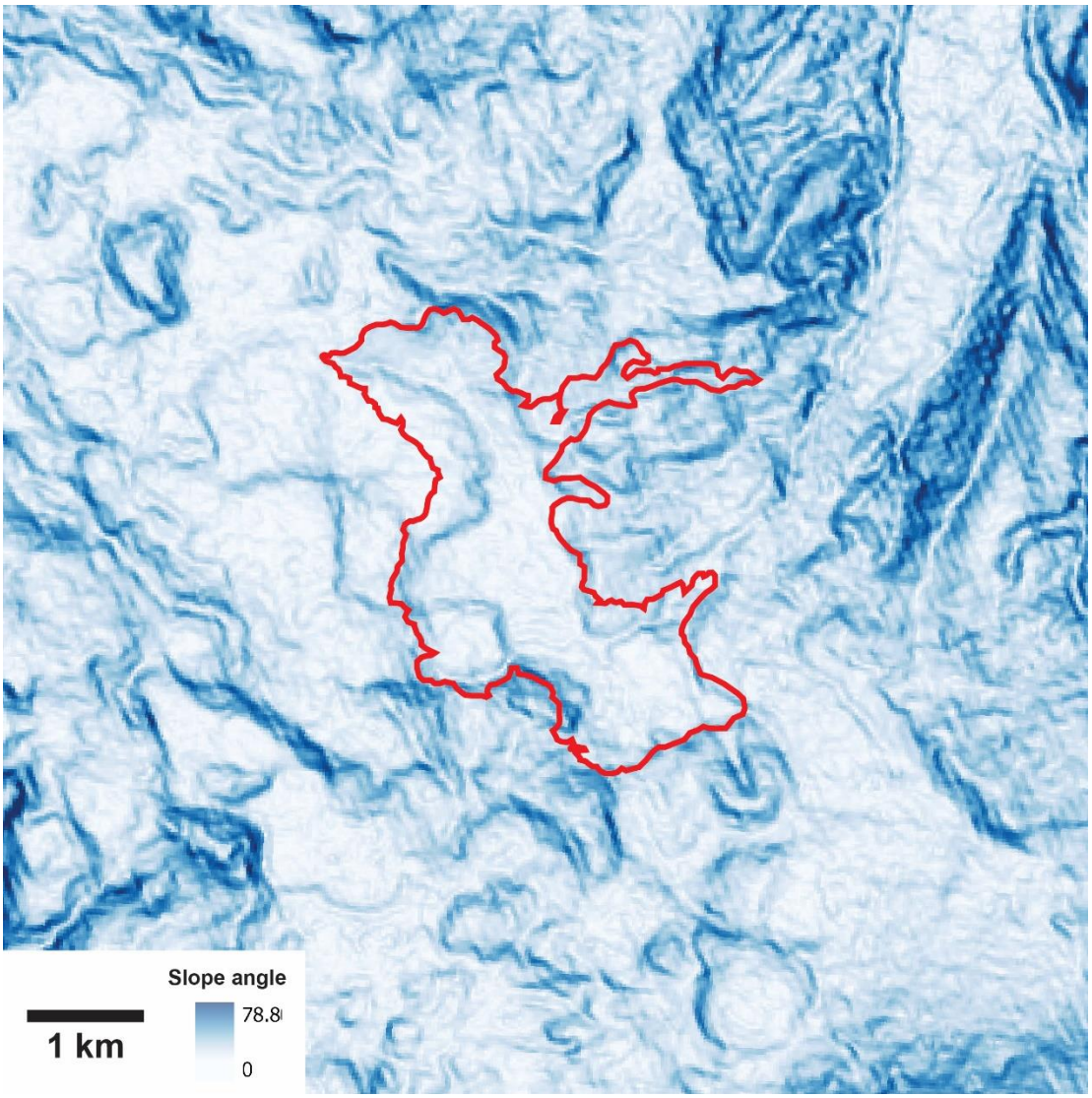


Figure 8A.20: Pre-eruption slope angle map of Cordón Caulle derived from the ASTER GDEM. The red line shows the extent of the 2011-2012 Cordón Caulle lava flow.

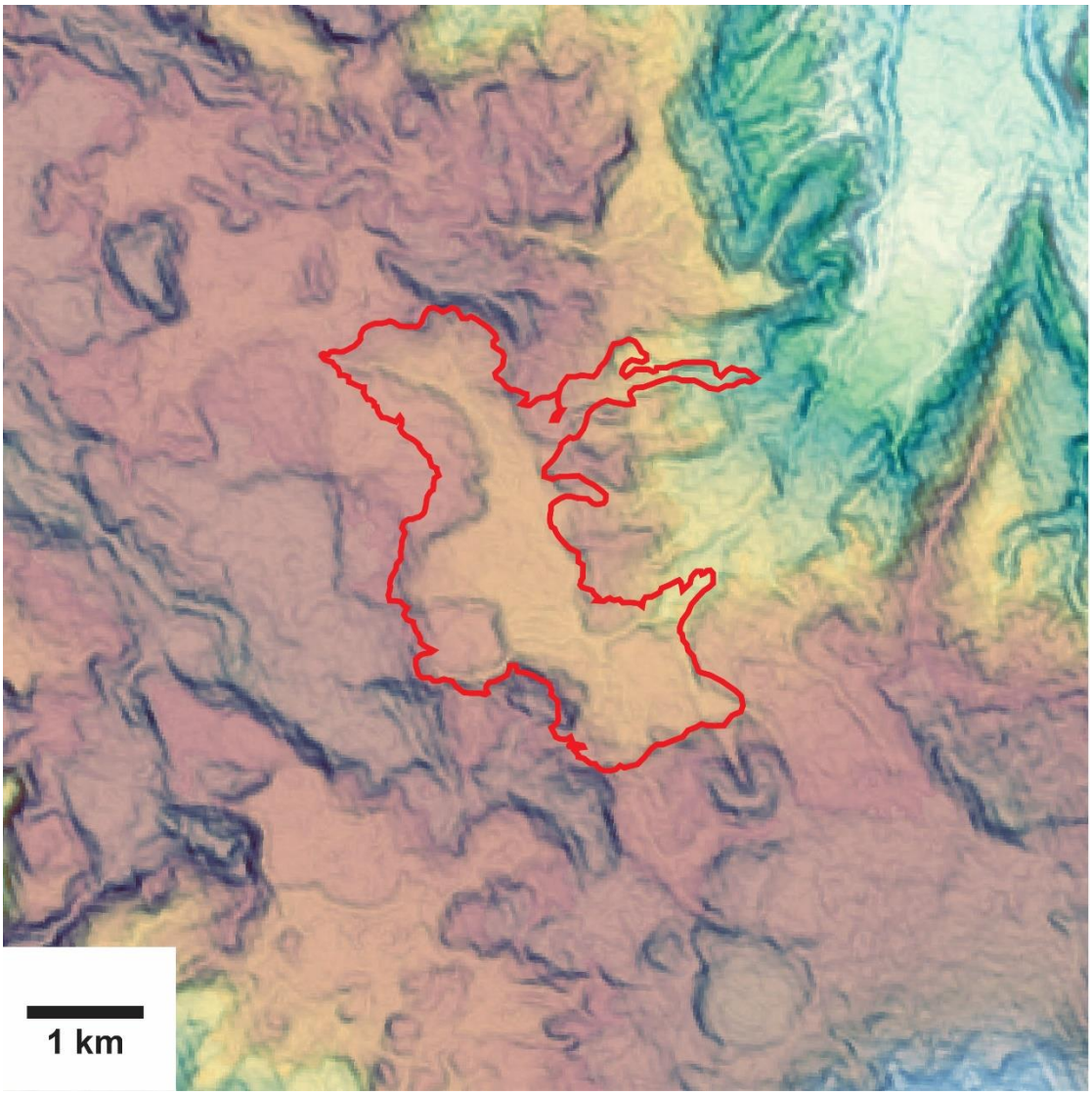


Figure 8A.21: Combined pre-eruption DEM (Fig. 2.16) and slope angle map (Fig. 2.17) of Cordón Caulle, derived from the ASTER GDEM. The red line shows the extent of the 2011-2012 Cordón Caulle lava flow.

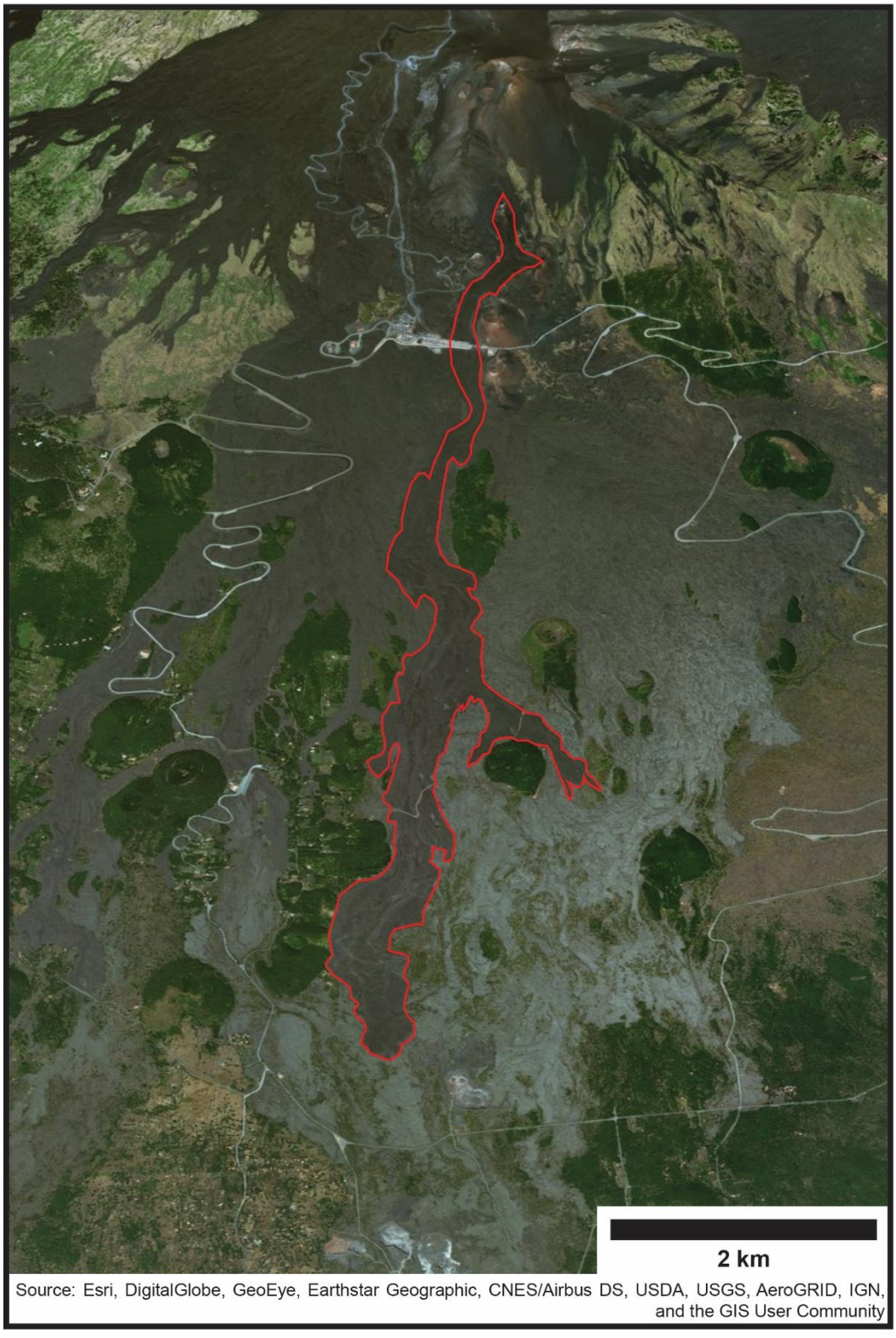


Figure 8A.22: Satellite image of the 2001 Mt Etna lava flow (highlighted in red).

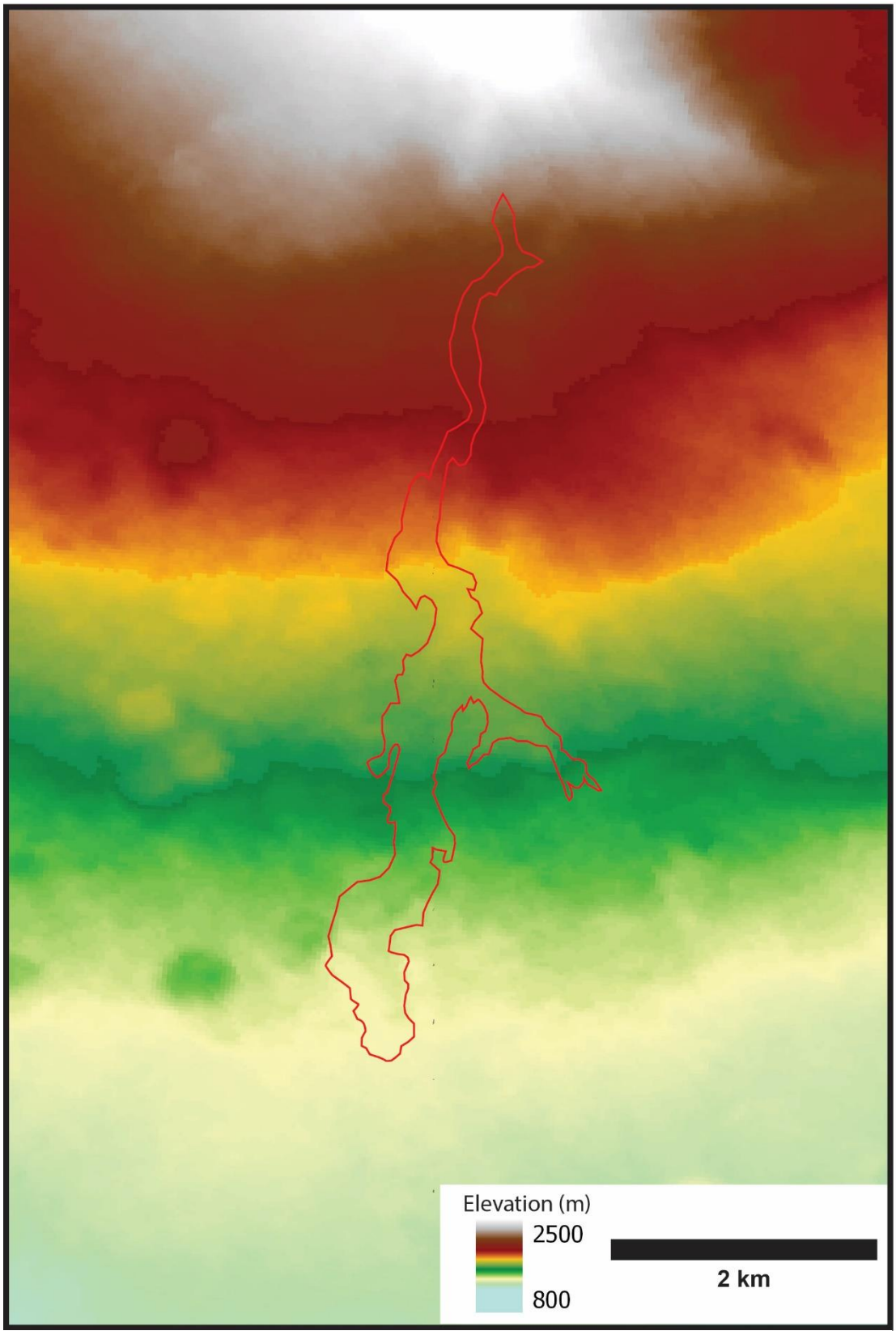


Figure 8A.23: ASTER GDEM of the 2001 lava flow and surrounding area (Fig. 8A.19, lava flow highlighted in red).

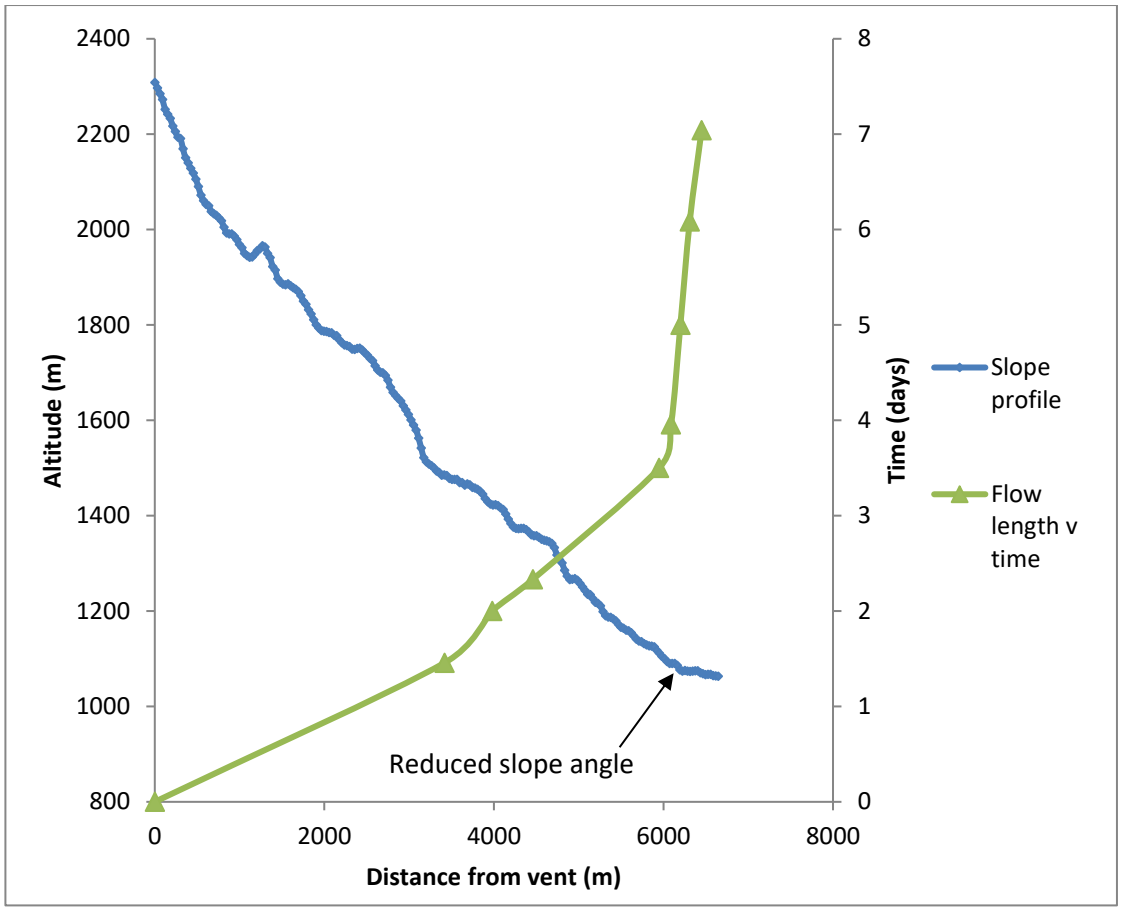


Figure 8A.24: Slope profile adjacent to the 2001 Mt Etna lava flow from the ASTER GDEM (blue line). Flow length with time (green line) there is a noticeable reduction in lava advance rate when the slope angle is reduced, flow length is taken from Applegarth (2008).

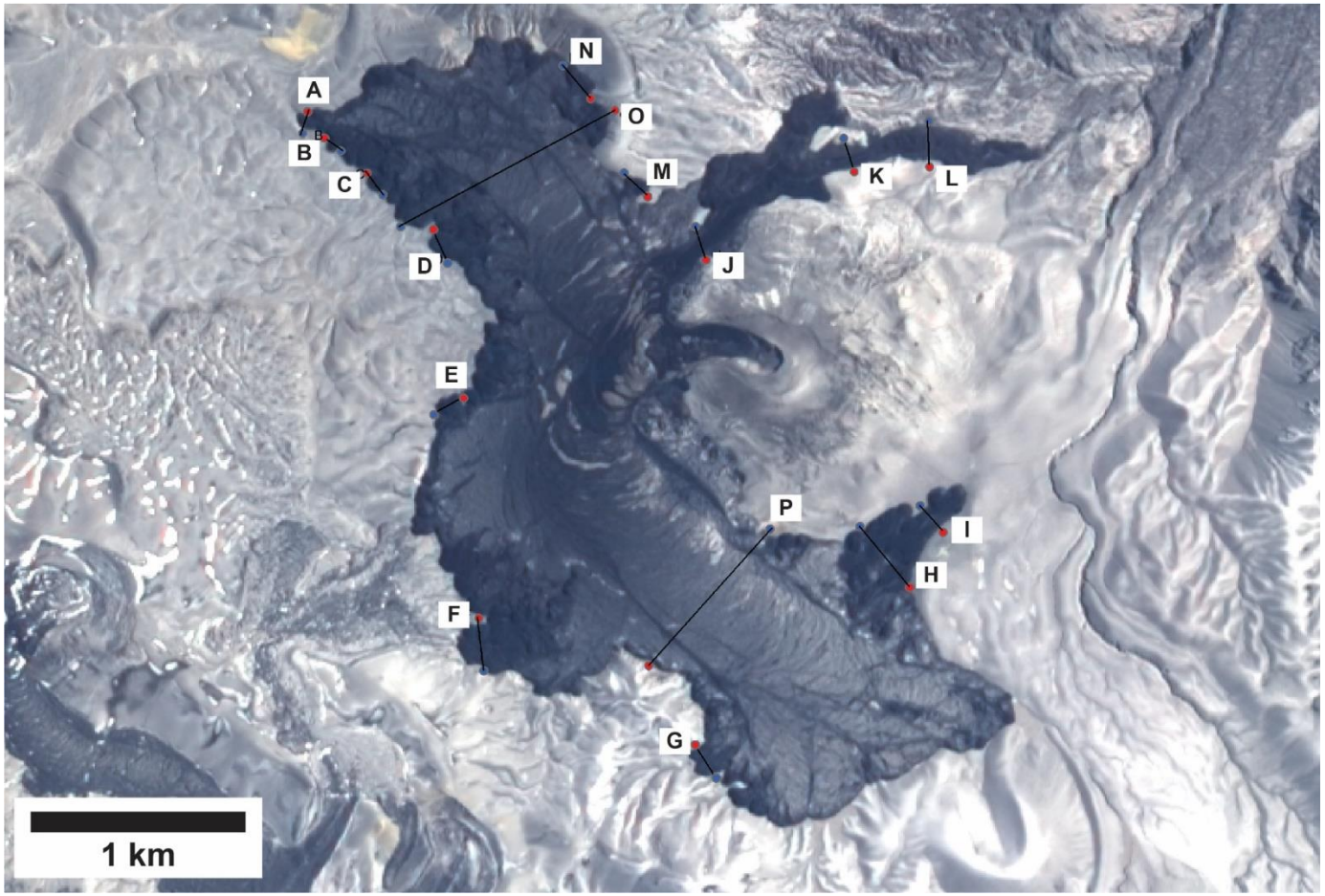


Figure 8A.25: EO-1 ALI image from 13/Jan/2013, letters show the locations of cross sections from a Pléiades DEM. Cross sections go from the red to blue spots.

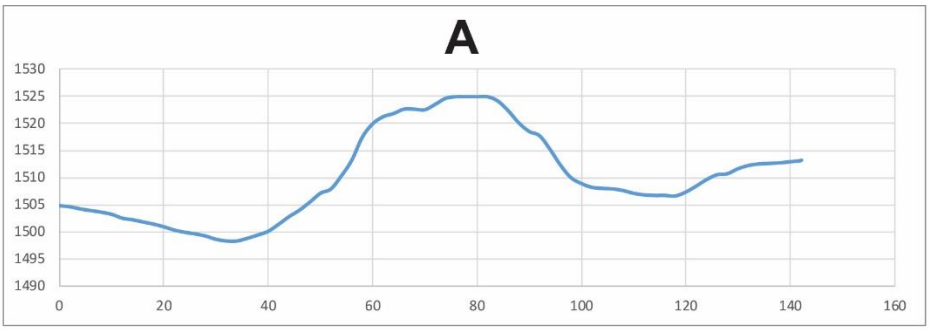
A
1530
1525
1520
1515
1510
1505
1500
1495
1490
0
20
40
60
80
100
120
140
160

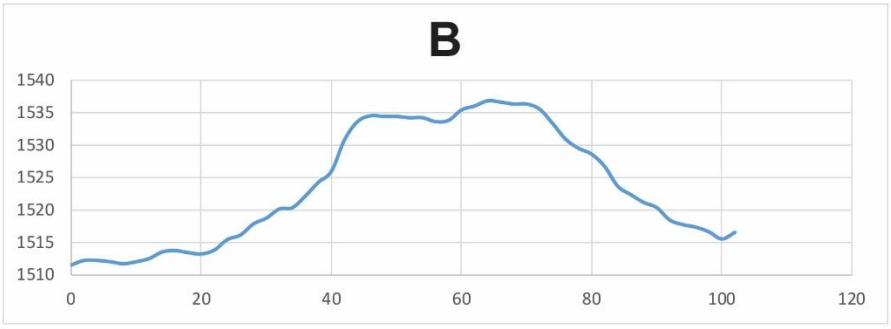
B
1540
1535
1530
1525
1520
1515
1510
0
20
40
60
80
100
120

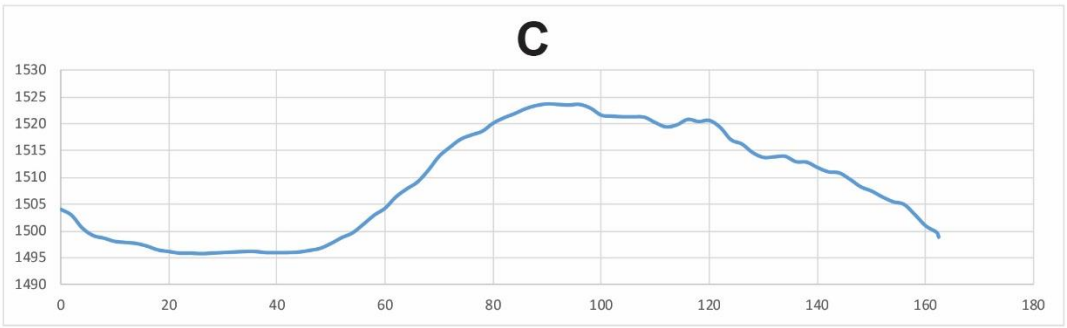
C
1530
1525
1520
1515
1510
1505
1500
1495
1490
0
20
40
60
80
100
120
140
160
180

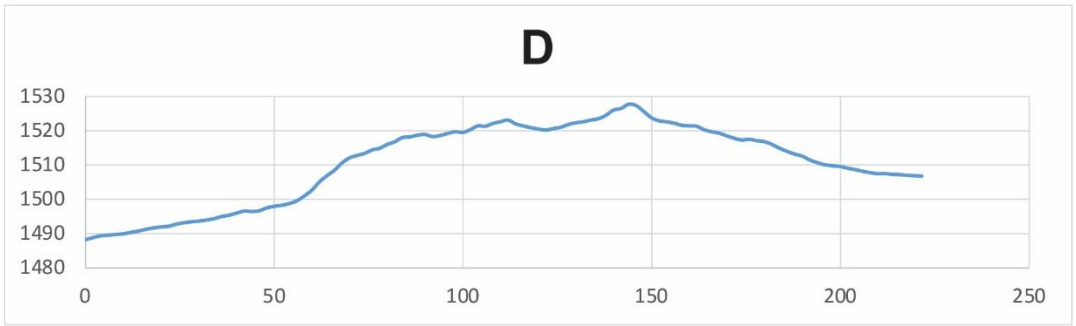
D
1530
1520
1510
1500
1490
1480
0
50
100
150
200
250

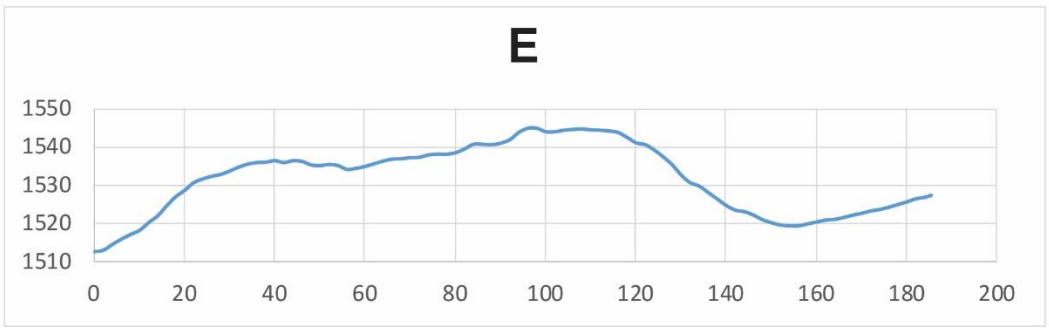
E
1550
1540
1530
1520
1510
0
20
40
60
80
100
120
140
160
180
200

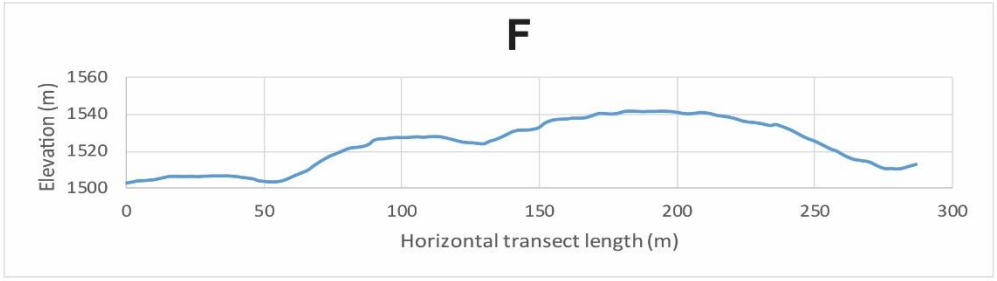
F
Elevation (m)
1560
1540
1520
1500
0
50
100
150
200
250
300
Horizontal transect length (m)

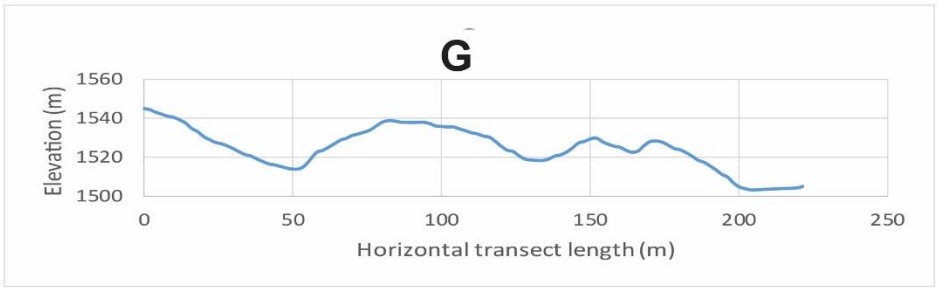
G
Elevation (m)
1560
1540
1520
1500
0
50
100
150
200
250
Horizontal transect length (m)

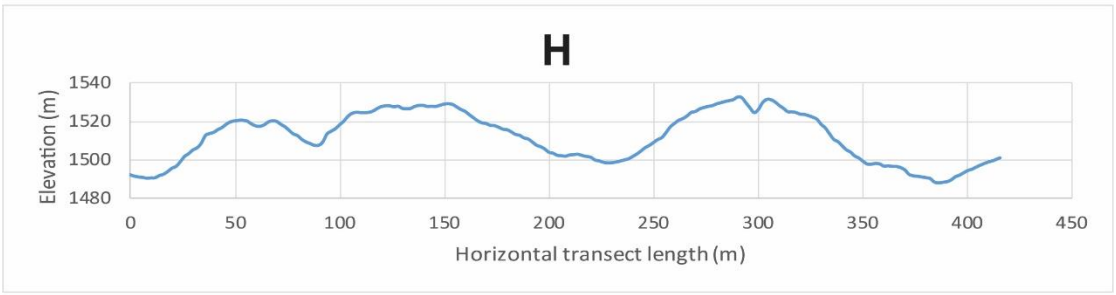
H
Elevation (m)
1540
1520
1500
1480
0
50
100
150
200
250
300
350
400
450
Horizontal transect length (m)

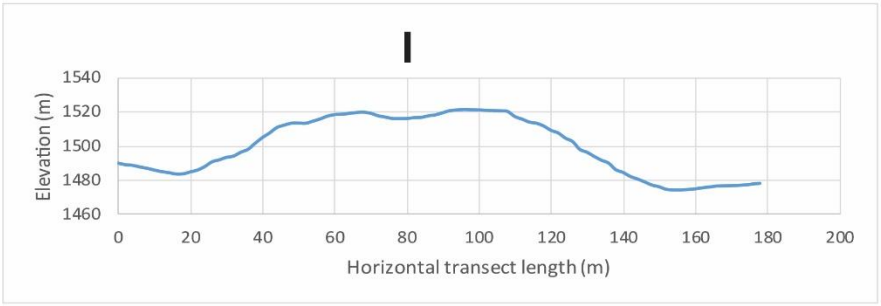
I
Elevation (m)
1540
1520
1500
1480
1460
0
20
40
60
80
100
120
140
160
180
200
Horizontal transect length (m)

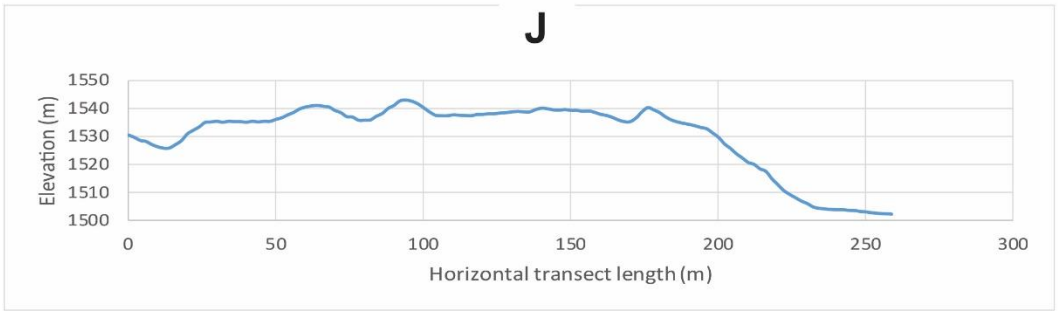
J
Elevation (m)
1550
1540
1530
1520
1510
1500
0
50
100
150
200
250
300
Horizontal transect length (m)

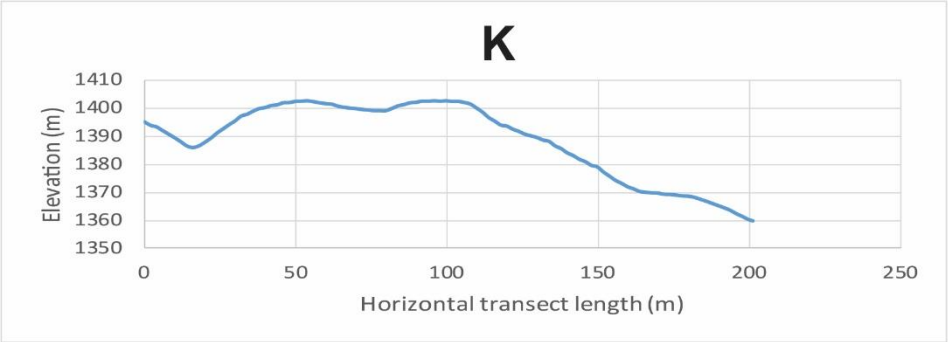
K
Elevation (m)
1410
1400
1390
1380
1370
1360
1350
0
50
100
150
200
250
Horizontal transect length (m)

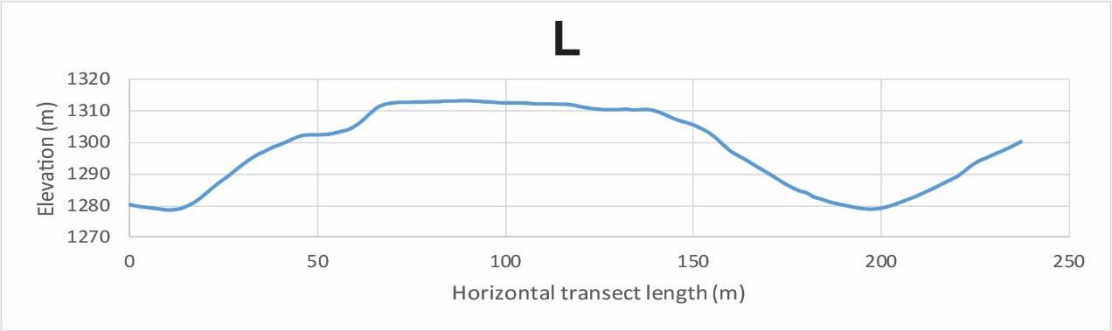
L
Elevation (m)
1320
1310
1300
1290
1280
1270
0
50
100
150
200
250
Horizontal transect length (m)

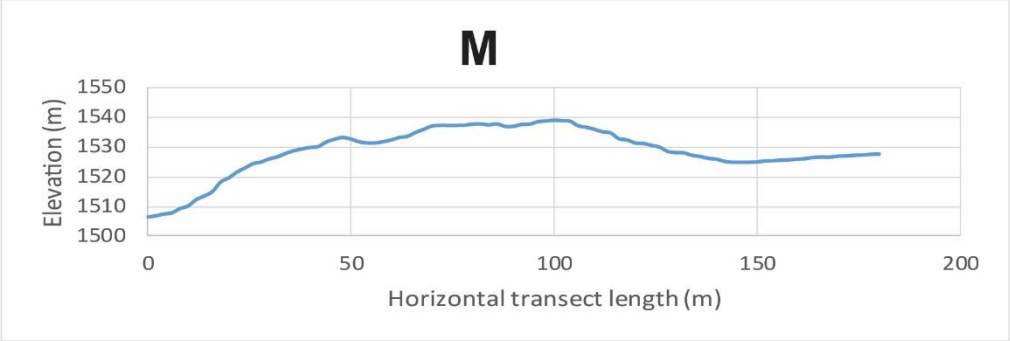
M
Elevation (m)
1550
1540
1530
1520
1510
1500
0
50
100
150
200
Horizontal transect length (m)

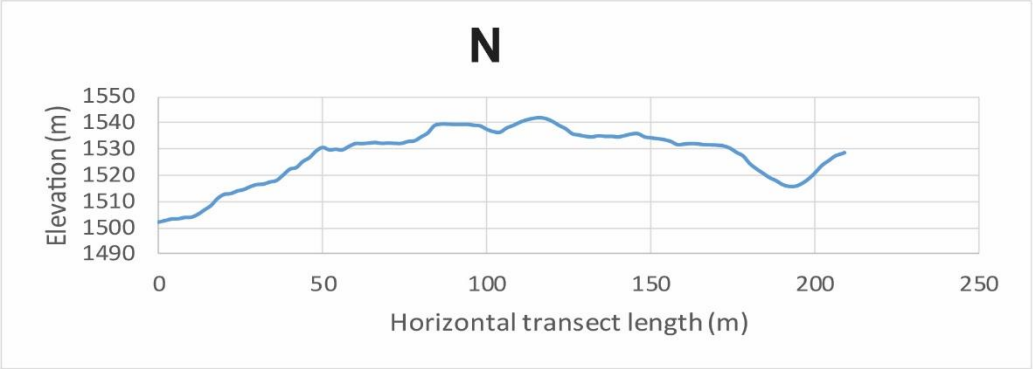
N
Elevation (m)
1550
1540
1530
1520
1510
1500
1490
0
50
100
150
200
250
Horizontal transect length (m)

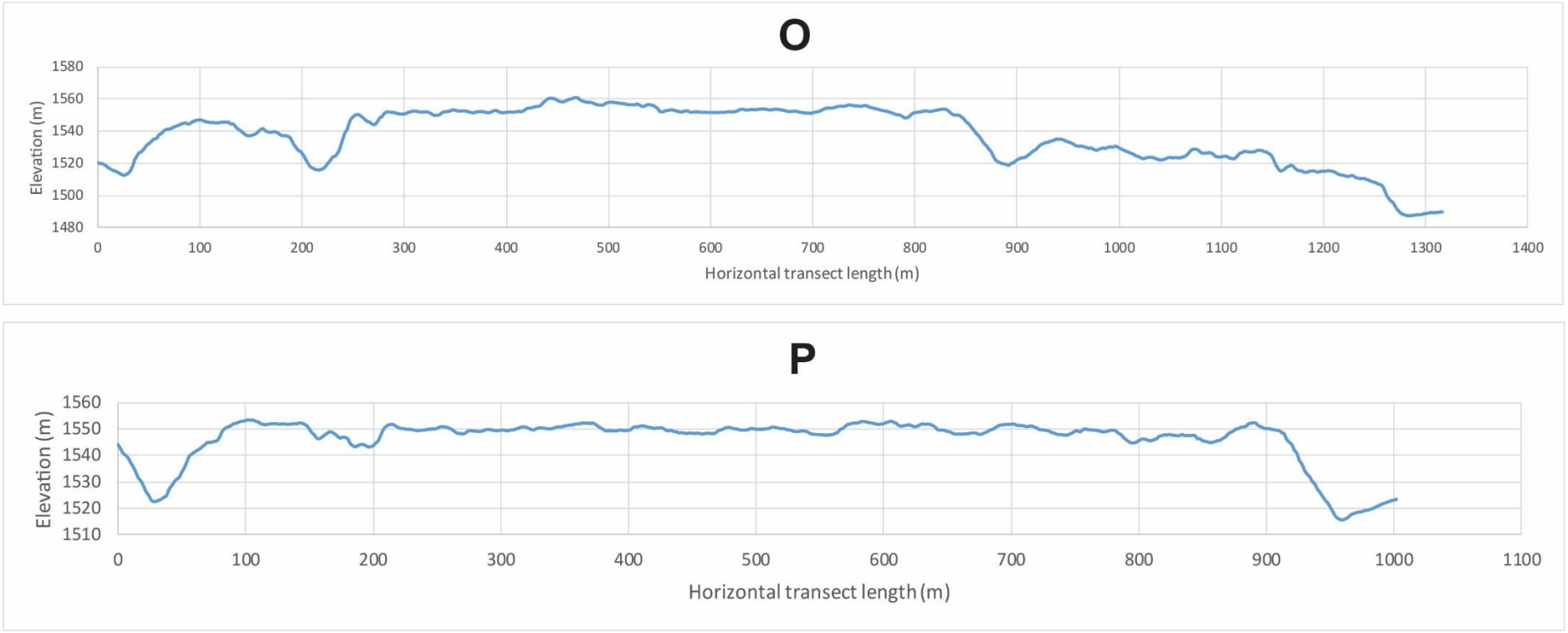


Figure 8A.26: **A-P**. Cross sections of the Cordón Caulle lava flow from a Pléiades DEM. The locations of these cross sections are found in Fig. 8A.21.

### *8.1.3 Structure-from-motion Photogrammetry*

The photogrammetry technique used here is outlined comprehensively in James and Robson (2012). The technique combines two computer vision approaches, structure from motion (SfM; Ullman, 1979) and multiview stereo (MVS; Seitz et al., 2006). SfM techniques were originally used to derive 3-D models from unordered image collections of a feature of interest, such as buildings (Snavely et al., 2006, 2008). The SfM technique is capable of building a sparse point cloud of the most prominent features. By linking the SfM technique with MVS image matching algorithms the data density in 3-D reconstructions has been greatly improved upon, generating two to three orders of magnitude more points than SfM alone (James and Robson, 2012). The resulting point clouds are of sufficient quality to produce a DEM, however the models lack geospatial information. As a result, geo-referencing must be added using control points (James and Robson, 2012). SfM photogrammetry can be used for ground based photographs, or for aerial photography using balloons/kites (Fonstad et al., 2013) and unmanned aerial vehicles (Niethammer et al., 2010). In volcanology SfM photogrammetry has been used to monitor the emplacement of basaltic lava flows (James and Robson, 2014; Kolzenburg et al., 2016), rhyolitic lava flows (Tuffen et al., 2013; Farquharson et al., 2015), lava domes (James and Varley, 2012), and lava lake levels (Smets et al., 2017).

#### 8.1.3.1 Application of SfM photogrammetry

Structure-from-motion photogrammetry was used to generate 3-D models of portions of the lava flow at Puyehue-Cordón Caulle (Section 4). This involved taking a large number of field photos (>100) using a digital SLR camera at regular intervals around the feature of interest, ensuring a large overlap between images. The photos were then processed in Agisoft PhotoScan Professional (v1.3.2) to produce a dense point cloud of the feature of interest (Fig. 8A.27). The 3-D model was scaled using the known

distance between features co-identified in a georeferenced satellite image, the model can also be georeferenced in a similar manner but this is not required to generate a scaled model. Model scaling is accurate to ~5-10%. The model was manually orientated to ensure the appropriate orientation of the upward Z axis. Anomalous data points arising from production of the point cloud (anomalous points being defined as those separate from the rest of the 3-D model) were manually removed in PhotoScan.

The 3-D model is most easily visualised in CloudCompare, which also allows sectioning of the model. A high resolution (~10 cm) DEM generated from the 3-D model in PhotoScan, was imported into ArcGIS and cross sections of the DEM were made using

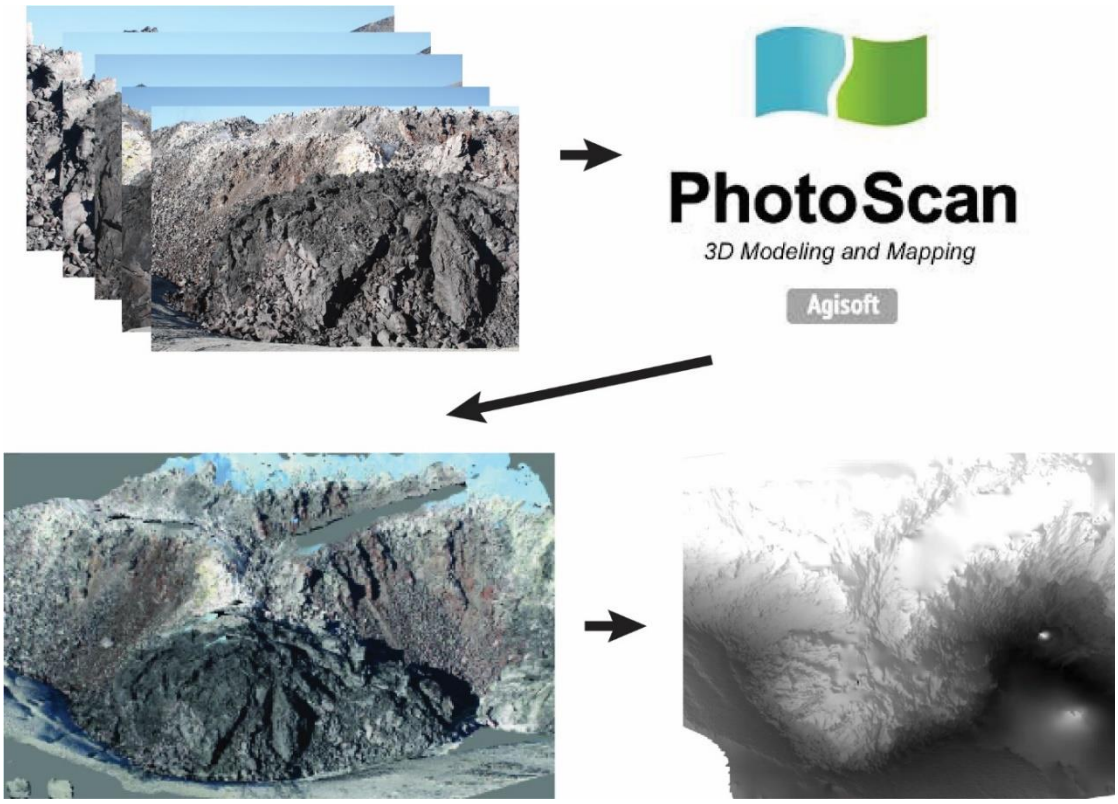


Figure 8A.27: Illustration of the methodology to derive a 3D model and associated DEM of a portion of the lava flow. Photos are taken at regular intervals around a feature of interest, these photos are imported into Agisoft PhotoScan professional, this generates a 3D model and from that a DEM.

the 3-D analyst tool. As the models were produced from photographs taken on foot, the top surface of the features of interest cannot always be imaged, which limits the

usefulness of these models. However, by using natural topographic rises to look down on the surface of the lava flow useable data can be gathered.

UAV photogrammetry (Section 5) was conducted using a DJI Phantom drone equipped with a downward facing DJI FC300X camera. Georeferenced photographs were processed in Agisoft PhotoScan Professional (v1.3.2) to produce a 3-D model, from which a 2 cm resolution orthophoto and 5 cm resolution DEM were produced; these were up to 300 m wide and 500 m long. The use of UAV photogrammetry allows for automated photo capture and consistent photo overlap, it also eliminates some of the data gaps typically associated with ground based photogrammetric surveys.

#### 8.1.3.2 SfM photogrammetry data provided

The DEM generated for a breakout at Cordón Caulle close to the vent (Fig. 4.7) is provided on Page 294. A DEM of the northern flow front is also provided on Page 295. An orthophoto and corresponding DEMs derived from UAV photogrammetry of a portion of the Medicine Lake Dacite Flow are provided on Pages 296 and 297.

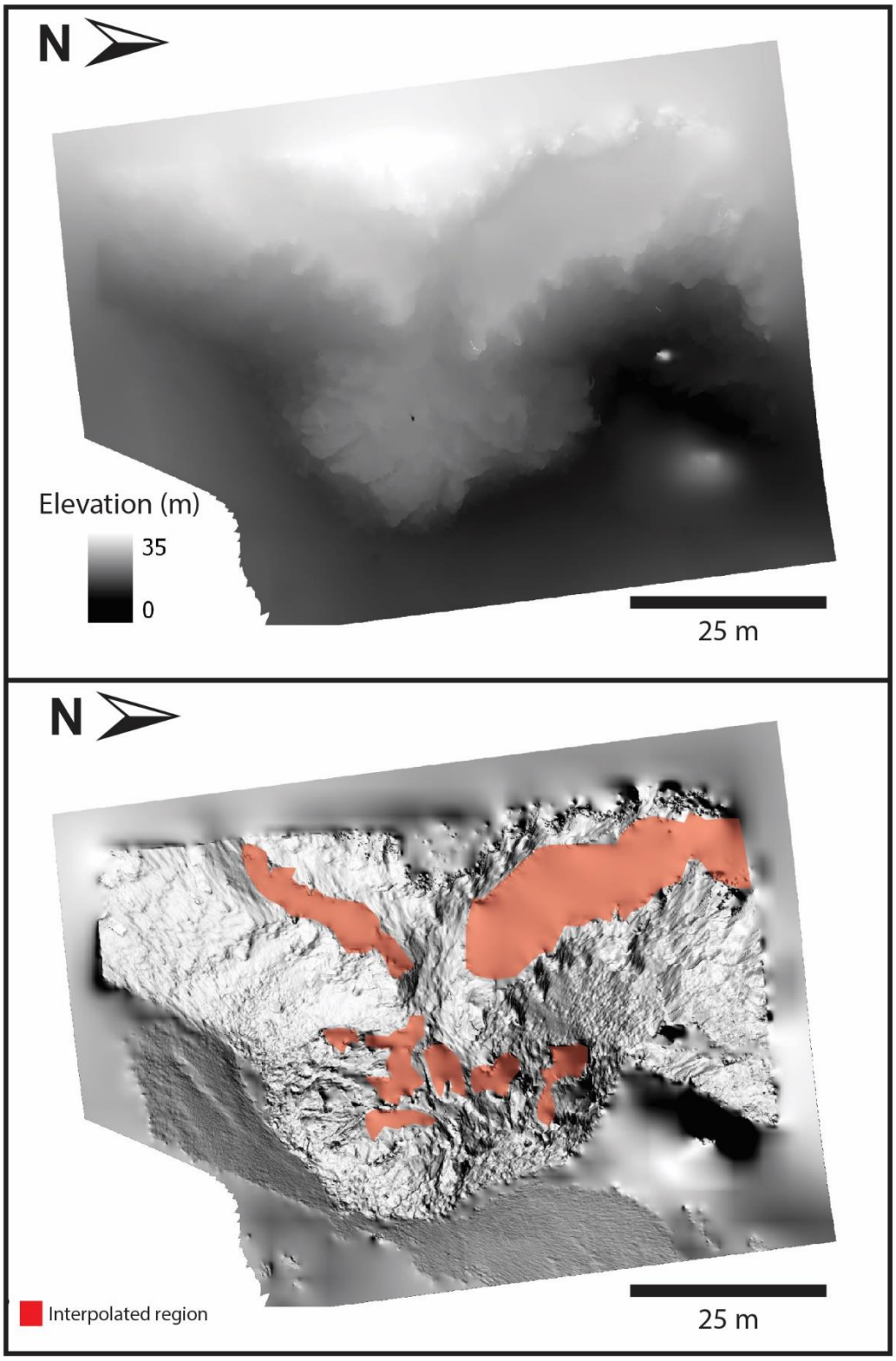


Figure 8A.28: **Top**. DEM of a breakout derived from ground based SfM photogrammetry. **Bottom**. Hill-shade DEM of the top image. Elevations are scaled from an arbitrary datum.

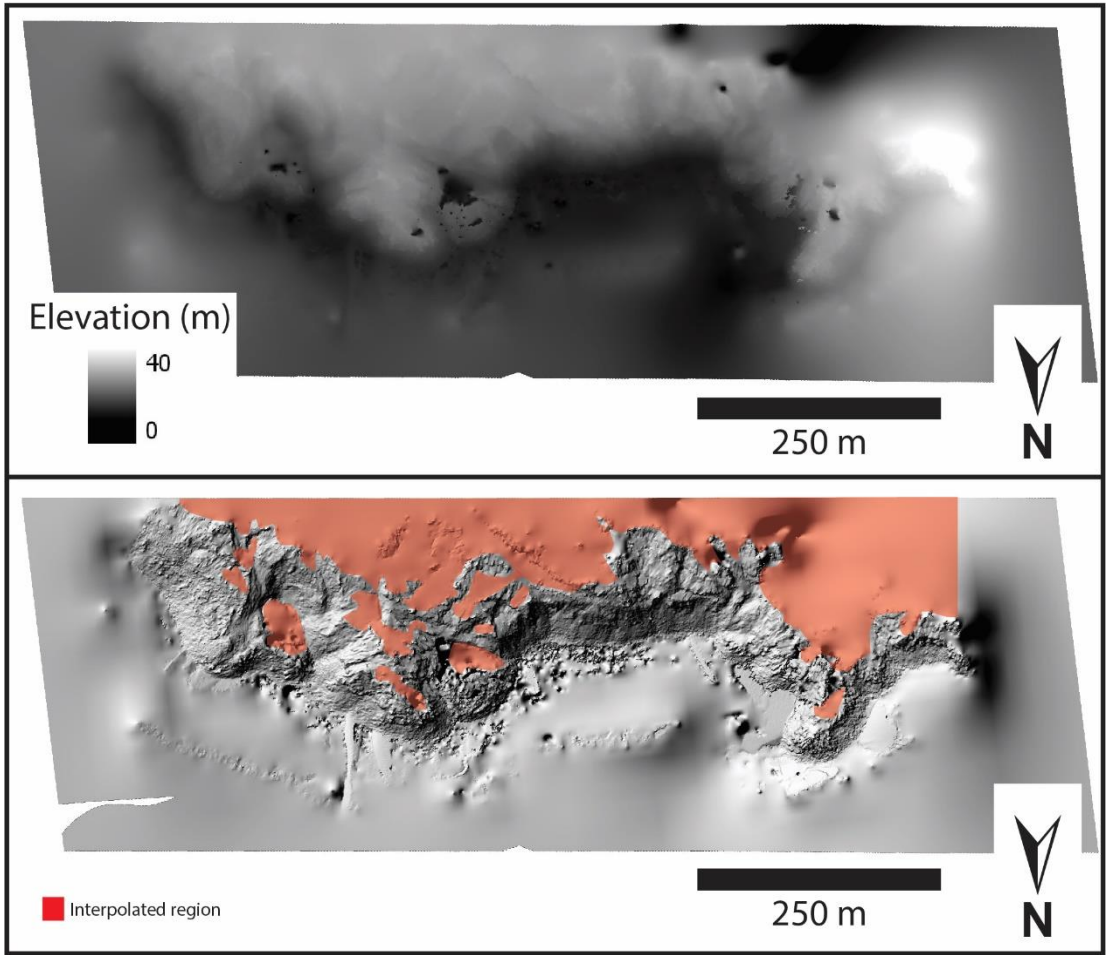


Figure 8A.29: **Top**. DEM of the Northern flow front derived from ground based SfM photogrammetry. **Bottom**. Hill-shade DEM of the top image. Elevations are scaled from an arbitrary datum.


Figure 8A.30: UAV derived orthophoto of a portion of the Medicine Lake Dacite Flow from Medicine Lake Volcano, California.

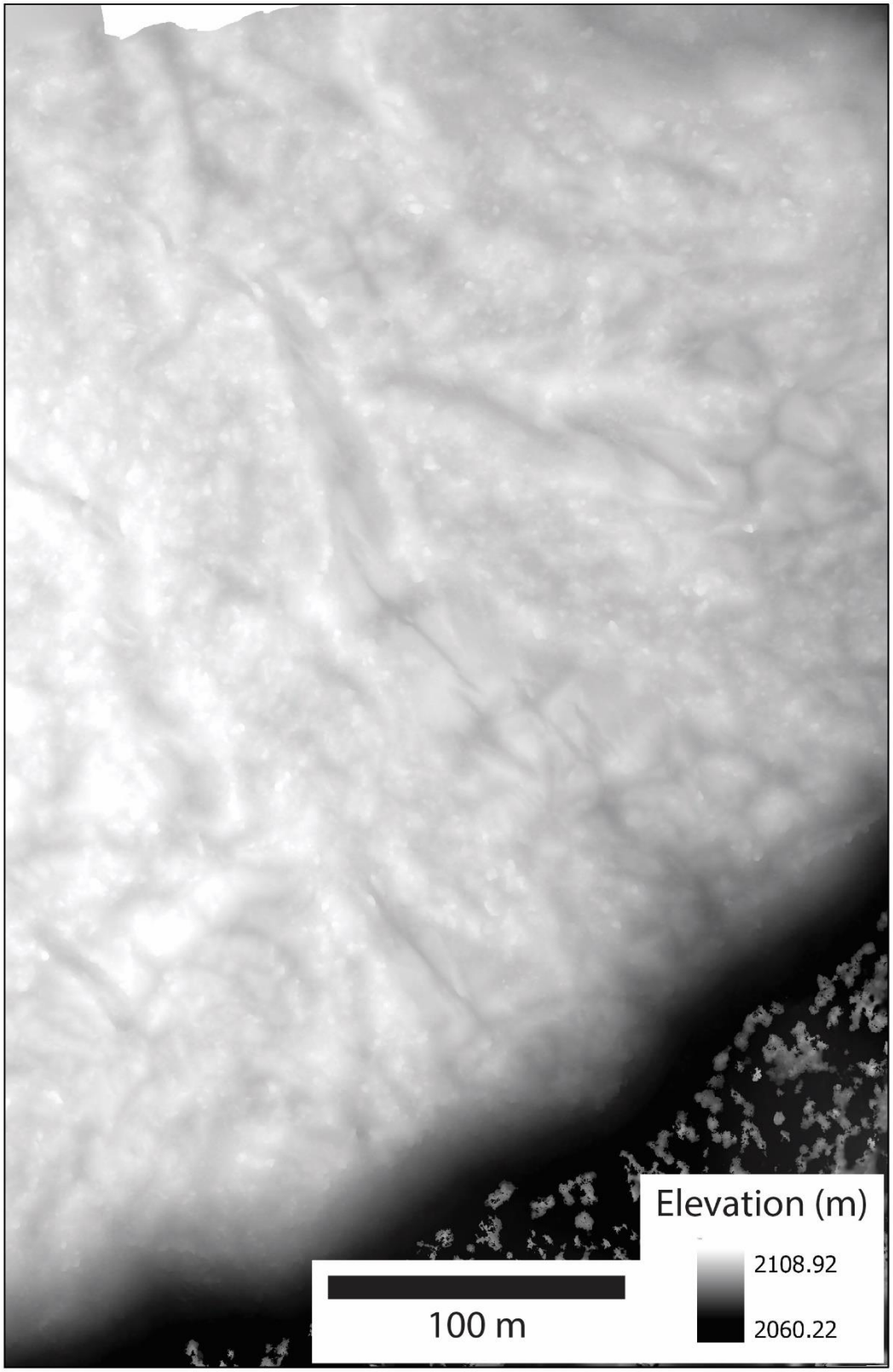


Figure 8A.31: UAV SfM photogrammetry derived DEM of a portion of the Medicine Lake Dacite Flow from Medicine Lake Volcano, California.

## 8.2 Appendix B: Fieldwork

Fieldwork was conducted at Puyehue-Cordón Caulle in Chile, Mt Etna in Sicily, and Medicine Lake Volcano, California, with work primarily focussed on elucidating flow emplacement processes. Fieldwork involved making field observations and interpretations of flow features. The work conducted on Mt Etna enabled comparison between the mafic and silicic compositions.

### *8.2.1 Puyehue-Cordón Caulle (Section 3-5)*

Fieldwork at Cordón Caulle was conducted in January 2015. This fieldwork aimed to (1) characterise the differing lithologies of the lava flow, (2) characterise the morphologies of breakouts, (3) determine the characteristic flow lithologies from vent, main channel and breakout, and (4) obtain representative samples. Fieldwork was assisted by helicopter overflights of the lava flow, which allowed aerial photography of parts of the lava that were otherwise inaccessible. Photos/videos were taken out of the window of the helicopter, and a GoPro camera was attached to the front of the helicopter pointing downwards, which continuously recorded video during return trips of the helicopter. Relevant frames from the video were then exported as still images.

Approximately 50 samples were gathered from different portions of the lava flow for analysis (Table 8B.1); these are representative of the different lithologies observed. Detailed field observations were made of the structure of ~20 breakouts and photos were taken of many more breakouts. Photos for SfM photogrammetric models were taken of ~5 breakouts. Observations of the lava emplacement have also been incorporated from fieldwork conducted by Hugh Tuffen and Mike James in January 2012, 2013 and 2014.

### *8.2.2 Mt Etna (Section 3)*

Fieldwork on Mt Etna took place in April 2015 and 2016 and aimed to (1) analyse the structure and morphology of the numerous late stage flow features, including breakouts, squeeze-ups, spines and tumuli, and (2) to provide a comparison to structural features observed in rhyolitic lava flows. Structural analysis of ~15 breakouts, and numerous squeeze-ups/tumuli, were made at the lower 2001 Mt Etna lava flow (Applegarth et al., 2010c).

### *8.2.3 Medicine Lake, USA (Section 5)*

Fieldwork was carried out on rhyolite lava flows in the Western USA in August 2016 and 2017 on fieldtrips led by Jon Fink, Steve Anderson and Curtis Manley. This fieldwork focussed on the rhyolite lava flows of Medicine Lake Volcano in Northern California, including Glass Mountain, Little Glass Mountain, Crater Glass Flow, Medicine Glass Flow (Donnelly-Nolan et al., 2016). The work aimed to (1) examine the late stage flow features of these lava flows, specifically the coarsely vesicular pumice diapirs at the lavas surface, (2) collect representative samples of different lithologies for further laboratory analysis, primarily microstructural characterisation, and (3) allow for comparisons between the structure, broad morphology and flow features, of the silicic lava flows at Medicine Lake and the Cordón Caulle lava flow. Approximately 20 samples were gathered for microstructural analysis (Table 8B.2). Two UAV surveys were conducted of the Crater Glass flow and the Medicine Lake Dacite flow in 2017.

### *8.2.4 Field data provided*

Tables of samples collected are given on Pages 300-301. A table of breakout sizes for different morphological types, derived from field observations and Google Earth is given on Pages 302-303.

Table 8B.1: Samples collected from Puyehue-Cordón Caulle

| Sample name | Day | Locality | Photo number | Notebook page | Description |
|---|---|---|---|---|---|
| A1-G1 | 2 | 2 S BO | 5987-6004 | 13 | Sequence through top of breakout slab. F1 missing |
| A2, B2, D2 | 3 | 2 Main flow | 6097-6099 and 2218-2225 | 30 | Sequence through main channel top |
| CR1 + CR2 | 3 | 2 Main channel | 6061-6068 | 24 | Platy fracture core lava |
| CH1 | 3 | 2 N BO | | 22 | Chisel mark |
| SU1-SU5 | 3 | 2 Main channel | 6072-6088 | 25 | Possible squeeze up - contact between platy and welded breccia |
| FT1 | 5 | 4 channel 1 | 2616-2620 | 42 | Orientated flow top |
| CH2-CH4 | 5 | 5 Large crease | 6307-6308, 2678-2685 | 44 | Crease samples away from crease structure in vent |
| A3-C3 | 5 | 3 vent lava | 6231-6235 and 6284-6286 | 35 | Vent lava sequence upwards |
| A4-D4 | 6 | 6 small BO | 6348-6352 | 50 | Upward sequence through breakout |
| A5-B5 | 6 | BRKOUT TOP SAM (7) | 2818-2819 | 61 | Deep breakout lava and top surface |
| CR3 | 7 | 8 in fracture | 6413-6416 | 66 | Platy fracture deep in gash |
| A6-E6 | 7 | 9 fallen boulder | 6443-6449 | 74 | Sequence to top surface through a ductile tearing feature (BO) |
| BOCR1+2 | 8 | 11 | 6511-6514 | 89 | Break out platy lava |
| GC1 | 10 | 12 | 6789 | 97 | Glassy cavitation in boulder |
| FG1-FG2 | 10 | 12 | 6782-6783, 6799-6802,6960 | 115 | Friction/impact glass |
| FG3-FG4 | 12 | 12 | 6782-6783, 6799-6802,6961 | 115 | Friction/impact glass |
| SBO1-SBO3 | 12 | 12 | 6961, 6977-6980 | 119 | Spherulitic obsidian (BO) |
| VN1 | | VE (vent extrusion) | | | Vent nozzle |
| Bomb 1 | | Near vent | | | Bread crust bomb from near vent |

Table 8B.2: Samples collected from Medicine Lake Volcano

| Sample number | Location | Photo number | Notebook page | Description |
|---|---|---|---|---|
| BGM01 | Big glass mountain | 2237 | 22 | Obsidian from spine |
| BGM02 | Big glass mountain | 2247 | 23 | CVP, highly vesicular. Bottom |
| BGM03 | Big glass mountain | 2248 | 23 | CVP, highly vesicular. Top |
| BGM04 | Big glass mountain, GPS 356 | 2253 | 24 | Interbanded obsidian and CVP |
| BGM05 | Big glass mountain, GPS 356 | HT 5456-5462 | 24 | CVP with dense obsidian band |
| BGM06 | Big glass mountain | 2266 | 25 | Denser CVP |
| BGM07 | Big glass mountain | 2272 | 25 | Denser CVP |
| LGM1.1 | Little glass mountain | | 3 | Lithophysae obsidian |
| CGF-S-01 | Crater glass flow south | 2093 | 7 | CVP |
| CGF-M-01 | Crater glass flow middle | 2417 | 30 | CVP diapir, inflated and sheared |
| CGF-M-02 | Crater glass flow middle | 2506 | 38 | CVP diapir |
| CGF-M-03 | Crater glass flow middle | 2507 | 38 | CVP diapir partially collapsed |
| CGF-M-04 | Crater glass flow middle | 2508 | 38 | CVP diapir partially collapsed |
| CGF-M-05 | Crater glass flow middle | 2509 | 38 | Denser CVP diapir |
| CGF-M-06 | Crater glass flow middle | | 39 | FVP with ash nozzle |
| MLD01 | Medicine lake dacite | 2224 | 20 | Dense dacite |
| MLD02 | Medicine lake dacite | 2228-2230 | 21 | Flow banded dacite collapsed and vesicular |
| MLD03 | Medicine lake dacite | 2231 | 22 | Vesicular dacite |

Table 8B.3: Summary of breakout types and sizes

| Type | Location | Length (m) | Width (m) | Height (m) | Volume ($m^3$) | Block Size (m) |
|---|---|---|---|---|---|---|
| Domed | 40°31'42.69"S, 72° 8'56.60"W | 30 | 40 | 15 | 1.80E+04 | 5 - 15 |
| Domed | 40°31'25.63"S, 72° 9'8.32"W | 70 | 70 | 20 | 9.80E+04 | |
| Domed | 40°32'2.26"S, 72° 8'20.68"W | 15 | 17 | 15 | 3.83E+03 | |
| Domed | 40°32'40.14"S, 72° 8'56.86"W | 80 | 100 | 30 | 2.40E+05 | |
| Domed | 40°30'28.80"S, 72° 9'41.61"W | 75 | 67 | 30 | 1.51E+05 | |
| Domed | 40°31'46.18"S, 72° 8'11.13"W | 70 | 85 | 30 | 1.79E+05 | |
| Average | | 56.7 | 63.2 | 23.3 | 1.15E+05 | |
| Petaloid | 40°30'38.21"S, 72°10'33.35"W | 180 | 80 | 25 | 3.60E+05 | 5-10 |
| Petaloid | 40°30'42.51"S, 72°10'27.92"W | 70 | 66 | 30 | 1.39E+05 | |
| Petaloid | 40°31'49.44"S, 72°10'11.44"W | 125 | 70 | 30 | 2.63E+05 | |
| Petaloid | 40°31'28.50"S, 72°10'3.82"W | 170 | 80 | 30 | 4.08E+05 | |
| Petaloid | 40°30'42.62"S, 72°10'23.99"W | 160 | 110 | 30 | 5.28E+05 | |
| Petaloid | 40°30'31.00"S, 72°10'16.97"W | 200 | 150 | 25 | 7.50E+05 | |
| Petaloid | 40°32'30.49"S, 72° 9'10.07"W | 170 | 80 | 30 | 4.08E+05 | |
| Petaloid | 40°32'17.65"S, 72° 9'37.36"W | 100 | 90 | 30 | 2.70E+05 | |
| Petaloid | 40°31'26.82"S, 72° 9'58.06"W | 160 | 80 | 30 | 3.84E+05 | |
| Petaloid | 40°30'48.82"S, 72°10'17.01"W | 230 | 130 | 30 | 8.97E+05 | |
| Average | | 156.5 | 93.6 | 29 | 4.41E+05 | |
| Rubbly | 40°31'0.32"S, 72°10'4.27"W | 440 | 130 | 30 | 1.72E+06 | 1-5 |
| Rubbly | 40°31'20.36"S, 72° 9'51.40"W | 270 | 140 | 30 | 1.13E+06 | |
| Rubbly | 40°30'51.24"S, 72° 9'18.63"W | 110 | 130 | 30 | 4.29E+05 | |
| Rubbly | 40°30'54.77"S, 72° 9'10.82"W | 370 | 220 | 30 | 2.44E+06 | |
| Rubbly | 40°31'51.26"S, 72° 8'21.92"W | 300 | 130 | 30 | 1.17E+06 | |

| | | | | | | |
|---|---|---|---|---|---|---|
| Rubbly | 40°31'54.62"S, 72°10'3.28"W | 270 | 140 | 30 | 1.13E+06 | |
| Rubbly | 40°31'57.79"S, 72°10'0.66"W | 350 | 125 | 30 | 1.31E+06 | |
| Rubbly | 40°32'11.53"S, 72° 9'53.51"W | 450 | 150 | 30 | 2.03E+06 | |
| Rubbly | 40°32'7.78"S, 72° 9'52.32"W | 340 | 130 | 30 | 1.33E+06 | |
| Rubbly | 40°30'50.83"S, 72° 8'47.33"W | 2000 | 200 | 30 | 1.20E+07 | |
| Rubbly | 40°31'9.70"S, 72° 9'52.21"W | 170 | 100 | 30 | 5.10E+05 | |
| Average | | 460.9 | 145 | 30 | 2.29E+06 | |
| Cleft-split | 40°32'0.63"S, 72° 8'20.86"W | 200 | 110 | 35 | 7.70E+05 | 1-15 |
| Cleft-split | 40°30'57.04"S, 72°10'2.40"W | 180 | 100 | 30 | 5.40E+05 | |
| Cleft-split | 40°31'50.61"S, 72° 8'13.27"W | 340 | 140 | 35 | 1.67E+06 | |
| Cleft-split | 40°32'32.92"S, 72° 9'8.37"W | 160 | 80 | 30 | 3.84E+05 | |
| Cleft-split | 40°31'57.23"S, 72° 8'29.28"W | 250 | 150 | 35 | 1.31E+06 | |
| Cleft-split | 40°31'23.44"S, 72° 9'51.94"W | 190 | 50 | 30 | 2.85E+05 | |
| Average | | 220 | 105 | 32.5 | 8.26E+05 | |

## 8.3 Appendix C: Microstructural characterisation

Microstructural analysis focussed on identifying crystal types, sizes and volumes, as well as the proportion and shape of vesicles. Samples collected for microstructural analysis from the Cordón Caulle lava flow and Medicine Lake Volcano, were cut using a precision thin sectioning saw at Lancaster University and the cut face was marked-up with the preferred thin section location. The cut face of the hand specimen was photographed using a digital SLR camera. Polished thin sections of samples were produced at Durham University and University of Leicester. Samples were vacuum-impregnated with clear resin prior to thin sectioning to help preserve delicate vesicle textures.

Microscopy of samples was performed using a petrographic microscope and scanning electron microscopy (SEM). Optical microscopy of thin sections was performed at Lancaster University to identify textures and microstructural characteristics. This identified features of interest, such as crystalline masses, for further SEM analysis at the British Geological Survey, and aided in mineral phase identification. Images of thin sections were captured using a camera mounted on top of the microscope. Data from SEM analysis, as well as associated image analysis, contributed to Sections 4 and 5. Analysis from synchrotron-cT data of lava samples from Cordón Caulle are also used in Section 4 to show the true shapes of vesicles.

### *8.3.1 SEM analysis*

In order to understand the data generated from SEM imagery of lava samples, it is first worth considering how an SEM works. SEMs use a beam of concentrated electrons to build a rasterised image of a sample that shows the intensity of reflected/emitted electrons from a sample. In some cases an SEM can image down to a resolution of 1 nm (depending on the beam width and current used), but imaging to resolutions of tens

to hundreds of nanometres is more common. To generate the electron beam, a tungsten filament is heated to >2000 °C, the resultant electrons are then passed through condensers and apertures to give a concentrated beam (Reed, 2005). The SEM works under vacuum conditions to reduce electron scattering and avoid filament burnout. The electron beam does not just record the surface of the sample but can penetrate the sample to ~2 orders of magnitude greater than the beam width (Wells, 1974), depending whether operation is in secondary electron (surface only) or backscatter (surface and penetrates) mode.

Here, SEM images were captured in backscatter electron (BSE) mode. BSE images are used to analyse textural and compositional variations across the surface of a sample, such as a thin section (Reed, 2005). These images are produced from the interaction between the electron beam and atomic nuclei, with the electrons being deflected by the atomic nucleus, the electrons are then detected by a backscatter detector. In BSE mode, the angle of deflection is greater with a higher atomic mass and, as such, electrons deflected by a high amount do not travel as far before reaching the detector, which reduces the amount of energy lost by these electrons (Reed, 2005). As a result, minerals with a higher atomic mass appear lighter in BSE images, due to the higher energy electrons reaching the detector (Ginibre et al., 2002).

X-ray spectroscopy can be conducted synchronously with SEM analysis as X-rays are a by-product of the ejection of a secondary electron (Reed, 2005). After the ejection of an inner atomic electron, an outer atomic electron will move to fill the space previously occupied by the ejected electron. As the atomic structure of each element is unique, the energy released during movement of an electron is indicative of the elemental composition (Reed, 2005). X-ray spectrometry can be used to produce elemental maps across a sample, or can be used for spot analysis to determine the elemental make up of a feature of interest.

#### 8.3.1.1 Application of SEM

The SEM was used to look at variations in crystallinity and vesicularity between samples and lava flows. SEM analysis of thin sections from Cordón Caulle and the Medicine Lake lava flows, was performed at the British Geological Survey using a LEO 435VP variable pressure digital scanning electron microscope. Thin sections were carbon coated at the British Geological Survey to help reduce charging of the surface of the sample. Phase/mineral identification was aided by qualitative observation of energy-dispersive X-ray spectra recorded simultaneously during SEM observation, using an Oxford Instruments INCA energy-dispersive X-ray microanalysis (EDXA) system. Images were captured from thin sections in back scatter electron (BSE) mode for further image analysis. BSE mode was chosen as it allows for textural analysis of petrographic thin sections. SEM images are presented in Section 4 and 5.

The SEM was used at high vacuum, with EHT (Extra High Tension, i.e. the voltage through which electrons are accelerated) set at 20 kV, the beam current (I Probe, i.e. the number of electrons in the beam and a proxy for beam width) at 400/500 pA, and WD (working distance, i.e. the distance between the sample and detector) set at 19 mm. These settings were optimal for imaging between 1 mm and ~2 microns. To resolve features <1 micron, the beam current was reduced to 250 pA, to reduce the beam width, and the WD was reduced to 10 mm, to increase the number of electrons reaching the detector at the lower beam current values.

#### 8.3.1.2 Image analysis

Image analysis of BSE SEM images was conducted in ImageJ to determine microlite crystallinity of samples from Cordón Caulle. Due to the poor contrast between microlites and the interstitial glass, the microlite outlines were first traced in Adobe Illustrator to give a black and white image of the thin section (Fig. 8C.1). This image

was then imported into ImageJ, scaled, and analysed for crystal area, centroid and fit ellipse, as required for use with CSD corrections (Fig. 8C.1). The results were then imported into CSD corrections (Higgins, 2000, 2002), to give the crystal volume, and other data such as crystal size distributions. The volumes presented in Section 4 are from intersection data (CSD corrections), which permits automatic stereological

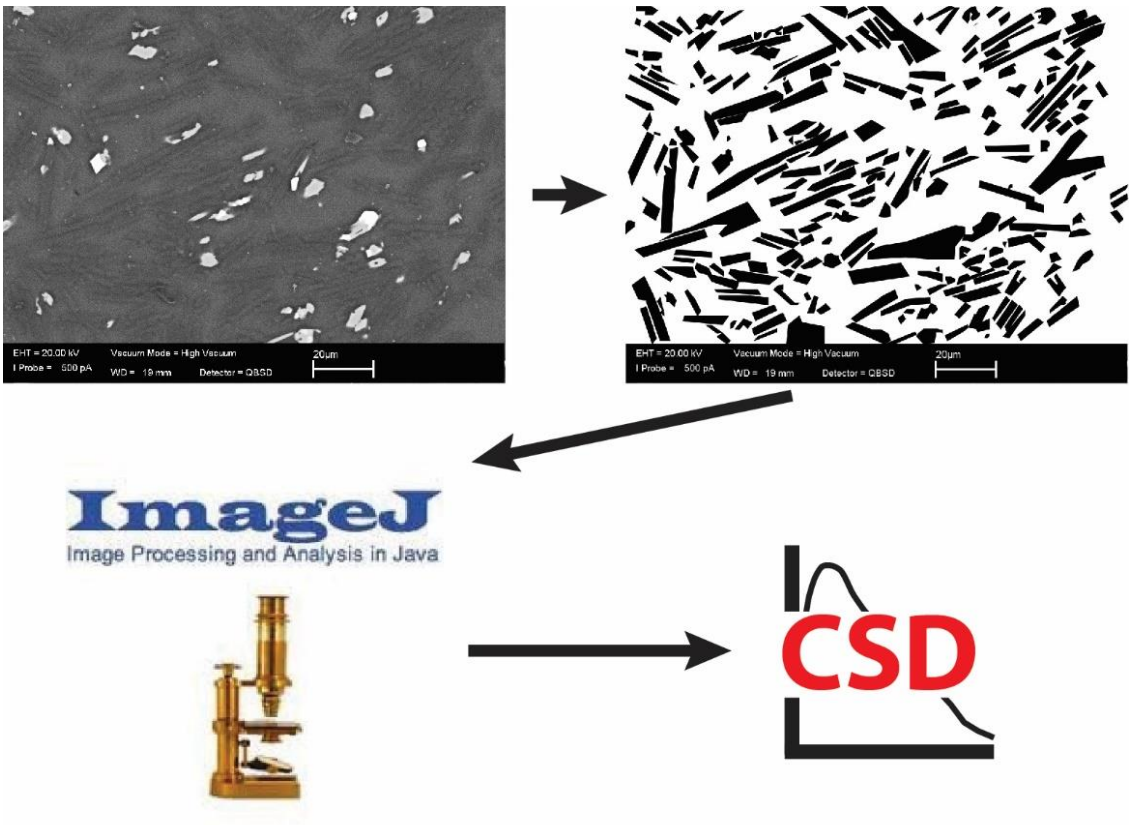


Figure 8C.1: Illustration of the methodology to determine crystal volumes. An initial SEM image is traced to highlight the microlites. This is imported into ImageJ to measure the traced microlites, this information is then imported into CSD corrections, where a stereographic correction is applied.

correction within CSD corrections (Higgins, 2002). This is needed to correct for the effect of randomly cutting through a crystal population within a rock, but does not incorporate the effect of variable aspect ratio.

To test the accuracy with which ImageJ measures the areas of shapes that are similar in size and shape (rectangular) to the microlites analysed in the samples, of known

size were imported into ImageJ and measured for area of the total image. This found deviations from the true total areas of 0.5 – 4.5%, with errors on individual rectangles up to 7%. These errors were at their highest when the rectangles were rotated 45° from horizontal. The larger errors in the rotated image could be due to pixilation of what would have been a true straight line, leading to a larger number of pixels and so a greater area. Alternatively, the errors could arise when setting the scale, to do this in ImageJ a line is drawn between two points of known distance. It is difficult to do this to a high precision and so a small error (~1 – 2% of the scale bar length) could be introduced at this stage of processing, but errors should be similar for comparable magnifications.

Given the low contrast between microlites and glass in the SEM images it is not always possible to trace every crystal and so some may be omitted. However, relatively few crystals will have been missed during tracing, so the effect on the results will likely be small. Furthermore, we find good agreement (within 5%) with crystal volumes determined by Schipper et al. (2015) from BSE image crystal areas and from X-Ray Diffraction (XRD) analysis of comparable samples from the same lava flow.

### *8.3.2 Microstructural data provided*

SEM images and resulting microlite traces are provided on Pages 309-313. A table summarising the microlite volume is given on Page 314. A table showing vesicularities in different samples is given on Page 315. The inferred crystallisation history of the Cordón Caulle lava flow is provided on Page 316.

# Breakouts (1/3)

## CC_A1_05

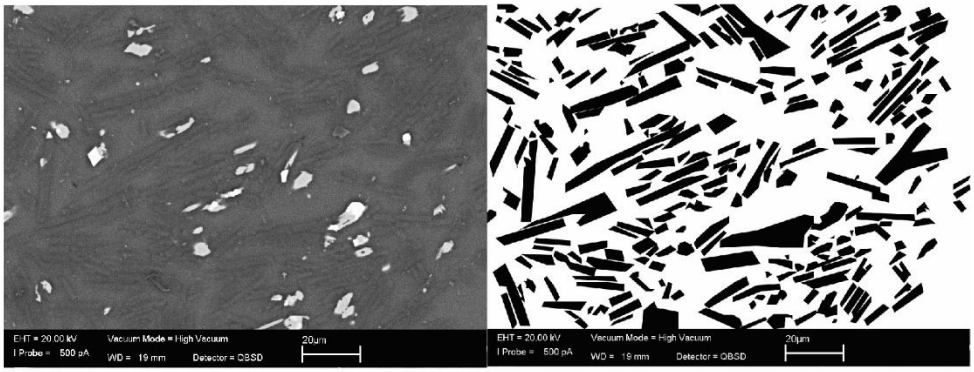


## CC_A1_15

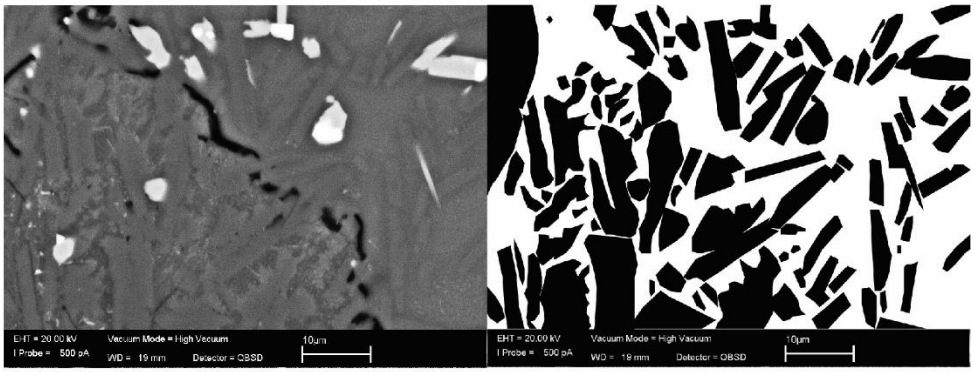


## CC_B5_19

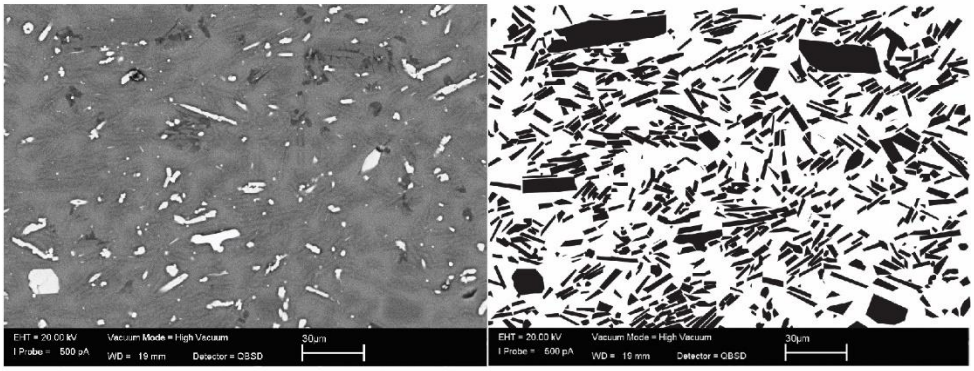


## CC_C1_10

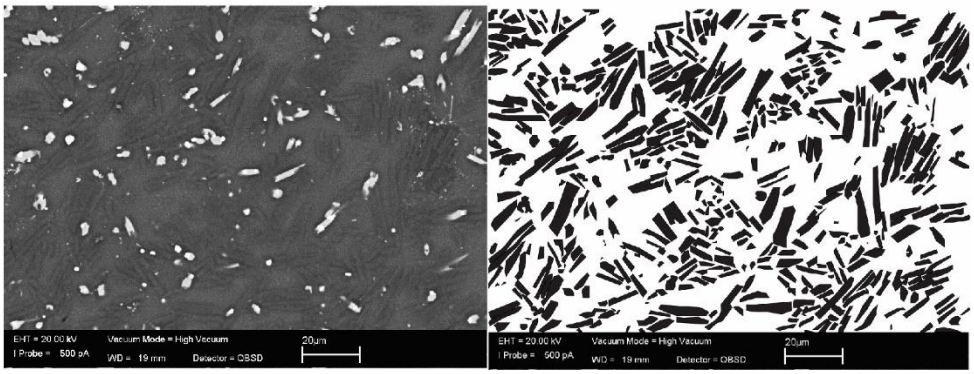

## Breakouts (2/3)

### CC_C1_13

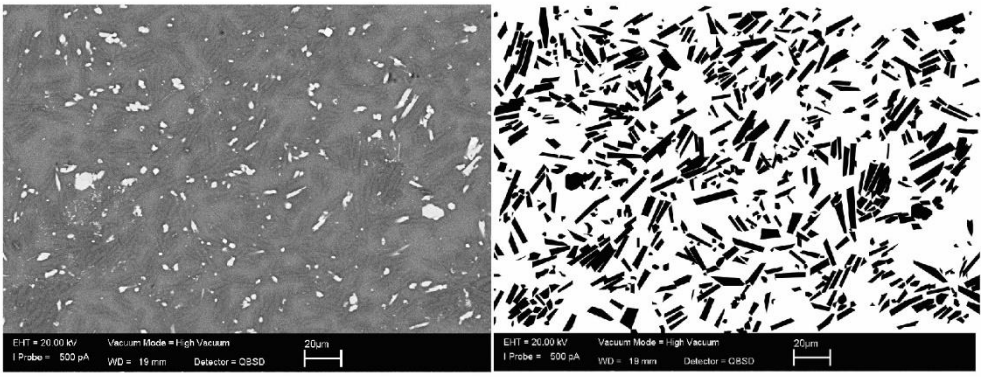


### CC_D1_03

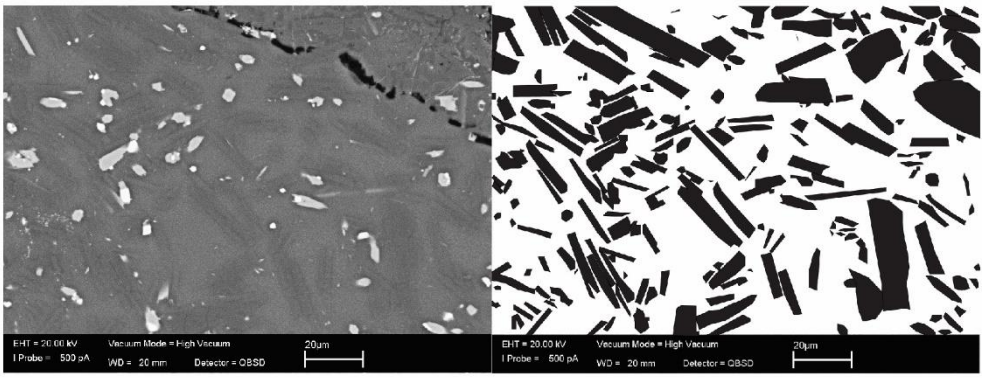


### CC_D1_15

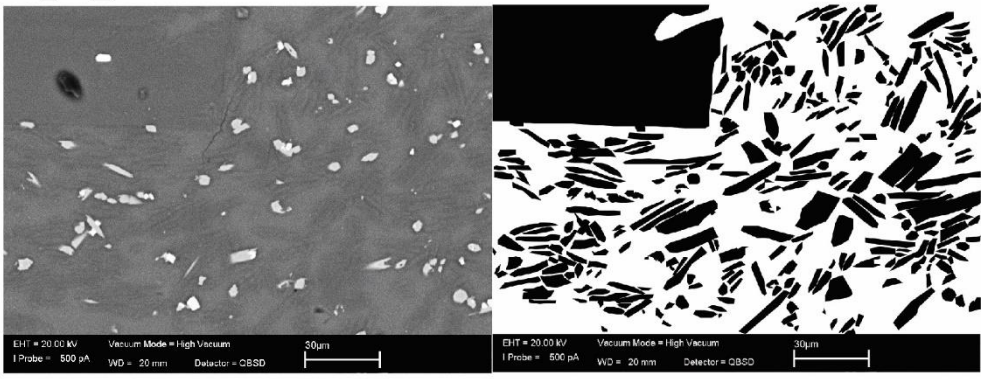


### CC_G1_09

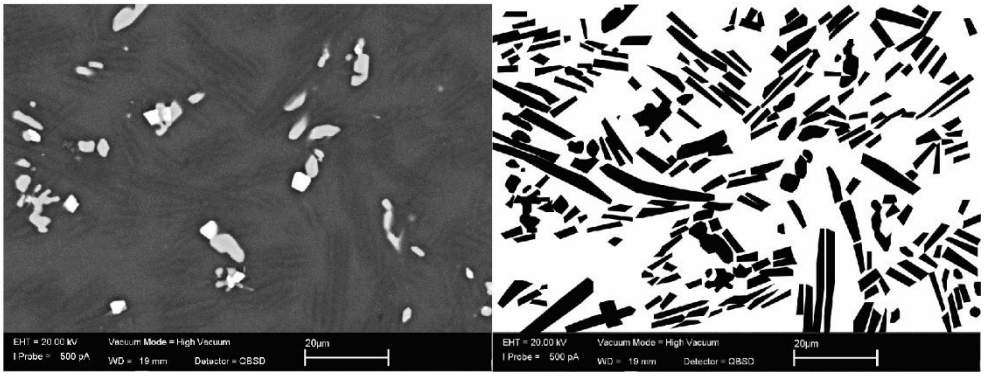

## Breakouts (3/3)

### CC_G1_20

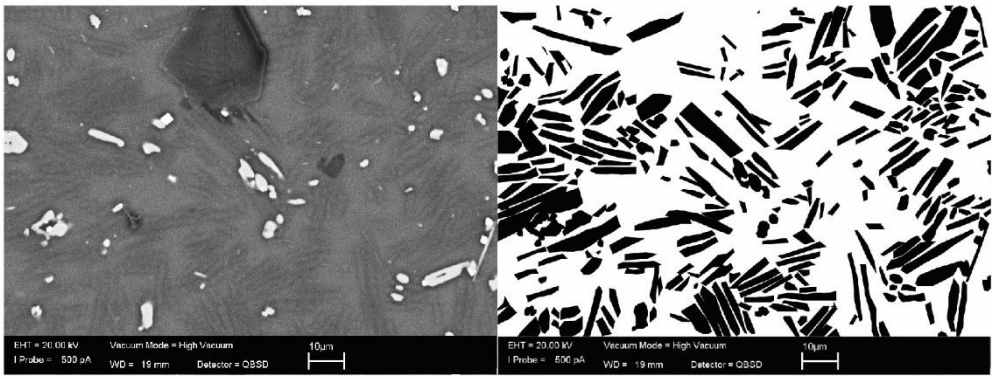


### CC_SB02_34

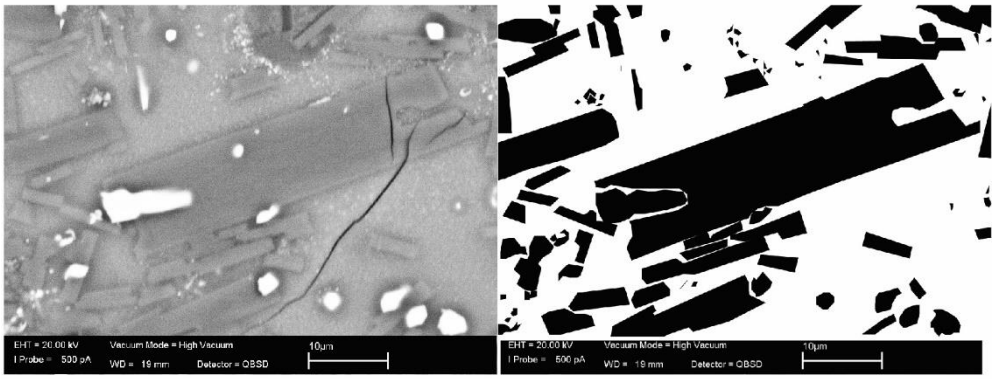


### CC_SB03_17

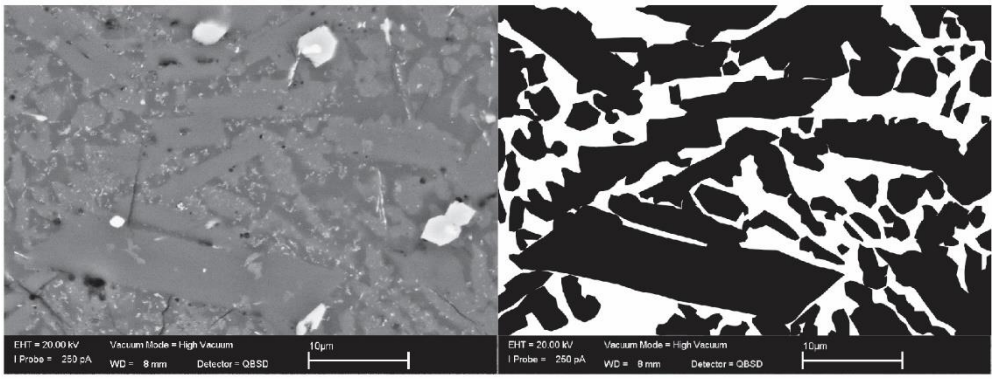


### CC_SB03_18

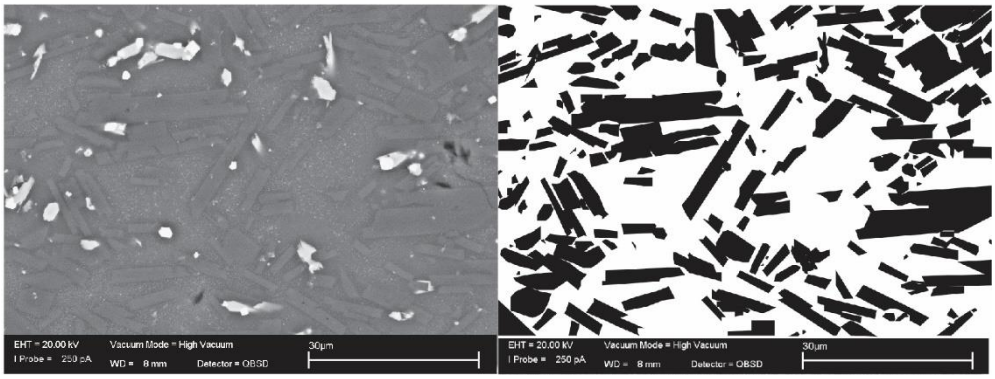

# Vent samples (1/1)

## CC_B3_05

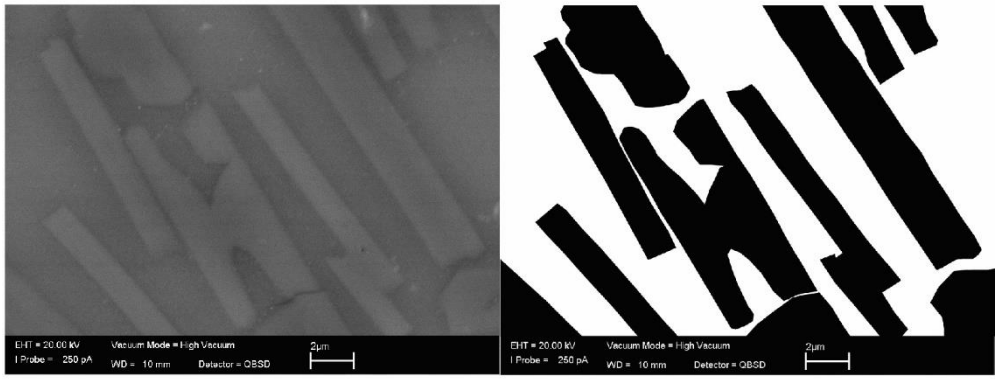


## CC_B3_06

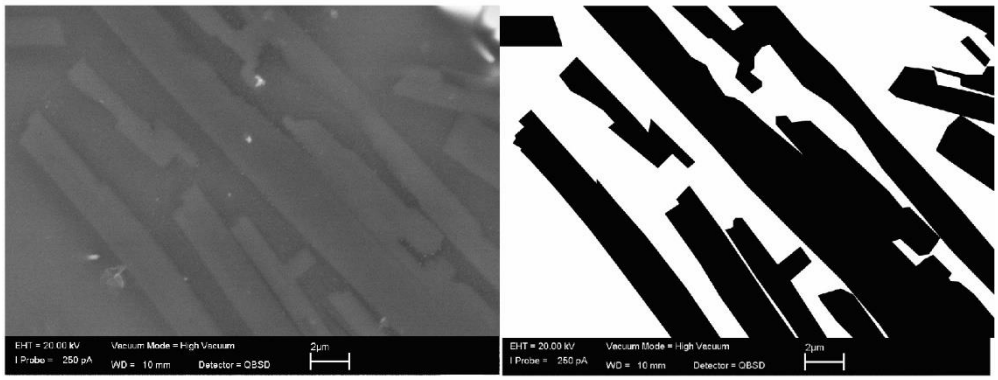


## CC_B3_12

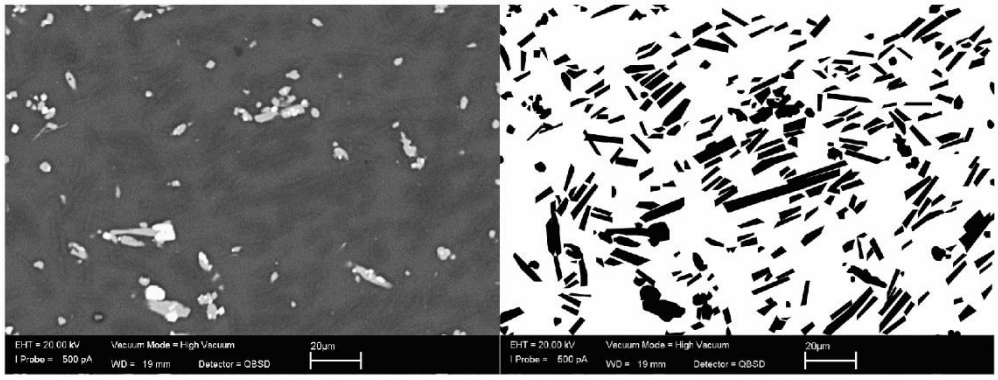


## CC_C3_14

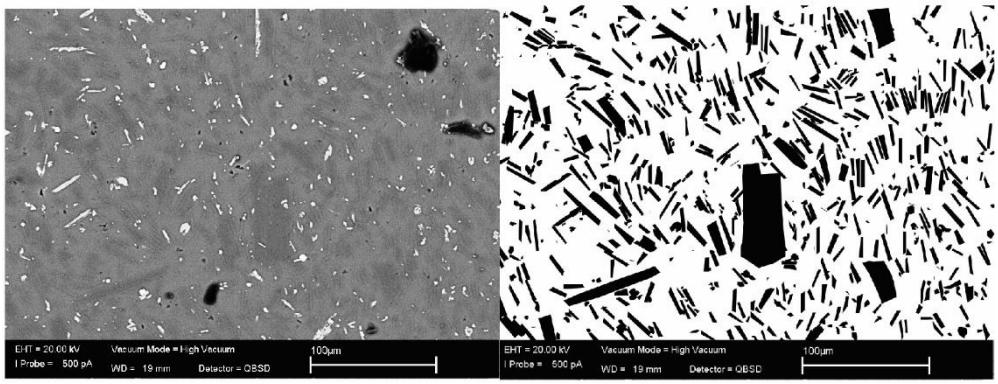

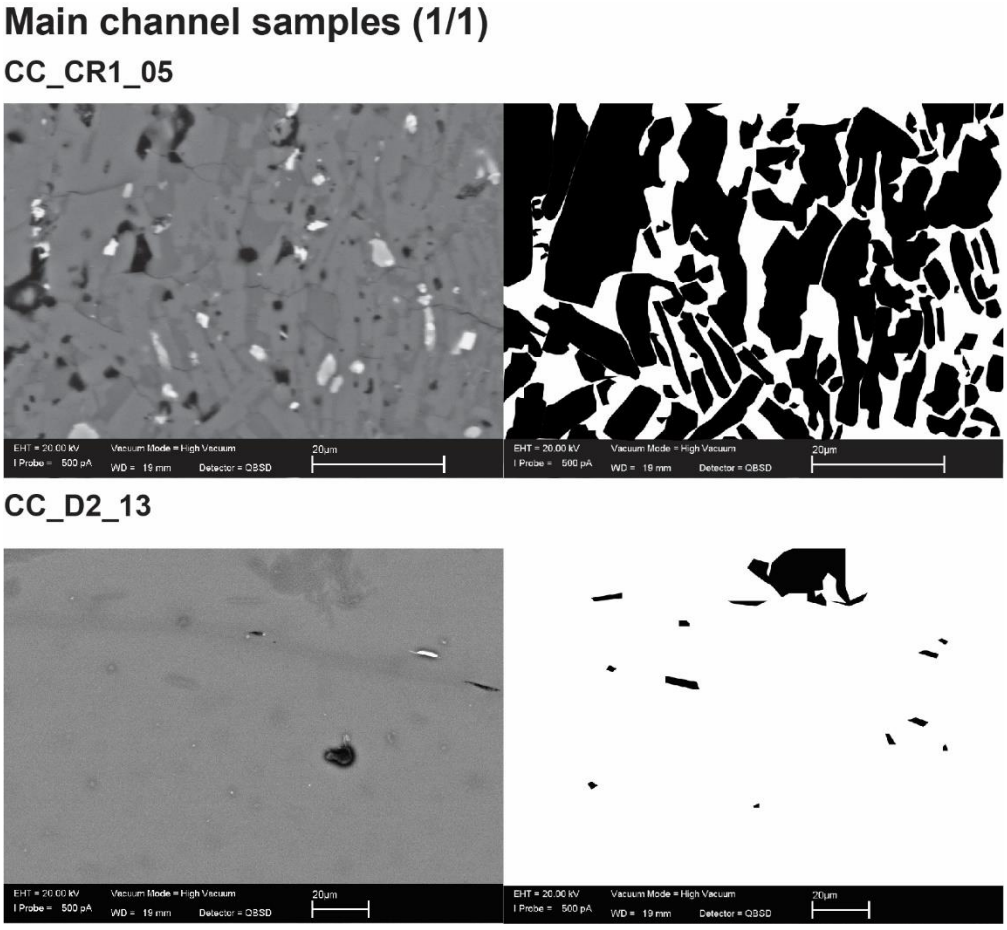


Figure 8C.2: SEM images and associated microlite traces of samples used to derive crystal volumes (provided in Table 8C.1). Samples are from breakouts, vent, and main channel lava.

Table 8C.1: Crystallinity of Cordón Caulle samples

| Sample number | Crystal area (%) | Crystal volume from intersection data (%) | Notes |
|---|---|---|---|
| **Breakouts** | | | |
| CC_A1_05 | 49.4 | 30.61 | |
| CC_A1_15 | 49 | 48.49 | Half of image devitrified band |
| CC_C1_10 | 29.8 | 31.76 | |
| CC_C1_13 | 25.6 | 27.11 | |
| CC_D1_03 | 30.8 | 25.8 | With devitrification in ~1/8 of image |
| CC_D1_03 | 40.4 | 34.46 | With devitrification in ~1/8 of image including crystals on image edge |
| CC_D1_15 | 44.8 | 42.13 | |
| CC_G1_09 | 34.9 | 31.03 | |
| CC_G1_20 | 35.3 | 33.63 | |
| CC_B5_19 | 37.2 | 32.27 | |
| CC_SBO2_34 | 55 | 38.36 | |
| CC_SBO3_18 | 32.5 | 40.93 | |
| CC_SBO3_17 | 58.4 | 67.84 | Devitrified band |
| **Vent** | | | |
| CC_B3_05 | 28.2 | 46.08 | High mag images |
| CC_B3_06 | 41.4 | 51.03 | High mag images |
| CC_B3_12 | 22.8 | 21.35 | |
| CC_C3_14 | 18.8 | 22.45 | |
| **Main channel Surface** | | | |
| CC_D2_13 | 4.48 | 2.707 | |
| **Main channel core** | | | |
| CC_CR1_05 | 92.9 | 67.37 | |

Table 8C.2: Vesicularity of samples

| Sample number | Vesicle area (%) |
|---|---|
| **Breakouts** | |
| CC_A1_07 | 16.29 |
| CC_B1_01 | 20.46 |
| CC_B5_07 | 23.03 |
| CC_C1_14 | 17.34 |
| CC_G1_15 | 29.19 |
| CC_SB02_24 | 15.88 |
| **Vent** | |
| CC_B3_01 | 39.41 |
| CC_B3_09 | 48.01 |
| CC_C3_10 | 33.51 |
| **Main channel core** | |
| CC_CR1_11 | 6.02 |
| CC_CR2_03 | 3.15 |
| **Main channel surface** | |
| CC_A2_01 | 28.67 |
| CC_A2_15 | 33.45 |

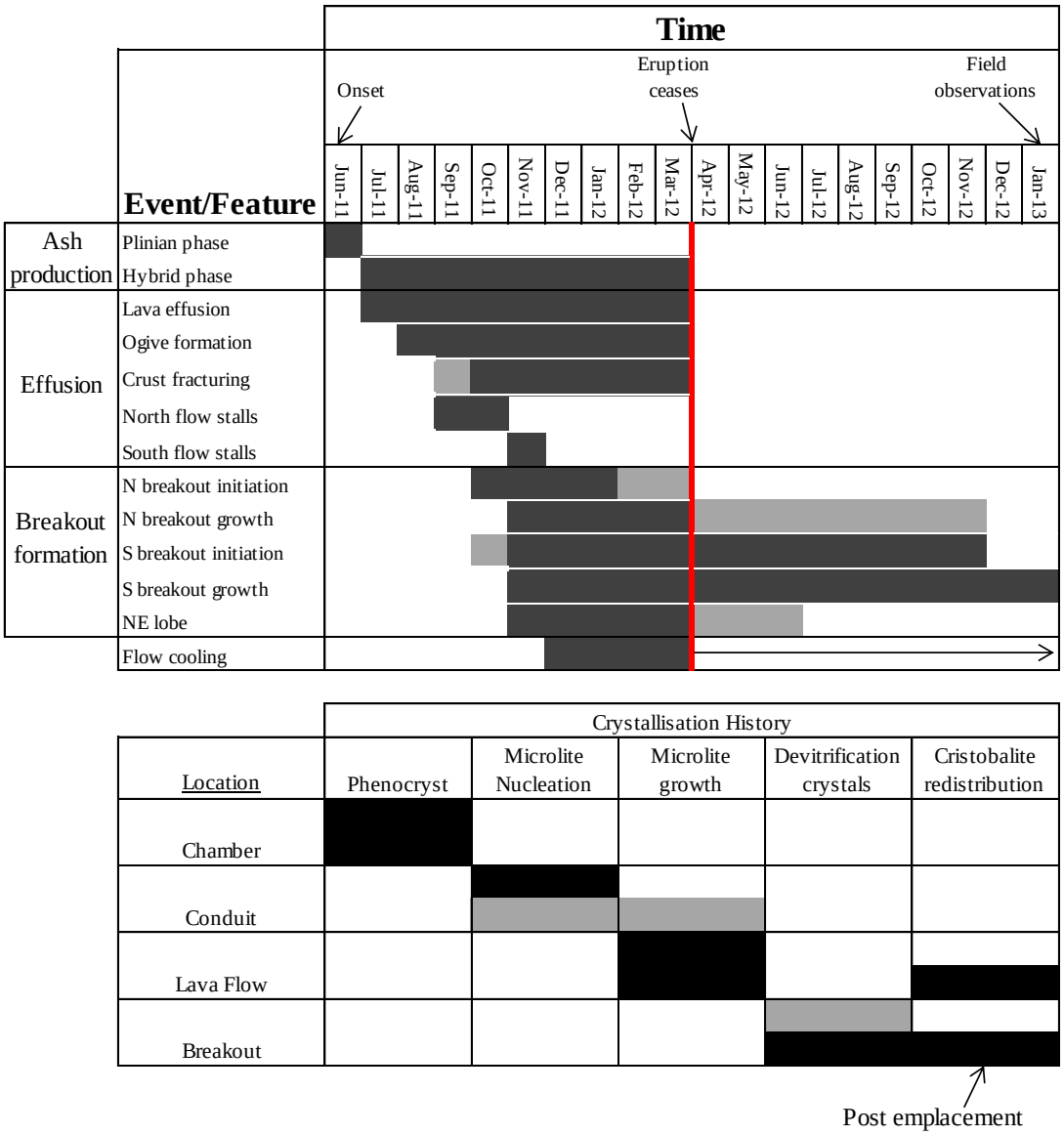


Figure 8C.3: Timeline of observed eruption and lava flow emplacement processes, grey bars show that the process was not pervasive or it was unclear whether it was occurring. The bottom section shows the inferred timing and location of formation of different crystal populations.

## 8.4 Appendix D: Analytical modelling of lava flow lengths

Analytical modelling of lava flow lengths in Section 3 was carried out using Microsoft EXCEL. The models were selected in part due to their ease of use, relative simplicity and their demonstrable ability to model lava flows across the compositional spectrum (Castruccio et al., 2013). Full spreadsheet versions of the modelling results can be found on the attached CD. The details of the modelling, the sources of the inputs used and their uncertainties, can be found in Section 3, as well as the effects of varying key parameters on modelled results. The graphs presented in Section 3 were generated from the EXCEL data using QtiPlot.